Targeting the M_1 muscarinic acetylcholine receptor in neurodegeneration

Sarah Hesse

MSc (Hons)

Submitted in fulfilment of the requirements for the Degree of

Doctor of Philosophy

School of Molecular Biosciences

College of Medical, Veterinary & Life Sciences

University of Glasgow

December 2022

Abstract

Alzheimer's disease (AD) is the most common neurodegenerative disorder, and to date, no disease-modifying treatments exist. The M_1 muscarinic acetylcholine receptor (mAChR) is an established therapeutic target for the symptomatic treatment of AD, and drugs activating the M_1 mAChR have been shown to improve cognitive decline and behavioural symptoms in several clinical trials. Pre-clinical evidence also suggests that M_1 mAChRs may also have disease-modifying effects in neurodegeneration, such as modification of the classical AD hallmarks, amyloid ß (Aß) and tau. Due to the conserved nature of the classic orthosteric binding site of the five mAChR subtypes, targeting one subtype via this binding site specifically has proved challenging. The development of compounds targeting the less conserved allosteric site has enabled significant improvements in subtype selectivity. Chronic dosing with the M_1 mAChR positive allosteric modulator (PAM) VU0486846 has demonstrated disease-modifying potential in a murine prion model of terminal neurodegeneration and in an Aß-based genetic AD model. This thesis aimed to assess the effect of chronic treatment with the M_1 mAChR PAM VU0486846 in the rTG4510 tauopathy mouse model. The results show that VU0486846 did not affect the expression of neuropathological markers of disease, such as phosphorylated tau and glial fibrillary acidic protein, but reversed elevated levels of coagulation factor III and cystatin C that were observed in diseased mice when compared to controls. The normalisation of coagulation factor III and cystatin C, which have both been shown to be dysregulated in AD patients, remains an interesting avenue for further research. As part of trying to understand the potential of the M_1 mAChR as a drug target, it is crucial to also determine receptor localisation. Therefore, this thesis also aimed to assess M_1 mAChR distribution in the brain using a M_1-monomeric enhanced green fluorescent protein (meGFP) mouse line, which expresses the meGFP tagged version of the M_1 mAChR in the endogenous gene locus. Tissue clearing was used to visualise the receptor and a range of studies was performed to explore the utility of the meGFP-tagged M_1 mAChR. Overall, this thesis identified some novel changes following chronic treatment with a M_1 mAChR PAM in a tauopathy mouse model, which warrant further investigation to fully evaluate the potential of targeting the M_1 mAChR in neurodegeneration.

Table of Contents

List of Tables

List of Figures

List of Publications

Marsango, S., Jenkins, L., Pediani, J.D., Bradley, S.J., Ward, R.J., **Hesse, S.**, Biener, G., Stoneman, M.R., Tobin, A.B., Raicu, V. and Milligan, G., 2022. The M1 muscarinic receptor is present in situ as a ligand-regulated mixture of monomers and oligomeric complexes. Proceedings of the National Academy of Sciences of the United States of America, 119(24), p.e2201103119.

Scarpa, M., Molloy, C., Jenkins, L., Strellis, B., Budgett, R.F., **Hesse, S.**, Dwomoh, L., Marsango, S., Tejeda, G.S., Rossi, M. and Ahmed, Z., 2021. Biased M1 muscarinic receptor mutant mice show accelerated progression of prion neurodegenerative disease. Proceedings of the National Academy of Sciences, 118(50).

Scarpa, M., **Hesse, S.,** and Bradley, S.J., 2020. M1 muscarinic acetylcholine receptors: a therapeutic strategy for symptomatic and disease-modifying effects in Alzheimer's disease?. Advances in Pharmacology, 88, pp.277-310.

Acknowledgements

Just like raising a child, completing a PhD takes a village. It can be done without, but thankfully I did not have to.

First, I would like to thank my supervisors Sophie and Andrew. There were many challenges over the years, and it was a learning experience for all of us. Andrew, thank you for sharing your vast expertise. Sophie, you have particularly been a shining star by providing a positive role model as a successful and compassionate researcher and leader. Without you this PhD would never have been completed, so thank you for helping me cross the finish line.

I cannot begin to express my gratitude to Aisling, Louis, Natasja, Gonzalo, Becca and Miriam, who have read various chapters and helped me improve this thesis. Thank you to Colin and Lisa, and everyone at the animal unit for their help with the mouse work. I would also like to recognise the assistance that I received from Danny Allen (University of Oxford) by providing the MATLAB code for analysing the results of the cytokine array, from Colin Loney (CVR) for all the help in imaging brain samples on the Zeiss Lightsheet Z.1 and from Cristina Martinez Gonzalez (University of Edinburgh) for providing the modified iDISCO protocol and her help with the Ultramicroscope II Light Sheet Microscope for imaging cleared samples. I would also like to acknowledge Sophie for letting me use the fear conditioning data in Figure 3.10 and the open field results in Figure 5.8, as well as Aisling for providing the data on changes in basal freezing response in M_1-WT mice in Appendix Figure 3.

A big thanks go to my beloved biology teacher Anjali Bhardwaj, who sparked my interest in neuroscience and set me on the path to this PhD.

Thank you also to Rachel Paisley for keeping my body running throughout my PhD. After every appointment with you, I felt both physically and mentally much lighter.

I am especially grateful to my friends in and outside of the lab in Glasgow, at home and around the world. Lunch breaks with Becca, walks in the park with Emily and Narissa and frequent zoom check-ins with Henni and Jule, just to

name a few, have particularly helped to keep me afloat during the pandemic and beyond. There are many more and if I haven't mentioned you specifically, know that I appreciate you anyway!

While the pandemic made it difficult to see family abroad, thank you to my family for always being there for me and believing in me, anyway. Danke Mama und Papa, Oma Hilde und Oma Ita, Mia, Lennart und Claudia! Ohne euch wäre ich niemals so weit gekommen!

Leonie, as always you have been my rock. Your loving and calming presence and reassurance have helped me manage a chronic pain condition, welcome a baby into our lives in the middle of a pandemic without family support and complete my PhD. Without you, none of this would have been possible. Finally, Frieda, my little ray of sunshine, thank you for being there and helping me live in the moment.

Author's Declaration

December 2022

"I declare that, except where explicit reference is made to the contribution of others, this thesis is the result of my own work and has not been submitted for any other degree at the University of Glasgow or any other institution."

Sarah Hesse

Definitions/Abbreviations

3DISCO	3D imaging of solvent-cleared organs
Aß	amyloid ß
AC	adenylyl cyclase
ACh	acetylcholine
AChE	acetylcholinesterase
AChEI	acetylcholinesterase inhibitor
AD	Alzheimer's disease
ADAM	a disintegrin and metalloproteinase
AICD	APP intracellular domain
AP	adaptor protein
ApoE	apolipoprotein E
APP	amyloid precursor protein
APS	ammonium persulfate
AUC	area under the curve
BQCA	benzyl quinolone carboxylic acid
BSA	bovine serum albumin
CA	cornu ammonis
CaMKIIα	Ca2+/calmodulin-dependent protein kinase IIα
CD86	cluster of differentiation 86
ChaT	choline acetyltransferase
CHO	Chinese hamster ovary
CHRM	cholinergic receptor muscarinic
CLARITY	Clear Lipid-exchanged Acrylamide-hybridized Rigid Imaging/ Immunostaining/ in situ-hybridization-compatible Tissue hYdrogel
CNS	central nervous system
CoA	acetyl coenzyme A
COPD	chronic obstructive pulmonary disease
CRD	cysteine rich domain
cryo-EM	cryogenic electron microscopy
C_T	cycle threshold
DAB	3,3′-Diaminobenzidine
DAG	diacyl glycerol
DAPI	4',6 diamidino-2-phenylindole
DBE	dibenzyl-ether
DBPS	Dulbecco's Phosphate Buffered Saline

DCM	dichloromethane
DEPC	diethyl pyrocarbonate
DG	dentate gyrus
DIV	days in vitro
ECL	extracellular loop
eGFP	enhanced green fluorescent protein
EMA	European Medicines Agency
EOAD	early-onset Alzheimer's disease
ERK	extracellular signalling-regulated kinase
ES	embryonic stem
FAD	familial Alzheimer’s disease
FBS	fetal bovine serum
FDA	Food and Drug Administration
FTLD	frontotemporal lobar dementia
FGF1	fibroblast growth factor 1
GAIN	GPCR autoproteolysis-inducing
GAP	GTPase-accelerating protein
GASP	GPCR-associated sorting protein
GDP	guanosine diphosphate
GEF	guanine nucleotide exchange factor
GFAP	glial fibrillary acidic protein
GFP	green fluorescent protein
GI	gastrointestinal
GPCR	G protein-coupled receptor
GRK	G protein-coupled receptor kinase
GSK-3β	glycogen synthase kinase 3 β
GTP	guanosine triphosphate
GWAS	genome wide association studies
HBSS	Hanks' Balanced Salt Solution
H&E	haematoxylin & eosin
HM	hydrogel monomer
HRP	horseradish peroxidase
IBA1	ionized calcium binding adaptor molecule 1
ICC	immunocytochemistry
ICL	intracellular loop
iDISCO	immunolabeling-enabled imaging of solvent cleared organs
IHC	immunohistochemistry

IL	interleukin
IMPase	inositol monophosphatase
IP1	inositol monophosphate
IP2	inositol diphosphate
IP3	inositol trisphosphate
iPSCs	induced pluripotent stem cells
KO	knockout
LOAD	late onset Alzheimer's disease
LSFM	light sheet fluorescence microscopy
mAChR	muscarinic acetylcholine receptor
MAPK	mitogen-activated protein kinase
MCI	mild cognitive impairment
meGFP	monomeric enhanced green fluorescent protein
MW	molecular weight
NAL	neutral allosteric ligand
NAM	negative allosteric modulator
NFTs	neurofibrillary tangles
NMDA	N-methyl D-aspartate
NMS	N-methyl scopolamine
PAM	positive allosteric modulator
PB	phosphate buffer
PBS	phosphate buffered saline
PD	Parkinson’s disease
PFA	paraformaldehyde
PKA	protein kinase A
PIP2	phosphatidylinositol 4,5-bisphosphate
PKC	protein kinase C
PLC	phospholipase C
PLP	periodate–lysine–paraformaldehyde
PS	presenilin
pTau	phosphorylated tau
qPCR	quantitative PCR
RAMPs	receptor activity-modifying proteins
RFP	red fluorescent protein
RGS	regulator of G protein signalling
ROI	region of interest
RI	refractive index

RIPA	radio immunoprecipitation assay
RT	reverse transcription
sAPPα	soluble APP α fragment
sAPPβ	soluble APP β fragment
SBC	SDS/ boric acid clearing buffer
TEMED	tetramethylethylenediamine
THF	tetrahydrofuran
TM	transmembrane
TRE	tetracycline operon–responsive element
TREM2	triggering receptor expressed on myeloid cells
tTA	tetracycline-controlled transactivator
vDISCO	nanobody(V_HH)-boosted 3D imaging of solvent-cleared organs
VEH	vehicle
VFT	venus flytrap
WT	wild-type

Chapter 1 Introduction

1.1 G protein-coupled receptors

The G protein-coupled receptors (GPCR) superfamily forms the largest class of cell surface receptors in the human genome encompassing more than 800 receptors (Fredriksson et al., 2003, Lefkowitz, 2007, Hauser et al., 2017). Due to their importance in many physiological processes, GPCRs are the most common target of clinically used drugs, with about a third of drugs on the market targeting this superfamily (Santos et al., 2017, Hauser et al., 2017, Erlandson et al., 2018). Nevertheless, only about a third of human non-olfactory GPCRs have been targeted and approved as therapeutics, leaving more than 200 GPCRs to be explored for their therapeutic potential, which have been suggested to be particularly promising in genetic, eye, immune and skeletal system disorders based on the receptors' disease associations (Hauser et al., 2017). Within the GPCR superfamily, preferred ligands can range from ions to small molecules, hormones, large proteins and sensory stimuli, such as odorants, due to the highly divergent sequences in the extracellular ligand-binding regions (Southan et al., 2016, Wacker et al., 2017). GPCRs are generally characterised by an extracellular *N* terminus, seven transmembrane (TM)-spanning α-helices (TM1-7) connected by intra- (ICL) and extracellular loops (ECL), and an intracellular *C* terminus (Rosenbaum et al., 2009). Upon extracellular ligand binding, generally to the *N* terminus or TM binding pocket, intracellular signalling cascades are activated, commonly involving G proteins (Lefkowitz, 2007, Wacker et al., 2017).

1.1.1 Classification of GPCRs

Over the years, several classification systems for GPCRs have been proposed based on different characteristics, such as location of the ligand binding pocket, physiological, structural or functional features (Bockaert and Pin, 1999, Fredriksson and Schiöth, 2005). The commonly used GRAFS system is followed here, grouping GPCRs in the human genome into phylogenetical families based on shared sequence and structural features (Fredriksson et al., 2003, Fredriksson and Schiöth, 2005, Schiöth and Fredriksson, 2005). According to the GRAFS system, GPCRs can largely be categorised into five main families, namely the Glutamate (class C), Rhodopsin (class A), Adhesion (class B2), Frizzled (class F)/Taste2 (class T2) and Secretin (class B1) families (Figure 1.1) (Fredriksson et

al., 2003, Fredriksson and Schiöth, 2005, Schiöth and Fredriksson, 2005). In the current GPCR database (GPCRdb, gpcrdb.org), the GRAFS system is largely followed with the only difference that Frizzled and Taste2 receptors are split into separate groups (Fredriksson et al., 2003, Fredriksson and Schiöth, 2005, Kooistra et al., 2021).

The **glutamate receptor family** (class C) contains the metabotropic glutamate receptors, γ-aminobutyric acid type B receptors, a calcium-sensing receptor and sweet and amino acid Taste1 (TAS1) receptors (Okamoto et al., 1998, Fredriksson et al., 2003, Ellaithy et al., 2020, Kooistra et al., 2021). Receptors of this family commonly exist as dimers (Zhang et al., 2014). While the TM domains do not share significant overall sequence similarity with other GPCRs, most members of the glutamate family possess a large extracellular *N* terminus containing the venus flytrap (VFT) domain, which is the orthosteric binding site for endogenous ligands, and a cysteine-rich domain, which connects the VFT domain and the TM domains with the exception of $GABA_B$ receptors (Figure 1.1) (Malitschek et al., 1999, Pin et al., 2003). It has been proposed that the glutamate receptor family originated from fusion of a bacterial periplasmic amino acid binding protein, which evolved into the VFT domain, with an ancestral rhodopsin-like receptor (O'Hara et al., 1993, Pin et al., 2003).

The **rhodopsin receptor family** (class A) is the largest and most diverse superfamily with receptors exhibiting diverse primary structures and ligand preferences including hormones, neurotransmitters and olfactory molecules (Baldwin, 1994, Fredriksson et al., 2003, Fredriksson and Schiöth, 2005, Lagerström and Schiöth, 2008, Kooistra et al., 2021). The rhodopsin family comprises an estimated 320 to 460 olfactory receptors in addition to 286 other receptors with a range of functions (Glusman et al., 2001, Fredriksson et al., 2003, Kooistra et al., 2021), and is the GPCR family containing the largest number of therapeutically targeted receptors (Tyndall and Sandilya, 2005). Amongst these are muscarinic receptors, which are the topic of this thesis. Most receptors in the rhodopsin family are activated by a ligand binding to the TM domains or the ECLs (Figure 1.1) (Bockaert and Pin, 1999, Lagerström and Schiöth, 2008). In 2000, the bovine rhodopsin receptor was the first crystallised GPCR reported (Palczewski et al., 2000), and seven years later a high-resolution

structure of the β_2-adrenergic receptor was published (Cherezov et al., 2007). Since then increasing numbers of high-resolution structures for all GPCR families have been investigated using X-ray crystallography and more recently cryogenic electron microscopy (cryo-EM), resulting in 136 unique receptor complexes being available as of 2022, with 101 of those belonging to the rhodopsin family according to the GPCRdb (Kooistra et al., 2021). While most rhodopsin family GPCRs have a short *N* terminus without any common conserved domains, most heterogeneity can be found within the TM regions, even though some sequence motifs are shared by most receptors in the rhodopsin family (Lagerström and Schiöth, 2008).

The **adhesion receptor family** (class B2) is the second largest GPCR family in human and accounts for 33 receptors (Fredriksson et al., 2003, Lagerström and Schiöth, 2008, Kooistra et al., 2021). Preferred ligands are extracellular matrix molecules, and receptors of this family generally have long and diverse *N* termini, which possess a range of conserved domains also found in other proteins (Figure 1.1) (Bjarnadóttir et al., 2004, Krishnan et al., 2016, Purcell and Hall, 2018). These domains have been shown to be important for the binding of specific ligands (Lin et al., 2001, Lagerström and Schiöth, 2008). Additionally, almost all adhesion receptors contain a GPCR autoproteolysis-inducing domain (Krasnoperov et al., 1997, Lagerström and Schiöth, 2008, Araç et al., 2012, Nieberler et al., 2016)

The **frizzled** (class F)**/Taste2** (class T2) **receptor family** consists of two distinct clusters; the frizzled and smoothed receptor, and the Taste2 (TAS2) receptor clusters account for 11 and 25 receptors, respectively (Lagerström and Schiöth, 2008, Kooistra et al., 2021). While the two receptor clusters did not show much similarity, they have several features in common, such as the consensus sequences IFL in TM2 and SFLL in TM5, which cannot be found in the other receptor families (Fredriksson et al., 2003, Fredriksson and Schiöth, 2005). The frizzled and smooth receptors bind Wingless/Int-1 glycoproteins and Hedgehog proteins, respectively (Bhanot et al., 1996, Chen and Struhl, 1996, Lagerström and Schiöth, 2008), and are involved in control of cell fate, proliferation and polarity in the development of multi-cellular organisms (Fredriksson et al., 2003). These receptors are characterised by a 200 to 320 amino acid-long *N*

terminus containing a cysteine-rich domain, which is important for ligand binding in most of these receptors (Figure 1.1) (Wang et al., 1996, Fredriksson et al., 2003, Lagerström and Schiöth, 2008, Janda et al., 2012). The TAS2 receptor family are bitter taste receptors characterised by short *N* and *C* termini (Matsunami et al., 2000, Adler et al., 2000, Shi et al., 2003, Lagerström and Schiöth, 2008) and tastants bind to the TM domain (Figure 1.1) (Alfonso-Prieto et al., 2019).

The **secretin receptor family** (class B1) comprises 15 receptors in human and are activated by peptide hormones (Attwood and Findlay, 1994, Kolakowski, 1994, Lagerström and Schiöth, 2008, Kooistra et al., 2021). Most of the variation within this group is found in the *N* terminus, however, this region has been identified to be particularly important for ligand binding (Figure 1.1) (DeAlmeida and Mayo, 1998, Grace et al., 2004, Lagerström and Schiöth, 2008).

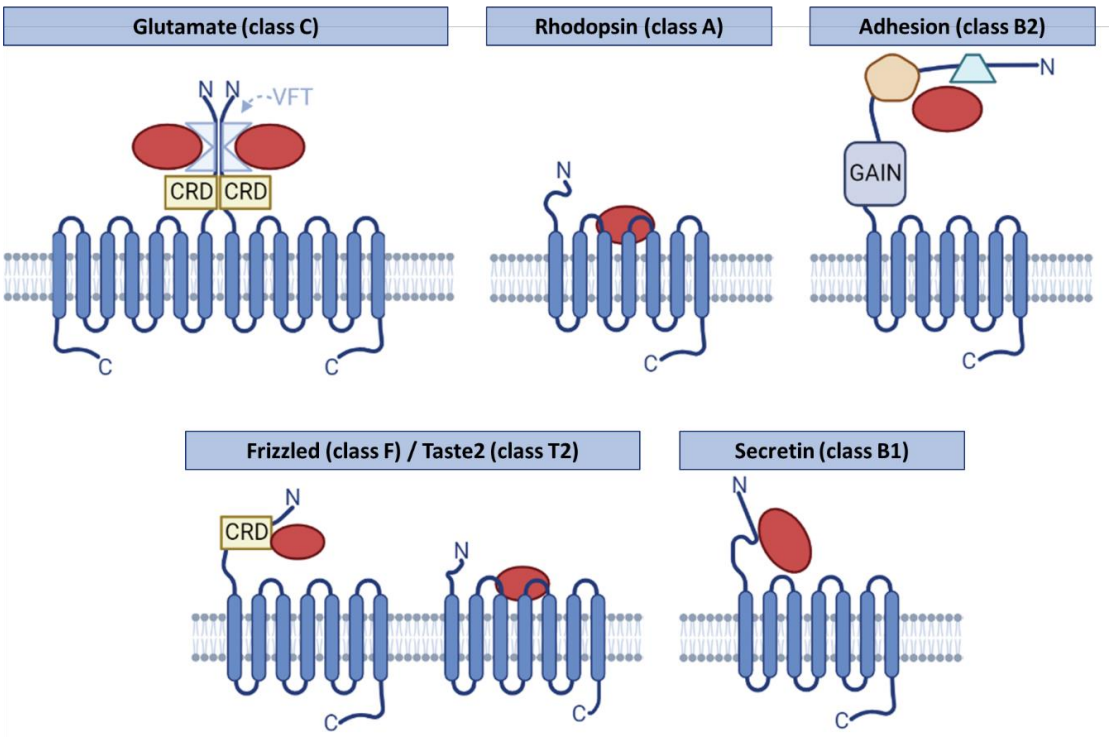

Figure 1.1 Simplified structural features of GPCR families according to the GRAFS classification system. GPCRs share a common architecture including an extracellular *N* terminus, seven transmembrane (TM) α-helices and an intracellular *C* terminus. The extracellular region is particularly diverse between GPCR families. Stereotypical ligand binding is shown as red shapes. Receptors in the glutamate family frequently dimerise. The *N* terminus contains a cysteine-rich domain (CRD) and the venus flytrap (VFT) domain, where ligand binding characteristically occurs. Receptors of the rhodopsin family generally have short *N* termini and orthosteric ligands bind within the TM cavity. Receptors of the adhesion family have long *N* termini with diverse domains important for ligand binding and contain a GPCR autoproteolysis-inducing (GAIN) domain. Receptors of the frizzled family exhibit a CRD in the *N* terminus, which is important for ligand binding. While receptors of the Taste2 family have short termini and ligands bind to the TM region, receptors of the secretin family exhibit diverse *N* termini important for ligand binding. Created using BioRender.com.

1.1.2 GPCR activation, signalling and desensitisation

1.1.2.1 G protein-dependent signalling

While GPCRs are structurally diverse, some common concepts of receptor activation and intracellular signalling apply. Ligand-induced GPCR stimulation induces active receptor conformations and triggers intracellular signalling pathways predominantly via activation of heterotrimeric guanine nucleotide-binding proteins (G proteins). These G proteins consist of Gα, Gß and Gγ subunits (Lambright et al., 1996). In the basal state, guanosine diphosphate (GDP) is bound to Gα, which in turn is tightly associated with Gßγ forming a heterotrimer (Lambright et al., 1996). Following stimulation, GPCRs undergo conformational changes and function as guanine nucleotide exchange factors (GEF), which catalyses the exchange of GDP for guanosine triphosphate (GTP). This exchange results in structural changes in the then GTP bound-Gα protein leading to the release of the Gßγ subunit complex (Hamm, 1998, Cabrera-Vera et al., 2003). Both the Gα and Gßγ subunits can activate or inhibit downstream signalling pathways (Hamm, 1998). Due to the wealth of G protein subunits encoded in the human genome, including at least 16 Gα, 5 Gß and 13 Gγ subunits (Milligan and Kostenis, 2006, Wootten et al., 2018), a range of signalling pathways can be modulated. Four main classes have been identified based on sequence similarities and preferred downstream signalling, namely $G\alpha_s$, $G\alpha_{i/o}$, $G\alpha_{q/11}$ and $G\alpha_{12/13}$ (Simon et al., 1991, Oldham and Hamm, 2006). While members of the $G\alpha_s$ and $G\alpha_{i/o}$ stimulate (Ross and Gilman, 1977) and inhibit (Hsia et al., 1984) adenylyl cyclase (AC) enzymes, respectively, $G\alpha_{q/11}$ generally activate phosphoinositide-specific phospholipase C (Rhee, 2001) and $G\alpha_{12/13}$ activate Rho-specific GEFs (Hamm, 1998, Sah et al., 2000, Worthylake et al., 2000, McCudden et al., 2005).

While it was initially thought that the only function of the Gßγ complex was to bind Gα for signal termination (Oldham and Hamm, 2006), a wealth of studies has shown that Gßγ can modulate a range of effectors, such as AC (Tang and Gilman, 1991, Taussig et al., 1994), the mitogen-activated protein kinase (MAPK) pathway (Inglese et al., 1995) and Ca^{2+}- and K^+-ion channels (Logothetis et al., 1987, Reuveny et al., 1994, Herlitze et al., 1996). The Gßγ complex has also been found to modulate regulators of G protein signalling (RGS) (Snow et al.,

1998) and regulate G protein-coupled receptor kinases (GRK)2 and GRK3, including recruitment to the membrane to stop receptor signalling (for more details see 1.1.2.2) (Haga and Haga, 1992, Stoffel et al., 1997, Li et al., 2003).

The Gα subunit possesses intrinsic GTPase activity, which hydrolyses GTP to GDP, thereby encouraging re-association of the Gαβγ heterotrimer and termination of signalling (Li et al., 1998, McCudden et al., 2005). RGS are GTPase-accelerating proteins (GAPs) and can accelerate this intrinsic GTPase activity of the Gα subunit, thereby determining the magnitude and duration of the downstream responses stimulated by GPCR activation (Hepler, 1999, Ross and Wilkie, 2000, Stewart and Fisher, 2015). Additionally, RGS can also contain scaffolding and signalling domains, thus modulating downstream signalling (Saitoh et al., 1997, Bünemann and Hosey, 1998, McCudden et al., 2005). Downstream effectors, such as members of the PLC-β family, can in turn exhibit GAP activity (Berstein et al., 1992, Kristiansen, 2004).

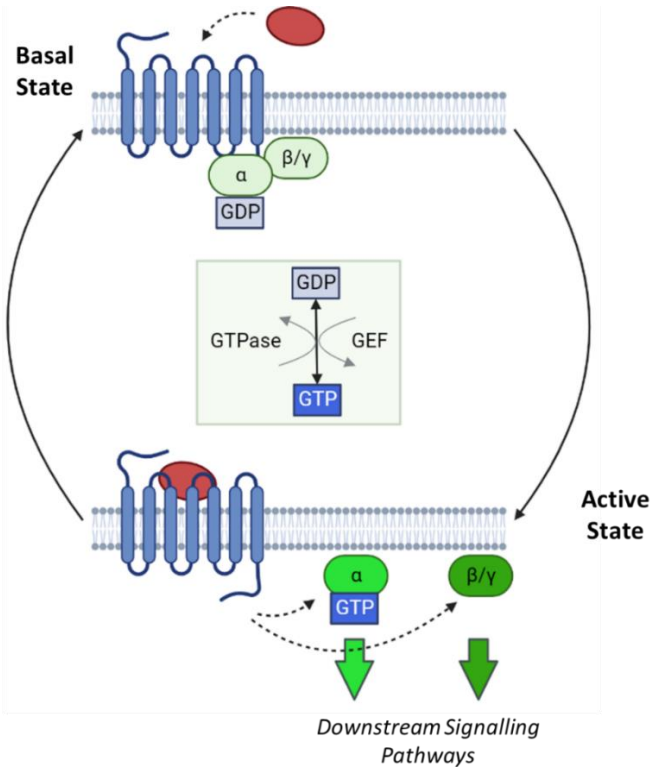

Figure 1.2 GPCR activation and the heterotrimeric G protein cycle. In the basal state, guanosine diphosphate (GDP) is bound to the Gα subunit, which forms a complex with the Gβγ subunits. Upon ligand binding (red shape), conformational changes occur and the GPCR acts as a guanosine exchange factor (GEF), facilitating the exchange of GDP to guanosine triphosphate (GTP). In the resulting active state GTP-bound Gα dissociates from both the receptor and the Gβγ subunits, where Gα and Gβγ can modulate intracellular signalling. Signalling is terminated by hydrolysis of GTP to GDP via intrinsic GTPase activity of the Gα subunit and this can be facilitated by GTPase-activating proteins. The GDP-bound Gα reassociates with both the receptor and the Gβγ subunits to form the Gαβγ heterotrimer and return to the basal state. Created using BioRender.com.

1.1.2.2 G protein-independent signalling and GPCR desensitisation

In addition to the heterodimeric G protein cycle, GPCRs can also be desensitised despite the continued presence of ligand, leading to reduced GPCR signalling, via two mechanisms termed homologous and heterologous desensitisation (Pierce and Lefkowitz, 2001). During both mechanisms specific residues within the intracellular domain of GPCRs are phosphorylated resulting in uncoupling of GPCRs from their heterotrimeric G proteins.

Homologous desensitisation is mediated by GRKs and is agonist-dependent and -specific, since GPCRs are phosphorylated in their agonist-bound, active conformation (Kühn and Dreyer, 1972, Benovic et al., 1986, Pierce and Lefkowitz, 2001). This intracellular phosphorylation by GRKs, typically at the *C* terminus and in the ICLs (Tobin, 2008, Ranjan et al., 2017), induces conformational changes in the receptor structure significantly increasing receptor affinity for other interacting partners, such as arrestins (Gurevich et al., 1995, Gurevich and Gurevich, 2006, Tobin, 2008). Binding of an arrestin to the GPCR uncouples G proteins from the receptor through steric hinderance, thereby terminating G protein-dependent signalling pathways (Benovic et al., 1987, Krupnick and Benovic, 1998, Gurevich and Gurevich, 2006, Tobin, 2008, Gurevich and Gurevich, 2019). Receptor-bound arrestin also exhibits increased binding affinity for clathrin and its adaptor protein (AP)2 (Goodman et al., 1996, Laporte et al., 1999) to facilitate receptor internalisation (Kohout et al., 2001, Gurevich and Gurevich, 2003), which is important for receptor resensitisation (Oakley et al., 1999, Gupta et al., 2018, Thomsen et al., 2022).

Heterologous desensitisation is mediated by second messenger kinases, such as protein kinase A (PKA) and protein kinase C (PKC), and is agonist-independent, since this mechanism can take place regardless of activation state of the receptor (Pierce and Lefkowitz, 2001, Carmona-Rosas et al., 2019). In this instance, phosphorylation impairs coupling of the G protein to the receptor (Pitcher et al., 1992, Freedman and Lefkowitz, 1996), and can alter G protein-selectivity from stimulatory $G\alpha_s$ to inhibitory $G\alpha_{i/o}$ subunits, such as for the β_2-adrenergic receptor (Daaka et al., 1997, Zamah et al., 2002), effectively reversing the effect of receptor activation on downstream signalling cascades, such as cyclic adenosine monophosphate production (Luttrell, 2008).

While arrestins were previously thought to only be involved in the termination of GPCR signalling, a range of studies suggests that receptor-bound arrestin can also stimulate G protein-independent signalling cascades, such as MAPK cascades (McDonald et al., 2000, Tohgo et al., 2003, Shenoy et al., 2006, Perry et al., 2019). The downstream effects of arrestins are thought to be driven by activated receptors displaying distinct phosphorylation patterns, resulting in differential arrestin conformations and thereby driving specific functional outcomes (Sente et al., 2018).

Therefore, while GPCRs canonically signal via G proteins, other proteins, such as the already mentioned arrestin and RGS, as well as receptor activity-modifying proteins (RAMPs) (McLatchie et al., 1998, Bomberger et al., 2005, Bouschet et al., 2005) and GPCR-associated sorting proteins (GASPs) (Whistler et al., 2002, Bartlett et al., 2005), can also modulate intracellular signalling cascades.

1.1.3 Pharmacology of GPCRs

Generally, when endogenous ligands or drugs bind to GPCRs, these exhibit certain characteristics, such as affinity, potency and efficacy. Affinity reflects the strength of binding between the receptor and a ligand. Potency and efficacy are measures of the amount of drug required for an effect of a given magnitude and the ability of a drug to stimulate physiological responses upon receptor binding, respectively (Kenakin, 2002a, Kenakin, 2002b).

Compounds binding to the classic orthosteric site can generally be further classified into full, partial, neutral and inverse agonists, as well as antagonists (Figure 1.3 A, B). Additionally, most GPCRs contain at least one distinct allosteric binding pocket, to which allosteric compounds bind (Conn et al., 2009a, Kruse et al., 2014). This allosteric site is generally less conserved between receptor subtypes, allowing for greater subtype selectivity (Christopoulos, 2002). Generally, binding of allosteric ligands can cause conformational changes in the receptor (Kruse et al., 2014), modulating the binding affinity of an orthosteric ligand, or the downstream signalling efficacy of one pathway over another (Figure 1.3 C, D) (Conn et al., 2009a, Scarpa et al., 2020, Van der Westhuizen et al., 2021, Dwomoh et al., 2022b).

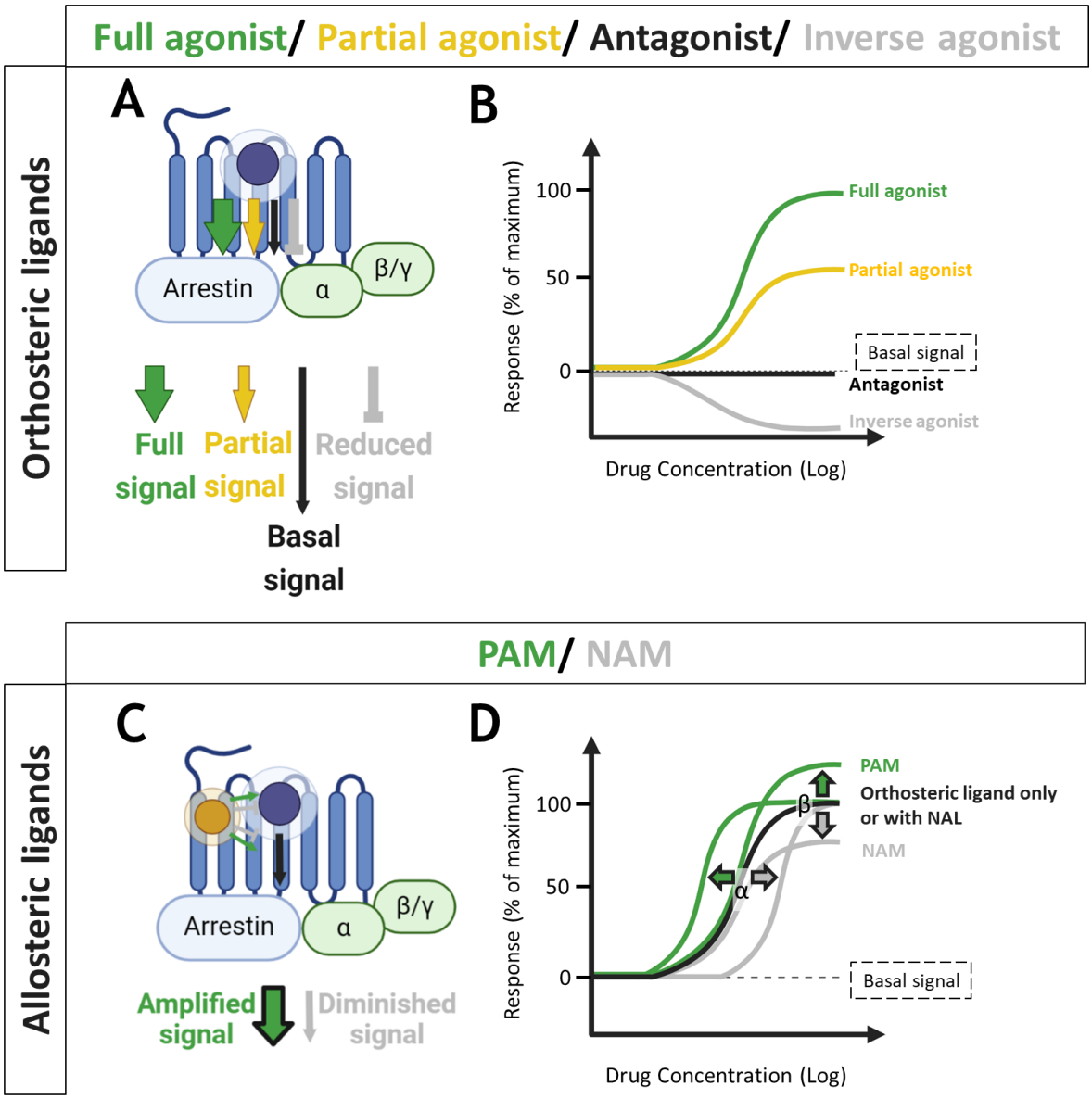

Figure 1.3 Schematic of the pharmacology of GPCR ligands. Orthosteric ligands bind to the orthosteric binding site in the TM (blue shaded circle) of GPCRs to affect downstream signalling (A). Full (green) and partial (orange) orthosteric agonists result in a full or partial downstream signal, respectively (positive efficacy). Orthosteric antagonists (black) compete with agonists for binding to the receptor, but do not affect basal signalling (neutral efficacy). Inverse agonists (grey) reduce constitutive signalling (negative efficacy) (De Ligt et al., 2000). Representative concentration response curves for the discussed orthosteric compound are also shown (B). Allosteric ligands interact with the allosteric binding site (orange shaded circle) to modulate signalling initiated by the orthosteric ligand (C) and can be classified as positive allosteric modulators (PAMs) and negative allosteric modulators (NAMs), which enhance or inhibit orthosteric ligand-induced receptor activity, respectively (C), or neutral allosteric ligands (NALs). While PAMs (green) can enhance the efficacy and/or affinity of orthosteric ligand binding and have positive co-operativity factors α and/or β (D) to amplify downstream signalling, NAMs (grey) reduce the affinity and/or efficacy of the orthosteric ligand and have negative co-operativity factors α and/or β (D) leading to decreased signalling. Binding of NALs does not affect signalling and has the same effect as binding of an orthosteric ligand in the absence of an allosteric modulator (black, D) (Kruse et al., 2014, Christopoulos et al., 2014). In the ternary complex model, the co-operativity factor α represents the modulation of the affinities of the orthosteric and allosteric ligands at the receptor, while β describes modulation of the efficacy of the activated receptor (Jakubík et al., 2020). It is important to note, that allosteric agonists can also act as allosteric agonists directly or Ago-PAMs, which act as both allosteric agonists and modulators (Dwomoh et al., 2022b). Figure created using BioRender.com.

Another important characteristic of allosteric modulators is saturability, meaning that no further increase in receptor activity is possible above a certain threshold and therefore, allosteric modulators are safer than orthosteric ligands even in larger doses (Christopoulos, 2000, Gregory et al., 2007, Chan et al., 2008, Keov et al., 2011, Kruse et al., 2014, Dwomoh et al., 2022b).

It is also important to note that the characteristics of affinity, potency and efficacy, as well as the classification of ligands are context- and probe-dependent (Shirey et al., 2009, Canals et al., 2012, Kruse et al., 2014). For allosteric modulators the direction and magnitude of the allosteric modulation can change depending on the orthosteric ligand co-bound to the receptor (Kenakin, 2005; Valant et al., 2012; Kruse et al., 2014). One example for this is LY2033298 acting as a PAM with oxotremorine-M and as a NAM with xanomeline at the M_2 mAChR (Valant et al., 2012).

1.1.4 Muscarinic receptors as therapeutic targets

As discussed, about a third of all currently used drugs target GPCRs (Santos et al., 2017, Hauser et al., 2017, Erlandson et al., 2018). This is because GPCRs are crucial for many physiological processes, exhibit good druggability, can interact with a wide range of molecules and are expressed on the cell surface resulting in good accessibility for therapeutic ligands (Russ and Lampel, 2005, Hauser et al., 2017). Currently, GPCR-based drugs are used in a range of diseases and disorders, including Type 2 diabetes, depression, insomnia, chronic obstructive pulmonary disease (COPD) and different forms of cancer (Hauser et al., 2017). Nevertheless, a large proportion of non-olfactory receptors in the GPCR family (~70%), including over 100 orphan GPCRs (Laschet et al., 2018, Hauser et al., 2020), are not being targeted by drugs yet and contain the potential for new therapeutic candidates (Hauser et al., 2017, Sriram and Insel, 2018).

The muscarinic acetylcholine receptor (mAChR) family mediates the effect of a range of successful therapeutics, including muscarinic agonists, such as pilocarpine in the treatment of glaucoma (Lee and Higginbotham, 2005), and muscarinic antagonists, such as tiotropium in COPD (Tashkin et al., 2008) and asthma (Gosens and Gross, 2018), and trospium in overactive bladder (Biastre and Burnakis, 2009). Barriers for the drug development of muscarinic agents

include the already highlighted challenges with receptor subtype selectivity and the lack of comprehensive *in vivo* rodent models for neurological disorders (for more details on Alzheimer's disease (AD) models see 1.3.2) resulting in unexploited areas of mAChR-based therapeutic potential, particularly in neuroscience. The M_1 mAChR subtype specifically has been established as a key target in treating cognitive dysfunction and therefore, has been proposed as a therapeutic target in a range of central nervous system (CNS) disorders (for more detail see 1.2.4), including AD (Conn et al., 2009b, Lebois et al., 2018, Felder et al., 2018, Scarpa et al., 2020). Since this is the topic of this thesis, the remainder of the introduction will focus on the M_1 mAChR and AD.

1.2 The M_1 muscarinic receptor as a therapeutic target

1.2.1 Overview of the muscarinic receptor family

The M_1 mAChR belongs to the mAChR family, which are classified as rhodopsin family receptors (class A) (Fredriksson et al., 2003). There are five muscarinic subtypes (M_1-M_5), which are encoded by the corresponding cholinergic receptor muscarinic (CHRM) genes 1-5 (Kubo et al., 1986, Bonner et al., 1987, Buckley et al., 1988, Hulme et al., 1990). The endogenous ligand for these mAChRs is acetylcholine (ACh), which can also activate nicotinic acetylcholine receptors. The mAChRs are further classified into two groups based on their preferred signal transduction pathways (Felder, 1995, Caulfield and Birdsall, 1998). While M_1, M_3 and M_5 mAChRs preferentially signal through $G\alpha_{q/11}$ to activate phospholipase C, and thereby increase intracellular calcium levels, M_2 and M_4 mAChRs signal through $G\alpha_{i/o}$ to inhibit adenylyl cyclase, and thereby reduce intracellular calcium (Gallo et al., 1993, Felder, 1995, Caulfield and Birdsall, 1998, Felder et al., 2000, Lebois et al., 2018).

1.2.2 Structure and activation of the M_1 muscarinic receptor

Crystal structures of all five mAChR subtypes in their inactive states have been published confirming the structurally highly conserved TM core and the orthosteric site within, which is where the endogenous ligand ACh binds (Haga et al., 2012, Kruse et al., 2012, Thal et al., 2016, Vuckovic et al., 2019). Amino acid residues within TM3, TM5 and TM7 have been shown to be particularly

important for binding of orthosteric ligands (Hulme et al., 2003, Lebon et al., 2009), and conserved residues include C98$^{3.25}$, D99$^{3.26}$, D105$^{3.32}$, Y106$^{3.33}$, C178$^{45.50}$, T188$^{5.39}$, T189$^{5.40}$, T192$^{5.43}$, A193$^{5.44}$, A196$^{5.46}$, W378$^{6.48}$, Y381$^{6.51}$ (superscripts indicate Ballesteros-Weinstein numbering for GPCRs (Ballesteros and Weinstein, 1995)) (Thal et al., 2016, Scarpa et al., 2020).

Subtle differences in the intracellular and extracellular regions have also been identified between the mAChR subtypes, including striking divergence in residues in the large extracellular vestibule contributing to the allosteric binding site, which is adjacent to but distinct from the orthosteric site (Thal et al., 2016, Hollingsworth et al., 2019). Studies have suggested the importance of the interface between TM7 and ECL2 and ECL3 for allosteric binding (Birdsall and Lazareno, 2005, Gregory et al., 2007). Additionally, a recent study reported the existence of a hidden pocket at the allosteric binding site, which was found to be more frequently open in the M_1 mAChR and dependent on Y86$^{2.64}$ and E402$^{7.36}$ for stabilisation of the open pocket (Hollingsworth et al., 2019). This cryptic pocket was shown to be crucial for binding of high affinity, non-planar M_1 mAChR-selective allosteric ligands (Hollingsworth et al., 2019). These studies further highlight the importance of allosteric modulators in achieving subtype-selective drug design at the mAChRs (Haga et al., 2012, Kruse et al., 2012, Thal et al., 2016, Vuckovic et al., 2019).

A recent study using cryo-EM obtained a structure of the M_1 mAChR bound to the agonist iperoxo and in complex with the $G\alpha_{11}$ subunit (Maeda et al., 2019). This structure was compared to the previously resolved structure of inactive M_1 mAChR bound to the muscarinic inverse agonist tiotropium (Thal et al., 2016) to assess activation-dependent conformational changes. An outward displacement of the TM6, accompanied by a small rotation of the helix and tilt of TM5 towards TM6, was found (Maeda et al., 2019). On the extracellular side, the rearrangement of TM6 and TM5 also resulted in TM6 moving closer to ECL2 causing a contraction of the extracellular vestibule. Since the extracellular vestibule is a binding site for allosteric modulators (Dror et al., 2013), it was hypothesised that the contraction might be a key component for cooperativity with PAMs (Maeda et al., 2019). Active conformations of M_1 and M_2 mAChR, including key residues and activation-dependent rearrangement of TM6, TM5 and

ECL2, were similar, suggesting that the activation mechanism between these receptors is similar despite different G protein preference (Dror et al., 2015, Maeda et al., 2019). The observed conformational changes allow the engagement of the *C* terminal helix of the Gα subunit with the receptor core (Maeda et al., 2019). In the M_1 mAChR/ $G\alpha_{11}$ complex, an extended helix from the receptor's TM5, forming more extensive interactions with the $G\alpha_{11}$ subunit, and a polybasic cluster in the *C* terminus, that interacts with the Gα-Gß interface, were found, most likely playing an important role in the determination of G protein selectivity (Maeda et al., 2019).

1.2.3 Expression and function of the M_1 muscarinic receptor

The M_1 mAChR is the predominant muscarinic receptor, constituting around 50% of the total muscarinic receptor population (Levey, 1993, Flynn et al., 1995, Jiang et al., 2014). M_1 mAChRs are expressed in salivary glands, autonomic and sympathetic ganglia in the periphery, and in the brain (Levey, 1993, Lebois et al., 2018). The receptor's distribution and function in the brain will be discussed in more details here.

1.2.3.1 Expression of the M_1 mAChR in the brain

In the brain, M_1 mAChR are generally expressed on post-synaptic neurons. Cholinergic projections from the nucleus basalis of Meynert, the medial septum and the vertical and horizontal bands of the diagonal band of Broca provide the majority of cholinergic innervation to these M_1 mAChR in the hippocampus, cortex and amygdala (Mesulam et al., 1983b, Haam and Yakel, 2017, Lebois et al., 2018). Tracer studies, where horseradish peroxidase conjugated to wheat germ agglutinin was injected into the olfactory bulb, the hippocampus, neocortex or thalamus, showed more specifically that cholinergic neurons in the medial septum and the horizontal bands of the diagonal band of Broca provide most of the cholinergic input to the hippocampus (Mesulam et al., 1983a, Mesulam et al., 1983b, Mesulam, 2004).

Previous studies have analysed the localisation and distribution of the mAChR subtypes using binding, quantitative immunoprecipitation, immunohistochemistry (IHC) and mRNA expression studies in rodent, primate and

human tissue (Volpicelli and Levey, 2004, Lebois et al., 2018). While radioligands were not sufficiently selective to demonstrate subtype selective expression, results from mRNA expression and IHC studies with subtype selective antibodies show similar overall localisation (Buckley et al., 1988, Weiner et al., 1990, Levey et al., 1991, Levey, 1993, Hersch et al., 1994). In the CNS, the M_1 mAChR is the predominant mAChR subtype expressed in the cortex, hippocampus, and amygdala (Mash and Potter, 1986, Mash et al., 1988, Levey et al., 1991, Hersch et al., 1994, , Levey et al., 1995, Lebois et al., 2018). More specifically, in rodent brain the M_1 mAChR is the predominant mAChR subtype in the cortex accounting for about 40%, while the M_2 and M_4 mAChRs represent 37% and 15%, respectively (Levey et al., 1991). The M_1 mAChR can be found throughout the cortex on dendrites and spines of pyramidal cells across all layers of the cortex, but particularly in the external granular and pyramidal layers, as well as the multiform layer (Levey et al., 1991, Volpicelli and Levey, 2004). In the rodent hippocampus, the M_1, M_2 and M_4 mAChRs comprise 36%, 33% and 27% of the total mAChR expression, respectively (Levey et al., 1995). Interestingly, in the hippocampus in human, the M_1 mAChR accounts for a larger proportion of about 60%, whereas the M_2 and M_4 mAChRs comprise about 20% each (Flynn et al., 1995). In the rat hippocampus, studies with M_1 mAChR antibodies showed that the receptor is expressed widely in the hippocampus including the pyramidal layers, stratum oriens and radiatum, with levels increasing from the cornu ammonis (CA)3 to the CA1 regions (Levey et al., 1995, Lebois et al., 2018). In the dentate gyrus (DG), diffuse staining was found in the strati moleculare and granulosum (Levey et al., 1995, Lebois et al., 2018). Other reports demonstrate expression only in the pyramidal layer in the CA areas and the granular layer of the DG using M_1 mAChR in situ hybridisation (Buckley et al., 1988). However, since mRNA can mostly be found in the cell bodies of neurons that make the receptor (Buckley et al., 1988), this supports the results by Levey et al. (1995). More specifically, M_1 mAChRs are thought to be expressed mainly on the soma and dendrites of excitatory neurons, as well as on inhibitory neurons to some degree (Levey et al., 1995, Yamasaki et al., 2010, Yi et al., 2014). In the rodent striatum, the M_1, M_2 and M_4 mAChR all have relatively equal expression levels, accounting for about 33%, 30% and 31%, respectively (Levey et al., 1991). Here, the M_1 mAChR is mainly found on the spiny dendrites of medium-sized spiny

projection neurons and is thought to modulate excitability (Shen et al., 2005, Wang et al., 2006, Shen et al., 2007, Xiang et al., 2012, Lebois et al., 2018).

In addition to the already mentioned distribution studies, human and mouse RNA and protein expression data, as well as IHC images can also be found in the Human Protein Atlas (proteinatlas.org; Sjöstedt et al., 2020). The early distribution studies were dependent on antibody specificity and the sectioning of the brains. While data in the Human Brain Atlas provides more comprehensive data, there is still a need to study the M_1 mAChR distribution particularly at a high anatomical detail (Lebois et al., 2018) and to document how neurodegeneration can affect this localisation.

1.2.3.2 M_1 mAChR function in the CNS

The mAChRs are expressed throughout the brain and involved in a variety of functions ranging from learning and memory, temperature, cardiovascular and sleep-wake cycle regulation, nociception, to sensorimotor processing and control (Velazquez-Moctezuma et al., 1989, Gomeza et al., 1999, Miyakawa et al., 2001, Yamada et al., 2001, Bernardini et al., 2002, Anagnostaras et al., 2003, Bymaster et al., 2003b, Wess, 2004, Lebois et al., 2018). Based on the subcellular localisation of the mAChRs, the overall effect of mAChRs is thought to increase sensitivity of neurons to a reduced input, while also modulating synaptic plasticity (Dasari and Gulledge, 2010, Lebois et al., 2018).

Function of the M_1 mAChR, and the other muscarinic receptors, has been studied using pharmacological strategies and knockout (KO) mice. Inhibiting muscarinic signalling generally by non-selective muscarinic antagonists led to cognitive deficits (Bartus et al., 1982, Rusted and Warburton, 1988, Flicker et al., 1990), highlighting the importance of muscarinic cholinergic transmission for cognitive function, with the M_1 mAChR being identified as a key component in learning and memory processes. More specifically, the M_1 mAChR regulates memory processes such as hippocampal synaptic plasticity (Shinoe et al., 2005, Anisuzzaman et al., 2013, Dennis et al., 2016), episodic memory encoding (Nathan et al., 2013), working memory and consolidation (Anagnostaras et al., 2003), and spatial working memory (Lebois et al., 2016). Additionally, the M_1 mAChR is also

involved in the control of locomotor activity (Miyakawa et al., 2001, Anagnostaras et al., 2003, Bradley et al., 2020)

1.2.4 Therapeutic potential of the M_1 mAChR in disorders of the CNS

Due to its distribution and function in the brain, the M_1 mAChR has been suggested as a therapeutic target in a range of diseases of the CNS, including schizophrenia, substance abuse, Parkinson's disease (PD), and AD.

In schizophrenia, changes in muscarinic receptor levels, including the M_1 mAChR, and associated subtype-specific deficits have been reported (Crook et al., 2000, Dean et al., 2002, Raedler et al., 2003, Erskine et al., 2019). In a subgroup comprising 25% of patients with schizophrenia, reduced levels of the M_1 mAChR by 75% were found in the cortex (Scarr et al., 2009). In this patient subgroup, the reduction in M_1 mAChR levels meant that allosteric modulators were not effective (Salah-Uddin et al., 2009, Dean et al., 2016, Erskine et al., 2019). These findings highlight the importance of the identification of pathology subgroups and the resulting patient stratification for clinical studies and beyond, since in this group therapeutics targeting M_1 mAChR might be not as effective due to the reduction in target receptor levels. Clinical trials with the M_1/M_4-preferring muscarinic agonist xanomeline resulted in promising improvements in measures of cognition and psychosis, however, a significant side effect profile was also observed (Shekhar et al., 2008). It has been hypothesised that the improvements in psychosis are driven by M_4 rather than M_1 mAChR activation (Erskine et al., 2019). Since some of the side effects are thought to be due to the off-target activation of M_2 and M_3 mAChR in the periphery, a recent clinical trial combined xanomeline with trospium, which is a peripherally-restricted muscarinic antagonist (Staskin et al., 2010, Brannan et al., 2018, Brannan et al., 2021). Similar to the previous trial, improvements in psychosis symptoms were observed as well as some cholinergic side effects (Brannan et al., 2018, Brannan et al., 2021) suggesting that some, but not all of these, are M_1 mAChR-driven side effects.

In substance abuse, a potential therapeutic benefit of M_1 mAChR activation has also been suggested with administration of xanomeline or allosteric M_1 mAChR

agonists reducing cocaine self-administration in mice and rats (Thomsen et al., 2010, Weikop et al., 2020).

Studies in rodent models of PD have suggested that blockage of the M_1 and M_4 mAChRs in the striatum could have beneficial effects in the treatment of motor symptoms (Ztaou et al., 2016, Chambers et al., 2019).

Due to the localisation of the M_1 mAChR in areas critical for cognition and memory, such as the hippocampus and cortex, it does not come as a surprise that the M_1 mAChR could be a drug target in AD. Strategies to target the M_1 mAChR specifically (see 1.2.5) and the therapeutic potential of the M_1 mAChR in AD (see 1.3) will be discussed in the following sections.

1.2.5 Targeting the M_1 muscarinic receptor

1.1.1.1 Targeting the M_1 mAChR with orthosteric agonists

Due to the therapeutic potential of M_1 mAChR-based drugs in AD and other diseases, such as schizophrenia, several pharmaceutical companies have attempted to develop these. Generally, orthosteric ligands have the benefit of exhibiting higher affinity for their target receptors compared to allosteric ligands (Christopoulos, 2002, Valant et al., 2009). Xanomeline, developed by Eli Lilly, was one the first orthosteric M_1- and M_4-mAChR-preferring agonists that showed improvements in cognitive function and behavioural disturbances, such as orientation, word-finding difficulties, suspicion, agitation, and hallucinations, in Phase 2 clinical trials for AD (Bodick et al., 1997a, Bodick et al., 1997b). In a small trial, treatment with xanomeline also led to cognitive improvements in schizophrenia (Shekhar et al., 2008). However, due to a lack of muscarinic subtype selectivity of this orthosteric ligand and the resulting dose-limiting cholinergic side effect profile, including gastrointestinal (GI) disturbances, sweating, and salivation, studies with xanomeline were discontinued (Bodick et al., 1997b, Melancon et al., 2013, Dwomoh et al., 2022b). New studies by Karuna Therapeutics aiming to reduce cholinergic side effects by combining xanomeline with trospium, a muscarinic antagonist restricted to the periphery, showed some indications of an improved side effect profile (Brannan et al., 2018, Brannan et al., 2021). Due to positive outcomes in Phase 3 clinical trial, it is possible that

this so-called KarXT approach will be the first muscarinic therapy approved for the treatment of schizophrenia (Dean and Scarr, 2020, Karuna Therapeutics, 2022).

Advances in GPCR structural biology, such as X-ray crystallography and cryo-EM, have allowed for the design of selective, high-affinity therapeutic candidates at GPCRs using structure-based drug discovery (Salon et al., 2011, Congreve et al., 2017, Lee et al., 2018). Sosei-Heptares used structure-based drug design to develop the M_1 mAChR orthosteric partial agonist HTL9936 (Brown et al., 2021). In a range of preclinical models, cognitive improvements were observed upon acute treatment with HTL9936. In humans, treatment caused cholinergic side effects mostly at higher doses with improved safety margins and resulted in activation of memory and learning brain centres (Brown et al., 2021). Other M_1 mAChR orthosteric compounds, such as AF267B, CDD-0102A, and WAY-132983, have also produced cognitive improvements in preclinical animal models though with varying levels of cholinergic adverse effects (Bartolomeo et al., 2000, Fisher et al., 2003, Ragozzino et al., 2012).

Overall, mainly pro-cognitive effects of orthosteric M_1-preferring ligands have been reported.

1.1.1.2 Development of M_1 mAChR-specific allosteric and bitopic compounds for AD

As alluded to in 1.2.2, the orthosteric site in the mAChR family is highly conserved, making it difficult to develop subtype-specific compounds (Kruse et al., 2013, Venkatakrishnan et al., 2013, Scarpa et al., 2020). Therefore, mAChR subtype-specific drug development efforts have increasingly focused on targeting the less conserved allosteric binding pocket, leading to the development of bitopic and allosteric compounds.

Allosteric modulators without intrinsic activity do not affect the spatial and temporal patterns of orthosteric ligand-induced receptor activation (Kenakin, 2004, Kruse et al., 2014, Scarpa et al., 2020), meaning that these ligands have the potential to specifically potentiate M_1 mAChR signalling in a physiologically relevant manner in AD (Foster et al., 2014, Scarpa et al., 2020). One of the first

highly selective M_1 mAChR PAMs investigated was benzyl quinolone carboxylic acid (BQCA; structure in Figure 4.2), developed by Merck (Ma et al., 2009). BQCA could rescue cognitive deficits in scopolamine-induced deficient mice and in disease models, such as a murine prion model of terminal neurodegeneration and the APP_{Swe} model, which expresses human *APP*$^{KM670/671NL}$ (Shirey et al., 2009, Ma et al., 2009, Bradley et al., 2017). The structurally related PQCA was also shown to enhance cognitive function in mice, rats and non-human primates and to be devoid of the cholinergic side effects seen with donepezil and xanomeline (Uslaner et al., 2013, Lange et al., 2015, Vardigan et al., 2015). However, Merck's clinical PAM candidate MK-7622, also developed from the same chemical scaffold as BQCA did not show improvements in cognitive performance and led to adverse effects in about 20% of subjects (Voss et al., 2018). Another study suggested the lack of efficacy of MK-7622 to be due to overactivation of the receptor (Moran et al., 2018). These results agree with further studies suggesting that these highly selective M_1 mAChR compounds can result in on-target M_1 mAChR-driven side effects, thereby contributing to the cholinergic adverse effect profile in addition to the off-target activation of peripheral M_2 and M_3 mAChRs (Bymaster et al., 2003a, Melancon et al., 2013, Davoren et al., 2016, Rook et al., 2017, Engers et al., 2018, Moran et al., 2018, Voss et al., 2018).

Bitopic ligands, which attempt to combine the high affinity properties of orthosteric ligands with the subtype selectivity of allosteric ligands (Valant et al., 2009, Lane et al., 2013, Kruse et al., 2014), have also been developed. GSK's clinical candidate GSK1034702, which was described previously as an allosteric agonist at the M_1 mAChR, showed enhanced cognitive function in rats and episodic memory in a clinical nicotine withdrawal test in human, but also caused cholinergic adverse effects (Nathan et al., 2013). It was later observed that GSK1034702 was a non-selective bitopic mAChR compound with intrinsic agonist activity (Bradley et al., 2018, Scarpa et al., 2020).

Over the years, a range of structurally diverse PAMs for the M_1 mAChR have been developed by pharmaceutical companies, such as Pfizer, Merck, GSK, and academic centres, such as the Warren Center for Neuroscience Drug Discovery at Vanderbilt University and the Monash Institute for Pharmaceutical Sciences.

However, the structural profile required to enhance cognition in the absence of cholinergic side effects is still unclear. Interestingly, structurally related compounds, such as PF-06764427 and VU6004256, can result in distinct outcomes *in vivo* including adverse effects (Rook et al., 2017). Both compounds are classified as ago-PAMs and have similar pharmacological properties *in vitro*, even though PF-06764427 has slightly higher efficacy *in vitro* and more agonist activity compared to VU6004256 (Rook et al., 2017). Nevertheless, administration of PF-06764427 caused behavioural convulsions and cholinergic side effects, whereas administration of VU6004256 did not (Rook et al., 2017). The authors argued that the differences observed could be due to differences in biased agonism or agonist activity levels of the ago-PAM, in line with another study suggesting that the adverse effects seen with some PAMs could be due to their intrinsic agonist activity (Moran et al., 2018). Therefore, an M_1 mAChR PAM without intrinsic activity should be considered for further investigations into the benefit of targeting the M_1 mAChR with a PAM in preclinical studies and clinical trials in AD. One such compound is VU0486846, which is a M_1 mAChR PAM with limited intrinsic activity and has shown some promising results in a murine prion mouse model of terminal neurodegeneration and the APP_{Swe} model (see 4.1.1). A summary of compounds targeting the M_1 mAChR can be found in Table 1.1.

Table 1.1. Summary of selected compounds targeting the M_1 mAChR. Details of the pharmacology (binding site and agonist/PAM), reported beneficial and side effects are presented with corresponding references.

Drug	Pharmacology	Beneficial effect	Side effects	Reference
Xanomeline	Orthosteric agonist	improvements in cognitive function and behavioural disturbances	cholinergic side effects	Bodick et al., 1997a, Bodick et al., 1997b
HTL9936	orthosteric partial agonist	activation of learning and memory centres	cholinergic side effects mostly at higher doses with improved safety margins	Brown et al., 2021
BQCA	Ago-PAM	rescue cognitive deficits in animal models	No	Shirey et al., 2009, Ma et al., 2009, Bradley et al., 2017

MK-7622	Ago-PAM	improved cognition in scopolamine-induced cognitive deficit model, no in human	20% of human subjects	Uslaner et al., 2018, Voss et al., 2018, Moran et al., 2018
GSK1034702	non-selective bitopic mAChR compound with intrinsic agonist activity	enhanced cognitive function in rats, improved episodic memory in human	Cholinergic side effects	Nathan et al., 2013, Bradley et al., 2018
PF-06764427	Ago-PAM	No	convulsions and cholinergic side effects	Rook et al., 2017
VU6004256	Ago-PAM	improved cognitive function in rats	No	Rook et al., 2017
VU0486846	PAM with limited intrinsic activity)	rescue cognitive deficits in animal models	No	Rook et al., 2018, Abd-Elrahman et al., 2022, Dwomoh et al., 2022a

1.3 Therapeutic potential of M_1 mAChR in AD

Over the last decades, the M_1 mAChR has been established as a target for symptomatic treatment of AD (Scarpa et al., 2020), with a potential for disease-modifying effects also being explored (Bradley et al., 2017, Lebois et al., 2017).

1.3.1 Alzheimer's disease

AD is a progressive neurodegenerative disorder and the most common form of dementia, resulting in cognitive decline and memory loss (Prince et al., 2016, Eid et al., 2019). Accounting for about 60-70% of all dementia cases, more than 30 million people were affected by AD in 2011, with cases predicted to double roughly every 20 years due to an increasingly aging population (Barker et al., 2002, Goldberg, 2007, Holtzman et al., 2011, Prince et al., 2016). Despite much progress in the last century, since the documentation of the first case by Alois

Alzheimer (1907), only symptomatic treatments are currently available (Yiannopoulou and Papageorgiou, 2013). Therefore, the development of disease-modifying treatments to slow, stop or even prevent AD is crucial.

A small proportion (estimates ranging from 1 to 5%) of AD cases are familial, early-onset AD (EOAD) driven by rare genetic autosomal-dominant mutations (see 1.3.1.1) (Holtzman et al., 2011, Bateman et al., 2011, Tanzi, 2012). Most AD cases, however, are classified as sporadic, late-onset AD (LOAD) with a general onset from 60 years of age (Tanzi, 2012). LOAD is a complex, multifactorial condition driven by environmental and genetic risk factors (Kamboh, 2004, Eid et al., 2019). The first gene associated with increased LOAD risk was the *Apolipoprotein E (ApoE)* gene, and particularly the *ApoE* ε4 allele (Corder et al., 1993, Verghese et al., 2011), encoding a protein important for lipid metabolism (Huang and Mahley, 2014). Over 20 further genetic risk factors have been identified mainly by genome wide association studies (GWAS) including genes involved in endocytosis, lipid metabolism, inflammation and the immune response (Karch and Goate, 2015). Some environmental factors, such as certain medications, cognitive and physical activity were associated with a lower risk of developing AD, whereas other factors, such as heavy smoking, stress, and some pre-existing conditions, including hypertension and depression, were associated with a higher risk (Xu et al., 2015, Zhang et al., 2021).

Despite the ongoing research efforts, the exact neuropathological basis of AD remains unclear (Vagnucci and Li, 2003, Pooler et al., 2014, Area-Gomez and Schon, 2017). Nevertheless, amyloid ß (Aß) plaques and neurofibrillary tangles (NFTs) are considered the main neuropathological hallmarks of AD and reduced cholinergic innervation has also been found. Hence, these will be discussed in turn.

1.3.1.1 Aβ plaques and NFTs

Aß plaques are mostly extracellular deposits consisting of aggregates of misfolded Aß peptides, which are produced via proteolysis of the amyloid precursor protein (APP) (Armstrong, 2009). It is now understood that APP can be processed via two main pathways: the amyloidogenic and the non-amyloidogenic pathway (Figure 1.4) (Haass et al., 2012). Mutations leading to EOAD generally

affect APP processing to Aß peptides (Scheuner et al., 1996, Kuperstein et al., 2010, Holtzman et al., 2011). In 1990, the first mutation leading to EOAD was identified in the *APP* gene. Since then, several other mutations in the *APP* gene as well as in *Presenilin (PS)1* and *PS2* genes have been found (Hardy, 1997, Ertekin-Taner, 2007, Holtzman et al., 2011, Lanoiselée et al., 2017). PS1 or PS2 form the catalytic component of γ-secretases, which are involved in APP processing (Selkoe and Wolfe, 2007) (see Figure 1.4). The fact that EOAD-causing mutations generally result in an increase in Aß production overall or cause an overproduction of certain Aß isoforms, deemed more toxic (Scheuner et al., 1996, Kuperstein et al., 2010, Holtzman et al., 2011), has been the basis of the amyloid hypothesis. The amyloid hypothesis postulates that accumulation of Aß in the brain is the primary driver of AD pathology, including tau accumulation into NFTs (Hardy and Selkoe, 2002, Selkoe and Hardy, 2016).

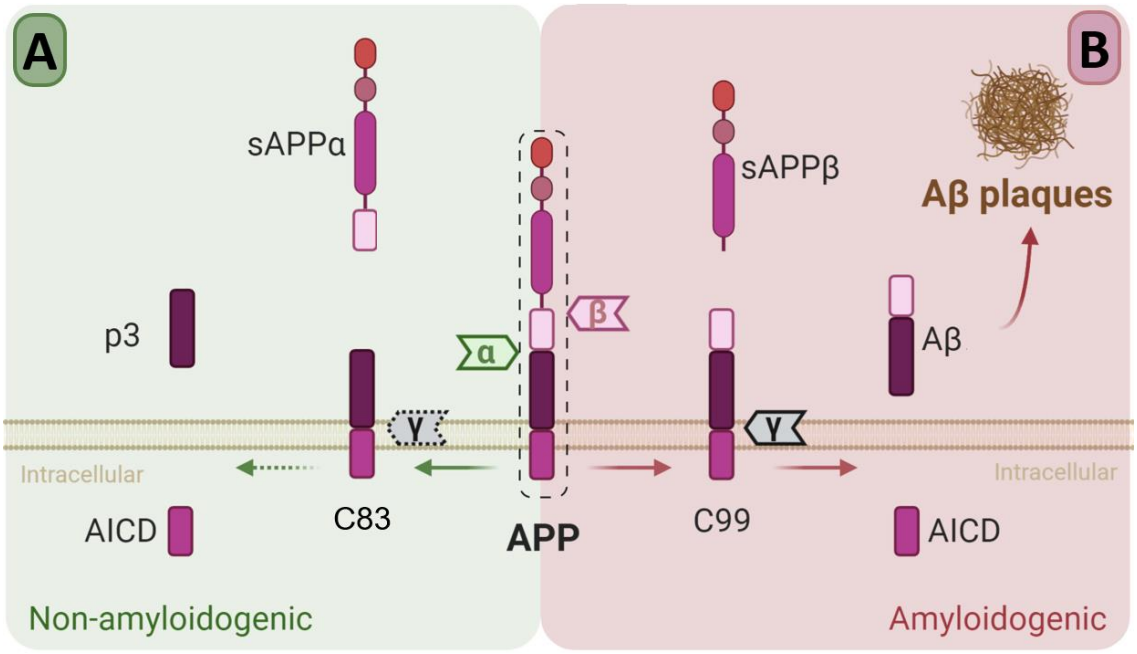

Figure 1.4 APP processing. Amyloid Precursor Protein (APP) can be cleaved via the non-amyloidogenic (A) or the amyloidogenic (B) pathway. For the non-amyloidogenic pathway, APP is cleaved by α secretases, such as A Disintegrin And Metalloproteinase (ADAM)10 or ADAM17/TACE, at the plasma membrane or in the trans Golgi network, resulting in a membrane bound fragment called C83 and a soluble APP α (sAPPα) fragment (Skovronsky et al., 2000). These α-secretases cut within the Aβ peptide sequence, thereby blocking Aβ production (Esch et al., 1990). The C83 fragment can be cleaved further by γ secretases yielding p3 and APP intracellular domain (AICD) fragments (Haass et al., 1993). Amyloidogenic APP processing mainly operates in the trans Golgi network, endoplasmic reticulum and recycling endosomes (Greenfield et al., 1999). Here, the APP protein is first cleaved by a β-secretase, such as BACE1, resulting in the production of the membrane bound fragment termed C99 and a soluble APP β fragment (sAPPβ) (Cai et al., 2001). This is then followed by cleavage of the C99 in the transmembrane domain by γ-secretases releasing an AICD fragment and the Aβ peptide (Iwatsubo, 2004). Figure created using BioRender.com.

NFTs are intracellular inclusions consisting of hyperphosphorylated tau, which has misfolded and aggregated (Grundke-Iqbal et al., 1986, Hallinan et al., 2019). Tau can associate with microtubules in neurons and has a range of functions including stabilisation of microtubules, axonal transport and neurogenesis (Brandt et al., 1995, Trinczek et al., 1999, Kent et al., 2020). Hyperphosphorylated tau, however, disrupts synaptic function and axonal transport and promotes neuroinflammation (Sherman et al., 2016, Zhou et al., 2017, Otero-Garcia et al., 2022). NFT pathology has a stronger correlation with neuronal and synaptic loss, and cognitive deficits compared to Aß plaques (Terry et al., 1991, Bennett et al., 2004, Serrano-Pozo et al., 2011), which build up years before cognitive decline becomes apparent and then plateau in the early symptomatic stages (Ingelsson et al., 2004, Jack Jr et al., 2013). Nevertheless, evidence suggests that various toxic forms of the Aß and tau proteins, not just the fully aggregated Aß plaques and NFTs, act synergistically to cause AD pathogenesis (Guo et al., 2006, Miller et al., 2011, Sherman et al., 2016) and progression, including cognitive decline and atrophy, in AD patients (Desikan et al., 2011, Sperling et al., 2019, Busche and Hyman, 2020). Interestingly, despite tau aggregates and NFTs playing a key role in the disease pathogenesis and progression, AD has so far not been linked to mutations in *MAPT*, the tau gene.

Interestingly, the misfolded Aß and tau proteins, which lead to the formation of the respective aggregates, show a prion-like spread of seeding and propagation *in vivo* and *in vitro* with the exact pattern depending on the model and type of misfolded protein used (Figure 1.5) (Guela et al., 1998, Meyer-Luehmann et al., 2006, Clavaguera et al., 2009, Frost et al., 2009, Hallinan et al., 2019). While the spread of Aß plaques and NFTs was thought to follow a stereotypic pattern in AD (Braak and Braak, 1991), there is now evidence that several distinct patterns exist (Vogel et al., 2021).

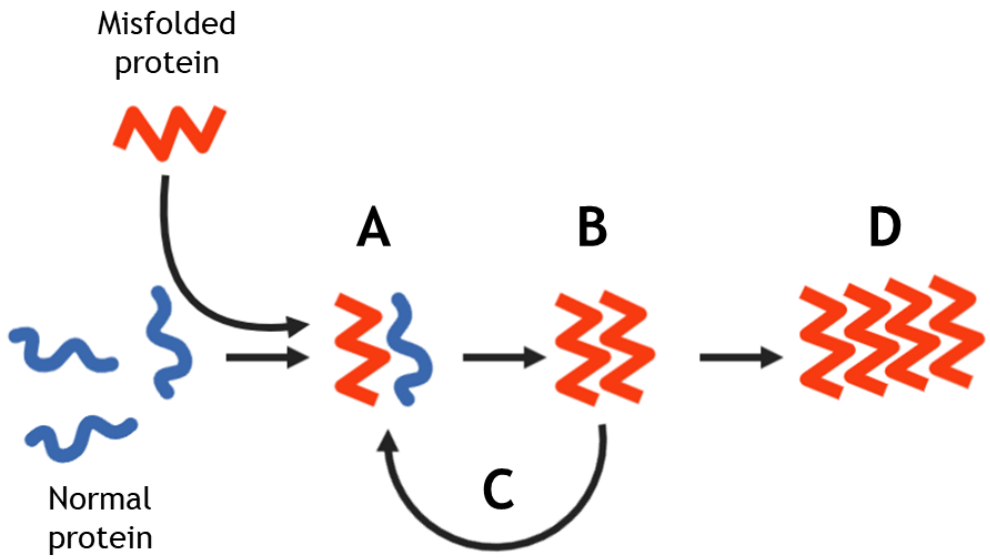

Figure 1.5 The prion-like spread of misfolded proteins in AD. A protein can become misfolded (red) due to a variety of reasons such as genetic predisposition, the local microenvironment or random chance. The abnormal protein, such as Aβ or tau, then interacts (A) with other normal proteins of the same type (blue), changing their conformation and converting them to the abnormal form (B) (Perrett and Jones, 2008, Hallinan et al., 2019). These abnormal proteins can then either interact with further normal proteins (C, seeding) or form aggregates (D). Figure created using BioRender.com.

1.3.1.2 The cholinergic hypothesis

In addition to the hallmarks of Aß plaques and NFTs, impaired cholinergic signalling has also been observed in the brains of AD patients, particularly in the cortex and hippocampus (Figure 1.6). More specifically, a reduction in pre-synaptic cholinergic neurons, resulting in reduced cholinergic innervation in the cortex and hippocampus, has been reported (Whitehouse et al., 1981, Whitehouse et al., 1982), while the post-synaptic neurons and receptor populations, such as the M_1 mAChR, remain largely intact (Bartus et al., 1982, Mash et al., 1985, Bradley et al., 2017). Additionally, levels of ACh, acetylcholinesterase (AChE), and choline acetyltransferase have been found to be reduced in AD patients (Bowen et al., 1976, Davies and Maloney, 1976, Iyo et al., 1997) and to correlate with cognitive deficits observed (Gil-Bea et al., 2005). These findings in combination with the importance of cholinergic transmission for cognition (see 1.2.3.2) has led to the cholinergic hypothesis of AD. According to this hypothesis, the cholinergic hypofunction contributes significantly to the observed cognitive decline in patients with AD (Bartus et al., 1982). Many of the currently approved symptomatic treatments for AD are based on this hypothesis (see 1.3.3).

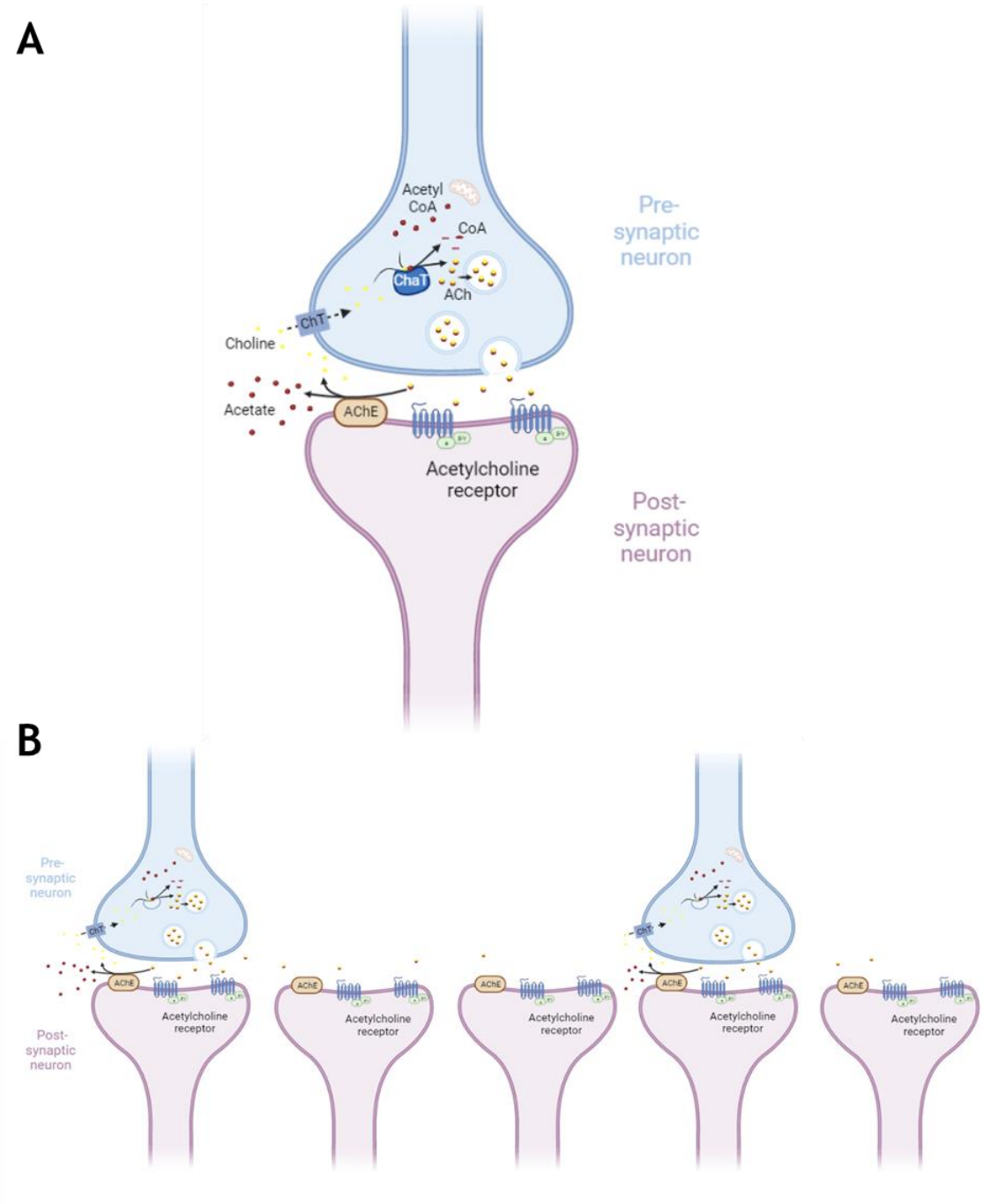

Figure 1.6 Cholinergic transmission in AD. Cholinergic signalling (A) relies on a system of synthesis, storage, release, and recycling of acetylcholine (ACh). In the presynaptic neuron, ACh is synthesised by choline acetyltransferase (ChaT) from acetyl coenzyme A (CoA), which is produced in mitochondria, and choline (Prado et al., 2002). ACh is then transported by vesicular ACh transporter into vesicles for storage (Nguyen et al., 1998). For neurotransmitter release, the vesicle fuses with the membrane of the pre-synaptic neuron and ACh enters the synaptic cleft (Ceccarelli and Hurlbut, 1980). Here, ACh can activate muscarinic and nicotinic acetylcholine receptors on the post-synaptic neuron, such as the M_1 mAChR. Then ACh is hydrolysed by acetylcholinesterase (AChE) into acetate and choline (Soreq and Seidman, 2001). Choline is taken back up into the pre-synaptic neuron by choline transporters (Okuda et al., 2000), and the cycle can then start all over again. In AD, the number of pre-synaptic neurons is reduced (Whitehouse et al., 1981), leading to diminished cholinergic signalling (B). Figure created using BioRender.com.

1.3.1.3 Inflammation and oxidative stress

In addition to the already discussed neuropathological hallmarks, additional processes have been proposed to be involved in the pathobiology of AD. While innate immune system activation in response to Aß aggregates and plaques assists in clearance of these aggregates to some degree, excessive inflammatory mechanisms including secretion of pro-inflammatory cytokines, chemokines and reactive oxygen species are also thought to drive neurodegeneration (Varnum and Ikezu, 2012, Minter et al., 2016, Rojas-Gutierrez et al., 2017). In turn, cytokines and chemokines have also been found to upregulate Aß aggregation and abnormal tau phosphorylation (Domingues et al., 2017).

Astrocytes and microglia form part of the innate immune system and a range of inputs can trigger their activation leading to astrogliosis and microgliosis, respectively (Ransohoff and Brown, 2012). While astrocyte activation, or astrogliosis, has neuroprotective features, aberrant astrogliosis has been found in proximity to Aß plaques in AD patients and animal models and can lead to neuronal damage (Chun et al., 2018, Kumar et al., 2021). Astrocytes can also take up pathological tau resulting in accumulation and propagation (Chiarini et al., 2017, Martini-Stoica et al., 2018), even though the underlying mechanism of glia-based tau propagation remains to be explored further (Perea et al., 2019, Kumar et al., 2021). Based on post-mortem findings in the brains of AD patients and PET studies in animal models, Kumar *et al.* (2021) proposed a two-wave model of astrogliosis. In the first wave, which precedes Aß deposition, astrocytes are thought to become reactive in response to the initial injury by Aß species (Narayan et al., 2014, Wyssenbach et al., 2016), but then become non-functional during disease progression. A second wave of astrogliosis was also observed, which could represent a sub-population of astrocytes, which were dormant during the first wave, but became reactive during later stages (Kumar et al., 2021). Microglia could also follow a two-wave pattern of activation in AD (Kumar et al., 2021) and several studies have shown a potentially detrimental effect of Aß-induced microgliosis exacerbating tau spread (Ising et al., 2019, Pascoal et al., 2021).

Other factors involved in AD pathology are mitochondrial dysfunction and oxidative stress. Studies have suggested an early and critical role of

mitochondrial dysfunction in AD pathogenesis (Nunomura et al., 2001, Moreira et al., 2010). In a positive feedback loop, oxidative stress has been found to contribute to mitochondrial dysfunction, which can subsequently lead to the release of further reactive oxygen species (Moreira et al., 2010). These reactive oxygen species are also thought to be involved in cell death in AD (Rojas-Gutierrez et al., 2017). Additionally, in another positive feedback loop neuroinflammation results in increased oxidative stress, which then upregulates inflammation (Fischer and Maier, 2015).

Overall, while only outlining some factors contributing to neuropathology in AD, this section shortly highlights some of the complex interplay observed in AD pathology.

1.3.2 Models of Alzheimer's disease

While some aspect of AD disease pathology can be studied in patients directly, many aspects requiring tissue samples cannot. Additionally, therapeutic candidates need to be tested for safety and efficacy in *in vitro* and *in vivo* models, before entering clinical trials in human. A range of models for AD have been developed and some of these will be described here.

1.3.2.1 Natural animal models of AD

Several animal species have been reported to spontaneously develop AD-like pathology with age including dogs, cats, bears, goats, sheep, wolves, some non-human primate species and the *Octodon degus* (Braak et al., 1994, Cummings et al., 1996, Roertgen et al., 1996, Tekirian et al., 1996, Voytko and Tinkler, 2004, Gunn-Moore et al., 2006, Van Dam and De Deyn, 2011). Some of these, such as dogs and cats, show cognitive decline in addition to Aß and tau pathology (Cummings et al., 1996, Gunn-Moore et al., 2006, Rofina et al., 2006, Klug et al., 2020, Sordo et al., 2021). The Octodon degu has been reported to be the only rodent naturally developing Aß plaques and tau tangles, neuroinflammation and age-dependent cognitive decline (Inestrosa et al., 2005, Ardiles et al., 2012, Deacon et al., 2015, Du et al., 2015, Hurley et al., 2018). However, a contradictory study found no AD-like pathology in Octodon degus bred for research (Steffen et al., 2016). This difference could be due to unknown

environmental factors or caused by the unpredictable nature of sporadic disease, and therefore the Octodon degu should be researched further before being more widely utilised as a natural animal model for AD. Generally, these spontaneous models offer the benefit of capturing a spectrum of disease states, including neuropathological changes and cognitive impairment (Milgram et al., 1994, Head et al., 1998, Papaioannou et al., 2001, Van Dam and De Deyn, 2011). However, their use in research is not routinely feasible due to availability, the sporadic nature of disease, and ethical and economic challenges associated with their long life spans (Van Dam and De Deyn, 2011, Kaushal et al., 2013). Despite the relatively long-lived Octodon degu offering one potential option of a rodent model, rodents do not generally develop AD-like pathology spontaneously with age, and therefore a range of induced and transgenic animal models have been developed.

1.3.2.2 Induced models of AD

In induced models of AD, pathology is caused by the injection of pharmacological or chemical compounds, or physical lesions (Van Dam and De Deyn, 2011). Many induced models have been developed based on the cholinergic hypothesis of AD (see 1.3.1.2). One of these, and the most commonly used pharmacological model, is scopolamine-induced amnesia (Flood and Cherkin, 1986, Sunderland et al., 1986, Ebert and Kirch, 1998, Araujo et al., 2011). Administration of the muscarinic antagonist scopolamine leads to memory deficits by disrupting information encoding and consolidation, with a stronger effect found with age (Rush, 1988, Molchan et al., 1992), but is limited by the absence of other AD hallmarks, such as Aß plaques and tau tangles (Van Dam and De Deyn, 2011). Another pharmacological model involves injection of the nicotinic antagonist mecamylamine also leading to learning deficits (Moran, 1993). This is interesting, as in AD muscarinic receptor densities are usually not affected, while the cholinergic input to these receptors is disrupted (Bartus et al., 1982, Mash et al., 1985), and reduced nicotinic receptor expression levels are also found (Perry et al., 1990). Similarly lesion models specifically targeting pathways or brain regions involved in memory and learning, such as the hippocampus, striatum or cortex, can model AD-like memory deficits to some degree (Gray and McNaughton, 1983, Alonso et al., 1996, Glenn et al., 2003, Sloan et al., 2006). However, both pharmacologically and lesion-induced models

do not recapitulate AD-like pathology and disease progression. Nevertheless, the use of these antagonist- and lesion-induced amnesia models has significantly progressed our understanding of the role of the cholinergic system in memory and learning (Moran, 1993, Hasselmo and Wyble, 1997, Van Dam and De Deyn, 2011).

In other induced models, intracerebral or intracerebroventricular injections of Aß peptides into the brains of rodents are used to induce some AD-like pathology. The rationale behind many induced models is the amyloid cascade hypothesis, according to which accumulation and aggregation of Aß peptides and soluble Aß oligomers is one of the primary drivers of AD pathogenesis (Hardy and Selkoe, 2002, Gong et al., 2003, Walsh and Selkoe, 2007). Aß species can either be administered acutely using one stereotactic injection (Harkany et al., 1998, Harkany et al., 2000) or using repeated injections through an implanted cannula to mimic the progressive pathology of AD (Nakamura et al., 2001, Yamada et al., 2005). Pathology observed in these models depends on the duration of administration and Aß species used, but can include disruption of the cholinergic system, cognitive deficits, brain inflammation, oxidative stress and neuronal loss (Harkany et al., 1998, Weldon et al., 1998, Yamada et al., 2005, Sipos et al., 2007). These Aß-induced models have the benefit of being relatively quick and allowing the study of the effect of specific Aß species and therapeutic candidates on pathology and symptoms. However, limitations of these Aß-infusion models are that they only provide a partial model of AD pathology due to the reliance on Aß only, the possibility of the brain injury caused by the injection contributing to the pathology observed, and the un-physiologically high concentrations of the administered Aß (Lawlor and Young, 2011, Van Dam and De Deyn, 2011).

1.3.2.3 Transgenic models of AD

Transgenic mouse models are the most used type of model for studying AD. These models usually rely on the overexpression of a transgene associated with early onset, familial forms of AD (Van Dam and De Deyn, 2011, Drummond and Wisniewski, 2017). Over the past 30 years significant advances in molecular genetics and transgenesis have enabled the identification of disease-causing gene mutations and the creation of mouse lines carrying those mutations (Van

Dam and De Deyn, 2011, Drummond and Wisniewski, 2017). These transgenic mouse lines have strongly enhanced our knowledge about the molecular basis of neurological and neurodegenerative disorders, such as AD, and allowed the evaluation of potential therapeutic compounds (Van Dam and De Deyn, 2011). While mice have mainly been used for transgenic models of AD, rat models, and transgenic models in non-mammalian species such as fruit flies (*Drosophila melanogaster*) (Prüßing et al., 2013), nematodes (*Caenorhabditis elegans*) (Giunti et al., 2021) and zebrafish (*Danio rerio*) (Saleem and Kannan, 2018) also exist. These non-mammalian models have been used to study genetic interactions, AD-related molecular pathways, and to perform drug toxicology and screening assays (Prüßing et al., 2013, Saleem and Kannan, 2018, Giunti et al., 2021). The benefits of these models are their availability, high cost-effectiveness, short generation time, and genetic amenability, but the limitations are the relative simplicity of these models in comparison to the mammalian brain as well as the limited insight into symptomatic and behavioural aspects of disease (Van Dam and De Deyn, 2011).

While several transgenic rat models have been developed in the last decade expressing a variety of mutant human *APP*, *MAPT* and *PS* genes (Cohen et al., 2013, Agca et al., 2016, Tambini et al., 2020), the summary of mammalian transgenic AD models presented here will focus on mouse models as all work presented in this thesis is conducted in mouse models.

Almost 200 transgenic mouse models for AD are currently listed on Alzforum (2022), with the research model database only including models that have been well-characterised in literature and exhibiting pathological hallmarks of AD. Due to this wealth of mouse animal models, only some of the most commonly used models will be described here. The first transgenic models developed in the 1990s were based on the amyloid hypothesis and utilised mutations found in familial EOAD. These included the PDAPP model overexpressing human *APP* carrying the Indiana mutation (V717F) driven by a platelet derived growth factor-ß promoter (Games et al., 1995), and the Tg2576 and APP23 models expressing human *APP* carrying the Swedish mutation (KM670/671NL) but driven by different promoters (Hsiao et al., 1996, Sturchler-Pierrat et al., 1997). When EOAD mutations in the *PS* genes (see 1.3.1) were found (Ertekin-Taner, 2007),

PS1 and PS2 transgenic mouse models were created (Duff et al., 1996, Elder et al., 2010). While mice with mutations in a *PS* gene show only minor pathology (Elder et al., 2010), the combination of different *APP* and *PS* mutations to create double-transgenic mice was used to produce more severe pathology with earlier onset depending on the combination (Holcomb et al., 1998). Generally, APP transgenic mice (in the presence or absence of PS mutations) display Aß plaques in the cortex and hippocampus, neuroinflammation, synaptic impairment and cognitive and behavioural deficits. However, they are limited by the absence of NFTs and limited neurodegeneration (Van Dam and De Deyn, 2011, Drummond and Wisniewski, 2017).

As tau pathology, including NFTs, is thought to be crucial for AD pathology, tau models with mutations in the *MAPT* gene were created (Elder et al., 2010). In many of these lines, transgenic mice express the P301L or P301S mutations, which cause frontotemporal lobar dementia (FTLD) in human. A widely used model in this category is the rTG4510 model, which expresses human tau containing the P301L mutation ($MAPT^{P301L}$) driven by the Ca^{2+}-calmodulin kinase IIα (CaMKIIα) promoter (Santacruz et al., 2005). This model will be used in this thesis and more details can be found in Chapter 3. Generally, these models allow the study of the interplay of NFTs, neurodegeneration, motor deficits and neuroinflammation *in vivo*, however, the mutations used in these models are not associated with AD in human and mice do not develop Aß plaques (Lewis et al., 2000, Yoshiyama et al., 2007, Götz and Ittner, 2008, Drummond and Wisniewski, 2017).

Efforts have been made to create transgenic mice with mutations in *APP*, *MAPT*, and sometimes *PS* genes to develop models with Aß plaque and NFT pathology. The most commonly used model out of these is the 3xTg AD model combining the $PS1^{M146V}$, $APP^{KM670/671NL}$, and $MAPT^{P301L}$ mutations. These mice develop Aß plaques and then NFTs with a similar progression pattern to the one found in AD in human as well as neuroinflammation, synaptic impairments and cognitive decline (Oddo et al., 2003a, Oddo et al., 2003b).

1.3.2.4 *In vitro* AD models

Relatively simple *in vitro* models, for example culturing neural cell lines in the presence of Aß or tau peptides, allowed some insight into molecular mechanisms in AD (Pérez et al., 2002, Ferrari et al., 2003). However, the development of induced pluripotent stem cells (iPSCs) enabled the interrogation of disease-relevant neurons and other cell types generated from samples from both EOAD and LOAD patients. These studies showed increased levels of Aß and hyperphosphorylated tau in comparison to iPSCs derived from age-matched controls (Israel et al., 2012, Kondo et al., 2013, Muratore et al., 2014). Further advances in *in vitro* models, allowing the creation of more complex 3D models using matrigels or microfluidics, have enabled more detailed dissection of molecular pathways *in vitro* (Raja et al., 2016, Drummond and Wisniewski, 2017). A 3D human AD triculture model of neurons, astrocytes and microglia in a microfluid platform was able to model Aß aggregation and accumulation of phosphorylated tau suggesting a microglia-induced neuronal cell death mechanism dependent on Interferon-γ and Toll-like receptor 4 (Henstridge and Spires-Jones, 2018, Park et al., 2018). While the initial study used an immortalised human microglial cell line, an updated version employs neurons, microglia and astrocytes derived from human iPSCs with the APP_{Swe} mutation. While there are still some limitations, complex *in vitro* models like these offer the benefit of using cells derived from patient samples to study the molecular mechanisms involved in neuroinflammation, cell death, interactions between cell types as well as the effect of potential therapeutics (Guttikonda et al., 2021). Furthermore, techniques such as CRISPR could be used to induce targeted mutations when needed. Therefore, whilst *in vitro* models are routinely used in AD research by groups globally, they will most likely play a more significant role in translational drug research in AD as these models mature (Henstridge and Spires-Jones, 2018, Chun et al., 2018, de Medeiros et al., 2019, Shin et al., 2019, Blanchard et al., 2022, Barak et al., 2022).

1.3.2.5 Potential and challenges of AD models

Both *in vivo* and *in vitro* models have significantly contributed to our understanding of AD pathology and the underpinning molecular mechanisms. Generally, the benefits of animal models are rapid disease onset depending on

the model used and the availability of large group sizes. *In vitro* models have the main benefit of being able to study molecular interactions between cell types with specific mutations in detail. However, there are limitations to all these models, since none of them can recapitulate the complete disease found in human. As discussed above, many models lack some AD-related pathology such as Aß plaques and NFTs, or do not present with age-related and progressive disease including neurodegeneration (Irizarry et al., 1997a, Irizarry et al., 1997b). Transgenes tend to be overexpressed to cause a quicker disease onset, however, this can be problematic as many proteins or their cleavage products can have toxic effects at unphysiologically high levels (Ghosal et al., 2009, Elder et al., 2010, Drummond and Wisniewski, 2017). Differences in disease progression have also been found, as many APP mouse models exhibit cognitive deficits before substantial plaque pathology (Jacobsen et al., 2006, Elder et al., 2010), whereas in AD in human significant plaque pathology usually develops in advance of behavioural symptoms (Price and Morris, 1999, Jack Jr et al., 2013). Additionally, many transgenic mice express a humanised form of APP or tau, but the endogenous protein processing and cleavage mechanisms differ in mice compared to human (Kuo et al., 2001, Kalback et al., 2002, Drummond and Wisniewski, 2017). Therefore, for example, the lack of post-translational modifications of the Aß protein in mice leads to the formation of more soluble Aß plaque cores in transgenic mice compared to those found in the brains of AD patients (Kuo et al., 2001, Kalback et al., 2002, Drummond and Wisniewski, 2017). This is particularly important to keep in mind when testing compounds targeting Aß plaques in mice, as the effect might be less pronounced in human. Furthermore, despite being the most commonly used type of model, transgenic models are generally based on mutations found in EOAD, which account for less than 5 % of AD cases (Holtzman et al., 2011). Studies have revealed some differences between EOAD and LOAD including the pattern of Aß and tau accumulations, cognitive symptoms and the possibly even differing underlying disease mechanisms (Hellström-Lindahl et al., 2009, Castellano et al., 2011, Shinohara et al., 2014, Drummond and Wisniewski, 2017, Drummond et al., 2017, Condello et al., 2018). As most cases of AD are sporadic LOAD in nature, efforts have been made to develop mouse models that are based on genetic risk variants for LOAD such as the ε4 variant of *ApoE* and the R47H variant of the *triggering receptor expressed on myeloid cells 2* (*TREM2*^{R47H}) genes (Coon et al.,

2007, Guerreiro et al., 2013). These models have only been created recently by the MODEL-AD Consortium with the aim of developing more relevant AD models and it will be interesting to see how these models compare to AD in human (Pandey et al., 2020, Kotredes et al., 2021, Sasner et al., 2021).

Therefore, no perfect model of AD, which recapitulates AD in human, exists (Van Dam and De Deyn, 2011, Selkoe, 2011, LaFerla and Green, 2012). When planning a study, the selection of an appropriate model needs to be carefully considered to ensure its suitability for the proposed research question. It is generally best to conduct studies in at least two complementary animal models to mitigate against problems arising from the limitations of specific transgenic models.

1.3.3 Current therapeutics and clinical trials for AD

Most of the currently approved frontline treatments for AD are based on the cholinergic hypothesis of AD (see 1.3.1.2). These aim to restore the reduced cholinergic transmission observed in AD by stopping the breakdown of AChE at the synaptic cleft, and thereby upregulating ACh levels (see Figure 1.6) (Bartus et al., 1982, Francis et al., 1999, Sanabria-Castro et al., 2017, Verma et al., 2018). However, these AChE inhibitors (AChEIs), generally only provide temporary and modest symptomatic relief in mild and moderate cases of AD (Neugroschl and Wang, 2011, Marucci et al., 2021, Uddin et al., 2021). Additionally, due to the non-specific nature of these drugs, side effects caused by the unspecific, systematic upregulation of ACh include GI symptoms, bradycardia and sleep disturbances, resulting in both dose limitations and non-compliance (Inglis, 2002, Thompson et al., 2004, Neugroschl and Wang, 2011, Marucci et al., 2021).

The also approved N-methyl D-aspartate (NMDA) receptor antagonist memantine can indirectly affect cholinergic signalling, but more importantly reduces glutamate-induced excitotoxicity (Wang and Reddy, 2017, Kabir et al., 2019). However, all of these approved treatments for AD only have symptomatic rather than disease-modifying properties (Caccamo et al., 2009) and common significant side effects highlighting the need to develop AD therapeutics that can slow or halt the underlying neuropathology in the absence of side effects.

The majority of treatment candidates for AD have been developed based on the amyloid hypothesis, however, currently only the Aß antibody therapy, aducanumab (Biogen & Eisai), has been approved by the Food and Drug Administration (FDA) in the USA in June 2021 with the promise of disease-modifying effects (Walsh et al., 2021, Lythgoe et al., 2022). While this human IgG1 monoclonal antibody has been shown to reduce Aß levels in the brain, more data is needed to see whether this reduction leads to any cognitive improvements or disease-modifying effects (Cummings et al., 2021, Thomas et al., 2021, Walsh et al., 2021, Salloway et al., 2022). Results of an extensive nine-year post-approval confirmatory study will not be available until 2030 at the earliest (Walsh et al., 2021). Additionally, significant side effects including amyloid-related imaging abnormalities, such as oedema and haemorrhage, have been reported (Cummings et al., 2021, Thomas et al., 2021, Salloway et al., 2022). Due to these concerns about the risk-benefit ratio aducanumab has not been approved by the European Medicines Agency (EMA; Walsh et al., 2021, Lythgoe et al., 2022). A range of further passive monoclonal immunotherapies against Aß peptides are at various stages of development, such as gantenerumab (Roche), donanemab (Eli Lilly) and lecanemab (Biogen & Eisai) (Cummings et al., 2022). For lecanemab, significant improvements in cognitive scores and compared to placebo in Phase 3 clinical trials in early AD have recently been reported, with Eisai applying for FDA drug approval for spring 2023 (Eisai, 2020, van Dyck et al., 2022). Other therapeutic candidates targeting Aß pathology have been developed, including active immunotherapy to boost the immune response against pathogenic Aß isoforms (Gilman et al., 2005, Wiessner et al., 2011), or inhibitors of the ß-secretase BACE1 to inhibit amyloidogenic processing of APP (Moussa-Pacha et al., 2020). To date, none of these have been successful (Huang et al., 2020).

In 2022, 143 therapeutical candidates were in clinical trials for AD, with 83.2% aiming for disease-modification. Of those disease-modifying candidates, 20 and 13 candidates were targeting amyloid and tau pathology, respectively (Cummings et al., 2022). While a range of tau-based therapeutics are in clinical trials, TRx0237 (LMTM; TauRx Therapeutics) is the only clinical candidate currently in Phase 3 trials and none have been approved yet (Cummings et al., 2022). TRx0237 is a tau aggregation inhibitor with the aim of reducing levels of

aggregated tau, and thereby reducing tau-induced pathology (Huang et al., 2020). TRx0237 was safe and improvements in brain atrophy rates and cognitive measures were found (Wilcock et al., 2018), however, further studies are ongoing (Cummings et al., 2022). Furthermore, active immunotherapies, such as ACI-35 (AC Immune & Janssen) and several passive immunotherapies against pathogenic forms of tau are currently undergoing Phase 2 clinical trials, including bepranemab (UCB Biopharma), E2814 (Eisai), and semorinemab (RO7105705; Genentech) (Cummings et al., 2022).

Since AD is a complex, multifactorial disease, novel therapeutic candidates based on other strategies, such as targeting neuroinflammation, proteostasis, synaptic plasticity, cell death, and epigenetic regulators, have been developed and advanced to clinical trials as potentially disease-modifying therapeutics (Cummings et al., 2022, Anand et al., 2014).

1.3.4 M_1 mAChR as a therapeutic target in Alzheimer's disease

Targeting the reduced cholinergic transmission is the rationale of the AChEIs in AD leading to symptomatic improvements (see 1.3.3). Evidence suggests that targeting the M_1 mAChR more specifically could lead to both symptomatic and disease-modifying effects (Scarpa et al., 2020).

As discussed, the M_1 mAChR is abundant in regions of the brain important for memory and learning, including the cortex and hippocampus (Levey, 1993, Volpicelli and Levey, 2004, Lebois et al., 2018) and plays a crucial role in cognition and memory (see 1.2.3.2). These regions are also affected in AD with severely reduced cholinergic innervation (Whitehouse et al., 1981, Whitehouse et al., 1982), while the M_1 mAChR receptor populations on post-synaptic neurons were found to be relatively unchanged in AD (Bartus et al., 1982, Mash et al., 1985, Bradley et al., 2017). Additionally, activation of the M_1 mAChR could have disease-modifying potential in the treatment of AD including modulation of the classical hallmarks of Aß and tau (see 4.1.1).

In the treatment of AD, different types of M_1 mAChR ligands are most likely needed due to the neuropathology of the disease. While at early stages of AD, M_1 mAChR PAMs provide an opportunity to boost the endogenous ACh signal in a

physiological spatiotemporal manner, at moderate AD stages, exhibiting reduced cholinergic input, ago-PAMs could both enhance the signal of the remaining ACh at the synapse and activate the M_1 mAChR directly. Finally, at later stages of AD, when cholinergic innervation is significantly reduced, an orthosteric or bitopic M_1 mAChR ligand would be more appropriate, which can directly activate the receptor to enhance signalling, and ultimately cognition (Dwomoh et al., 2022b). A range of M_1 mAChR ligands have been developed and tested in preclinical and clinical AD models (for more details, see 1.2.5).

1.4 General Thesis Aims

As discussed, despite significant research efforts, no disease-modifying treatments exist for neurodegenerative disorders, such as AD (Yiannopoulou and Papageorgiou, 2013). The M_1 mAChR has been proposed as a therapeutic target with symptomatic and disease-modifying potential in AD. This thesis contains two M_1 mAChR-focused projects: The first two results chapters encompass the study of the promising M_1 mAChR PAM VU0486846 in a tauopathy mouse model, whereas the third results chapter focuses on the study of M_1 mAChR distribution in the brain for a better understanding of the receptor's function and potential. Therefore, the three general aims of this thesis were to

1. Characterise the rTG4510 tauopathy mouse model to identify neuropathological and behavioural markers for use in an efficacy study (Chapter 3)

2. Investigate the effect of chronic treatment from 3.0 to 5.0 months-of-age with the M_1 mAChR PAM VU0486846 in the rTG4510 mouse model (Chapter 4)

3. Assess the localisation of the M_1 mAChR on a whole systems level in a M_1-meGFP mouse line using microscopy (Chapter 5)

Chapter 2 Materials and Methods

2.1 Materials

All chemicals and reagents used were obtained from Sigma-Aldrich unless stated otherwise. Listed below are key materials used in this project, corresponding suppliers, and catalogue numbers (Cat#) where possible.

2.1.1 Pharmacological compounds

The muscarinic agonists **Acetylcholine** (Cat# A6625) and **Carbachol** (Cat# PHR1511) as well as the muscarinic antagonist **Atropine** (Cat# A0257) were purchased from Sigma-Aldrich. The M_1 mAChR PAM **VU0486846** (Bertron et al., 2018, Rook et al., 2018) was kindly provided by Professor P.J. Conn (Vanderbilt Brain Institute, Nashville, Tennessee, USA). The tritiated form of the muscarinic antagonist N-methyl scopolamine (**[^{3}H]-NMS**; Cat# NET636001MC) and **[^{35}S]-GTPγS** (Cat# NEG030X001MC) were purchased from PerkinElmer.

2.1.2 General materials and reagents

4–15% Mini-PROTEAN TGX Precast Protein Gels, 15-well, 15 µl (Bio-Rad, Cat# 4561086)

384-well MicroAmp Optical PCR plates (Applied Biosystems, Cat# 4309849)

384-well Optiplate (PerkinElmer, Cat# 6007290)

Acrylamide Bis-Acrylamide Stock Solution, 30% Acrylamide (w/v) Ratio 37.5:1 (Severn Biotech Ltd, Cat# 20-2100-10)

Acrylamide 40% solution (Bio-Rad, Cat# 1610140)

Amersham Hyperfilm Mp, X-ray films (GE Healthcare, Cat# 28906843)

Amersham Protran Nitrocellulose western blotting membranes (GE Healthcare, Cat# GE10600002)

Apex Superior adhesive slides (Leica Biosystems, Cat# 3800081E)

Bis-Acrylamide 2% solution (Bio-Rad, Cat# 1610142)

Bloxall (Vector Laboratories, Cat# SP-6000-100)

Boric acid (Sigma-Aldrich, Cat# B7901)

Bradford protein assay reagent (Sigma-Aldrich, Cat# B6916-500ml)

Brilliant III Ultra-Fast SYBR Green (Agilent, Cat# 600882)

B-27 Plus Neuronal Culture System (Gibco, Cat# A3653401)

cOmplete, Mini, EDTA-free Protease Inhibitor Cocktail (Sigma-Aldrich, Cat# 11836170001)

Cover slips, round, 30 mm diameter, thickness no. 1 (VWR, Cat# 631-0174)

Dibenzyl-ether (Sigma-Aldrich, Cat# 33630)

Dichloromethane (Sigma-Aldrich, Cat# 270997)

Diethyl Pyrocarbonate (DEPC)-Treated Water, nuclease free (Invitrogen, Cat# AM9920)

DPX Mountant for Histology (Sigma-Aldrich, Cat# 06522)

Dulbecco's Phosphate Buffered Saline (DPBS) (Gibco, Cat#14190-094)

0.5M EDTA, pH 8.0 (Invitrogen, Cat#15575-038)

Ethyl Cinnamate (Sigma-Aldrich, Cat# 8.00238)

Fetal Bovine Serum (FBS) (Sigma-Aldrich, Cat# F9665)

Gelatine (Sigma-Aldrich, Cat# 1.04070)

$G\alpha_q$-specific antiserum (Santa Cruz, Cat# sc-393)

Goat serum (Sigma-Aldrich, Cat# G6767)

Guanosine 5′-[ß,γ-imido]triphosphate trisodium salt hydrate (GppNHp; Sigma-Aldrich, Cat# G0635)

Hank's Balanced Salt Solution (HBSS), no calcium, no magnesium, no phenol red (Gibco, Cat# 14175129)

Hanks' Balanced Salt Solution (HBSS; 10X), calcium, magnesium, no phenol red (Gibco, Cat# 14065049)

Harris Haematoxylin Acidified (Epredia, Cat# 6765003)

N-(2-Hydroxyethyl)piperazine-N′-(2-ethanesulfonic acid) (HEPES; VWR Chemicals, Cat# 441485H)

ImmEdge Hydrophobic Barrier PAP Pen (Vector Laboratories, Cat# H-4000)

Immobilon Western Chemiluminescent horseradish peroxidase (HRP) Substrate (Millipore, Cat# WBKLS0050)

Isoflurane (Zoetis, Cat# ISOFLO)

Laminin Mouse Protein, Natural (Gibco, Cat# 23017015)

L-Glutamine 200 mM (Thermo Fisher Scientific, Cat# 25030081)

Microscint-20 (PerkinElmer, Cat# 6013621)

Nutrient Mixture F-12 HAM with L-glutamine and sodium bicarbonate (Sigma-Aldrich, Cat# N6658)

OCT compound (AgarScientific, Cat# AGR1180)

Paraformaldehyde (PFA) powder, 95% (Sigma-Aldrich, Cat# 158127)

Penicillin-Streptomycin (Pen-Strep) (10,000U/mL) (Gibco, Cat# 15140122)

Phosphatase Inhibitor Cocktail tablets, 20 tablets (PhosSTO EASTpack) (Sigma-Aldrich, Cat# 04906837001)

Poly-D-lysine hydrobromide powder (Sigma-Aldrich, Cat# P6407)

Precision Plus Protein All Blue Prestained Protein Standards (Bio-Rad, Cat# 1610373)

Protein A-Sepharose CL-4B beads (GE Healthcare, Cat# 17-0780-01)

Rabbit serum (Sigma-Aldrich, Cat# R9133)

Reflex 7 mm Wound Clips (Stoelting Europe, Cat# 59035)

Restore Plus Stripping Buffer (Thermo Fisher Scientific, Cat# 46430)

REVERT 700 Total Protein Stain for Western Blot Normalization (LI-COR Biosciences, Cat# 926-11011)

Radio-immunoprecipitation assay (RIPA) buffer (Sigma-Aldrich, Cat# R0278; 50 mM Tris, 150 mM NaCl, 1.0% NP-40, 0.5% sodium deoxycholate, 0.1% sodium dodecyl sulphate, pH 8.0)

RNase*Zap* RNase Decontamination Solution (Invitrogen, Cat# AM9780)

Saponin (Sigma-Aldrich, Cat# 47036)

Sodium dodecyl sulphate (Sigma-Aldrich, Cat# L3771)

TA-F10 implantable probes (Data Sciences International, Cat# TA-F10)

Tetrahydrofuran (Sigma-Aldrich, Cat# 186562)

Tris Glycine SDS 10x solution (Severn Biotech Ltd, Cat# 20-6400-50; 250 mM Tris, 1.92 M glycine, 1% SDS)

Triton X-100 (Sigma-Aldrich, Cat# T9284)

Trypan Blue Solution (0.4%) (Sigma-Aldrich, Cat# T8154)

TrypLE Select Enzyme (10X), no phenol red (Gibco, Cat# A1217701)

Tween 20 (Sigma-Aldrich, Cat# P7949)

Tween 80 (Sigma-Aldrich, Cat# P1754)

Ultima Gold Liquid Scintillation Counting Cocktail (PerkinElmer, Cat# 6013326)

UniFilter-96 GF/C glass fibre filter-bottom microplates (PerkinElmer, Cat# 6055690)

VA-044 (2,2'-Azobis[2-(2-imidazolin-2-yl)propane] Dihydrochloride), thermal initiator (FUJIFILM Wako, Cat# 011-19365)

VECTASHIELD Hardset Antifade Mounting Medium with DAPI (Vector Laboratories, Cat# H-1500)

Whatman Grade 3MM Chr Cellulose Chromatography Paper (Cytiva, Cat# 3030-917)

Whatman GF/C filters (Brandel, Cat# FP-200)

Xylene Substitute (Sigma-Aldrich, Cat# A5597)

Zeocin (solution) 1 g (10 x 1 ml) (InvivoGen, Cat# ant-zn-1)

2.1.3 Assay kits

3,3′-Diaminobenzidine (DAB) substrate kit, peroxidase (with nickel) (Vector Laboratories, Cat# SK-4100)

High-Capacity cDNA Reverse Transcription Kit (Applied Biosystems, Cat# 4368814)

ImmPRESS HRP Horse Anti-Rabbit IgG Polymer Detection Kit, Peroxidase (Vector Laboratories, Cat# MP-7401, RRID: AB_2336529)

Inositol phosphate (IP)-One – Gq kit HTRF assay (Cisbio Bioassays, Cat# 62IPAPEC)

Proteome Profiler Mouse XL Cytokine Arrays (R and D Systems, Cat# ARY028)

RNeasy Plus Mini Kit (Qiagen, Cat# 74134)

2.2 Cell and tissue culture

2.2.1 Chinese hamster ovary cells

2.2.1.1 CHO cell line maintenance

Non-transfected Flp-In Chinese Hamster Ovary (CHO) cells were used as a control when indicated. CHO cells were cultured at 37°C in a 5% CO_2 humidified atmosphere in F12 HAM medium supplemented with 10% FBS, 100 U/ml penicillin/streptomycin and 0.1 mg/ml Zeocin for non-transfected Flp-In CHO cells.

To passage cells, the culture medium was aspirated, cells were washed with sterile DPBS, and then incubated in 1mM EDTA in DPBS for 5-10 min at 37°C to detach cells. Detached cells were then mixed with the supplemented F12 HAM medium, transferred to a centrifuge tube and centrifuged for 5 min at 200 x g. Cell pellets were resuspended in the respective medium and added to the appropriate volume of fresh culture medium in a sterile culture vessel to achieve the desired dilution of 1:5-20 followed by further incubation at 37°C until confluent.

2.2.1.2 Cryopreservation

Cell lines were cryopreserved for long-term storage in liquid nitrogen. In short, culture medium was aspirated, cells washed with DPBS and confluent cells were detached by incubation in 1mM EDTA in DPBS for about 5-10 min at 37°C. Detached cells were then mixed with some of the respective cell medium, transferred to a centrifuge tube and centrifuged for 5 min at 94 x g. Cell pellets

were resuspended in FBS + 10% DMSO (1 ml per T75 flask) and 1 ml aliquots were frozen at −80°C in a cell freezing container allowing for a gradual cooling rate of roughly −1°C per min before transfer to liquid nitrogen storage. Cryopreserved cells were revived by rapid thawing in a 37°C water bath and transferring to 10 ml of pre-warmed culture medium in a flask. Cells were split after 16-24 hr.

2.2.2 Neuronal cultures

2.2.2.1 Coating of plates and coverslips

Coverslips (round, 30 mm diameter) for immunocytochemistry (ICC) were sterilised in pure ethanol and left to dry at room temperature in a tissue culture flow cabinet. Tissue culture plates and coverslips were coated using 6 µg/ml of laminin mouse protein and 4 µg/ml of poly-D-lysine in DEPC-treated water overnight at 37°C. Coated plates and coverslips were then washed three to five times in DEPC-treated water and dried for 2 hr at room temperature in a tissue culture flow cabinet.

2.2.2.2 Primary neuronal cultures

Male and female M_1-wild-type (WT) (C57BL/6J), homozygous M_1-meGFP (C57BL/6N background) and M_1-KO mice (inducible M_1 mAChR strain, C57BL/6J background) (defined in 2.3.3) between 8 and 16 weeks old were used for timed matings for preparing primary neuronal cultures. Hippocampal and cortical areas of the brain were isolated from E15-17 embryos. Isolated areas were cut into small pieces and washed three times in HBSS. The washed tissue pieces were transferred to a centrifuge tube containing 4 ml of TrypLE Select 10X and incubated at 37°C for 10 min. TrypLE Select 10X was then inactivated by the addition of 8 ml of neurobasal complete media (Neurobasal Plus medium supplemented with 20 ml/L B-27 plus, 0.292 mg/ml L-glutamine, 100 U/ml penicillin/streptomycin, 0.1 mg/ml streptomycin) followed by centrifugation for 5 min at 200 x g. The pellet was resuspended in neurobasal complete media to a final density of 5 x 10^5 cells/ml. Cells were then seeded onto the pre-coated plates or coverslips and maintained at 37°C in a 5% CO_2 humidified atmosphere until used on the 7th day *in vitro* (DIV7).

2.2.3 Determination of cell count

Cell viability was assessed using trypan blue staining and either manual haemocytometer counting or an automated cell counter. Cell suspensions were gently mixed and combined 1:1 with 0.4% trypan blue. Trypan blue is a dye that penetrates and bypasses the plasma membrane of severely damaged and dead cells staining them blue and thereby allowing determination of cell viability. Using a manual haemocytometer, an estimate of the percentage of live cells per suspension volume could be obtained manually. For automated cell counting using a Countess II Automated Cell Counter (Invitrogen), a volume of 15 µl of cell suspension/ tryphan blue mixture was loaded into a chamber and placed in the machine. Cells were counted automatically and estimates of total live cell number per ml of suspension were calculated.

2.3 Experimental animals

2.3.1 Ethical approval and mouse maintenance

Animals were cared for in accordance with national guidelines on animal experimentation. All experiments were performed under the Animals (Scientific Procedures) Act of 1986 from the British Home Office under appropriate home office licenses. Mice were group-housed in individually ventilated cages (GM500 for mice, floor area 501 cm^2; Tecniplast) of two or more animals, unless stated otherwise in the relevant experiment sections. Cages contained corn cob bedding (changed fortnightly or when wet), cardboard houses and tube as well as shredded brown paper as nesting material. Animals were fed ad libitum with a standard mouse chow and water and were maintained in controlled environmental conditions at 18-23°C, air humidity of 40-60% and 12-hr light/dark cycle with lights on from 7:30 am to 7:30 pm.

2.3.2 rTG4510

The rTG4510 mouse model was supplied by Eli Lilly and Company via Envigo (Ramsden et al., 2005, Santacruz et al., 2005). For the generation of bi-transgenic mice, a responder line carrying human $MAPT^{P301L}$ cDNA downstream of a tetracycline operon–responsive element (TRE) was crossed with an activator

line expressing a tetracycline-controlled transactivator (tTA) under control of the CaMKIIα promoter (CaMKIIα-tTA activator line). The resulting bi-transgenic mice constitutively express human tau with the P301L mutation, typically found in familial FTLD, unless inactivated by the administration of doxycycline. Male bi-transgenic, diseased and healthy littermate controls rTG4510 mice were used when indicated. From here on, they will be referred to as diseased and control rTG4510 mice, respectively.

For experiments in Chapter 3, 10 male control and diseased rTG4510 were used each at 2.5, 5.0, 7.5 and 10.0 months of age.

For the efficacy study in Chapter 4, control and diseased rTG4510 mice were treated with vehicle (10% Tween 80) or VU0486846 (10 mg/kg in 10% Tween 80; half-life 1.2 hr, Rook et al., 2008) intraperitoneally from 3.0 to 5.0 months of age (n = 10 per group, for more details see 4.1.3). Sample sizes were based on previous studies and publications.

2.3.3 M_1-meGFP mice

Transgenic knock-in mice with monomeric enhanced green fluorescent protein (meGFP) added to the *C* terminus of the M_1 mAChR (M_1-meGFP) on the C57BL/6N background were generated by GenOway using the Cre/loxP recombination system (Lyon, France) (Marsango et al., 2022). In short, a loxP-stop-loxP cassette containing the sequence encoding M_1-meGFP (for a structure diagram see 5.2) was inserted into the M_1 mAChR endogenous locus (CHRM) in embryonic stem (ES) cells. These ES cells were then microinjected into blastocysts. These blastocytes were implanted in pseudo-pregnant females for the generation of chimeric mice. Breeding of chimeric mice with Cre-recombinase-expressing mice resulted in mice in which M_1-mEGFP replaced M_1 mAChR.

For experiments for Chapter 5, M_1-WT (20 females and 15 males aged 8 to 16 weeks, 35 E15-17 embryos; C57BL/6J), homozygous M_1-meGFP (20 females and 15 males aged 8 to 16 weeks, 28 E15-17 embryos; C57BL/6N background), heterozygous M_1-meGFP (20 females and 15 males aged 8 to 16 weeks; C57BL/6N background) and M_1-KO mice (20 females and 15 males aged 8 to 16

weeks, 27 E15-17 embryos; inducible M_1 mAChR strain, C57BL/6J background) were used as indicated in the relevant figures.

2.3.4 Tissue harvest

Brain tissues (cortex and hippocampus) were harvested at sacrifice by cervical dislocation unless used for histology. Harvested tissues were snap frozen on dry ice and stored at –80°C until use. For the VU0486846 efficacy study in the rTG4510 mice (timeline 4.1.3), weight of the whole body, brain, spleen, liver, heart and kidneys was recorded immediately after sacrifice before snap freezing of cerebral tissues.

For all histology protocols, anaesthesia was initiated using 5% isoflurane and maintained using 2.5-3.5% isoflurane in 100% O_2 at 2 l/min.

2.4 Pharmacological and functional assays

2.4.1 [^{3}H]-NMS saturation binding

Saturation studies with the membrane impermeable, tritiated muscarinic antagonist [^{3}H]-NMS were performed to measure muscarinic receptor levels at the membrane surface.

2.4.1.1 Sample preparation for [^{3}H]-NMS saturation binding

Membrane preparation from rTG4510 brain samples

Crude membranes were prepared from frozen hippocampi previously collected from control and diseased rTG4510 mice aged 2.5, 5.0, 7.5 and 10.0 months. Tissue was thawed and homogenised in 1 ml of ice-cold homogenisation buffer (50 mM Tris HCl, 0.32 M sucrose, pH 8.0; supplemented with protease inhibitor cocktail) on ice with 20 strokes of a glass grinder followed by 10 sec sonication. Homogenates were centrifuged at 1,000 x g for 10 min at 4°C. Supernatants were transferred to new tubes and centrifuged at 17,000 x g for 55 min at 4°C. Pellets were then resuspended in TRIS buffer (50 mM Tris HCl, pH 7.4) and sonicated for 10 sec. Protein concentrations were determined using a Bradford

assay, adjusted to 200 µg/ml, aliquoted and stored at -80°C for use in [^{3}H]-NMS saturation binding experiments.

Membrane preparation from control and M_1-meGFP brain samples

Alternatively, a simplified protocol for preparation of crude membranes from brain samples was used for hippocampal and cortical samples from M_1-WT, homozygous M_1-meGFP and M_1-KO mice (Chapter 5). Samples were homogenised in TE buffer (10 mM Tris-HCl, 0.1 mM EDTA, pH 7.5) containing protease and phosphatase inhibitors using a 1.5 ml handheld homogeniser. Homogenised samples were centrifuged for 5 min at 211 x g and 4°C. Supernatants were transferred to new tubes to remove insoluble materials, followed by centrifugation at 18,407 x g for 1 h at 4°C in a benchtop centrifuge. Resulting pellets were resuspended in TE buffer. Protein concentrations were measured using a Bradford assay (see 2.4.1.2) and then adjust to 1 mg/ml and stored at -80°C until used.

2.4.1.2 Bradford protein assay

A Bradford assay was used to measure protein concentrations when indicated. A volume of 5 µl of each protein sample (tissue samples were diluted 1:3 in RIPA) and a RIPA control were diluted with 495 µl of distilled water and combined with 500 µl of Bradford protein assay reagent. Protein concentrations were measured on a BioPhotometer+ (Eppendorf) using the pre-calibrated Bradford settings.

2.4.1.3 Saturation Binding Assay

Binding in samples from rTG4510 mice

[^{3}H]-NMS saturation binding was performed to determine the B_{max}, a measure of total receptor concentration, of muscarinic receptors in membrane prepared as described above. In the presence of 100 µM GppNHp (a GTP analog that interconverts high to low affinity state receptors; Leach et al., 2010) increasing concentrations of [^{3}H]-NMS, ranging from 0 to 4 nM final concentration in binding buffer (100 mM NaCl, 10 mM $MgCl_2$, 20 mM HEPES), were added to 10 µg of protein. Non-specific binding was determined in the presence of 1 µM atropine, a muscarinic receptor antagonist. Tubes containing reaction mixtures were

covered with aluminium foil and incubated for 2 hr at 37°C. The reactions were stopped by rapid filtration of membrane-bound ligand onto Whatman GF/C filters with ice-cold 0.9% NaCl solution using a M-24TI harvester (Brandel). Dried filters were placed in scintillation tubes, 3 ml of Ultima Gold scintillation fluid was added and then counted on a Tri-Carb 2910TR Low Activity Liquid Scintillation Analyzer (PerkinElmer).

Binding in samples from controls and M_1-meGFP mice

Alternatively, a simplified saturation binding was used for hippocampal and cortical samples from M_1-WT, homozygous M_1-meGFP and M_1-KO mice (Chapter 5). A range of [^{3}H]-NMS concentrations (0 – 10 nM final concentration) were added to 10 µg of membrane sample in the presence or absence of 1 µM atropine (non-specific binding) in binding buffer (110 mM NaCl, 5.4 mM KCl, 1.8 mM $CaCl_2$, 1 mM $MgSO_4$, 25 mM glucose, 20mM HEPES, 58 mM sucrose) and incubated for 2 hr at 37°C. Reactions were terminated by rapid filtration of membrane-bound ligand onto GF/C glass fibre filter-bottom 96-well microplates, followed by three washes with ice-cold 0.9% NaCl, using a Unifilter-96 FilterMate Harvester (PerkinElmer). Filter plates were dried overnight, 50 µl/ well of Microscint-20 was added and plates counted using a TopCount NXT (Packard).

2.4.1.4 Analysis of binding parameters

Binding studies are used to estimate pharmacological parameters indicative of ligand affinity. The muscarinic antagonist [^{3}H]-NMS used in these saturation binding studies is membrane impermeable allowing the measurement of surface mAChR expression. In these studies, specific binding of [^{3}H]-NMS to mAChRs at increasing concentrations of [^{3}H]-NMS was calculated by subtracting non-specific binding in the presence of the muscarinic antagonist atropine from total[^{3}H]-NMS binding measurements. From this, B_{max} corresponding to receptor expression levels and the equilibrium binding constant K_D, which is a measure of ligand affinity and corresponds to the concentration of ligand required to occupy half of the receptor sites, could be calculated. The one-site specific binding analysis of non-linear regression in GraphPad Prism was used to calculate these measurements using the following model, where X is the radioligand concentration:

$$Specific\ binding\ (Y) = Bmax\ \times \frac{Bmax\ \times\ X}{KD + X}$$

2.4.2 IP-One accumulation assays in primary neuronal cells

Primary neuronal cells were seeded at a density of 2.5 x 10^4 cells/well in a 96-well plate and maintained at 37˚C in a 5% CO_2 humidified atmosphere. On DIV7, cells were washed once with 100 µl of pre-warmed IP_1 stimulation buffer (20 mM HEPES, 12 mM $CaCl_2$, 30 mM LiCl in HBSS, pH 7.4) and cells were incubated for 30 min at 37˚C in a 5% CO_2 humidified atmosphere in 40 µl pre-warmed IP_1 stimulation buffer. A volume of 5 µl of atropine (1 µM final concentration) or buffer were added to respective wells and incubated for a further 30 min at 37˚C in a 5% CO_2 humidified atmosphere. A range of carbachol concentrations (1 µM - 1 mM) were added as required and incubated for 1 hr at 37˚C in a 5% CO_2 humidified atmosphere. Following this incubation, the stimulation buffer was aspirated, 25 µl of kit-supplied lysis buffer (50 mM HEPES, 15 mM KF, 1.5% Triton-X 100, 3% FBS, 0.2% BSA) was added and cells incubated for 10 min on a Gyro-Rocker platform shaker (Stuart) at 40 RPM. A volume of 14 µl of lysate was transferred to a 384-well Optiplate and 6 µl/well of a solution containing acceptor-labelled IP_1 and donor-labelled anti-IP_1 antibodies were added and incubated for 1 hr at room temperature on a rapidly shaking MixMate plate shaker at 700 RPM (Figure 2.1 A-C). Fluorescence emissions at the wavelengths of 665- and 620 nm were measured using a CLARIOstar or PHERAstar FS microplate reader and calculated as ratio of 665 nm/620 nm. Data was normalised by setting the 665/620 nm ratio obtained from the lowest concentration of ligand used as 0% and the ratio obtained from the highest concentration of ligand used as 100%. Stimulation non-linear regression models in GraphPad Prism were used to estimate the ligand potency (EC_{50}). An overview of the IP-One assay can be found in Figure 2.1.

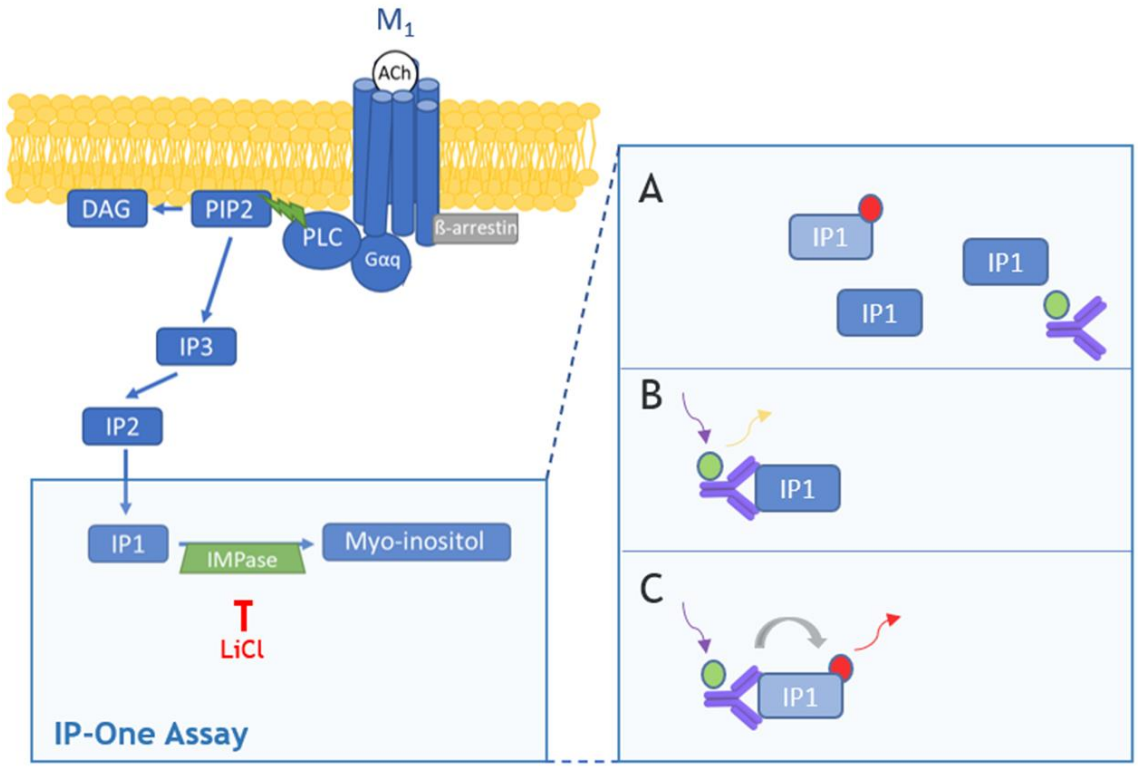

Figure 2.1 Overview of the IP-One Assay. Activation of the M_1 mAChR with a ligand can activate different intracellular pathways. Stimulation of $G\alpha_q$-coupled receptors, such as the M_1 mAChR, leads to activation of phospholipase C (PLC), which then breaks down phosphatidylinositol 4,5-bisphosphate (PIP2) to diacyl glycerol (DAG) and inositol trisphosphate (IP3). IP3 is dephosphorylated to inositol diphosphate (IP2), which is then dephosphorylated to inositol monophosphate (IP1). In normal cellular function, IP1 would be further degraded to myo-inositol by inositol monophosphatase (IMPase). In IP-One assays, lithium chloride is used to prevent this degradation of IP1 leading to IP1 accumulation following receptor activation. After ligand stimulation, acceptor-labelled IP1 (light blue IP1 with red tag) and donor-labelled anti-IP1 antibodies (purple symbol with green tag) are added to the cells. The ligand-induced endogenous IP1 (dark blue IP1) then competes with the acceptor-labelled IP1 for the donor-labelled anti-IP1 antibodies (A). When an endogenous IP1 binds to the donor-labelled anti-IP1 antibody, a fluorescence emission at 620 nm (yellow arrow) can be measured (B). When the donor-labelled anti-IP1 antibody binds to the acceptor-labelled IP1, a fluorescence emission at 665 nm (red arrow) can be measured (C). Therefore, the more IP1 accumulates due to ligand stimulation, the lower the measured 665 nm/ 620 nm ratio will be. Adapted from Nørskov-Lauritsen et al. (2014).

2.4.3 [^{35}S]-GTPγS immunoprecipitation assay

2.4.3.1 Membrane preparation from cortical samples for [^{35}S]-GTPγS immunoprecipitation assay

Cortical samples from M_1-WT, homozygous M_1-meGFP and M_1-KO mice were homogenised in TE buffer (10 mM Tris-HCl, 0.1 mM EDTA, pH 7.5) containing protease and phosphatase inhibitors using a 1.5 ml handheld homogeniser. Homogenised samples were centrifuged for 5 min at 211 x g and 4°C and the supernatant was transferred to remove insoluble materials. Supernatants were then centrifuged for 1 hr at 18,500 x g and 4°C in a benchtop centrifuge and the

resulting pellets were resuspended in TE buffer. Protein concentrations were measured using a Bradford assay and adjusted to 1 mg/ml.

2.4.3.2 [^{35}S]-GTPγS immunoprecipitation assay

[^{35}S]-GTPγS binding and immunoprecipitation of $G\alpha_q$ subunits was performed as previously described with slight modifications (Bradley et al., 2020) to assess agonist-induced G protein activation. Membranes were diluted in assay buffer (10 mM HEPES, 100 mM NaCl, 10 mM $MgCl_2$, 0.1% ascorbic acid, pH 7.4) containing a final concentration of 1 µM GDP. This mixture was incubated for 5 min on ice. A final assay concentration of 1 nM [^{35}S]-GTPγS in the presence (agonist condition) or absence (basal condition) of 1 mM carbachol was prepared in assay buffer. These mixtures and the membrane/GDP suspensions were then warmed at 30°C for 2 min. Membrane (75 µg in a total assay volume of 200 µl)/GDP suspensions were added to the [^{35}S]-GTPγS and agonist or basal mixtures and incubated at 30°C for 2 min. Reactions were terminated by the addition of ice-cold assay buffer and transferred to an ice bath, and [^{35}S]-GTPγS bound to $G\alpha_q$ subunits were enriched using immunoprecipitation as follows. Samples were centrifuged at 20,000 x g for 6 min at 4°C. Supernatants were discarded, and membrane pellets were resuspended in 50 µl of ice-cold solubilisation buffer (100 mM Tris, 200 mM NaCl, 1 mM EDTA, 1.25% NP-40, pH 7.4) containing 0.2% sodium dodecyl sulphate (SDS), vortexed and incubated at 4°C for 1 hr on a shaking Gyro-Rocker platform shaker at 40 RPM. Once protein was completely resolubilised, 50 µl ice-cold solubilisation buffer without SDS was added and samples were vortexed. To preclear the solubilised protein, rabbit serum at a dilution of 1:100 and 30 µl of Protein A-Sepharose beads (3% in TE buffer; 10 mM Tris, 10 mM EDTA, pH 8.0) were added. Samples were vortexed and rolled at 4°C for 1 hr. Tubes were then centrifuged at 20,000 x g for 6 min at 4°C to pellet beads and insoluble material. A volume of 100 µl of supernatant was then transferred to fresh tubes containing 5 µl of $G\alpha_q$-specific anti-serum and incubated overnight at 4°C. Protein A-Sepharose beads (70 µl) were added to the samples, vortexed and rotated at 4°C for 90 min. Beads were pelleted by centrifugation at 20,000 x g for 6 min at 4°C. Supernatants were aspirated and the protein A-Sepharose beads were washed three times with ice-cold solubilisation buffer without SDS. Recovered beads were then mixed with 1 ml of

Ultima Gold scintillation fluid and counted on a Tri-Carb 2910TR Low Activity Liquid Scintillation Analyzer (PerkinElmer).

2.5 Immunoblotting

2.5.1 Sample preparation for immunoblotting

2.5.1.1 Membrane extract preparation

Frozen hippocampi and cortices were homogenised using a 1.5 ml handheld homogeniser in TE buffer (10 mM Tris, 1 mM EDTA, pH 8.0) containing proteinase and phosphatase inhibitors. Samples were then centrifuged at 94 x g for 10 min at 4°C and supernatants were subsequently centrifuged at 21,130 x g for 1 hr at 4°C. The resulting pellets were solubilised in RIPA buffer containing phosphatase and proteinase inhibitors and incubated for 2 hr at 4°C with end over end rotation. After centrifugation of samples at 21,130 x g for 10 min at 4°C, the supernatants containing the membrane extracts were transferred to fresh tubes and protein concentrations were determined using a Bradford protein assay (see 2.4.1.2). Protein concentrations were adjusted to 4 mg/ml and samples stored at -80°C until use, or concentrations further adjusted to 1 mg/ml in Laemmli sample buffer (62.5 mM Tris, 1% SDS, 10% glycerol, 0.01% bromophenol blue, pH 6.8 + 5% ß-mercaptoethanol added fresh). Samples were heated for 30 min at 37°C in sample buffer before being loaded on an appropriate gel (see 2.5.2).

2.5.1.2 Preparation of Lysates from Primary Neuronal Cells and CHO Cells

Roughly 2.5 x 10^6 primary neuronal cells or 2.0 x 10^6 non-transfected CHO cells were seeded in large cell culture dishes and maintained at 37°C in a humidified atmosphere of 5% CO_2 in air. Cells were washed twice in ice-cold DBPS and lysed in RIPA buffer containing protease and phosphatase inhibitors with end over end rotation for 2 hr at 4°C. Samples were then centrifuged for 10 min at 21,130 x g at 4°C and the supernatant collected. Protein concentrations were determined using a Bradford protein assay, concentrations adjusted to 1 mg/ml and samples stored at -80°C until use, or concentrations further adjusted to 0.5 mg/ml in Laemmli sample buffer. Samples were heated for 30 min at 37°C in sample buffer before being loaded on an appropriate gel.

2.5.2 SDS-PAGE

Either 4–15% TGX precast gels were used, or polyacrylamide gels were cast using Bio-Rad Mini-PROTEAN III equipment. The percentage of the resolving gel used was based on the size of the protein of interest, with 7.5% typically used for proteins larger than 60 kDa and 12% for proteins smaller than 60 kDa. Resolving gels also contained 375 mM Tris (pH 8.8), 0.1% SDS, 0.05% ammonium persulfate (APS), and 200 nM TEMED in distilled water. Stacking gels were cast on top of the resolving gel once set. Stacking gels contained 4% acrylamide, 125 mM Tris (pH 6.8), 0.1% SDS, 0.05% APS, and 200 nM TEMED in distilled water. Equal amounts of samples (15 µg for lysates from tissue, 20 µg for lysates from neuronal cultures) were loaded into wells of appropriate gels, and samples were separated by electrophoresis in Tris-Glycine SDS running buffer (25 mM Tris-Cl, 192 mM glycine, 0.1% SDS) in a Bio-Rad Mini-PROTEAN electrophoresis chamber starting at 60 V and were then run at 100-200 V once samples had reached the end of the stacking gel, depending on type of gel used.

2.5.3 Probing and detection

Following SDS-PAGE, nitrocellulose membranes and gels were equilibrated in transfer buffer (25 mM Tris-base, 192 mM glycine, and 20% ethanol) for a few minutes. Each gel was then placed in direct contact with a membrane within a tight sandwich of transfer sponges and 1 mm Whatman chromatography paper in a transfer cassette. Transfer cassettes were placed in transfer tanks filled with transfer buffer. Transfers were run for 2 hr at a constant voltage of 60 V to electrophoretically transfer proteins from the gels onto nitrocellulose membranes.

Membranes were then stained with REVERT 700 Total Protein Stain for Western Blot Normalization (LI-COR Biosciences) and the Total Protein Stain was imaged using an Odyssey SA Infrared LI-COR Imaging System. Membranes were de-stained and incubated in 5% non-fat milk powder in TBST (0.1% Tween 20 in TBS; 20 mM Tris-HCl, 137 mM NaCl, pH 7.6) for 60 min at room temperature to block non-specific binding sites unless otherwise indicated (Table 2.1). Blocked membranes were incubated with primary antibody at 4°C overnight or room temperature for 2 hr with gentle agitation using the dilutions described in Table

2.1 . Membranes were washed with TBST followed by incubation with the appropriate secondary antibody (Table 2.2) for 1-2 hr at room temperature. Membranes were washed again with TBST, and proteins were visualised using an LI-COR Odyssey SA Infrared Imaging System (LI-COR Biosciences) using the appropriate lasers. When re-probing was required, membranes were stripped for 15 min at room temperature using Restore Plus Stripping Buffer, washed in TBST, blocked and incubated with primary and secondary antibodies for different proteins of interest as outlined above.

Table 2.1. List and description of primary antibodies used for immunoblotting. Primary antibodies are listed according to their antigen, and details include the species they are made in, and working dilutions. All antibodies were diluted in 5% milk in TBST respectively unless phospho-antibodies were used, in which case 5% BSA in TBST was used as indicated.

Antibody	Host Organism	Working Dilution	Supplier, Cat#, Antibody ID (Research Resource ID)
ApoE, EPR19378 clone	rabbit	1:1,000	Abcam, Cat# ab183596, RRID:AB_2832971
Glial Fibrillary Acidic Protein (GFAP)	mouse	1:5,000	Sigma-Aldrich, Cat# G3893, RRID:AB_477010
Green fluorescent protein (GFP)	rabbit	1:1,000	Abcam, Cat# ab6556, RRID:AB_305564
Ionized calcium binding adaptor molecule 1 (IBA1)	rabbit	1:1,000	Thermo Fisher Scientific, Cat# PA5-27436, RRID:AB_2544912
M_1 mAChR, G-9 clone	mouse	1:500	Santa Cruz Biotechnology, Cat# sc-365966, RRID:AB_10847359
Muscarinic Acetylcholine Receptor 1/CHRM1	rabbit	1:500	Novus, Cat# NBP1-87466, RRID:AB_11021120
NeuN	chicken	1:1,000	Sigma-Aldrich, Cat# ABN91, RRID:AB_11205760
Phospho-Tau Ser202, Thr205 (AT8)	mouse	1:1,000 (5% BSA in TBST)	Thermo Fisher Scientific, Cat# MN1020, RRID:AB_223647
SerpinA3N	goat	1:500	R and D Systems, Cat# AF4709, RRID:AB_2270116
Tau12	mouse	1:1,000	Millipore, Cat# MAB2241, RRID:AB_1977340
Tau46	mouse	1:1,000	Cell Signaling Technology, Cat# 4019, RRID:AB_10695394
Vimentin	mouse	1:1,000	R and D Systems, Cat# MAB21052, RRID:AB_2832972

Table 2.2. List and description of secondary antibodies used for immunoblotting. Working dilutions were made up in 5% milk in TBST unless primary phospho-antibodies were used, in which case antibodies were diluted in 5% BSA in TBST.

Antibody	Working Dilution	Supplier, Cat#, Antibody ID (Research Resource ID)
IRDye 800CW donkey anti-chicken	1:10,000	LI-COR Biosciences, Cat# 926-32218, RRID:AB_1850023
IRDye 800CW donkey anti-goat	1:10,000	LI-COR Biosciences, Cat# 926-32214, RRID:AB_621846
IRDye 800CW donkey anti-mouse	1:10,000	LI-COR Biosciences, Cat# 926-32212, RRID:AB_621847
IRDye 680LT donkey anti-mouse	1:10,000	LI-COR Biosciences, Cat# 926-68022, RRID:AB_10715072
IRDye 800CW donkey anti-rabbit	1:5,000-10,000	LI-COR Biosciences, Cat# 926-32213, RRID:AB_621848
IRDye 680LT donkey anti-rabbit	1:10,000	LI-COR Biosciences, Cat# 926-68023, RRID:AB_10706167

2.5.4 Densitometry for immunoblotting

Band intensities of proteins of interest or the REVERT Total Protein Stain were quantified by measuring median pixel intensity (arbitrary units) using Image Studio Lite (Version 5.2.5, LI-COR Biosciences), a free LI-COR-recommended software for blot analysis. The background signal was automatically corrected by this software. Band intensity of proteins of interest were then normalised to the signal measured for the corresponding Total Protein Stain. The resulting values were in turn then normalised to the value obtained by control samples as indicated in relevant figures.

2.6 Gene expression analysis

2.6.1 RNA extraction from brain tissue

RNA was isolated from the hippocampus or cortex of mice using a Qiagen RNeasy Plus Mini kit as per the manufacturer instructions. All steps were performed on ice or at 4˚C. In short, tissue was lysed and homogenised in RLT buffer containing 10% ß-mercaptoethanol using a 1.5 ml handheld homogeniser. Lysates were then centrifuged for 3 min at 21,130 x g. Supernatants were then centrifuged in a gDNA eliminator column for 30 sec at 10,000 x g to eliminate genomic DNA. The flow-through containing RNA was mixed 1:1 with 70% ethanol to provide appropriate binding conditions for RNA and then added to a RNeasy

Mini spin column. These were then centrifuged at 10,000 x g for 15 sec at room temperature with total RNA binding to the RNeasy spin column. The flow-through was discarded and the column was washed with guanidine containing stringent wash buffer, centrifuged at 10,000 x g for 15 sec, then washed with a mild wash buffer and centrifuged at 10,000 x g for 2 min. This was followed by another centrifugation at 21,130 x g for 1 min after the final wash to remove residual ethanol and eliminate possible carryover. A volume of 30 µl nuclease-free water was then directly added to the RNeasy Mini spin column and centrifuged at 10,000 x g for 1 min to elute the RNA.

2.6.2 Determination of RNA concentration

RNA concentration was quantified using a Nanodrop spectrophotometer. RNA purity was assessed using the A230/A260 and A260/A280 ratios, with ratios of 2-2.2 considered pure. RNA was used immediately for cDNA synthesis as outlined below and the remainder was stored at –80°C until required.

2.6.3 Reverse transcription

For cDNA synthesis, 1 µg total RNA template was reverse transcribed using High-Capacity cDNA Reverse Transcription Kit with RNase Inhibitor. Reactions were set up in PCR tubes with a total reaction volume of 20 µl using the following components: 1x reverse transcription (RT) buffer, 50 units MultiScribe Reverse Transcriptase, 4 mM dNTP Mix, 1x RT random primers, RNase-free water and 1 µg RNA. Each reaction was performed in the presence and absence of RT enzyme.

Reaction mixtures were incubated in a thermal cycler using the following conditions:

1.	Annealing	10 min	25°C
2.	Extension	120 min	37°C
3.	Inactivation	5 min	85°C
4.	Hold	(until removal of samples)	4°C

2.6.4 Quantitative PCR

Quantitative PCR (qPCR) was conducted using Brilliant III Ultra-Fast SYBR Green QPCR Master Mix. The primers used are detailed in Table 2.3. Each reaction was performed in duplicate or triplicate in 384-well MicroAmp Optical PCR plates. cDNA was diluted 5x before use. Each reaction was performed in a total volume of 14 µl:

7 µl	SYBR Green Master Mix
1.4 µl	primers (10 µM stock)
4.2 µl	RNase-free water
1.4 µl	diluted cDNA (or –RT control sample)

Table 2.3. List and description of primers used for qPCR.

Primer Template	Primer assay name	Cat#
Cluster of differentiation 86 (CD86; mouse)	Mm_Cd86_1_SG	QT01055250
Chrm1 (mouse)	Mm_Chrm1_1_SG	QT00282527
GFAP (mouse)	Mm_Gfap_1_SG	QT00101143
Coagulation factor III (mouse)	Mm_F3_1_SG	QT00159789
Cystatin C (mouse)	Mm_Cst3_1_SG	QT00113155
Fibroblast growth factor 1 (FGF1; mouse)	Mm_Fgf1_1_SG	QT00149296
ApoE (mouse)	Mm_Apoe_1_SG	QT01043889
MAPT (mouse)	Mm_Mapt_1_SG	QT00100170
α-tubulin (mouse)	Mm_Tuba1b_1_SG	QT00198877

Plates were read on a QuantStudio 5 Real-Time PCR System (Thermo Fisher Scientific) using the fluorescence channel for SYBR Green, which was measured at the end of each amplification cycle. The amplification cycles were set up using the following conditions:

1.	Preheating	3 min	95°C
2.	Denaturing	5 sec	95°C
3.	Annealing	12 sec	60°C
4.	Repeat steps 2-3 (x40)		

Followed by the following conditions to produce a melt curve:

1.	Heating	1 sec	95°C
2.	Annealing	20 sec	60°C
3.	Heating	1 sec	95°C

Comparative cycle threshold (C_T) values were obtained using QuantStudio Design and Analysis software (Thermo Fisher Scientific).

2.6.5 RT-qPCR data analysis

The comparative C_T method was used to quantify the results of the qPCR. In short, for normalisation C_T values of the samples of interest were compared with a suitable housekeeping gene run in parallel as an internal control, typically α-tubulin, to calculate ΔC_T values (ΔC_T = C_T of internal control − C_T of test gene). ΔC_T values of control conditions, typically healthy rTG4510 mice, were averaged and $\Delta\Delta C_T$ values were calculated (ΔC_T of test gene − averaged control ΔC_T for test gene). Data was expressed as $2^{-\Delta\Delta CT}$ to calculate the fold change in expression.

2.7 Analysis of cytokine levels using a cytokine array

Pooled cortices from VU0486846-treated and untreated diseased and healthy rTG4510 mice were homogenised in PBS supplemented with protease and phosphatase inhibitors and protein concentrations were measured using a Bradford assay (see 2.4.1.2). The Proteome Profiler Mouse XL Cytokine Arrays were performed according to the manufacturer's instructions. In short, array

membranes were blocked for 1 hr at room temperature. Tissue lysates prepared from the pooled samples (200 µg) per condition were added to array membranes in separate wells and incubated overnight at 4˚C. Membranes were washed and incubated in detection antibody cocktail for 1 hr with gentle agitation. Membranes were washed and incubated with Streptavidin-HRP antibody (supplied with kit) for 30 min at room temperature with gentle agitation, washed again and then incubated in chemiluminescent HRP substrate mix. Membranes were exposed to X-ray film, developed using a Medical Film Processor SRX-101A (Konica Minolta) and scanned. Relative protein levels were measured using the MATLAB Protein Array Tool (Danny Allen, 2017) in MATLAB R2018b (Version 9.5, MathWorks), which uses two identified reference spots to fit the template of spot locations using a rigid transformation. In "Film Mode" image intensities are inverted leading to spots being shown as bright on a dark background. The output values are given as raw pixel densities in the inverted image. As 8-bit images have 256 grey levels, the darkest spots in the original will have the highest value. For normalisation, the average of the negative control spots was then subtracted from the spot values for all cytokines, divided by the average of the reference spots and multiplied by 100.

2.8 Histology

2.8.1 Tissue harvest and preparation for histology

2.8.1.1 Standard perfusion and fixation protocol

Generally, mice were transcardially perfused with 20 ml of ice-cold DPBS followed by 20 ml of freshly prepared 4% PFA (in DPBS). Brains were removed immediately and fixed further in fresh 4% PFA at 4˚C for 24-48 hr and stored in PBS with 0.02% sodium azide at 4˚C until tissue processing.

2.8.1.2 Comparison of four perfusion and fixation protocols to image intrinsic fluorescence in M_1-meGFP mice

For the perfusion and fixation test in control M_1-WT and M_1-meGFP mice (Chapter 5), a modified version of our standard perfusion protocol and three other protocols were tested as follows:

1. Combining our laboratory's normal perfusion and fixation protocol with cryoprotecting in 30% sucrose, mice were perfused with 20 ml of ice-cold DPBS, followed by 20 ml of ice-cold 4% PFA in PBS. Brains were dissected out and post-fixed in 4% PFA at 4°C for 24 hr.

2. Based on a protocol used for imaging eGFP labelled opioid receptors (Faget et al., 2012), mice were perfused with ice-cold 9.25% sucrose in 0.1 M phosphate buffer, pH 7.4 (PB), followed by 40 ml of ice-cold 4% PFA in PB. Brains were dissected out and post-fixed in 4% PFA at 4°C for 24 hr.

3. Testing another protocol published by Herrick et al. (2017), mice were perfused with 20 ml of ice-cold DPBS, followed by 40 ml of ice-cold 1% periodate–lysine–paraformaldehyde (PLP; 1% PFA, 0.01 M mono-basic and di-basic phosphates, 90 mM lysine, 0.1 M sodium periodate, pH 7.0). Brains were dissected out and post-fixed in 1% PLP for 1 hr and then moved to PBS at 4°C overnight.

4. Lastly, as lower concentrations of PFA have been suggested to better preserve endogenous fluorescence in tissue, mice were perfused with 20 ml of ice-cold DPBS, followed by 20 ml of ice-cold 1% PFA in DPBS and ice-cold 15 ml of 5% sucrose in PBS. Brains were dissected out and immediately transferred to 30% sucrose (Renda and Nashmi, 2012).

Following post-fixation, all brains were transferred to 30% sucrose in the respective buffer for cryoprotection at 4°C and kept in this solution until brains descended to the bottom indicating saturation.

2.8.2 Tissue processing

2.8.2.1 Standard tissue processing

Brains used for histology, except for the samples used for the comparison of the four fixation and perfusion protocols, were processed by the University of Glasgow Histology Research service (Veterinary Diagnostic services) as follows:

1. 70% Ethanol	1 hr (2x)
2. 90% Ethanol	1 hr (2x)
3. 100% Ethanol	1.5 hr
4. 100% Ethanol	2 hr
5. Xylene	1 hr (2x)
6. Xylene	1.5 hr
7. Paraffin wax	2 hr (3x)

The University of Glasgow Histology Research service cut the paraffin-embedded brains sagittally or coronally (as indicated in relevant figures) in 5 µm sections using a Thermo Shando HM340 rotary microtome and sections were then baked in a 37˚C oven overnight.

2.8.2.2 Tissue processing of samples used for the comparison of different fixation and perfusion protocols

All brains used for the comparison of fixation and perfusion protocols outlined above were sliced into 3 mm-thick coronal tissue blocks containing the hippocampus (Figure 2.2) using an acrylic brain matrix for mouse brains (Stoelting).

These tissue blocks were embedded in OCT compound and sectioned into 30-40 µm sections using a Leica CM1860 UV Cryostat. Sections were then transferred to Apex Superior adhesive slides. Figure 2.2 shows the approximate position of the 3 mm-thick brain blocks that were used for cryosections and in CLARITY.

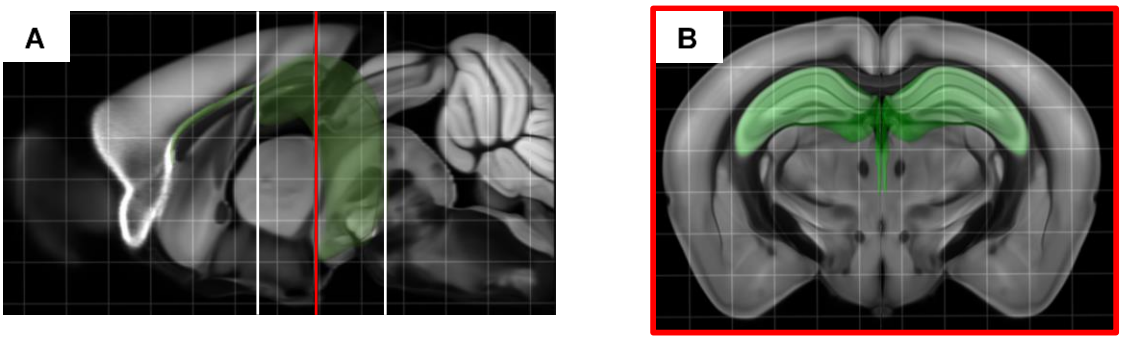

Figure 2.2 Anatomical position of 3 mm-thick coronal brain blocks used for cryosections and in CLARITY. Brain blocks were cut as indicated in white (A), and a reference coronal section at the level of the red plane is shown in B. Reference images highlighting the hippocampal region in green obtained from the Allen Brain Explorer 2 (Lau et al., 2008).

2.8.3 Deparaffinisation and rehydration of brain sections

2.8.3.1 Deparaffinisation and rehydration of brain sections for fluorescent staining

For most experiments unless otherwise indicated, deparaffinisation and rehydration were performed by the University of Glasgow Histology Research service as follows:

1. Histoclear (to de-wax)	5 min
2. 100% Ethanol	5 min (2x)
3. 70% Ethanol	5 min
4. Water	5 min

Following deparaffinisation and rehydration, sections were subjected either to antigen retrieval for IHC, or haematoxylin and eosin staining (H&E) staining.

2.8.3.2 Deparaffinisation and rehydration of brain sections for chromogenic staining (Protocol 1)

For the first chromogenic staining protocol (Chapter 5), deparaffinisation and rehydration was performed as follows:

1. Xylene Substitute (to de-wax)	15 min (2x)
2. 100% Ethanol	10 min
3. 100% Ethanol	5 min
4. 90% Ethanol	2 min
5. 70% Ethanol	2 min
6. Running Water	10 min

2.8.3.3 Deparaffinisation and rehydration of brain sections for chromogenic staining (Protocol 2)

For the second chromogenic staining protocol (Chapter 5), deparaffinisation and rehydration was performed. Slides were heated in an oven for 35 min at 60°C to soften the wax, followed by

1. Xylene Substitute (to de-wax)	5 min (2x)
2. 100% Ethanol	3 min (2x)
3. 90% Ethanol	3 min (2x)
4. 70% Ethanol	3 min (2x)
5. Distilled Water	3 min

2.8.4 Antigen retrieval protocols

2.8.4.1 Heat-induced epitope retrieval for fluorescent staining

For most experiments unless otherwise indicated, antigen retrieval was performed by the University of Glasgow Histology Research service using a Menarini Access Retrieval Unit with Sodium Citrate buffer (pH 6.0) for 1 min 40 sec at 125˚C and full pressure.

2.8.4.2 Antigen retrieval for chromogenic staining (Protocol 1)

For the first chromogenic staining protocol (Chapter 5), antigen retrieval was performed using 10 mM citric acid buffer (pH 6.0) for 2x 5 min in a microwave at 100% power. Sections were then cooled in solution for 20 min, washed in running water for 10 min, moved to 3% hydrogen peroxide in methanol for 20 min to quench endogenous peroxidase activity, and finally washed in running water for 10 min.

2.8.4.3 Antigen retrieval for chromogenic staining (Protocol 2)

For the second chromogenic staining protocol (Chapter 5), sections were incubated in Bloxall for 10 min to quench endogenous peroxidase activity. Slides were then washed in TBS + 0.05% Tween 20 for 3 min, and antigen retrieval was performed using 10 mM citric acid buffer (pH 6.0). In a microwave at full power, the citric acid buffer was brought to a boil, and then the heat was reduced to 20% for a further 10 min. Slides were then cooled to room temperature before moving on to the next step to avoid damaging the tissue.

2.8.5 Haematoxylin and eosin staining

Following sample rehydration, H&E staining was performed by the University of Glasgow Histology Research service as follows:

1.	Haematoxylin (Gill)	5 min
2.	Rinse in running water	
3.	Differentiate in 1% acid alcohol	quick dips
4.	Rinse in running water	
5.	Rinse in Scott's tap water substitute to blue (STWS; regional)	
6.	Eosin (Putts)	5 min
7.	Rinse in running water	
8.	70% Ethanol	5 min
9.	100% Ethanol	5 min (2x)
10.	Histoclear (to clear)	5 min
11.	Mount in synthetic resin mounting media	

Images were taken using NanoZoomer S60 Digital slide scanner (Hamamatsu) or on the EVOS FL Auto 2 Imaging System (Invitrogen) as indicated in the relevant figure legend. Surface area was quantified from the images of H&E staining when indicated. For this the outline of the region of interest (ROI) was marked using the freehand tool in ImageJ (Version 1.52a) and the resulting area measured.

2.8.6 Immunohistochemistry staining protocols

2.8.6.1 IHC protocol for fluorescent staining

Following antigen retrieval, sections were washed in TBST washing buffer (0.1% Triton x-100 in TBS) and blocked overnight at 4°C in blocking buffer (0.1% Triton X-100, 10% goat serum, 5% BSA in TBS). Incubation with primary antibodies (Table 2.4) in blocking buffer was conducted overnight at 4°C or for 2 hr at room temperature. Following three washes, slides were incubated with further primary antibodies (Table 2.4) as appropriate for 2 hr at room temperature. Slides were washed three times, and Alexa Fluor fluorescent secondary antibodies in blocking buffer (Table 2.5) were applied for 2 hr at room

temperature. Following three washes, slides were mounted on cover slides using VECTASHIELD HardSet Antifade Mounting Medium with DAPI, left to dry overnight at 4°C and sealed using nail polish the following day.

Table 2.4 List and description of primary antibodies used in IHC and ICC. Primary antibodies are listed according to their antigen, and details include species they are made in and working dilutions. All antibodies were diluted in the relevant blocking buffer unless indicated otherwise in text.

Antibody	Host Organism	Working Dilution	Supplier, Cat#, Antibody ID (Research Resource ID)
GFAP	mouse	1:1,000	Sigma-Aldrich, Cat# G3893, RRID:AB_477010
IBA1	rabbit	1:500	Thermo Fisher Scientific, Cat# PA5-27436, RRID:AB_2544912
NeuN EPR12763 clone	rabbit	1:100	Abcam, Cat# ab177487, RRID:AB_2532109
Phospho-Tau Ser202, Thr205 (AT8)	mouse	1:1,000	Thermo Fisher Scientific, Cat# MN1020, RRID:AB_223647
GFP	rabbit	1:500-1:2000	Abcam, Cat# ab6556, RRID:AB_305564
GFP	chicken	1:1000	Abcam, Cat# ab13970, RRID:AB_300798

Table 2.5 Secondary antibodies used for IHC and ICC. Working dilutions were made up in the relevant blocking buffer unless indicated otherwise.

Antibody	Working Dilution	Supplier, Cat#, Antibody ID (Research Resource ID)
Alexa Fluor 488-coupled goat anti-mouse	1:400	Thermo Fisher Scientific, Cat# A-11001, AB_2534069
Alexa Fluor 596-coupled goat anti-rabbit	1:400	Thermo Fisher Scientific, Cat# A-11037, AB_2534095
Alexa Fluor 647-coupled goat anti-chicken	1:1000	Abcam, Cat# ab150171, RRID:AB_2921318
ImmPRESS (Peroxidase) Polymer Horse anti-rabbit IgG (from kit)	Ready to use	Vector Laboratories, Cat# MP-7401, RRID:AB_2336529

2.8.6.2 IHC protocol for chromogenic staining (Protocol 1)

Following antigen retrieval, sections were washed in TBS and blocked for 1 hr at room temperature using 2.5% horse serum blocking buffer included in the ImmPRESS kit. Sections were incubated with rabbit anti-GFP antibody (Table 2.4) in PBS with 1% BSA overnight at 4°C. Following two washes, slides were incubated with the HRP horse anti-rabbit IgG secondary antibody included in the ImmPRESS kit (Table 2.5) for 1 hr at room temperature and washed twice. DAB

reaction was performed for 5 min, slides washed under running water for 10 min and counterstained for 3 min with Haematoxylin. Slides were then dehydrated, cleared and mounted as follows:

1. 70% Ethanol	2 min
2. 90% Ethanol	2 min
3. 100% Ethanol	5 min
4. Xylene Substitute	15 min (x2)
5. Mount with DPX mounting medium, dry overnight	

2.8.6.3 IHC protocol for chromogenic staining (Protocol 2)

Following antigen retrieval, sections were washed in distilled water followed by TBS + 0.05% Tween 20 for 3 min each. Sections were blocked for 30 min at room temperature using 2.5% horse serum blocking buffer included in the ImmPRESS kit supplemented with 2.5% mouse serum to block non-specific binding. Sections were then incubated overnight at 4°C with rabbit anti-GFP antibody (Table 2.4) in the blocking buffer included in the ImmPRESS kit supplemented with 2.5% mouse serum. Sections were washed in TBS + 0.05% Tween 20 for 3 min, and were then incubated with the HRP horse anti-rabbit IgG secondary antibody included in the ImmPRESS kit (Table 2.5) for 30 min at room temperature and washed in TBS + 0.05% Tween 20 for 3 min. DAB reaction was performed for 30 sec or 2 min, slides washed in TBS + 0.05% Tween 20 followed by distilled water for 3 min each and then counterstained with two dips in the nuclear stain Haematoxylin. Slides were then dehydrated, cleared and mounted as follows:

1. 70% Ethanol	3 min (2x)
2. 90% Ethanol	3 min (2x)
3. 100% Ethanol	3 min (2x)
4. Xylene Substitute	5 min (2x)
5. Mount with DPX mounting medium, dry overnight	

2.8.7 Immunocytochemistry staining protocol in neuronal cultures

For ICC staining in neuronal cultures, culture medium was aspirated from the wells containing the primary neurons cultured on cover slips. These were washed three times with warm DPBS and then 1 ml of 4% PFA (in DBPS) was added covering each cover slip and left at room temperature for 30 min. PFA was removed, cover slips rinsed with DBPS, followed by three 10 min washes in DPBS on a slowly shaking Gyro-Rocker platform shaker at 40 RPM. Blocking solution (1% BSA, 0.1% Triton-X 100 in DPBS) was added for 60 min at room temperature for blocking non-specific binding and permeabilising cells, followed by three 10 min washes in DPBS. Neuronal cultures were incubated with the primary chicken anti-GFP antibody (Table 2.4) for 2 hr at room temperature, washed three times for 10 min in DPBS, incubated in the secondary anti-chicken Alexa Fluor 647 antibody (Table 2.5) overnight at 4°C, washed three times for 10 min in DPBS. Finally cover slips were mounted on a microscope slide using VECTASHIELD HardSet Antifade Mounting Medium with DAPI, left to dry overnight at 4°C, and sealed using nail polish the following day.

2.8.8 Microscopy of immunostained samples

Images for IHC and ICC were acquired on confocal microscopes (Zeiss LSM 710 or LSM 880 confocal microscope) or the NanoZoomer S60 digital slide scanner with the fluorescence imaging module (Hamamatsu) using 10x, 20x, 40x (oil-based), or 63x (oil-based) objectives as indicated in the appropriate figures at the same configurations, respectively.

2.8.9 Quantification of staining in images obtained from rTG4510 mice using CellProfiler pipelines

Images were analysed using two CellProfiler (Version 4.2.1; Stirling et al., 2021) pipelines to semi-automatically determine % area stained by each antibody. As shown in Figure 2.3, appropriate regions of interest (ROIs) were selected from a larger image or whole images focused on specific ROIs were selected (Figure 2.3 A). The first CellProfiler pipeline was set up to pre-process images for analysis by splitting and converting channels (DAPI, red, green) to individual greyscale

images (Figure 2.3 B1) and saving those three versions for each image (Figure 2.3 B2). Using the second CellProfiler pipeline, the area covered by specific staining was calculated. For this, the greyscale images of the red (IBA1 or NeuN) or green (GFAP or pTau) staining were converted to binary images and adjusted to a threshold (Figure 2.3 C1) using Otsu global or adaptive thresholding with the specific details outlined in Table 2.6. Otsu thresholding is particularly useful when the image characteristics of all images are unclear and when the proportion of the image covered by staining varies significantly between images (Otsu, 1979, Stirling et al., 2021). The area covered by each stain and total area were calculated (Figure 2.3 C2), data saved (Figure 2.3 C3) and finally analysed by expressing staining as a % of total area for each antibody used and ROI analysed (Figure 2.3 C4).

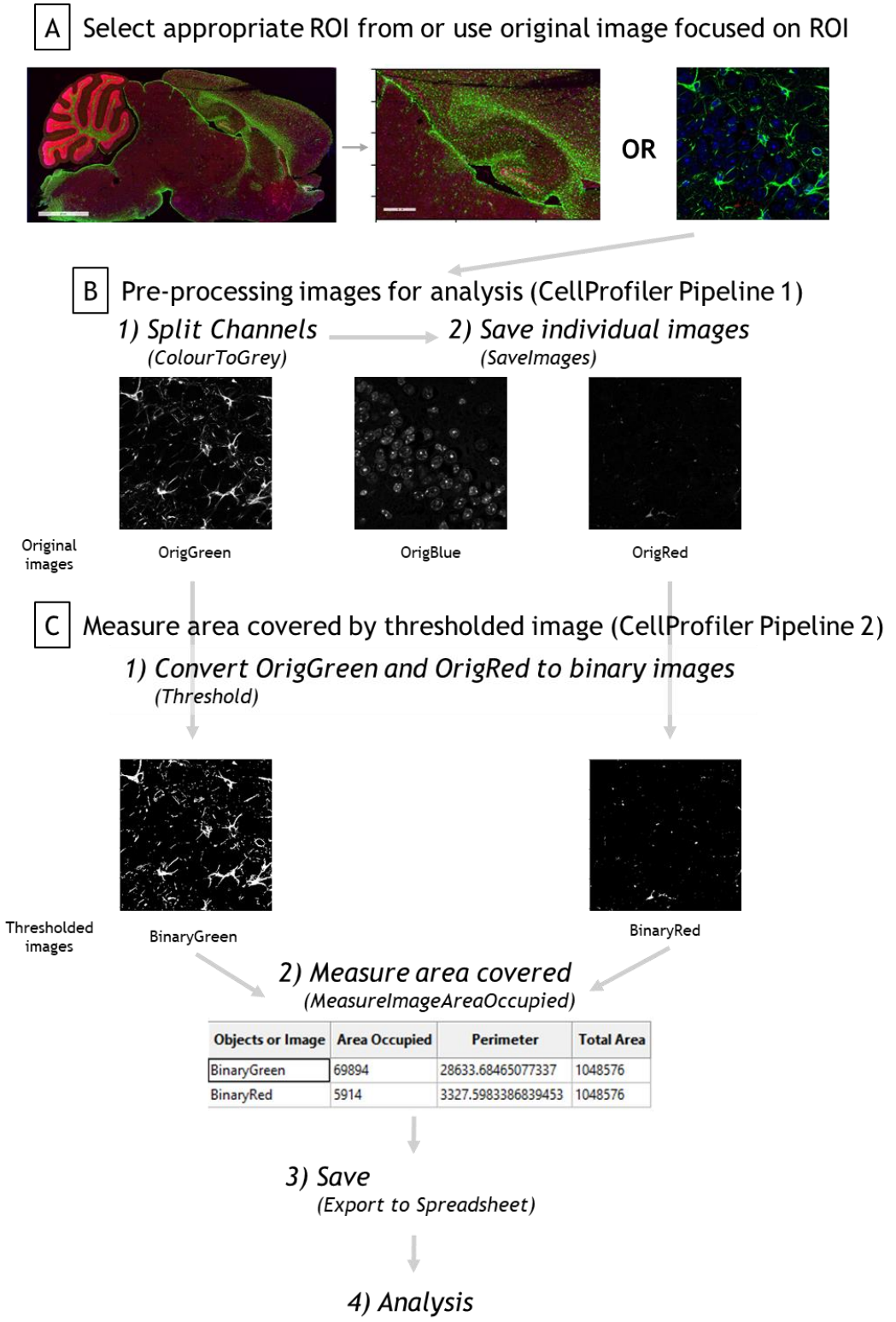

Figure 2.3 Visual representation of CellProfiler Pipelines for determining % area covered by various staining. Appropriate images focusing on specific regions of interest (ROI) were selected (A). In the first CellProfiler pipeline (B), channels were split (1) and saved as individual greyscale images (2). In the second CellProfiler pipeline (C), greyscale images were converted to binary images and thresholded (1), area covered was measured (2), values saved (3), and finally analysed and expressed as % area covered (4). CellProfiler Version 4.2.1 was used.

Table 2.6 Specific values used for Otsu thresholding for proteins of interest. Values shown are for quantifications of images in the CA1, CA3 and dentate gyrus (DG) regions taken at 63x magnification (Chapter 4; [a]), of the CA1 region taken at 40x magnification (Chapter 5; [b]), or of the hippocampus and cortex at an adjusted magnification of 10-20x (Chapter 5; [c]). Global thresholding was used when images were relatively uniform, especially at high magnification, while adaptive thresholding strategies were used for images at lower magnification and with less uniform backgrounds. The Otsu method for thresholding was selected, since this method is particularly useful if the proportion of the image covered by staining differs substantially between images. A two-class thresholding was used for staining, where the foreground and background were clearly distinguishable, and a three-class thresholding was used, where greyscale levels fell between the background and foreground classes and could then be classified as either. No threshold smoothing was performed for all proteins of interest as the images were converted to binary images prior to thresholding. The threshold correction factor was adapted as required to make the threshold more (>1) or less (0 – 1) stringent. The lower and upper bounds of the threshold could be adjusted to avoid false positive foreground pixels. While the lower threshold was set to exclude low level, non-specific signal after assessing a random selection of images per protein, the upper threshold was always set to 1. The size of the adaptive window was applied in adaptive thresholding to determine the area, which was used to calculate the threshold for each pixel across the image, and a multiple of the largest expected object size was usually used.

Protein of Interest	pTau	NeuN	GFAP	IBA1
Global or Adaptive	Global[a,b], Adaptive[c]	Global[a]	Global[a,b], Adaptive[c]	Global[a]
Two- or three-class thresholding	Two[a,b,c]	Two[a]	Two[a,c], Three[b]	Two[a]
Pixels in middle intensity class assigned to	Not applicable[a,b,c]	Not applicable[a]	Not applicable[a, c], Foreground[b]	Not applicable[a]
Threshold smoothing scale	0[a,b,c]	0[a]	0[a,b,c]	0[a]
Threshold correction factor	0.8[a], 1.1[b], 1.5[c]	1.0[a]	0.8[a], 1.4[b], 1.0[c]	1.0[a]
Lower bounds of threshold	0.01[a], 0.08[b], 0,15[c]	0.08[a]	0.08[a], 0.11[b], 0.1[c]	0.08[a]
Upper bounds of threshold	1.0[a, b, c]	1.0[a]	1.0[a, b, c]	1.0[a]
Size of adaptive window	Not applicable[a,b], 250[c]	Not applicable[a]	Not applicable[a,b], 250[c]	Not applicable[a]

2.9 Tissue clearing and imaging

2.9.1 CLARITY

Using the CLARITY (Clear Lipid-exchanged Acrylamide-hybridized Rigid Imaging/ Immunostaining/ in situ-hybridization-compatible Tissue hYdrogel) technique, brains were processed for clearing and light sheet microscopy with slight modifications from Tomer et al. (2014). In short, control M_1-WT and M_1-meGFP mice (n = 3) were perfused with 20 ml of ice-cold DPBS, followed by 20 ml of ice-cold hydrogel monomer (HM) solution (final concentrations 2% acrylamide, 0.025% bisacrylamide, 4% PFA, 0.25% VA-004 in 1x PBS). Brains were dissected immediately and incubated in a further 20 ml of HM solution for 24 hr at 4°C. Then brains were transferred to 15-20 ml of fresh HM solution and a layer of peanut oil was added to prevent oxygen from entering the solution. Tubes containing the brains in fresh HM solution were then incubated at 37°C for 2-3 hr to initiate polymerisation of the hydrogel. Following this, brains were washed in 50 ml of SDS/ boric acid clearing buffer (SBC; final concentration 4% SDS, 0.2 M boric acid buffer) three times for 24 hr at room temperature on a roller to dialyse remaining PFA and monomers. Tissue blocks containing the hippocampus were cut using the acrylic coronal brain matrix (see Figure 2.2) or whole hemispheres were used. For the following stage of passive clearing which aims to wash out lipids, samples were kept at 37°C in SBC buffer that was replaced every 2-3 days. Once tissue blocks looked clear, samples were washed twice in PBS + 0.1% Triton X for 24 hr at 37°C to remove all remaining SDS. Cleared brain blocks were then stored in PBS + 0.1% Triton X supplemented with 0.01% sodium azide and stored at 4°C. In preparation for imaging, brain blocks were placed in 87% glycerol overnight, which was used as the refractive index matching solution for CLARITY-cleared tissue. Samples were protected from light as much as possible at all stages of the protocol.

2.9.2 iDISCO

For iDISCO (immunolabeling-enabled imaging of solvent cleared organs) an adapted protocol was supplied by Cristina Martinez Gonzalez (University of Edinburgh) based on work from the Chedotal group (Liebmann et al., 2016, Belle

et al., 2017). This technique is an organic solvent-based clearing technique (Molbay et al., 2021).

Our standard perfusion protocol was used where mice were transcardially perfused with 20 ml of ice-cold DPBS followed by 20 ml of freshly prepared 4% PFA (in DPBS). Brains were removed immediately and fixed further in fresh 4% PFA at 4˚C for 3 hr only to reduce PFA-induced quenching of the endogenous florescence of the meGFP tag in the M_1-meGFP mice. Brains were stored in PBS with 0.01% sodium azide at 4˚C until tissue processing. Brains were split into hemispheres, which were dehydrated and rehydrated in methanol as follows to bleach the tissue to reduce autofluorescence as well as improve antibody diffusion:

1. 50% Methanol	1.5 hr
2. 80% Methanol	1.5 hr
3. 100% Methanol	overnight
4. 100% Methanol	1.5 hr (x2)
5. 80% Methanol	1.5 hr
6. 50% Methanol	1.5 hr
7. PBS	30 min (x3)

Samples were blocked in iDISCO blocking buffer (PBS + 0.5% Triton-X + 0.2% gelatine + 0.01% sodium azide) for 48 hr at room temperature using gentle agitation, followed by incubation with chicken anti-GFP primary antibody (Table 2.7) in iDISCO blocking buffer supplemented with 0.1% saponin for 7 days at 37˚C applying slow rotation. Hemispheres were washed 5x for 1 hr in PBS and then incubated with the anti-chicken Alexa Flour-647 secondary antibody (Table 2.7) in iDISCO blocking buffer supplemented with 0.1% saponin for 4 days at 37˚C applying slow rotation. The Alexa Flour-647 antibody was used due to its low autofluorescence compared to antibodies emitting at the blue-green spectrum (Renier et al., 2014, Cai et al., 2019, Ueda et al., 2020). Additionally, more complete illumination of cleared organs, and therefore better imaging, has been shown in the far-red spectrum compared to the red or green spectra (Cai et al., 2019).

Table 2.7 Primary and secondary antibodies used in iDISCO. Working dilutions were prepared in iDISCO blocking buffer (PBS + 0.5% Triton-X + 0.2% gelatine + 0.01% sodium azide) supplemented with 0.1% saponin

Antibody	Working Dilution	Supplier, Cat#, Antibody ID (Research Resource ID)
chicken anti-GFP antibody	1:1000	Abcam, Cat# ab13970, AB_300798
Alexa Fluor647-coupled goat anti-chicken, preadsorbed	1:1000	Abcam, Cat# ab150175, RRID:AB_2732800

Hemispheres were again washed 5x for 1 hr in PBS and then dehydrated and cleared as follows:

1. 50% Tetrahydrofuran (THF)	1 hr
2. 80% THF	1 hr
3. 100% THF	1 hr
4. 100% THF	overnight
5. 100% THF	1 hr
6. 100% Dichloromethane (DCM)	30 min
7. 100% Dibenzyl-ether (DBE)	1 hr
8. Ethyl cinnamate	storage

THF is used as a GFP-friendly dehydration medium to minimise noticeable tissue-diffusion and provide better tissue transparency upon successive clearing compared to ethanol. Additionally, reduced background fluorescence levels and improved fluorescence of the GFP signal were found (Becker et al., 2012, Renier et al., 2014). DCM removes lipids from the tissue, while DBE is an optical-clearing agent that reduces light scattering and improves optical depth for imaging (Becker et al., 2012, Ertürk et al., 2012, Renier et al., 2014). Ethyl cinnamate can be used as a clearing reagent but in this protocol is used as a refractive index matching solution in which iDISCO cleared brains can be stored and imaged (Klingberg et al., 2017).

2.9.3 Microscopy and image processing of cleared samples

As indicated in relevant figure legends, cleared samples were imaged on:

- Zeiss Lightsheet Z.1 (Zeiss) using the cleared tissue-optimised 20x, Clr Plan Neofluar objective (Zeiss; NA 1.0, working distance: 5.6mm, correction collar for refractive indexes: 1.45 ± 0.3)

- Ultramicroscope II Light Sheet Microscope (LaVision BioTec) using a 2x objective with optional manual zoom (NA: 0.5, working distance: 5.6mm, refractive index matching: 1.33 – 1.56) with the help of Cristina Martinez Gonzalez (University of Edinburgh).

When applicable, 3D reconstruction was performed using IMARIS Software (Bitplane).

2.10 Behavioural tests

All behavioural tests were conducted in the morning.

2.10.1 Open field test

The open field test was used to evaluate general locomotor activity levels. In M_1-WT (C57BL/6J), homozygous M_1-meGFP and M_1-KO mice (inducible M_1 mAChR strain) males and females aged 12-16 weeks were used (n = 8-10; Chapter 5). No sex-based difference was found and therefore, results were pooled per strain. In the rTG4510 experiments, male control and diseased mice at 2.5, 5.0, 7.5 and 10.0 months of age were used (n = 6-8; Chapter 3). Mice were acclimatised to the behavioural testing suite for at least 2 hr prior to testing. For testing, mice were placed into a clear Perspex square arena (50 × 50 cm), and activity was tracked for 10 min using ANY-maze software (Stoelting).

2.10.2 Fear conditioning

For fear condition testing in M_1-WT (C57BL/6J), homozygous M_1-meGFP and M_1-KO mice (inducible M_1 mAChR strain) (Chapter 5), male and female mice aged 12-16 weeks were used. Data for male and female mice was analysed separately

at first, but since no sex-based difference could be found, were then reanalysed as a combined data set (n = 8-12). For fear conditioning in rTG4510 mice, male control and diseased mice at 2.5, 5.0, 7.5 and 10.0 months of age were used (n = 7-8; Chapter 3).

Prior to starting the fear conditioning protocol, mice were acclimatised to the behavioural room overnight. Fear conditioning was performed over three days each approximately 24 hr apart and during the first half of the light cycle. On day 1, mice were placed in the conditioning chamber (ANY-maze Fear Conditioning System, Stoelting) and following a 2 min adaptation period were exposed to 3 tone-foot shock pairings: All tones (2.8 kHz; 85 dB; 30 sec) co-terminated with a foot shock (2 sec; 0.4 mA), and the tone-foot shock pairings were separated by 1 min intervals. After completion of the training sequence, mice remained in the conditioning chamber for 1 min and were then returned to their home cages. On day 2, mice were again placed in the conditioning chamber, and time spent freezing was recorded for 3 min to assess context-dependent learning. On day 3, the environment was changed to allow assessment of the cued response including the use of a different cleaning solution, covering the metal bars in the floor with a plastic surface and covering all walls with paper with different patterns (e.g. black stripes). Mice were placed in the conditioning chamber, and following a 2 min adaptation period, the tone was played for 2 min. During this 2 min period, time spent freezing was recorded to assess cue-specific (tone) learning. Data were analysed using ANY-maze software.

2.10.3 Telemetry

2.10.3.1 *In vivo* Telemetry

To investigate the basal locomotor activity and body temperature in freely moving male healthy control and diseased rTG4510 mice (n = 5 per group) aged3.0 to 8.0 months, a telemetric system (Data Sciences International) was employed. TA-F10 implantable probes (1.1 cc; 1.6 g; Data Sciences International) were subcutaneously implanted in 9-11 week-old mice under isoflurane anaesthesia (5% for induction, 1.5-2% for surgical procedure) and Carprofen (5 mg/kg subcutaneous; Zoetis) analgesia. During surgery, mice were

kept on a thermostable pad. The skin of the abdominal region was disinfected with betadine antiseptic solution (Aviro Health) after the mouse was shaved. Then a 1-1.5 cm long incision in the skin was made along the midline to the abdomen, and the body of the telemetric transmitter was placed subcutaneously. Following this, the skin of the abdominal region was closed with surgical staples. These surgical staples were removed 5-7 days after surgery. Animals were left in an incubator (39±1°C) for approximately 15 min for recovery. After surgery, mice were housed individually and left to recover for 7 days before the start of the experiment. Basal body temperature and locomotor activity were acquired in the home cages directly from the transponders for three consecutive days during which the animals were not disturbed. Receivers were connected through MX2 matrices directly to the PC into a single computer port, allowing for the determination of all parameters. The data were collected every 60 sec using the Ponemah acquisition system (Data Sciences International, Version 6.11), which was also used for initial processing of the data.

2.10.3.2 Biorhythm analysis

Data from telemetry collected by the Ponemah acquisition system were grouped into 10-min sequences, and calculated means were used for further analysis. The analysis was performed using the ChronosFit program (Arraj and Lemmer, 2006) employing Fourier analysis and the stepwise regression technique. For analysis of circadian temperature, data was analysed for outliers using the quartile method for extreme outliers, with values lower than the lower quartile – 3x interquartile range or higher than the upper quartile + 3x interquartile range classed as an outlier (Chromiński and Tkacz, 2010). This method was chosen because of its robustness and ease of use. Only extreme outliers were excluded (± 3x interquartile range rather than ± 1.5x interquartile range for mild outliers), since the main purpose of the outlier analysis was to remove data points that were obviously caused by technical problems. Then, the data were transferred into GraphPad Prism for further statistical analysis.

2.11 Statistical Analysis

Statistical analyses were carried out using GraphPad Prism (Version 9.1.2, GraphPad). Shapiro-Wilk normality tests were used to assess whether data was

normally distributed. Parametric tests were used for normally distributed data, while non-parametric tests were used for data that were not normally distributed. Statistical tests used are indicated in the relevant figure legends and results sections.

Chapter 3 Characterisation of a mouse tauopathy model (rTg4510)

3.1 Introduction

AD is the most prevalent form of dementia and no disease-modifying treatments exist (Prince et al., 2016, Scarpa et al., 2020, World Health Organization, 2021), as the currently approved therapeutics (for details, see 1.3.3) have symptomatic effects only (Yiannopoulou and Papageorgiou, 2013). One of the major challenges in the development of safe and effective treatments for AD, is the absence of a disease model that fully captures AD in human (for details on AD models, see 1.3.2) (Van Dam and De Deyn, 2011, Selkoe, 2011, LaFerla and Green, 2012). Therefore, drug candidates, that show promise in one model, need to be tested further in other preclinical models of AD to ensure that any effect seen is not model-specific.

3.1.1 Validating the M_1 mAChR PAM VU0486846 in the rTG4510 tauopathy mouse model

Previous work in the Bradley and Tobin groups has utilised the murine prion mouse model for investigating terminal neurodegeneration. This model exhibits a number of significant pathological similarities with neurodegenerative disorders in human, including AD. In both, the early loss of presynaptic terminals even prior to the accumulation of prion protein in the prion model or Aß in AD is correlated with cognitive deficits (Näslund et al., 2000, Mallucci et al., 2007, Mallucci, 2009), and cholinergic innervation to the hippocampus is disrupted, while postsynaptic expression of the M_1 mAChR remains unchanged (Bartus et al., 1982, Mash et al., 1985, Bradley et al., 2017). Furthermore, in the murine prion model neuroinflammation, increased oxidative stress and mitochondrial dysfunction are key mechanisms associated with disease (Dwomoh et al., 2022a). These mechanisms are also associated with neurodegeneration and AD in human (Amor and Woodroofe, 2014, Ransohoff, 2016, Abolhassani et al., 2017, Gan et al., 2018, Richards et al., 2018, Wang et al., 2020). As a final similarity, disease both in the murine prion model (Bradley et al., 2017) and in AD in human (Schmidt et al., 2011) leads to extensive and progressive neurodegeneration resulting in terminal disease, a characteristic that is lacking in most transgenic AD models.

Treatment with M_1 mAChR PAMs, such as VU0486846, in the prion mouse model restored memory and learning deficits, reduced neuroinflammation and neurodegeneration markers and extended lifespan potentially signifying disease-modifying effects (Bradley et al., 2017, Dwomoh et al., 2022a). As highlighted above, these disease-modifying properties of the M_1 mAChR PAM VU0486846 should be tested in AD models to establish whether the effects observed are model specific. The rTG4510 tauopathy mouse model was chosen for this investigation because of several reasons. First, a strong focus in AD research has been on the amyloid hypothesis, but nevertheless only one of the amyloid-based therapeutics has preliminarily been approved by the FDA and all other clinical trials have failed (for details, see 1.3.3) (Giacobini and Gold, 2013, Panza et al., 2016, Congdon and Sigurdsson, 2018). Second, a host of research suggests that NFTs rather than amyloid plaques are more closely linked to neurodegeneration and cognitive decline in AD (Giannakopoulos et al., 2003, Iqbal et al., 2005, Giacobini and Gold, 2013, Brier et al., 2016, Congdon and Sigurdsson, 2018). Third, a study comparing transcriptional differences between six mouse models and human diseases, including AD, found the rTG4510 mouse model to be the most transcriptionally robust model showing similar up- and down-regulations of gene sets compared to human AD (Burns et al., 2015). Fourth, as the transgene expression in the rTG4510 mouse model can be suppressed by administration of doxycycline, this potentially allows for the study of whether the M_1 mAChR PAM VU0486846 can prevent the formation of NFTs or restore deficits after NFTs have formed. The rTG4510 model is generally regarded as a good model for testing the effect of therapeutic candidates on tau-related pathology (Jankowsky and Zheng, 2017).

In the rTG4510 mouse model, human tau containing the P301L mutation ($MAPT^{P301L}$) is expressed, with the transgene expression being driven by the CaMKIIα promoter (Santacruz et al., 2005). The $MAPT^{P301L}$ mutation causes FTLD in human and is not associated with AD, however, mouse models overexpressing this mutation show some of the strongest AD-related neurodegeneration and NFT pathology (Ramsden et al., 2005, Santacruz et al., 2005, Jankowsky and Zheng, 2017), making it interesting to see whether administration of the M_1 mAChR PAM VU0486846 can affect this.

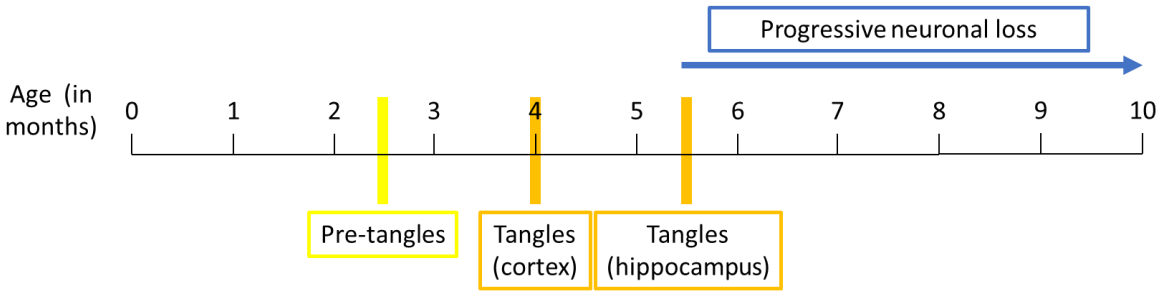

Figure 3.1 Schematic of typical disease progression in male rTG4510 mice.

As outlined in Figure 3.1, in the rTG4510 model pre-tangles can be observed as early as 2.5 months, with tangle-like inclusions being present in the cortex and hippocampus at 4 and 5.5 months, respectively (Ramsden et al., 2005, Santacruz et al., 2005). Additionally, significant atrophy of the forebrain including neuronal cell loss in a prototypic pattern has been reported from 5.5 months of age, whereas cognitive deficits could be observed from 2.5 months (Ramsden et al., 2005, Santacruz et al., 2005, Blackmore et al., 2017). Many of these changes observed are similar to changes seen in AD patients (Goedert and Spillantini Maria, 2006, Grothe et al., 2012), making the rTg4510 model an attractive option for assessing the disease-modifying effects of the M_1 mAChR PAM VU0486846 on tau-related pathology. However, as laboratory specific differences in pathological and behavioural experiments have been reported in this model (Ramsden et al., 2005, Santacruz et al., 2005, Spires et al., 2006, Yue et al., 2011, Brownlow et al., 2013, Cook et al., 2014, Jul et al., 2016, Blackmore et al., 2017, Wang et al., 2018), specific neuropathological and behavioural markers for the use in an efficacy study had to be established first.

3.1.2 Aims

Therefore, as one overarching objective of this thesis was to determine the disease-modifying potential of chronic administration of the M_1 mAChR PAM VU0486846 in the rTG4510 mouse model (Chapter 4), the aims of this chapter were to

- Identify potential changes in levels of the target receptor, the M_1 mAChR,
- Identify potential neuropathological markers,

- Identify behavioural markers associated with diseased state in the rTG4510 mouse model.

Based on previous publications, it was hypothesised that atrophy, increased levels of tau and the inflammatory markers, IBA1 and GFAP, as well as hyperactivity and cognitive deficits worsening with age would be observed in diseased compared to control rTG4510 mice.

3.2 Results

3.2.1 Changes in brain area and M_1 muscarinic receptor expression levels in the diseased rTG4510

3.2.1.1 Diseased rTG4510 have decreased brain size

Initial experiments aimed to assess gross morphological changes in brain sections of control and diseased rTG4510 mice at 2.5, 5.0, 7.5 and 10.0 months of age due to previous reports of laboratory specific differences in brain morphology (Ramsden et al., 2005, Santacruz et al., 2005, Spires et al., 2006, Yue et al., 2011, Jul et al., 2016, Blackmore et al., 2017, Wang et al., 2018). While the overall brain size was reduced in diseased compared to control rTG4510 mice (all $p \leq 0.0001$) and visibly worsened with age ($p = 0.0001$, Figure 3.2, Figure 3.3 A), the measured hippocampal area was consistently smaller in diseased compared to control rTG4510 mice (all $p \leq 0.0002$), but there was no progressive shrinkage with age (Figure 3.2, Figure 3.3 A B).

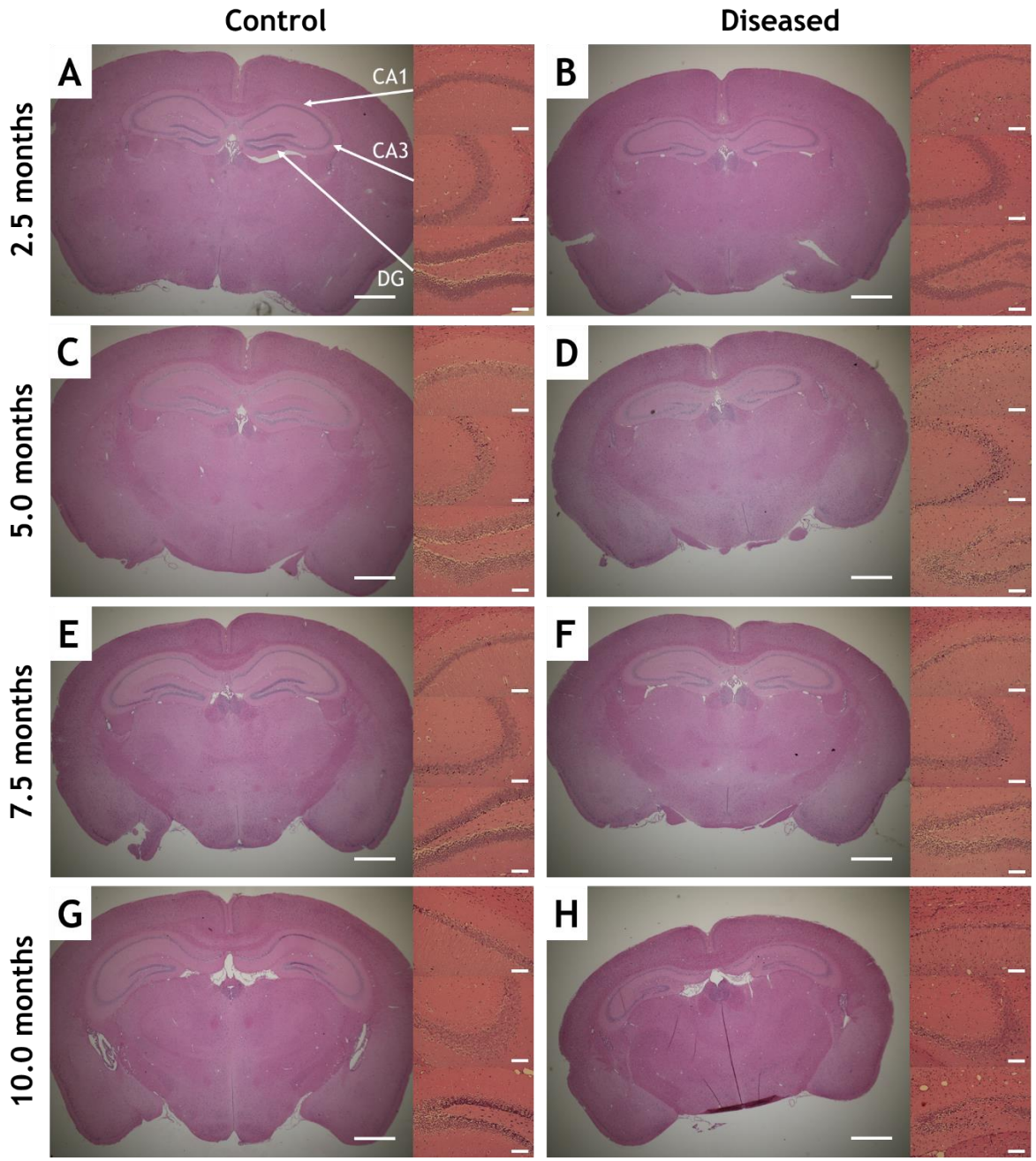

Figure 3.2 Reduced brain size in diseased rTG4510 mice compared to controls, with shrinkage increasing with age. Haematoxylin and eosin (H&E) staining of coronal brain sections of control (A-D) and diseased rTg4510 (E-H) mice at 2.5 (A, E), 5.0 (B, F), 7.5 (C, G) and 10.0 (D, H) months of age are shown. The larger image on the left for each condition shows H&E staining of the whole coronal section (2x magnification; scale bar represents 1000 µm). The smaller images on the right show (from top to bottom) magnifications of the CA1, CA3 and dentate gyrus (DG) (indicated in A) of the hippocampus (20x; scale bar represents 100 µm). Images were acquired using the EVOS FL Auto 2 Imaging System. Representative images of n = 4 are shown.

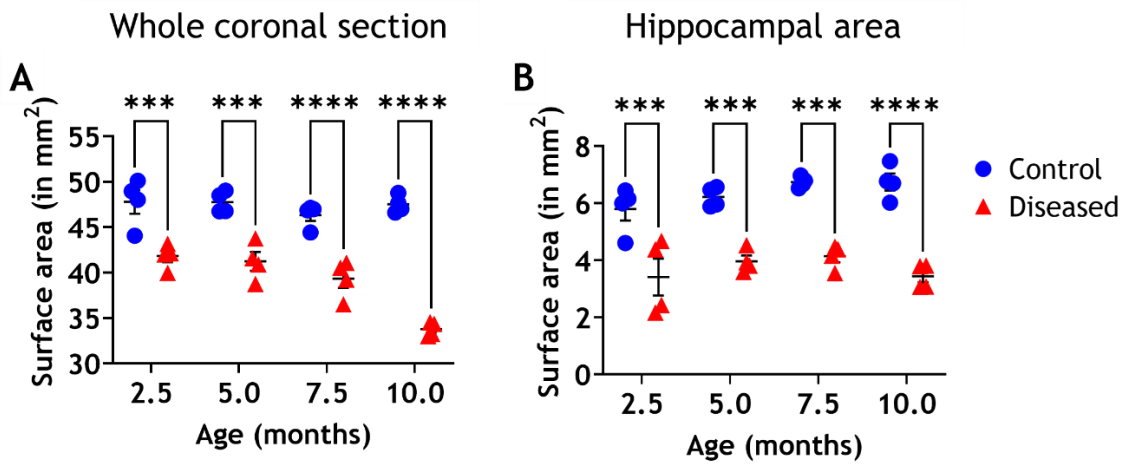

Figure 3.3 Surface area quantification of whole coronal section and hippocampal area show significant reductions in the diseased rTG4510 mice compared to controls. Surface area of the whole coronal section (A) and hippocampal area (B) was measured using ImageJ for n = 4 per group. Data are shown as individual samples and means ± SEM. Statistical analysis was performed using two-way-ANOVA for genotype and age, followed by Sidak's post-hoc correction for multiple comparisons, ** $p < 0.01$, *** $p < 0.001$, **** $p < 0.0001$.

3.2.1.2 Muscarinic receptor expression remains stable until 7.5 months in diseased rTG4510

Since the overall aim was to evaluate the effect of an M_1 mAChR PAM in the rTG4510 mouse model, muscarinic receptor expression levels were first assessed across various time-points of disease using [^{3}H]-NMS saturation binding. Saturation binding curves for all genotypes and age groups are shown (Figure 3.4 A-H) and the corresponding B_{max} values (total concentration of receptors) were obtained (Figure 3.4 I, J). Control and diseased mice showed similar muscarinic expression level from 2.5 to 7.5 months of age, ranging from 606.1 to 728.7 fmol/mg (Figure 3.4 A-F, I, Table 3.1). At 10.0-month-old, however, diseased rTG4510 mice, showed lower receptor expression levels of 370.9 ± 45.0 fmol/mg compared to 728.7 ± 49.3 fmol/mg in control mice (Figure 3.4 G-I, Table 3.1). K_D values, indicating receptor affinity, were also similar across time-points and genotypes (Table 3.1). No statistical analysis was performed due to the small sample size.

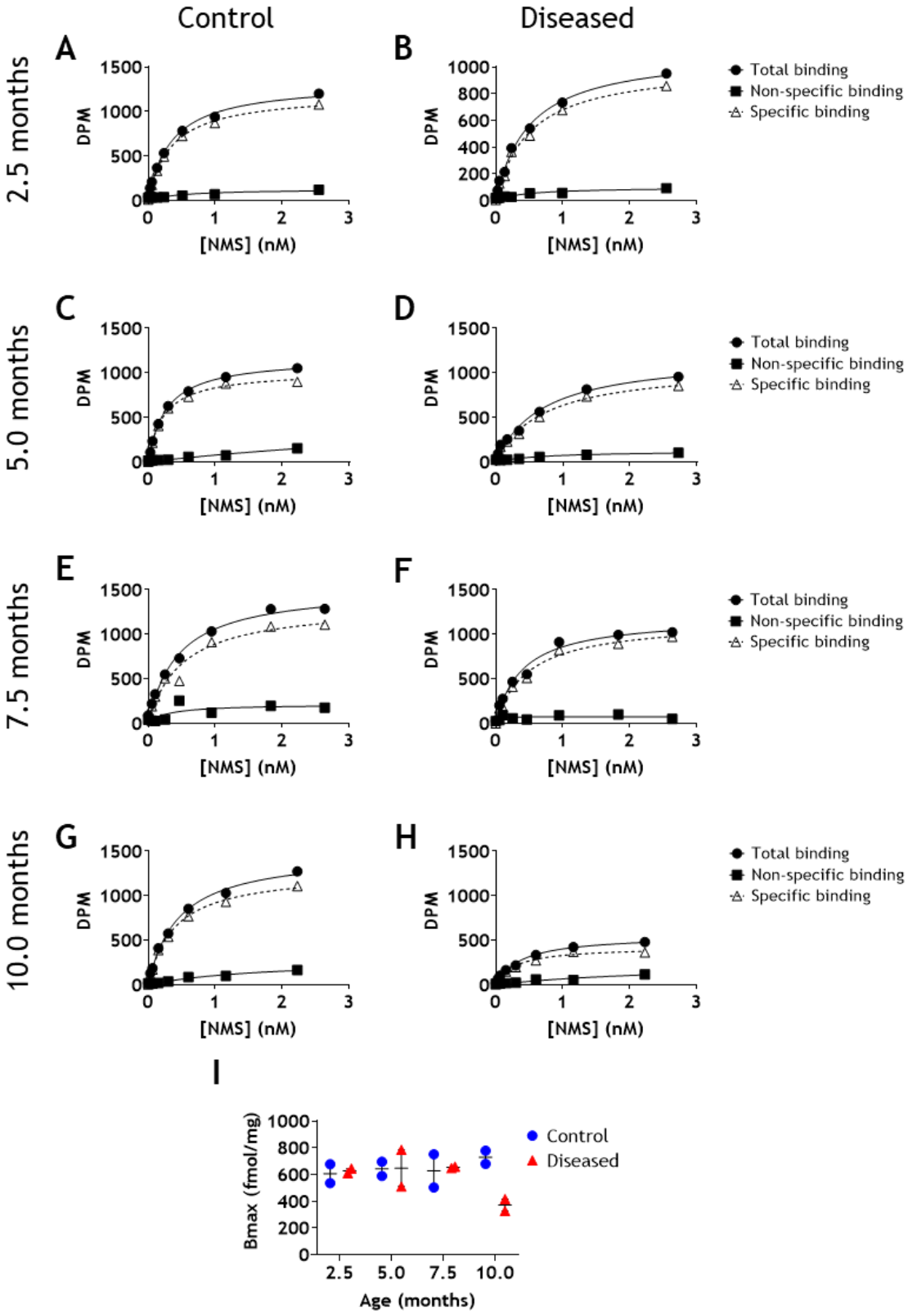

Figure 3.4 Saturation binding experiments suggest a decrease in muscarinic receptor density in the hippocampus in 10.0-month-old diseased rTg4510 mice. Representative graphs of total, non-specific (in the presence of 1 µM atropine) and specific binding in control and diseased rTG4510 mice at 2.5 months (A and B), 5.0 months (C and D), 7.5 months (E and F) and 10.0 months of age (G and H). Muscarinic receptor densities (B_{max}; fmol/mg) for all genotypes and ages were calculated (I). Data are shown as individual samples and means ± SEM, n = 2.

Table 3.1 B_{max} and K_D values for control- and diseased rTG4510 mice at the selected time-points

	B_{max} (fmol/mg)		K_D (nM)	
Age (months)	Control	Diseased	Control	Diseased
2.5	606.1 ± 71.1	626.9 ± 17.1	0.25 ± 0.04	0.46 ± 0.10
5.0	642.0 ± 53.6	646.8 ± 137.5	0.24 ± 0.05	0.72 ± 0.36
7.5	627.0 ± 124.2	653.5 ± 5.2	0.44 ± 0.16	0.64 ± 0.06
10.0	728.7 ± 49.3	370.9 ± 45.0	0.48 ± 0.05	0.29 ± 0.02

Saturation binding experiments with [^{3}H]-NMS cannot distinguish between specific muscarinic receptors and, therefore, it cannot be inferred from this experiment alone whether specific muscarinic subtypes are affected by neurodegeneration in the rTG4510 mouse model. Expression of M_1 mAChR was investigated using gene expression and immunoblotting analysis. RT-qPCR analysis of M_1 mAChR levels in samples from diseased and control rTG4510 mice was performed in samples taken from 8.0-month-old mice taken after completion of telemetry measurements (for more detail on these mice, see 3.2.3). No difference in M_1 mAChR gene expression levels between control and diseased rTG4510 mice were found in the hippocampus (Figure 3.5 A) or cortex (Figure 3.5 B).

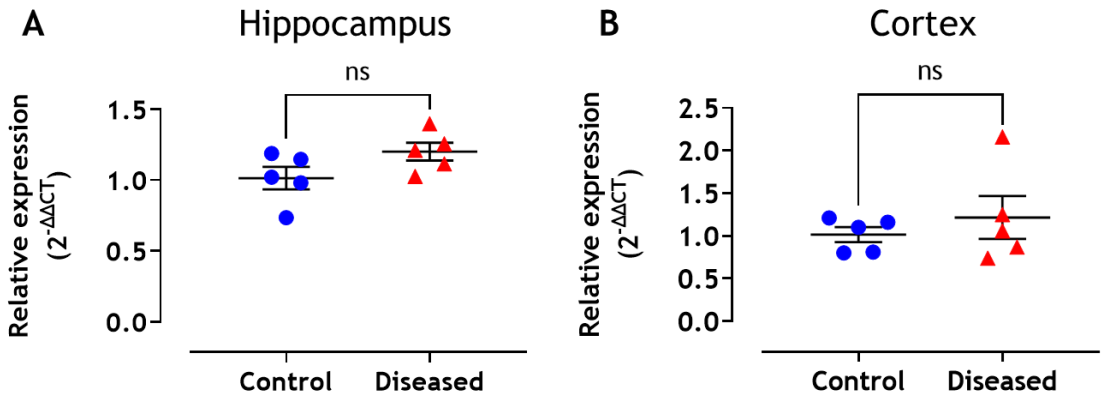

Figure 3.5 M_1 mAChR gene expression levels in 8.0-month-old control and diseased rTG4510 mice. RT-qPCR analysis of M_1 mAChR levels was performed in hippocampal (A) and cortical (B) samples collected from control and diseased rTG4510 mice following telemetry experiments at 8.0 months of age. To assess relative expression levels, data was analysed using the ΔΔCT method, normalising first to α-tubulin and then the mean of the control values for the M_1 mAChR. Data are shown as means ± SEM and data points represent individual mice. Statistical analysis was performed using unpaired t-tests.

Since gene expression does not directly translate to protein expression levels due to post-transcriptional regulation (Anderson and Seilhamer, 1997, Liu et al.,

2016, Buccitelli and Selbach, 2020), immunoblotting in hippocampal samples from control and diseased rTG4510 mice at 7.5 and 10.0 months was also performed. Some variation in the intensity of bands can be found at the expected molecular weight of the M_1 mAChR (Figure 3.6 B). Importantly, despite some background staining, this band is absent in the M_1-KO sample indicating that this is likely specific to and indicative of M_1 mAChR expression (Figure 3.6 B). When this is normalised to total protein expression (Figure 3.6 A), and expressed as fold relative to 7.5-month-old control samples, a trend towards a reduction in M_1 mAChR expression levels, particularly in the 10.0-month-old diseased rTG4510 samples, was observed (Figure 3.6 C). These results nevertheless indicate that the M_1 mAChR is one of the muscarinic receptors, whose expression is declining after 7.5 months in the diseased rTG4510 mice. Together, RT-qPCR, immunoblotting and [^{3}H]-NMS saturation binding experiments suggest a decrease in muscarinic receptor, and specifically M_1 mAChR, expression levels, particularly at 10.0 months in diseased rTG4510 mice.

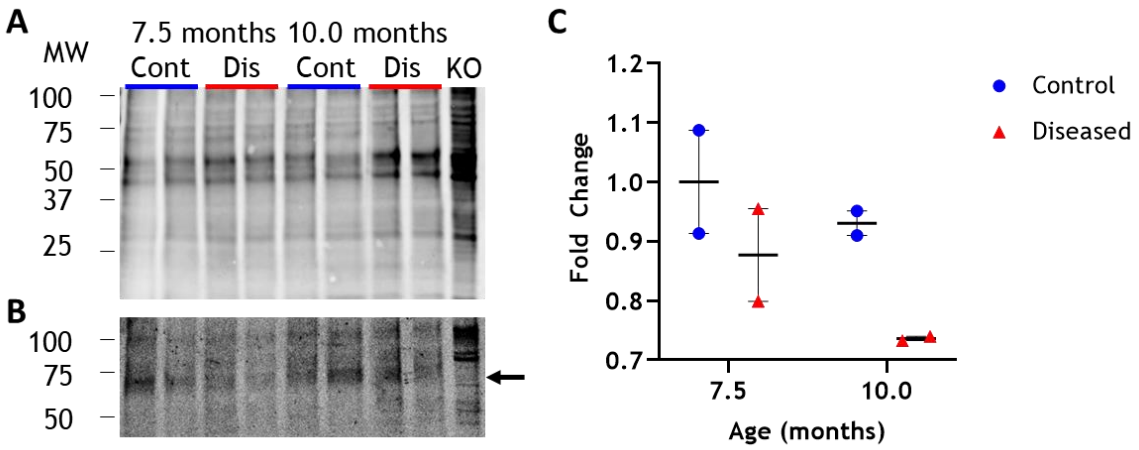

Figure 3.6 Protein levels of the M_1 mAChR in hippocampal samples from 7.5- and 10.0-month-old control and diseased rTG4510 samples. Representative blot of the REVERT 700 Total Protein Stain (A), staining for the M_1 mAChR (B), and quantification of relative protein levels are shown (C). Molecular weight (MW) of the M_1 mAChR is indicated on the right in B) as an arrow. Blots were analysed using Image Studio Lite Version 5.2. Protein levels were normalised to signal obtained from the REVERT Total Protein Stain, followed by normalisation to the average protein level observed in the 7.5-month-old control rTG4510 samples to express as fold change**.** Data are shown as individual samples and means ± SEM, n = 2. The last lane in A) and B) shows the Total Protein Stain and M_1 mAChR expression in a sample from a M_1 mAChR knockout (KO) mouse, respectively.

3.2.2 Characterisation of neuropathological markers in the diseased rTG4510

Staining for human phosphorylated tau (pTau, AT8 antibody, Tau p2002/205) revealed expression in diseased rTG4510, and not control mice, as expected (Figure 3.7). Expression levels of pTau were higher in diseased compared to control rTG4510 mice and increased with age (Figure 3.7 B). In the CA1 ($p \leq 0.0008$) and CA3 ($p \leq 0.0411$) regions, diseased rTG4510 mice had significantly higher levels of pTau compared to control mice from 5.0 months of age, whereas in the DG significantly higher levels were reached at 7.5 months ($p \leq 0.0281$) of age only (Figure 3.7 B).

Due to reports of significant neuronal loss in diseased rTG4510 (Ramsden et al., 2005, Santacruz et al., 2005, Spires et al., 2006) in combination with the reduced hippocampal area across ages in diseased rTG4150 mice described above (Figure 3.2, Figure 3.3), staining for the neuronal marker NeuN was performed to assess potential reductions in neurons. While a significant effect of genotype was found in the CA1 ($p = 0.0033$) and DG ($p = 0.0002$), but not the CA3 ($p = 0.5083$), no effect of age on observed NeuN staining was found (Figure 3.7 B). In line with this, the mean area immunoreactive to NeuN in the CA1 reduction of 58% at 7.5 months ($p = 0.0023$) and 57% at 10.0 months ($p = 0.0164$) and was reduced by 55% in the DG at 7.5 months ($p = 0.0020$) in diseased rTG4510 mice compared to controls, suggesting neuronal loss. In 10.0-month-old diseased rTG4510 mice in the DG ($p = 0.0752$) NeuN staining levels were reduced by 38% compared to controls, however, this reduction was not significant (Figure 3.7 B).

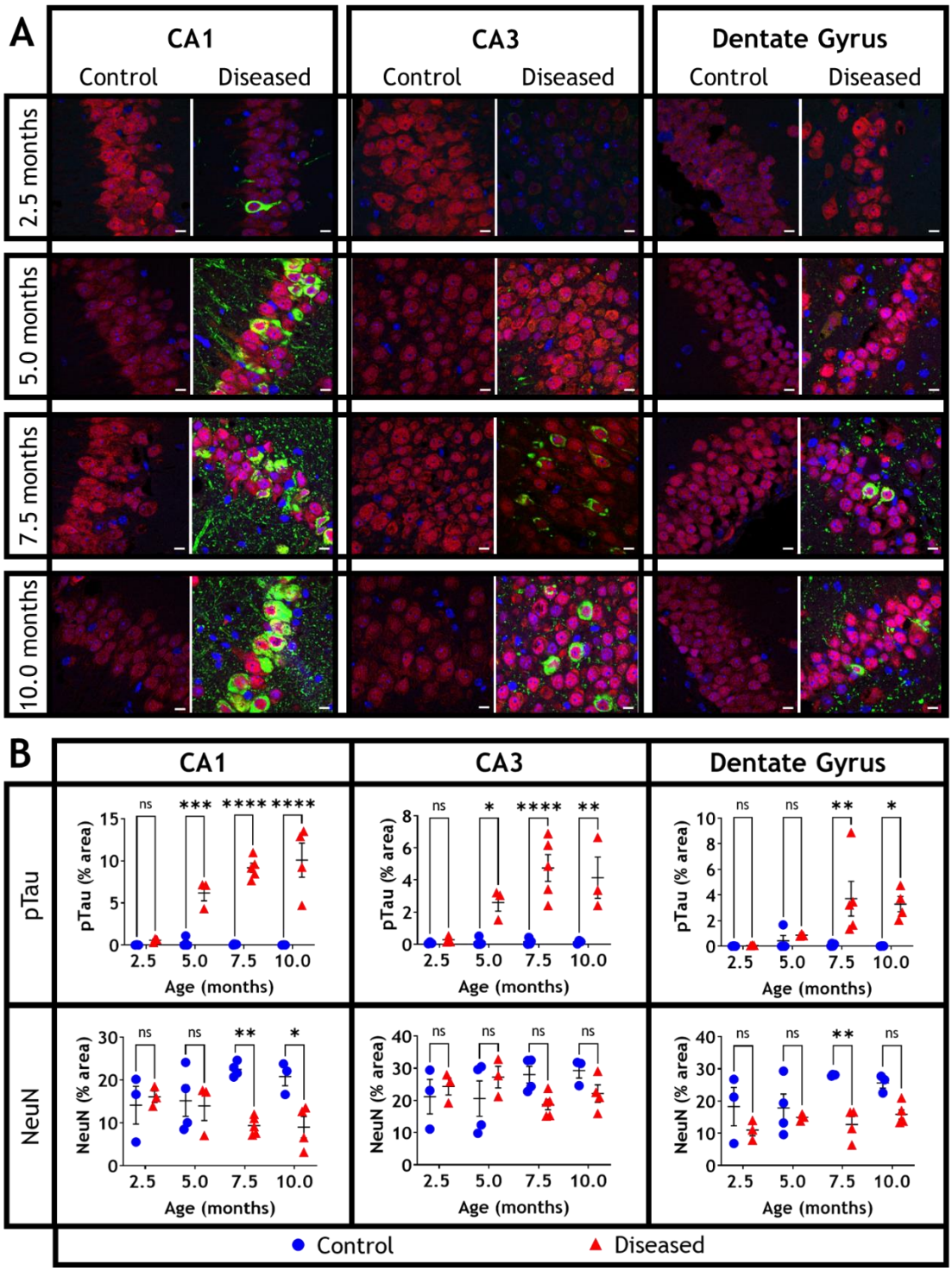

Figure 3.7 Immunostaining for phosphorylated tau and NeuN in control and diseased rTG4510 in the hippocampus. Representative images of the IHC (A) and quantification (B) are shown. Images show staining for DAPI (blue), the human phosphorylated form of tau (pTau, green), and the neuronal marker NeuN (red). Images shown in the left panel were acquired in the CA1, those in the middle panel in the CA3 region, and the ones in the right panel in the dentate gyrus. Staining was performed on 5 µm thick coronal sections and images acquired using a Zeiss LSM 710 confocal microscope at 63x magnification. Images shown are representative of at least 3 mice per group. Scale bars represent 10 µm. Semi-automated quantification of IHC staining at various stages of neurodegeneration in the rTG4510 mouse model was performed using a CellProfiler pipeline for pTau and NeuN. Data are shown as means ± SEM and individual data points represent individual mice; n = 3-5 mice. Statistical analysis using two-way-ANOVA for genotype and age, followed by Sidak's post-hoc correction for multiple comparisons was performed, * $p < 0.05$, ** $p < 0.01$, *** $p < 0.001$, **** $p < 0.0001$.

Since neuroinflammation is a hallmark of many conditions of the CNS, including chronic neurodegenerative disorders such as AD (Middeldorp and Hol, 2011, Heneka et al., 2015, Dansokho and Heneka, 2018, Kumar et al., 2021), markers of neuroinflammation were analysed using RT-qPCR and IHC. Gene expression levels of GFAP, a marker for astrogliosis (Kamphuis et al., 2014), and CD86, as a marker for activated microglia (Jurga et al., 2020), were assessed in hippocampal and cortical samples obtained from 8.0-month-old control and diseased rTG4510 mice used for telemetry measurements (for more detail on these mice see 3.2.3). Expression levels of GFAP and IBA1 in both the hippocampus and cortex of these mice shows relatively large variability between samples from the diseased mice (Figure 3.8). Overall, GFAP and CD86 gene expression levels appear to be higher both in the hippocampus and cortex, but only CD86 levels were significantly increased in the cortex ($p = 0.0141$; Figure 3.8).

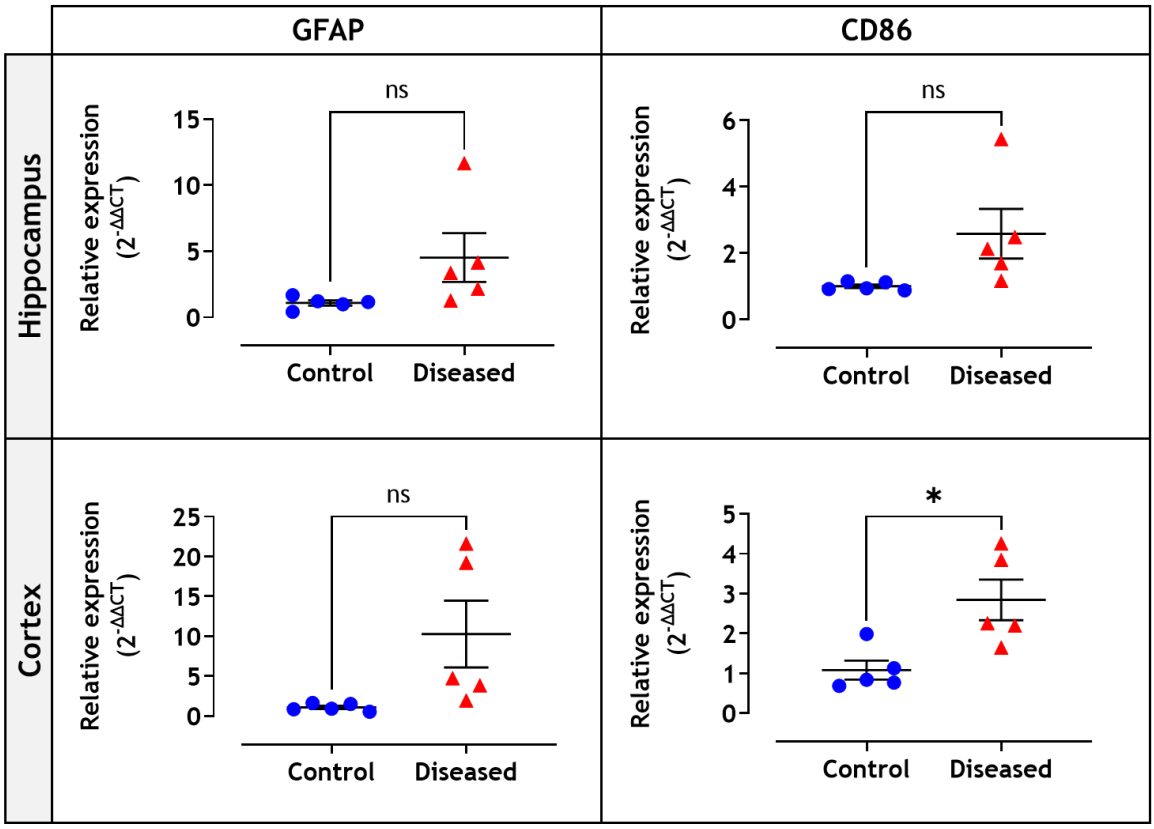

Figure 3.8 Gene expression levels of GFAP and CD86 in control and diseased rTG4510 mice at 8.0 months of age. RT-qPCR analysis of GFAP and CD86 levels, which are astrocyte and microglial markers respectively, was performed in hippocampal (upper panel) and cortical (lower panel) samples collected from control and diseased rTG4510 mice following telemetry experiments at 8.0 months of age. To assess relative expression levels, data was analysed using the ΔΔCT method, normalising first to α-tubulin and then the mean of the control values for each gene of interest. Data are shown as means ± SEM and data points represent individual mice. Statistical analysis was performed using unpaired t-tests, * $p < 0.05$.

Since gene expression and protein expression levels are not equivalent (Anderson and Seilhamer, 1997, Liu et al., 2016, Buccitelli and Selbach, 2020) and to enable assessment of region-specific changes in the CA1, CA3 and DG of the hippocampus, immunostaining was performed. There was a significant effect of genotype on GFAP expression in all regions analysed whereby GFAP expression was greater in diseased compared to control rTG4510 mice (Figure 3.9). This effect was strongest in the CA1 ($p < 0.0001$) and DG ($p < 0.0001$), and weaker in the CA3 ($p = 0.0114$). In the CA1, GFAP levels increased in an age-dependent manner ($p = 0.0117$). Although only reaching statistical significance at 7.5 (5.5-fold increase, $p = 0.0142$) and 10.0 months (8.9x increase, $p < 0.0001$), a 4-fold increase in GFAP levels could be observed as early as 5.0 months in diseased compared to control rTG4510 mice. In the CA3, a significant 3.8-fold increase in GFAP levels were found at 10.0 months ($p = 0.0338$) in diseased rTG4510 mice. In the DG, GFAP levels were significantly increased in the diseased rTG4510 across different time-points (3.1-5.2x increase, $p \leq 0.041$).

Levels of the microglial marker IBA1 were relatively low in both diseased and control rTG4510 mice (Figure 3.9 A, B). Nevertheless, a significant effect of genotype only was found in all regions analysed (CA1 and DG: $p < 0.0001$, CA3: $p = 0.002$). In the CA1, IBA1 levels were significantly increased at 7.5 (2.4x increase, $p = 0.0005$) and 10.0 months of age (3.3x increase, $p < 0.0001$) in the diseased rTG4510 mice. In the CA3, a significant 1.8-fold increase could only be found at 7.5 months ($p = 0.0405$), whereas in the DG, a significant 3.3-fold increase could be found at 2.5 ($p = 0.0011$) and 7.5 months (2.0x increase, $p = 0.0429$). Higher levels of IBA1 at 5.0 (1.9x increase, $p = 0.2295$) and 10.0 months (2.5x increase, $p = 0.0594$) were still observable in the DG, however, these were non-significant (Figure 3.9).

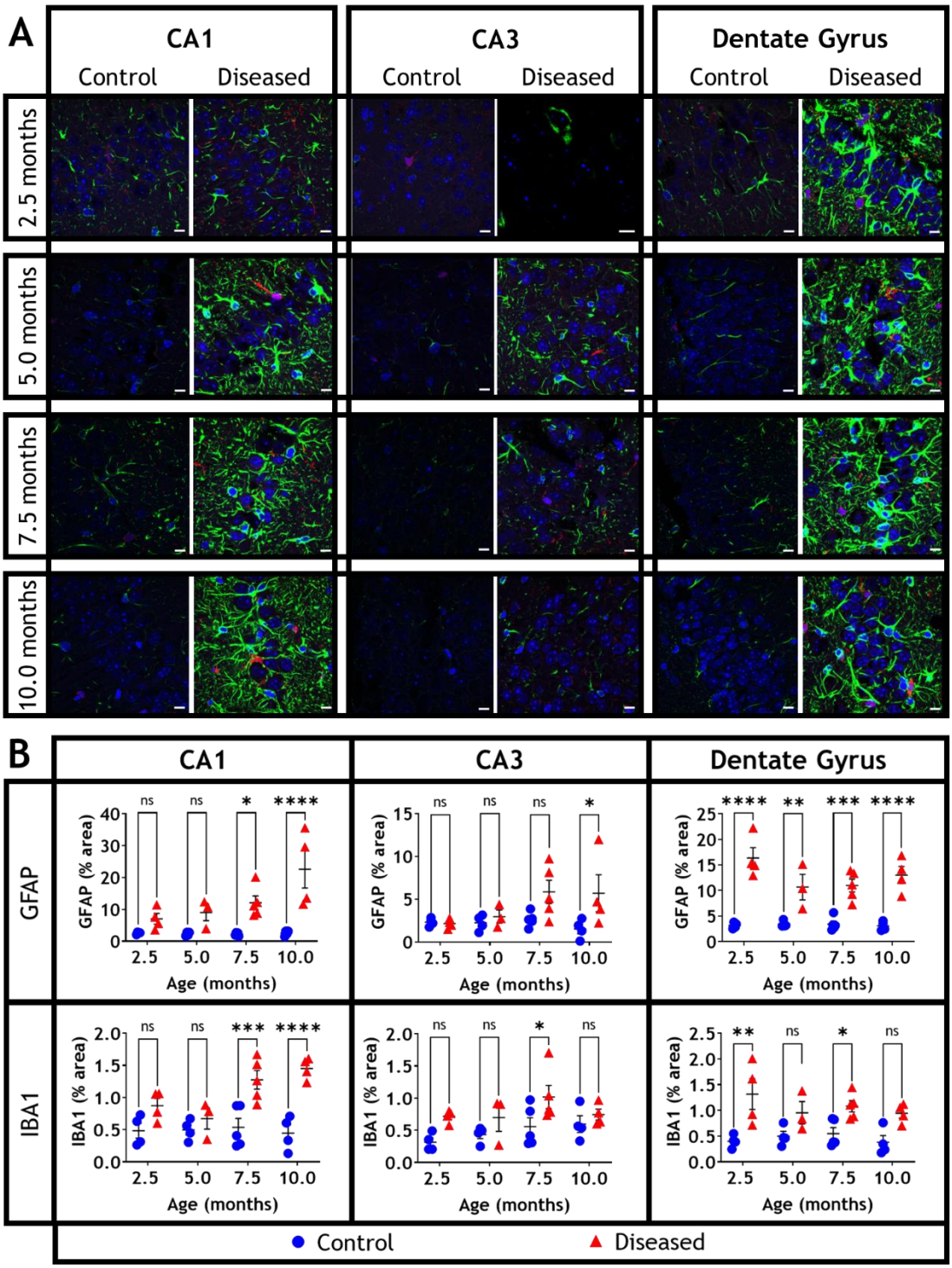

Figure 3.9 Immunostaining for GFAP and IBA1 in control and diseased rTG4510 in the hippocampus. Representative images of the IHC (A) and quantification (B) are shown. Images show staining for DAPI (blue), the astrocytic marker GFAP (green), and the microglial marker IBA1 (red). Images in the left panel were acquired in the CA1, those in the middle panel in the CA3 region, and the ones in the right panel in the dentate gyrus. Staining was performed on 5 µm thick coronal sections and images acquired using a Zeiss LSM 710 confocal microscope at 63x magnification. Images shown are representative of at least 3 mice per group. Scale bars represent 10 µm. Semi-automated quantification of IHC staining at various stages of neurodegeneration in the rTG4510 mouse model was performed using a CellProfiler pipeline for pTau and NeuN. Data are shown as means ± SEM and individual data points represent individual mice; n = 3-5 mice. Statistical analysis using two-way-ANOVA for genotype and age, followed by Sidak's post-hoc correction for multiple comparisons was performed, * $p < 0.05$, ** $p < 0.01$, *** $p < 0.001$, **** $p < 0.0001$.

3.2.3 Characterisation of behavioural markers in the diseased rTG4510 mice

Relatively few behavioural phenotypes in the rTG4510 mice have been described, but cognitive deficits and hyperactivity are among the most common ones (Ramsden et al., 2005, Santacruz et al., 2005, Brownlow et al., 2013, Cook et al., 2014, Jul et al., 2016). Various behavioural tests were assessed in rTG4510 mice in an effort to establish a tauopathy-sensitive behavioural readout to investigate functional decline.

In the fear conditioning paradigm, no differences between diseased and control rTG4510 mice were found (experiments performed by SJ Bradley). While age had a significant effect in both at baseline ($p = 0.0174$; Figure 3.10 A) and during context retrieval ($p = 0.0016$; Figure 3.10 B), genotype did not have a significant effect for either ($p = 0.2662$ and $p = 4220$, respectively). Interestingly, for both control and diseased rTG4510 mice at 7.5 and 10.0 months of age, the freezing response was significantly lower compared to the one observed at 2.5 months ($p = 0.0127$ – 0.0193).

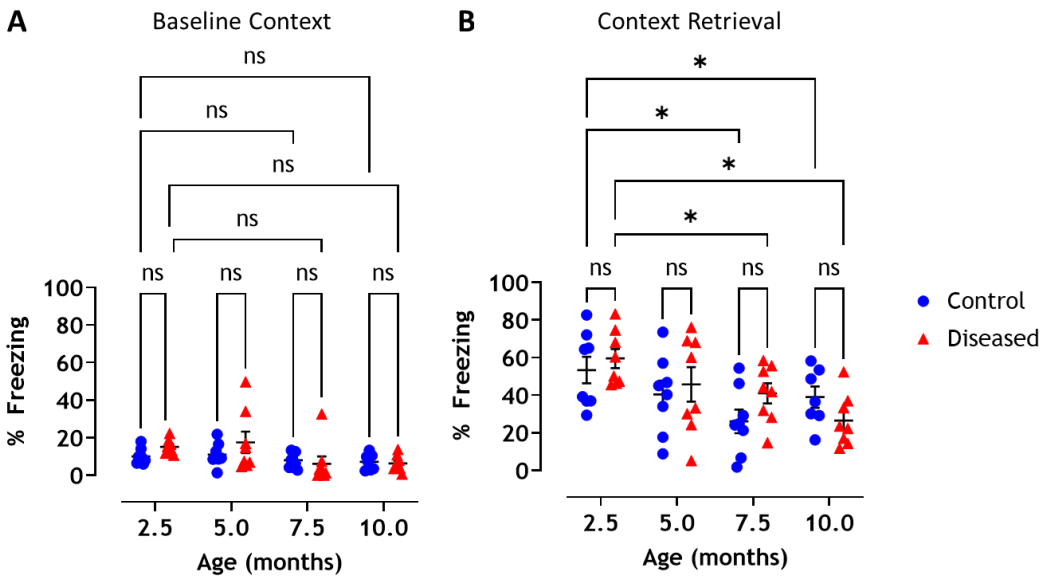

Figure 3.10 No difference in contextual fear conditioning response between control and diseased rTG4510 mice at all time-points assessed. Both at baseline (A) and during context retrieval (B) no difference between control and diseases was found. In context retrieval, response in control and diseased mice at 7.5 and 10.0 months was significantly lower compared to the respective freezing rates at 2.5 months. Data are shown as means ± SEM with individual data points representing individual mice, n = 7-8 for all groups. Two-way ANOVA for genotype and age, followed by Tukey's multiple comparison tests were performed for statistical analysis, where * $p < 0.05$. Data was collected by SJ Bradley and is being used with permission.

3.2.3.1 Assessment of locomotor activity in rTG4510

General locomotor activity was assessed in rTG4510 mice in an open field paradigm. No changes in distance travelled between control and diseased mice were found in the centre area (Figure 3.11 A, B). At 2.5 and 5.0 months, diseased rTG4510 showed no changes in general locomotor activity in the perimeter (Figure 3.11 A, B). However, older diseased rTG4510 mice exhibited increased activity levels compared to controls only in the perimeter of the arena (7.5 months p = 0.0001; 10.0 months p = 0.0005; Figure 3.11 B). Interestingly, more variability could be observed in the diseased rTG4510 mice, especially at 7.5 and 10.0 months (Figure 3.11 A, B). No difference in time spent in the centre or perimeter areas of the arena between control or diseased rTG4510 mice was found at any time-point (Figure 3.11 C, D). Overall, mice from all groups spent 83 - 96 % of the test duration in the perimeter region of the arena.

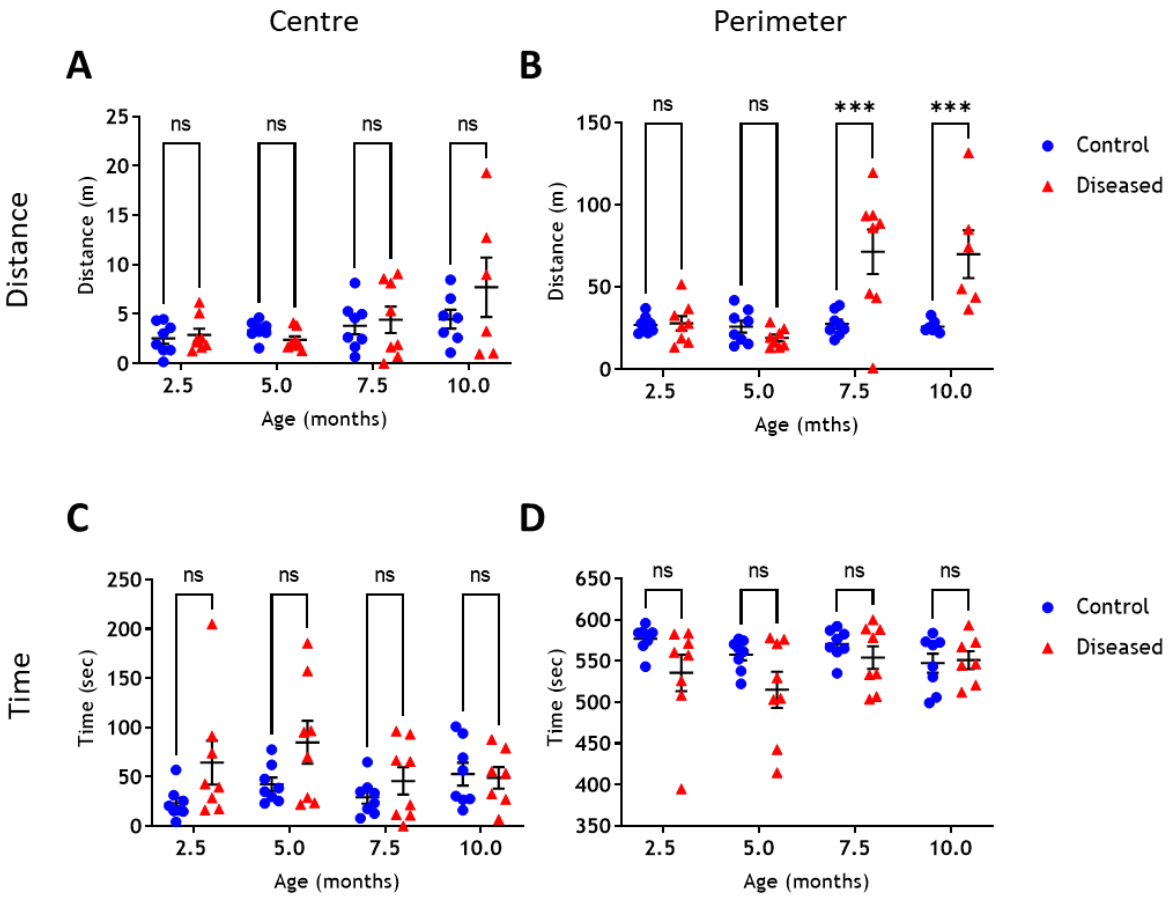

Figure 3.11 Locomotor activity measured in open field test in rTG4510 mice. Distance travelled by control and diseased rTG4510 mice was determined during a 10 min interval in the open field test in the centre (A) and perimeter (B) of the arena. Time spent in the centre (C) and perimeter (D) of the arena was also measured for the different groups. Data was analysed using two-way ANOVA for genotype and age, followed by Sidak's multiple comparisons test. Behavioural data are shown as means ± SEM with individual data points representing individual mice, n = 6-8 mice.

Telemetry was then used to investigate the basal circadian activity of control and diseased rTG4510 mice aged 4.0 to 8.0 months within their home-cage environment.

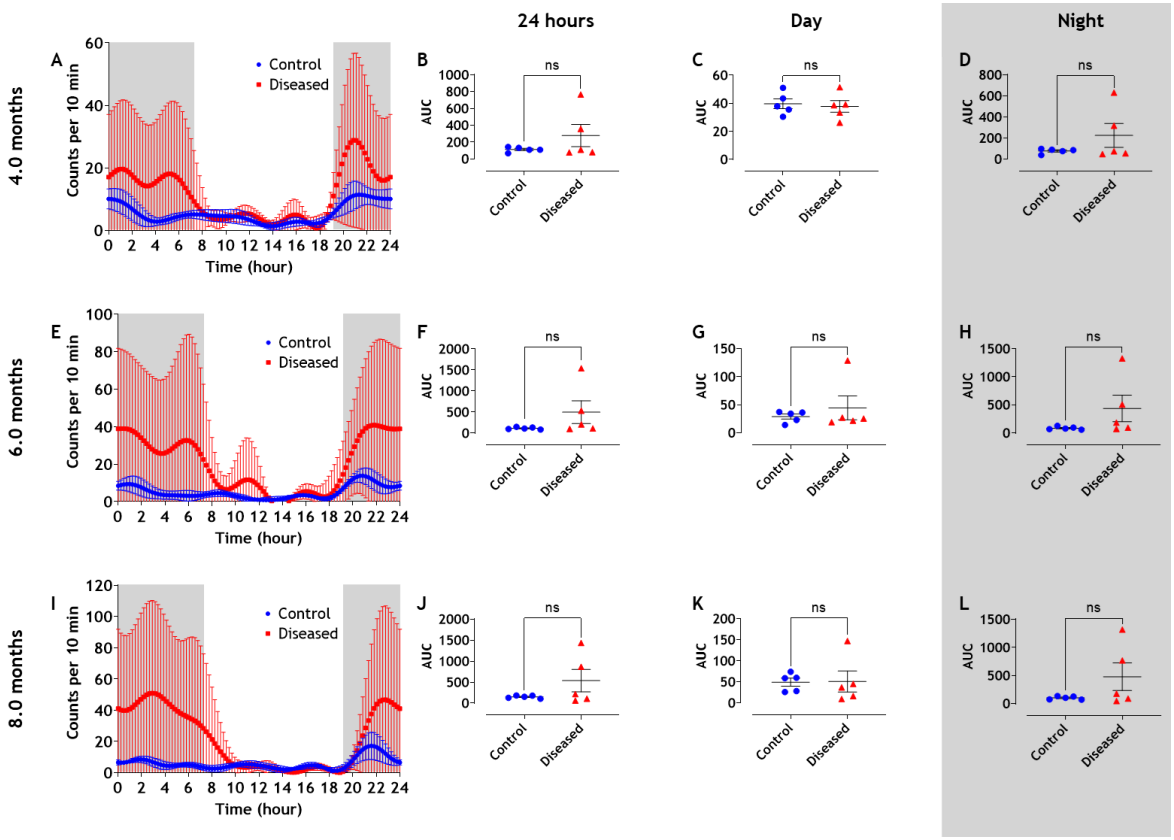

Figure 3.12 Measurement of basal circadian locomotor activity in rTg4510 mice at 4.0, 6.0 and 8.0 months. Basal circadian locomotor activity in control and diseased rTG4510 mice was acquired at the time-points indicated across three consecutive days using *in vivo* telemetry recordings. Data in 24-hour biorhythm graphs (A, E, I) are expressed as means ± SD. Locomotor activity during this period for individual mice was calculated by measurement of the area under the curve (AUC) over 24 hours (B, F, J), during the day (C, G, K) and at night (D, H, L) at the indicated time-points. Data are expressed as individual values and means ± SEM, n = 5 mice. Unpaired t-tests were used to compare AUC measurements between control and diseased rTG4510 mice.

No difference in basal activity levels between control and diseased mice at any disease time-point was recorded during the day. Relatively low activity levels were recorded for both genotypes during the day in line with the nocturnal nature of mice (Figure 3.12 C, G, K). However, during their active phase at night, a trend towards higher activity levels was observed in diseased rTG4510 mice at all time-points measured (Figure 3.12 D, H, L; grey box). Furthermore, two diseased rTG4510 showed a more hyperactive phenotype compared to the other mice and this effect increased with age (Figure 3.13).

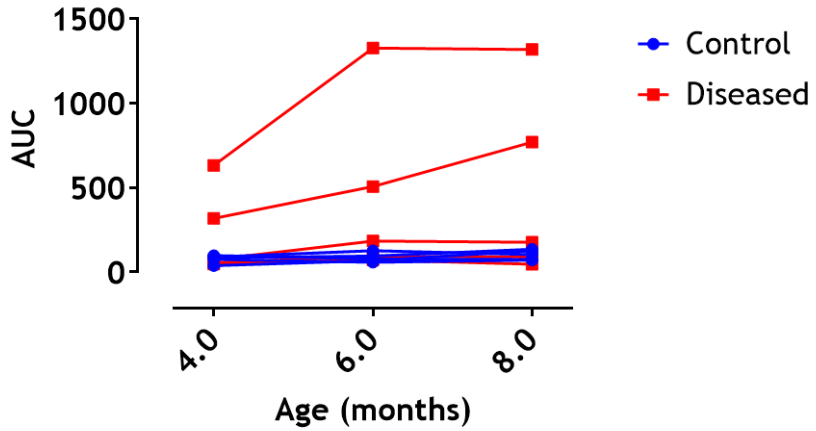

Figure 3.13 Activity levels increased with age in some diseased rTG4510 mice during their active phase. Area under the curve (AUC) measures of locomotor activity levels at night for individual animals are shown from 4.0 to 8.0 months.

Similarly to what was observed in the open field test, a large degree of variability between individual replicates within the diseased rTG4510 group could be found at all time-points (Figure 3.12 A, E, I) with apparent populations of control-like- and hyperactive phenotype groups in the diseased genotype (Figure 1.11 D, H, L, grey box). Therefore, the variability determined in the telemetry was consistent with the data collected in the open field test.

To assess how the biochemical markers of pathology correlated with behavioural outcome, a correlation plot was constructed for activity versus tau or GFAP expression at 8.0 months. The locomotor activity phenotype was the most robust of the behavioural phenotypes tested. Murine tau levels were also assessed. GFAP levels were found to be one of the most reliable disease marker in the prion mouse model (Dwomoh et al., 2022a). While murine tau expression was not significantly correlated with activity levels over a 24 hr period at 8.0 months in diseased rTG4510 mice ($r = 0.7763$, $p = 0.1226$, Figure 3.14 A), GFAP expression was ($r = 0.9065$, $p = 0.0338$; Figure 3.14 B).

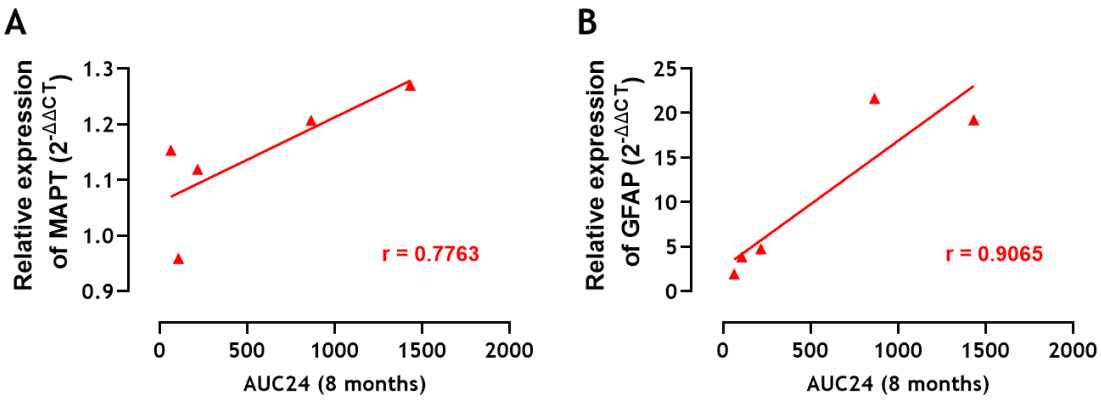

Figure 3.14 GFAP, but not murine tau expression, significantly correlated with general activity levels in diseased rTG4510 mice. Relative expression levels of murine tau (A) and GFAP (B) were measured using RT-qPCR analysis from cortical samples collected immediately after completion of the 8.0-month telemetry measurements. Activity levels over a 24-hour period were measured as area under the curve (AUC) at the 8.0-month time-point. Simple linear regression analyses were performed to assess correlation between tau and GFAP gene expression versus activity levels in diseased rTG4510.

3.2.3.2 Raised body temperature in 8.0-month-old diseased rTG4510 mice

Probes used for telemetry measurements also record core body temperature. During the inactive phase during the day, no difference between control and diseased rTG4510 mice was found (Figure 3.15 C, G, K). However, at 8.0 months, significantly higher body temperature measures were recorded in diseased rTG4510 mice (Figure 3.15 L) and this statistically significant effect also became apparent in the biorhythm graph (Figure 3.15 I).

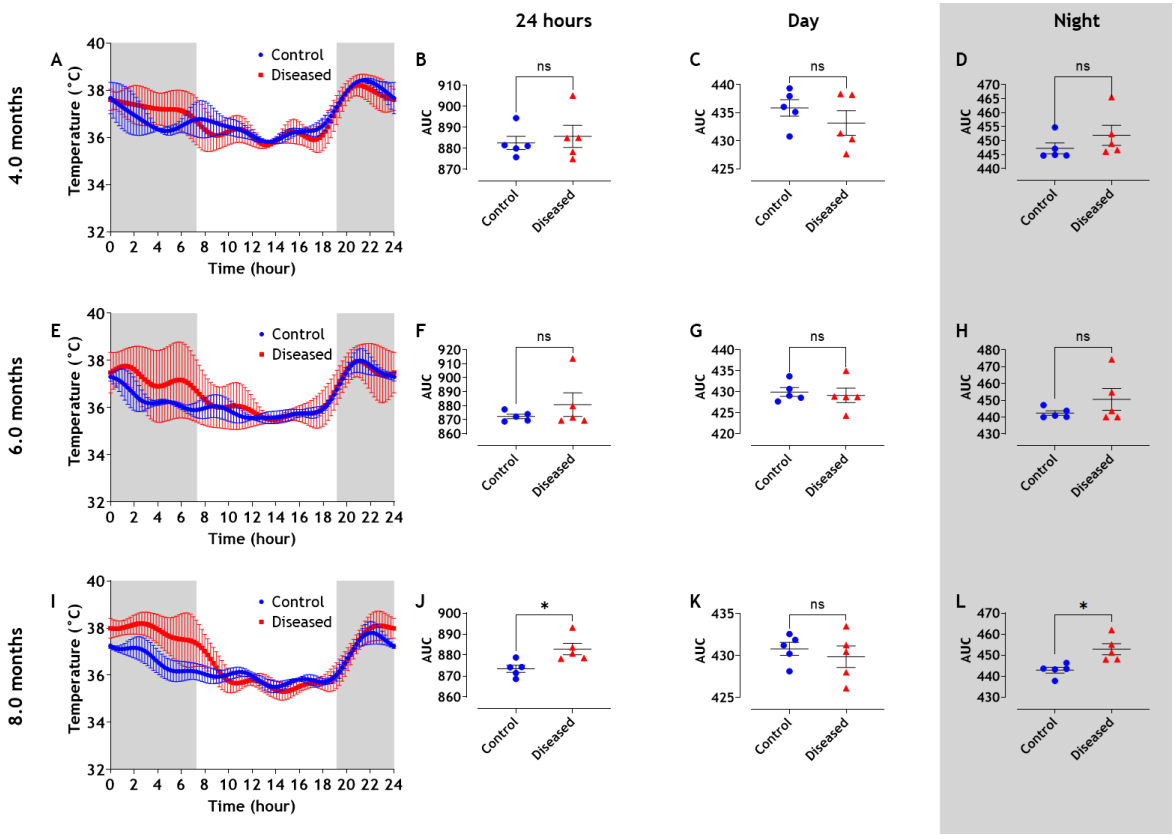

Figure 3.15 Circadian body temperature fluctuations in rTg4510 mice at 4.0, 6.0 and 8.0 months. Circadian body temperature fluctuations in control and diseased rTG4510 mice was acquired at the time-points indicated across three consecutive days using *in vivo* telemetry recordings. Data in 24-hour biorhythm graphs (A, E, I) are expressed as means ± SD. Body temperature during this period for individual mice was calculated by measurement of the AUC over 24 hours (B, F, J), during the day (C, G, K) and at night (D, H, L) at the indicated time-points. Data were expressed as individual values and means ± SEM, n = 5 mice. Unpaired t-tests were used to compare AUC measurements between control and diseased rTG4510 mice, * $p < 0.05$.

3.3 Discussion

Currently, no rodent models reliably recapitulate human AD and therefore, it is prudent to test therapeutic candidates in a range of models that show key pathological features. This chapter focussed on the characterisation of the Tg4510 tauopathy model to identify neuropathological and behavioural markers of pathology. In accordance with the hypothesis, although limited by small samples sizes due to sample acquisition issues, diseased rTG4510 mice display reduced brain size, increased levels of pTau and neuroinflammation markers, and a hyperactive phenotype at later disease stages in the open field test. Therefore, the rTG4510 model represents a useful preclinical model to investigate potential therapeutic benefits of novel drugs on pathological features that are relevant to human disease.

The rTg4510 mouse model has previously been characterised and used to assess the effect of doxycycline-induced transgene suppression in this model (Santacruz et al., 2005, Ramsden et al., 2005, Spires et al., 2006, Wang et al., 2018), as well as the effect of tau-based immunotherapy candidates (Sankaranarayanan et al., 2015, Schroeder et al., 2017), and colony-stimulating factor receptor 1a (Bennett et al., 2018) and p38αMAPK inhibitors (Roy et al., 2019). Even though it is important to keep in mind that immunoblotting is a semi-quantitative method, together with the [^{3}H]-NMS saturation and RT-qPCR experiments, these results suggest that M_1 mAChR expression decreases at later disease stages and particularly at 10.0 months.

A common feature of disease pathology in the rTG4510 is the accumulation of tau aggregates and neuroinflammatory markers from 3.0 months. Similar to the results presented here, several studies have reported a progressive series of distinct and hyperphosphorylated tau species similar to those found in AD patients leading to forebrain atrophy, as well as significantly increased levels of GFAP and IBA1 immunoreactivity in diseased rTG4510 (Ramsden et al., 2005, Santacruz et al., 2005, Spires et al., 2006, Dickey et al., 2009, Bennett et al., 2018, Brownlow et al., 2013). In the rTg4510 model, expression of P301L mutant tau is driven by CaMKIIα expression. CaMKIIα is predominantly expressed in the forebrain, including the hippocampus, and neuronal loss and atrophy mostly affects these forebrain regions (Miller and Kennedy, 1985, Ramsden et al., 2005,

Santacruz et al., 2005, Spires et al., 2006, Brownlow et al., 2013, Wang et al., 2013, Blackmore et al., 2017, Helboe et al., 2017). This is consistent with the reduced coronal section and hippocampal areas in diseased rTG4510 mice presented here. While brain size in different regions of the hippocampus was not assessed, the reduced immunoreactivity for NeuN in the CA1 and DG are in line with previous studies reporting highest levels of neurodegeneration in the CA1 and DG regions (Spires et al., 2006, Helboe et al., 2017). More specifically, others have found severe hippocampal neurodegeneration with 80% neuronal loss in the CA1 region by 8 months and DG by 8.5 months in rTG4510 mice (Spires et al., 2006) or a 43% reduction in neuronal number in the CA1 region between 8.0 and 12.0 months (Helboe et al., 2017). Similarly, the results reported here suggest 69% neuronal loss in the CA1 region at 7.5 months in diseased compared to control rTG4510 mice. A previous report of GFAP and IBA1 expression levels via IHC demonstrate an increase of approximately 2.3-2.8-fold in both GFAP and IBA1 levels in the hippocampus of diseased compared to control rTG4510 mice at 8.0 months (Brownlow et al., 2013). This agrees with the results presented here whereby an increase of 1.8-3.2-fold in both GFAP and IBA1 levels in diseased compared to control rTG4510 at 7.5 months was found in all assessed areas of the hippocampus, except for GFAP in the CA1, where a 5.5-fold change could be observed. GFAP expression increased with age, particularly in the CA1 region of the hippocampus. For IBA1, immunoreactivity levels do not seem to be as affected by age as the GFAP levels and generally have relatively low levels. In the prion mouse model of neurodegeneration, GFAP levels correlate well with disease progression and M_1 mAChR PAM-induced modification in efficacy studies with a M_1 mAChR PAM (Dwomoh et al., 2022a). Similarly, in this study the combination of high levels of neurodegeneration and GFAP in the CA1 and DG regions suggest that GFAP can also be used as a marker for neurodegeneration in the rTG4510 mouse model.

In neurodegeneration in human and specifically AD, neuroinflammation including astrogliosis has also been found to be a common pathological marker (Sofroniew and Vinters, 2010, Middeldorp and Hol, 2011, Kamphuis et al., 2014, Dansokho and Heneka, 2018), meaning that GFAP could potentially also be used in translational studies. While not having been used yet as a biomarker in clinical studies in AD, several studies have suggested the use of blood GFAP as a

biomarker for mild cognitive impairment (MCI) and AD (Cicognola et al., 2021, Pereira et al., 2021, Beyer et al., 2022, Oeckl et al., 2022). In a future preclinical study, serum GFAP levels could potentially also be used as a longitudinal measure and then be compared to histology at death.

Other phenotypes reported in diseased rTG4510 mice have been behavioural changes such as hyperactivity and memory and learning deficits (Ramsden et al., 2005, Santacruz et al., 2005, Brownlow et al., 2013, Cook et al., 2014, Jul et al., 2016). While a hyperactive phenotype was observed in diseased rTG4510 mice in the open field test from 7.5 months in line with the hypothesis, this finding was not corroborated using a telemetry system in the home-cage. Benefits of this type of telemetric testing are that it allows continuous and longitudinal recording in a less-stressful environment and might capture behaviours which are not observable using short-sampling standard methods like the open field test (Bains et al., 2018, Grieco et al., 2021). One disadvantage is that mice had to be in solitary housing for the type of recording system used and therefore, this could affect wellbeing and behaviour to some extent (Bains et al., 2018, Grieco et al., 2021, Benfato et al., 2022). The hyperactive phenotype displayed in 7.5- and 10.0-month-old diseased rTG4510 in the open-field paradigm are consistent with results by Blackmore et al. (2017) who demonstrated increased activity levels in old diseased rTG4510 mice. However, other laboratories have reported hyperactivity in diseased rTG4510 mice at 4.0 (Jul et al., 2016, Wang et al., 2018) or 6.0 months (Cook et al., 2014). Jul et al. (2016) did not use an open field paradigm, but rather placed mice in a new cage for 3 hr and measured activity by the frequency of animals crossing photo beams. Interestingly, they also reported heterogenous results where some diseased rTG4510 mice displayed a hyperactive phenotype, while some did not, and that the proportion of diseased mice displaying a hyperactive phenotype increased from 12% at 16 weeks to 62% at 24 weeks of age and older (Jul et al., 2016). This is in line with the open field data presented here where 62.5% (5 out of 8) of the diseased rTG4510 mice at 7.5 months appeared to be more hyperactive than the control mice. In the telemetry measurements, 40% (2 out of 5) of the diseased rTG4510 mice consistently showed increased activity levels increasing with age, however, in contrast to the discussed study (Jul et al., 2016) the proportion of hyperactive diseased mice did not increase with age. Variability in locomotor activity has

been reported previously (Wang et al., 2018). The authors proposed that a certain level of accumulated pathological tau species needs to be reached to cause hyperactivity and that one subpopulation had crossed that threshold, while the other had not (Wang et al., 2018). It remains unclear why diseased mice of the same age would show such variability in disease state, since the combination of the same genetic background and environmental factors should mean that these mice are similarly affected. It is also worth noting, of course, that the sample size here was small due to animal availability issues and increasing the sample size may reveal more alignment with previously published results. Interestingly, this study found cortical GFAP expression, which has been suggested to be a good marker of neuroinflammation and disease, to significantly correlate with locomotor activity in a 24-hour period in diseased rTG4510 mice. Levels of murine tau did not correlate with activity levels, however, a study of human tau levels, as the driver of neurodegeneration in this model, in relation to observed activity levels would have been interesting.

Contradicing the hypothesis that cognitive deficts would be found in diseased compared to control rTG4510 mice, results reported in this study are inconsistent with other fear conditioning studies (Brownlow et al., 2013, Cook et al., 2014). Cook et al. (2014) reported deficits in diseased rTG4510 mice compared to controls in contextual fear conditioning from 2.0 months of age, with deficits worsening with age up to the last measured disease time-point at 10.0 months. Similar to this study, Cook et al. (2014) performed training and context-retrieval in the first part of the light cycle, however, using slightly longer timings for the fear conditioning training and measurements, and a foot shock of 0.5 mA (compared to 0.4 mA used here). These minor protocol differences should not account for the stark difference seen between the reported results (Cook et al., 2014). Furthermore, Cook et al. (2014) also reported a hyperactive phenotype which increased with age between measurements at 6.0 and 10.0 months. This hyperactivity could confound the amount of freezing seen in the fear conditioning experiments, however at 2.0 months the reduction in freezing in the diseased rTG4510 mice is before a hyperactive phenotype is observed (Cook et al., 2014). Brownlow et al. (2013) did not specify during which part of the light/ dark cycle behavioural experiments were performed. Again, for fear conditioning, a 0.5 mA foot shock

was used, but otherwise, the reported training and testing regime was very similar to the regime used here with the exception of the freezing rates being recorded manually by a blinded observer (Brownlow et al., 2013). Interestingly, at 8.0 months, Brownlow et al. (2013) reported a 94 – 99% and 63 – 79% freezing rate in control and diseased rTG4510 mice respectively in the contextual fear response, depending on diet. These freezing rates are higher than those commonly observed within this research group, which is around 60 – 80% (Bradley et al., 2017). This could potentially be due to the manual assessment of freezing in the abovementioned study compared to the automated tracking with ANY-maze. In the fear conditioning experiments reported in this chapter, age-dependent decreases in freezing rates were found in both control and diseased rTG4510. While reduced freezing in the diseased rTG4510 would be in line with reports from other labs showing increasing memory deficits with age, it is unclear why the control mice also exhibited a lessened contextual fear response.

Interestingly, at 4.0 and 6.0 months of age, small bursts of activity during the day became apparent in the diseased compared to control mice in the biorhythm graphs from the telemetry experiments (Figure 3.12 A, E). These abnormal activity patterns of activity bursts during the light phases were also reported by another laboratory using a similar set up (Jul et al., 2016). Furthermore, Jul et al. (2016) linked the hyperactive phenotype to transgene expression, since doxycycline-induced suppression ameliorated the phenotype. In patients with AD, increased levels of restlessness and hyperactivity have also been reported (Cohen-Mansfield and Billig, 1986, Borson and Raskind, 1997, Scarmeas et al., 2007). The slight changes in circadian rhythm and sleep disturbances observed in diseased rTG4510 mice here and reported by Jul et al. (2016) also show some similarities to circadian dysregulation seen in AD patients (Wu and Swaab, 2007, Weldemichael and Grossberg, 2010, Hoyt and Obrietan, 2022, Sun et al., 2022). Unfortunately, the behavioural changes observed in the rTG4510 mice in this study are too variable to present a robust behavioural indicator of disease in the rTG4510 mouse model for the use in an efficacy study.

While not really a behavioural but rather a physiological phenotype, body temperature was significantly increased in 8.0-month-old diseased rTG4510

mice. While this has not been studied in the rTG4510 mouse model so far, in the 3xTg AD mouse model of AD, age-dependent increases in core body temperature, activity and food intake were detected before the onset of significant behavioural deficits (Knight et al., 2013). Since we could not detect any significant behavioural phenotypes in the telemetry measurements, the increased temperature measurements could be an early indicator of the onset of behavioural deficits. Due to time restrictions in animal license approval in performing the telemetry experiments, data from later time-points could not be collected. Some studies have reported higher metabolic rates in diseased rTG4510 mice, which is one explanation for a higher body temperature (Brownlow et al., 2013, Joly-Amado et al., 2016). Interestingly, one study reported an increased resting metabolic rate in diseased rTG4510 mice at 7.0 months (Joly-Amado et al., 2016), and this could at least partially explain the observed significantly higher body temperature in 8.0-months-old diseased rTG4510 mice.

In addition, it should be noted that only male control and diseased rTG4510 were used in this characterisation study. In recent years there has been a movement to address the sex imbalance within biomedical research with increasing recognition from funders for the importance of using both sexes in *in vivo* therapeutic studies (Lee, 2018, Karp and Reavey, 2019). However, only male mice were used for initial behavioural studies to exclude an effect of the oestrous cycle and there were supply problems for female rTG4510 mice from the industrial collaborator in this study. Studies have shown that neurodegeneration is more aggressive in female rTG4510 mice compared to male ones (Yue et al., 2011, Song et al., 2015). Therefore, if the efficacy study based on this characterisation were to find an effect of the M_1 mAChR PAM VU0486846 in male mice, then adjusted studies in female rTG4510 mice would be conducted.

Overall, the results of the characterisation of the rTG4510 mouse model suggest that GFAP and pTau expression can be used as neuropathological markers for neuroinflammation and neurodegeneration in an efficacy study with the M_1 mAChR PAM VU0486846.

Chapter 4 Determining the effects of an M_1 mAChR PAM in rTg4510 mice

4.1 Introduction

As discussed previously (see 1.3.3), most of the currently approved treatments for AD only provide temporary symptomatic effects, except for the Aß antibody drug aducanumab potentially (Cummings et al., 2021, Thomas et al., 2021, Walsh et al., 2021, Salloway et al., 2022). Due to the unspecific nature of AChEIs, the largest class of approved AD therapeutics, cholinergic transmission throughout the body is upregulated resulting in a range of dose-limiting side effects (Inglis, 2002, Thompson et al., 2004, Neugroschl and Wang, 2011, Marucci et al., 2021). However, the pro-cognitive effects of AChEIs are thought to be mediated via activation of the M_1 mAChR. This is corroborated by additional preclinical and clinical evidence and supports the approach of selectively targeting the M_1 mAChR to both improve cognition and minimise side effects associated with non-specific upregulation of cholinergic signalling (Bodick et al., 1997a, Inglis, 2002, Brown et al., 2021).

4.1.1 Disease-modifying potential of M_1 mAChR activation *in vitro* and in preclinical models

Several studies have shown that specific targeting of the M_1 mAChR could potentially result in disease-modifying effects in addition to the symptomatic, pro-cognitive effects demonstrated with current therapeutics (Caccamo et al., 2009).

As discussed in Chapter 1, M_1 mAChRs have been implicated in normal cognitive function in learning and memory, both of which are affected in AD. In summary, while KO of M_1 mAChR in mice results in some memory deficits (Anagnostaras et al., 2003), activation of M_1 mAChR amplified and stimulated mediators of learning and memory (Marino et al., 1998, Buchanan et al., 2010, Bradley et al., 2010, Dennis et al., 2016, Bradley et al., 2017).

4.1.1.1 Disease-modifying effects of M_1 mAChR on Aβ and tau pathology

A growing body of evidence suggests that M_1 mAChR activation can reduce levels of the proteins that are considered the classical AD hallmarks, including Aß plaques and tau tangles. *In vitro* studies suggest that stimulation of the M_1 mAChR promotes APP processing via the non-amyloidogenic pathway through

activation of PKC and the MAPK/ERK pathway (Figure 4.1 A, B) (Nitsch et al., 1992, Buxbaum et al., 1992, Hung et al., 1993, , Haring et al., 1998, Canet-Aviles et al., 2002, Jones et al., 2008) and inhibits processing via the amyloidogenic pathways (Figure 4.1 C) (Pittel et al., 1996, Lin et al., 1999, Nitsch et al., 2000, Beach et al., 2001, Davis et al., 2010). Fewer studies regarding the effect of M_1 mAChR activation on tau species have been conducted. However, *in vitro* studies suggest that M_1 mAChR-induced PKC activation also inhibits glycogen synthase kinase 3 ß (GSK-3ß), which in turn leads to reduced levels of tau phosphorylation in a time- and dose-dependent manner (Figure 4.1 D) (Sadot et al., 1996, Forlenza et al., 2000).
In the 3xTg AD model, a model exhibiting both amyloid and tau pathology, chronic treatment with the muscarinic agonist AF267B ameliorated cognitive deficits and reduced Aß and tau pathology (Caccamo et al., 2006), whereas ablation of the M_1 mAChR exacerbated cognitive decline and led to increased levels of neuroinflammatory responses, and Aß and tau pathology (Medeiros et al., 2011b). Additionally, in this model, treatment with AF267B increased APP processing via the non-amyloidogenic pathway with elevated levels of the α-secretase ADAM17/TACE and reduced levels of the ß-secretase BACE1 being found (Caccamo et al., 2006). Inversely, ablation of the M_1 mAChR in 3xTg AD mice increased levels of C99 and reduced PKC activity, indicating a shift to amyloidogenic processing of APP, and increased activity of the tau kinase GSK-3ß (Medeiros et al., 2011b) in line with effects observed upon M_1 mAChR antagonist treatment in the same AD model (Caccamo et al., 2006). In the amyloid-based APP_{Swe} model of AD, ablation of the M_1 mAChR led to increased levels of Aß pathology and of the C99 fragment, again indicating a shift to amyloidogenic APP processing (Davis et al., 2010). In agreement with the *in vitro* evidence discussed above, in AF267B-treated mice, activation of PKC and the MAPK/ERK pathway, as well as reduced levels of activated tau kinase GSK-3ß were observed (Haring et al., 1998, Forlenza et al., 2000, Canet-Aviles et al., 2002, Caccamo et al., 2006). These observations therefore provide evidence *in vivo* for a beneficial effect of M_1 mAChR activation on APP processing and tau phosphorylation. While the agonist used in this study was thought to be relatively M_1 selective, another study showed that AF267B has a similar potency at the M_1 and M_3 mAChR (Jones et al., 2008). While early agonists were relatively unselective in nature, targeting the allosteric binding pocket can allow for subtype selectivity between

muscarinic receptors (see 1.2.5). Treatment of 3xTg AD mice with AF710B, a highly selective and potent allosteric M_1 mAChR and σ1 receptor agonist, recovered cognitive deficits and decreased activity of BACE1 and the tau kinase GSK-3β, leading to reductions in Aβ and tau pathology (Fisher et al., 2016). Finally, decreased neuroinflammatory responses in the form of astrogliosis and microgliosis were found particularly surrounding plaques (Fisher et al., 2016). While the study did not attempt to elucidate whether the effects observed *in vivo* were due to activation of the M_1 mAChR, the σ1 receptor, or a combination thereof, *in v*itro experiments in hippocampal neuronal cultures indicated that beneficial effects of AF710B, including reducing neuronal spine loss, were mediated by both receptors (Fisher et al., 2016). In the aggressive, amyloid-based 5xFAD model of AD, neuroprotective effects of chronic administration of the M_1-selective bitopic agonist VU0364572 on Aβ pathology and cognitive outcome were observed (Lebois et al., 2011, Digby et al., 2012, Lebois et al., 2017).

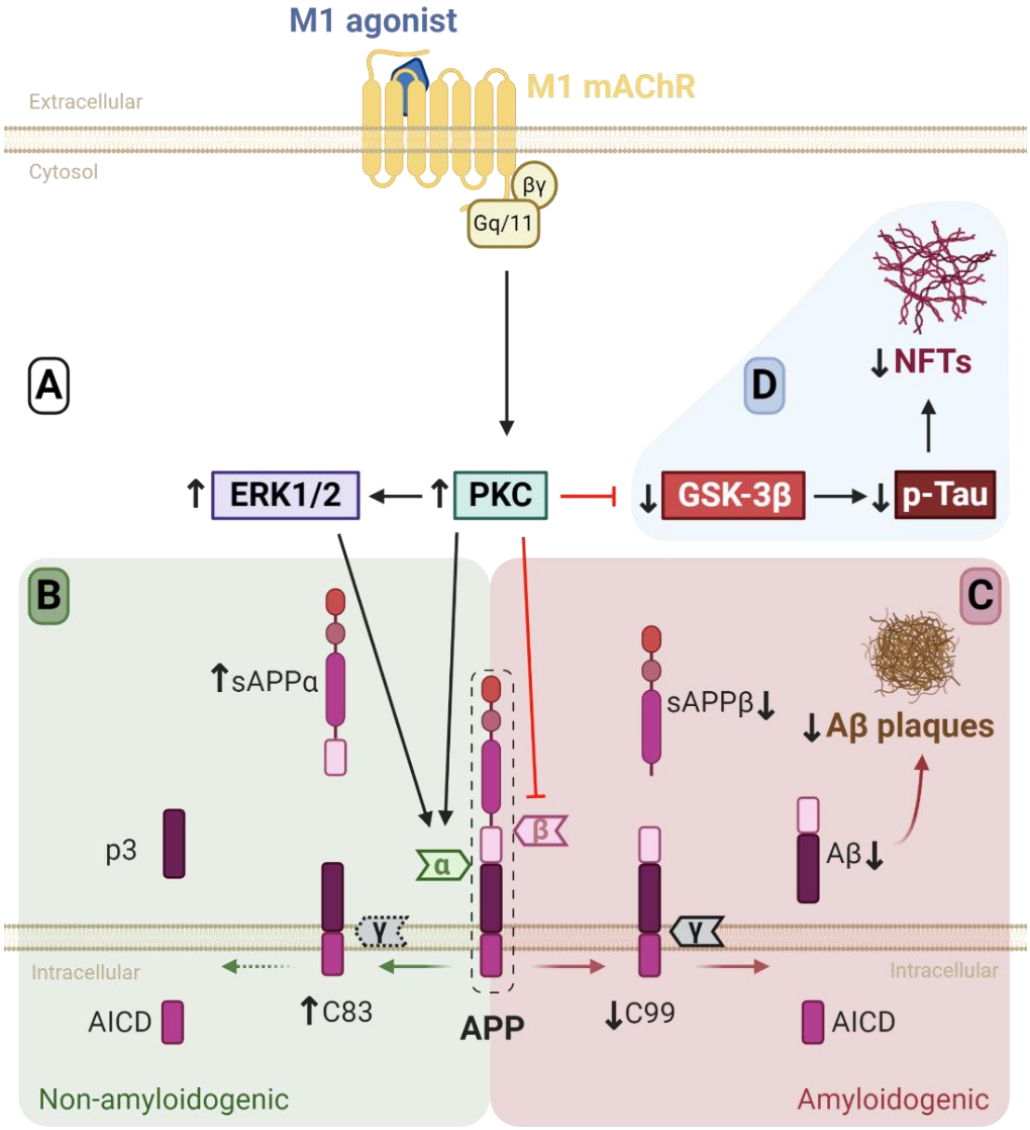

Figure 4.1 Potential disease-modifying effects of M_1 mAChR on APP processing. Activation of the M_1 mAChR by an agonist stimulates protein kinase C (PKC) which in turn activates the MAPK pathway including ERK1/2 (A). ERK1/2 and PKC have both been found to upregulate amyloid precursor protein (APP) processing via the non-amyloidogenic pathway by stimulation of the α-secretase ADAM17/TACE. Activation of the non-amyloidogenic pathway leads to higher levels of the soluble APPα (sAPPα) and C83 fragments. This can be followed by cleavage of C83 by γ-secretase producing p3 and amyloid precursor protein intracellular domain (AICD) fragments (B). Furthermore, PKC has also been found to inhibit the activity of β-secretases, such as BACE1, leading to less APP processing via the amyloidogenic pathway and therefore lower levels of the C99 and soluble APP β (sAPPβ) fragments. Finally, processing by the β-secretase usually would be followed by cleavage of C99 by γ-secretase rendering the pathogenic amyloid β (Aβ) peptides and AICD fragments. However, due to a combination of decreased β-secretase driven cleavage and increased α-secretase mediated cleavage, which cuts the protein within the Aβ domain, lower levels of Aβ peptide and plaques are produced (C). Finally, PKC has also been found to reduce the activity of the kinase GSK-3β, thereby reducing phosphorylation of tau and ultimately neurofibrillary tangles (NFTs) (D). Figure created using BioRender.com.

While the M_1 mAChR ligands used in the earlier studies especially are not as selective between muscarinic subtypes as thought at the time, the multitude of evidence from *in vitro* experiments in cell lines expressing only the M_1 mAChR, newer studies using selective M_1 mAChR agonists as well as *in vivo* studies

establish the critical role of M_1 mAChRs in pathological processes commonly observed in AD including Aß and tau pathologies, cognitive deficits, synaptic loss and neuroinflammation. Therefore, directly targeting the M_1 mAChR with highly selective ligands could provide pro-cognitive benefits along with the potential for disease-modifying reductions in plaques, tangles and neuroinflammation. A range of pharmacological compounds for targeting the M_1 mAChR has been discussed in 1.2.5 and the following will discuss the M_1 mAChR PAM VU0486846 used in this chapter.

4.1.2 Preclinical studies with the M_1 mAChR PAM VU0486846

VU0486846 (structure in Figure 4.2) has been described as an M_1 mAChR PAM with limited agonist activity (Rook et al., 2018), while showing high cooperativity with acetylcholine in second messenger assays *in vitro* (Rook et al., 2018, Dwomoh et al., 2022a). Importantly, *in vivo* studies in mice, rats and non-human primates suggest that VU0486846 does not cause cholinergic adverse effects (Rook et al., 2018, Norman et al., 2020). This M_1 mAChR PAM was also found to be highly selective with good drug metabolism and pharmacokinetic properties and CNS penetration (Bertron et al., 2018, Rook et al., 2018, Khajehali et al., 2020).

In female APP_{Swe} mice, chronic treatment for 4 or 8 weeks with VU0486846 reduced Aß pathology and neuronal loss in the hippocampus, and improved cognitive deficits (Abd-Elrahman et al., 2022). APP processing was also found to be shifted to the non-amyloidogenic pathway by reducing BACE1 expression and enhancing expression of the α-secretase ADAM10 (Abd-Elrahman et al., 2022). In the murine prion model of terminal neurodegeneration, acute treatment with VU0486846 rescued memory and learning deficits, while chronic treatment showed potential disease-modifying effects, such as an extended life span, and reduced levels of the disease-causing misfolded prion protein (Dwomoh et al., 2022a). Furthermore, using a proteomics approach, it was observed that expression levels of markers of neuroinflammation, mitochondrial dysfunction and aberrant complement function were normalised to control levels following chronic treatment (Dwomoh et al., 2022a).

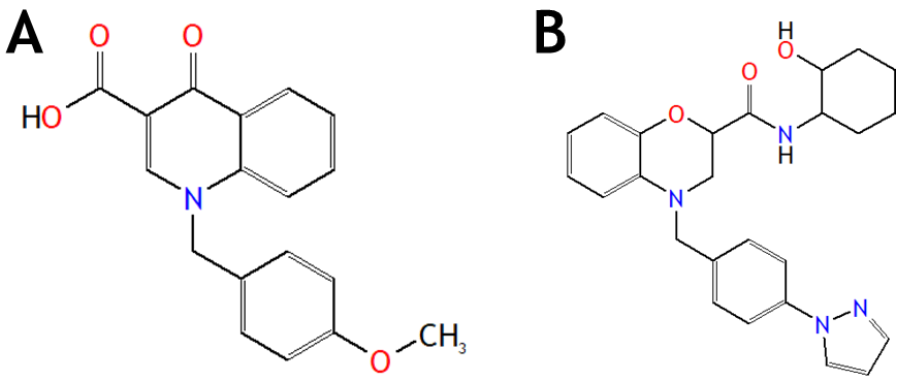

Figure 4.2 Chemical structures of BQCA and VU0486846. Benzyl quinolone carboxylic acid (BQCA; A) was one of the first selective M_1 mAChR PAMs developed. The more recently developed VU0486846 (B) is also a selective M_1 mAChR PAM.

4.1.3 Efficacy study with M_1 mAChR PAM VU0486846 in the rTG4510 tauopathy mouse model

As discussed above, the M_1 mAChR PAM VU0486846 has shown promising results in an amyloid mouse model and the murine prion model of terminal neurodegeneration (Abd-Elrahman et al., 2022, Dwomoh et al., 2022a). Therefore, this chapter aimed to test the mode of action of VU0486846 in the rTG4510 tauopathy model, which was carefully characterised in Chapter 3.

While ideally the ligand would have been tested at multiple time-points, due to the availability of animals, the optimal time-point at which to commence administration of the ligand had to be estimated. Since the identification of a disease point at which pathology could still be affected was crucial, one main driver for this decision were results from doxycycline-induced transgene suppression studies showing that pathology in diseased rTG4510 mice is tau-dependent until 4.0 months of age (Santacruz et al., 2005, Spires et al., 2006). Similar to efficacy studies with the same compound in the prion model of neurodegeneration, a starting point before 4.0 months would be before the onset of neuronal loss but after the onset of misfolded protein accumulation (compare Figure 3.1). Additionally, as reported in Chapter 3, M_1 mAChR expression levels were maintained until 7.5 months in diseased rTG4510 mice. Studies in tissues from AD patients suggest that the M_1 mAChR expression levels on postsynaptic terminals are not affected by neurodegeneration (Bartus et al., 1982, Mash et al., 1985, Bradley et al., 2017). Therefore, any efficacy study should conclude before 7.5 months to be comparable to the intact postsynaptic

M_1 mAChR expression levels in AD patients. Expression of both pTau and GFAP, the neuropathological markers selected, show a large increase in 5 months-old diseased rTG4510 mice compared to controls particularly in the CA1. Therefore, a starting point of 3.0 months was selected for the efficacy study with the M_1 mAChR PAM VU0486846 (for a timeline, see Figure 4.3).

As discussed above, the M_1 mAChR PAM VU0486846 has been extensively characterised previously (Bertron et al., 2018, Rook et al., 2018, Norman et al., 2020, Khajehali et al., 2020, Dwomoh et al., 2022a) and has been used in *in vivo* studies in mice (Abd-Elrahman et al., 2022, Dwomoh et al., 2022a). In this efficacy study, control and diseased rTG4150 mice were injected daily (intraperitoneal) with either vehicle or the M1 mAChR PAM VU0486846 (10 mg/kg) from about 3.0 months to 5.0 months for 9 weeks according to the following experimental plan (Figure 4.3). It was hypothesised that, similar to the abovementioned studies, chronic treatment with VU0486846 would normalise elevated levels of the selected neuropathological markers, which were pTau and GFAP in this study, in disease rTG4510 mice to those seen in controls.

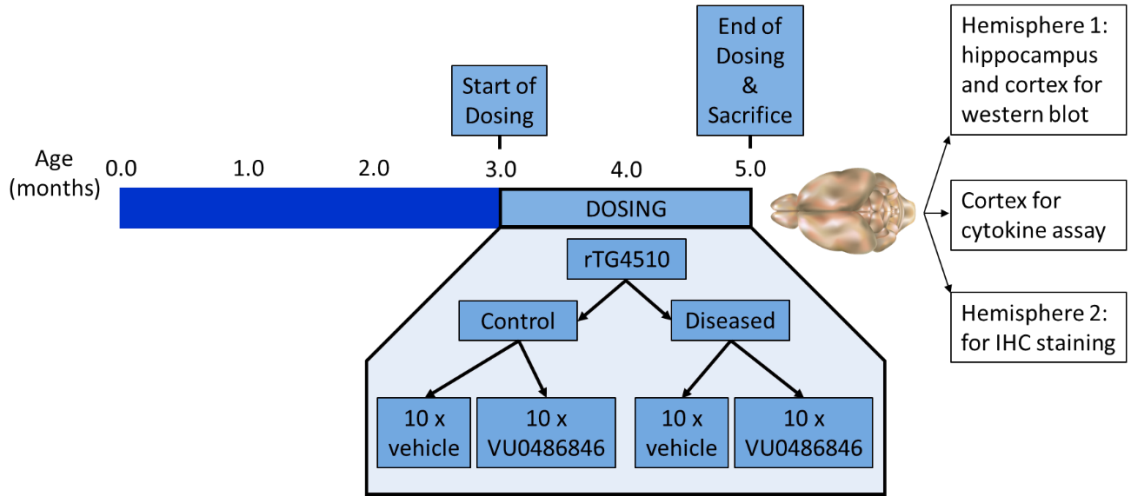

Figure 4.3 Schematic timeline of the efficacy study with the M_1 mAChR PAM VU0486846 in the rTG4510 tauopathy mouse model. Control and diseased mice were administered vehicle (10% Tween 80) or VU0486846 (10 mg/kg in 10% Tween 80) intraperitoneally from 3.0 to 5.0 months of age (n = 10 per group). At the end of the study, mice were sacrificed and for each mouse one hemisphere was dissected and the hippocampus and cortex were used for protein analysis by western blot, and an additional part of the cortex for cytokine analysis with a cytokine assay was taken. The other hemisphere was processed for immunohistochemistry (IHC).

4.1.4 Aims

The aim of this chapter was to assess the effect of chronic administration of the M_1 mAChR PAM VU0486846 from 3.0 to 5.0 months of age on pathological markers in the rTG4510 tauopathy mouse model.

Based on previous studies, it was hypothesised that targeting the M_1 mAChR with the M_1 mAChR PAM VU0486846 would ameliorate the increased levels of pathological markers in diseased rTG4510 mice.

4.2 Results

4.2.1 Physiological function of rTG4510 mice is not adversely influenced by treatment with VU0486846

In previous studies in our laboratory, chronic administration of VU0486846 did not lead to any adverse effects in the prion mouse model. Similarly, during observations throughout the course of chronic treatment in the rTG4510 mice, none of the animals showed any signs of adverse effects. Additionally, after completion of the study, the weight of various organs was measured as significant increases or decreases in VU0486846-treated animals could indicate an adverse effect of the drug (Figure 4.4, Figure 4.5).

During preclinical drug studies, the weight of the animals is closely monitored as a significant drop in weight suggests severe adverse effect of the treatment. When plotting body weight changes, all groups gained weight throughout the administration time ($p < 0.0001$) and an overall effect of treatment could be found ($p < 0.0001$), however, no difference between the groups at specific time-points could be identified (Figure 4.4).

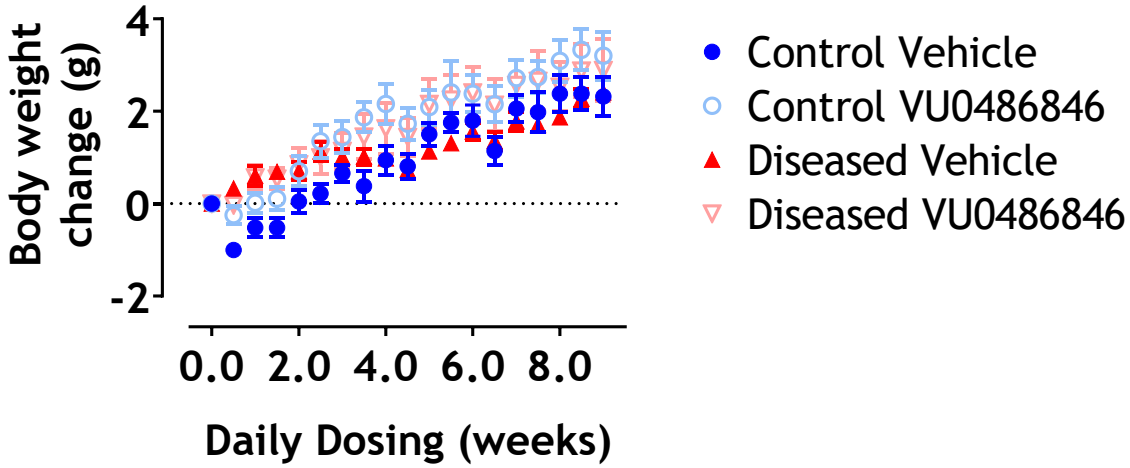

Figure 4.4 Body weight changes of the control and diseased rTG4510 mice recorded during chronic dosing with vehicle or VU048686. Body weight measurements were recorded twice a week. Data shown as means ± SEM, n = 10. Statistical significance was analysed using three-way ANOVA for genotype, treatment and duration of administration, followed by Tukey post-hoc comparison.

As diseased rTG4510 show atrophy, brain weight was measured as an indicator for this. As expected, significantly lower brain weights could be found in

diseased compared to control rTG4510 mice in both vehicle- and VU0486846-treated animals (both $p < 0.0001$; Figure 4.5 A). Other organs were also measured to identify potential adverse effects of chronic drug treatment. No differences between vehicle- and VU0486846-treated control or diseased rTG4510 mice could be found on the weight of the spleen (Figure 4.5 B), the liver (Figure 4.5 C), the heart (Figure 4.5 D) or the kidneys (Figure 4.5 E).

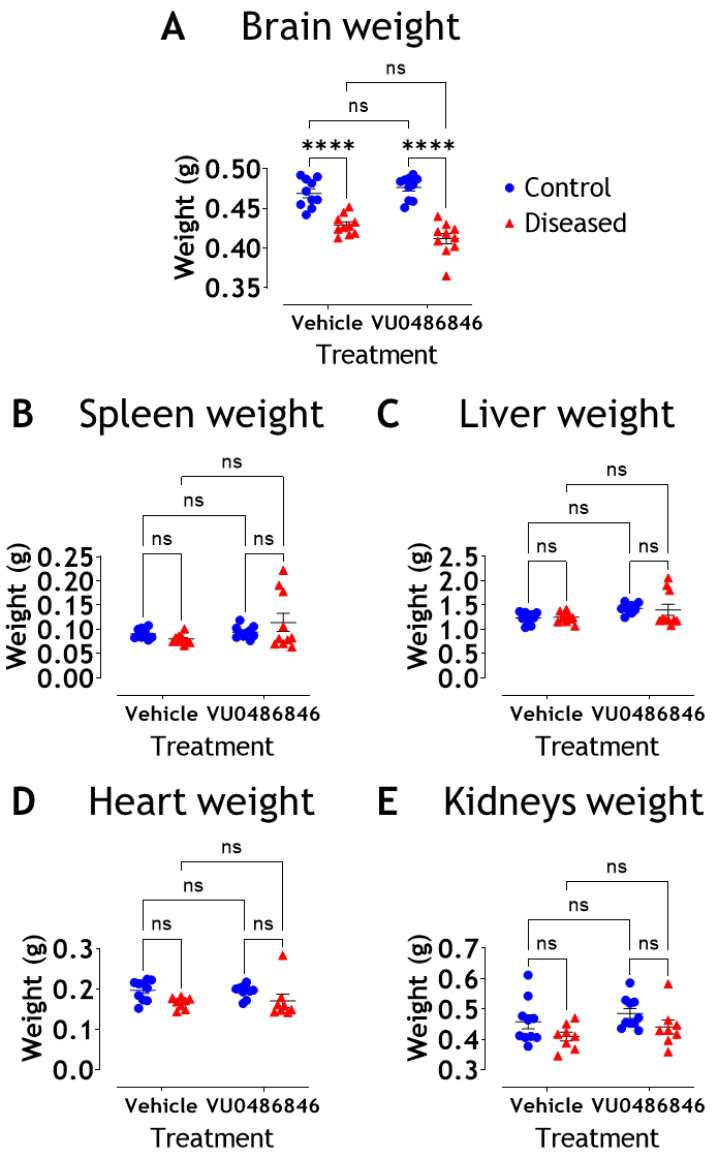

Figure 4.5 Effect of treatment with the M_1 mAChR PAM VU0486846 on physiological measurements compared to vehicle treatment in control and diseased rTG4510 mice. Data is shown as individual measurement per mouse, with means ± SEM shown, n = 8-10. Statistical significance was analysed using two-way ANOVA for genotype and treatment followed by Tukey post-hoc comparison test; $p = 0.01$, $p < 0.001$, $p < 0.0001$.

4.2.2 VU0486846 does not affect protein expression of disease markers

After establishing that the M_1 mAChR PAMs VU0486846 does not have any adverse effects in the control and diseased rTG4510, the effect of VU0486846 on pTau and GFAP levels were investigated using IHC and immunoblotting. For IHC, protein levels were assessed in the cortex and hippocampus as well as in the hippocampal CA1 area specifically, since pTau and GFAP changes in this area with age and genotype were most pronounced (Chapter 3). In both vehicle- and VU0486846-treated control rTG4510 mice, very little staining for human pTau could be observed (Figure 4.6), which was expected since these mice do not possess the transgene. In the cortex, hippocampus and the hippocampal CA1 region increased staining for pTau could be observed in diseased compared to control mice regardless of treatment (all $p \leq 0.0008$, except VU0486846-treated diseased compared to control mice in the hippocampus: $p = 0.0245$, Figure 4.6). While there is a suggestion of lower levels of pTau in drug-treated diseased rTG4510 mice, this was not significant in any area analysed (Figure 4.6 B). In summary, differences in pTau levels in all areas analysed were driven by genotype and no effect of VU0486846 could be found.

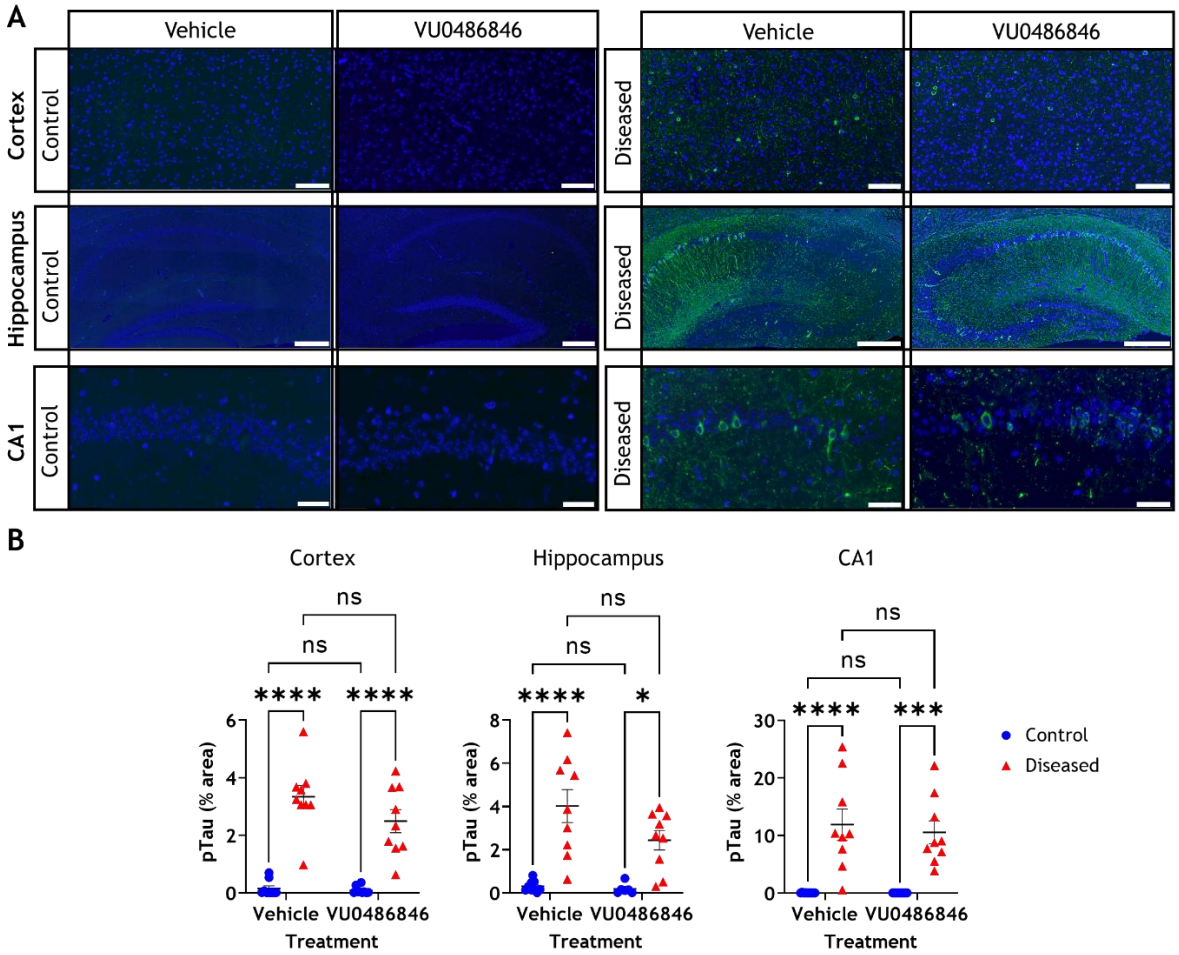

Figure 4.6 Immunostaining for pTau indicates that genotype, but not drug treatment, affects protein levels. Representative images for the human pTau staining (green) in the cortex, hippocampus and CA1 in vehicle- and VU0486846-treated control and diseased rTG4510 mice (A) and quantification of this staining (B) are shown. Nuclei have been stained with DAPI (blue). Staining was performed on 5 µm thick coronal sections and images acquired using a NanoZoomer S60 digital slide scanner with the fluorescence imaging module at 40x magnification. Images shown are representative of n = 6-10 mice per group. Scale bars represent 100 µm in the cortex, 250 µm in the hippocampus and 50 µm in the CA1. For the quantification, data are shown as means ± SEM with data points representing individual mice. For statistical analysis of the quantification, two-way ANOVA for genotype and treatment were used, followed by a Tukey's multiple comparison test; * $p < 0.05$, *** $p < 0.001$, **** $p < 0.0001$.

For GFAP, minimal staining was observable in the cortex in the control rTG4510 mice, while in the diseased rTG4510 mice more staining could be seen (Figure 4.7). In the hippocampus in general, and the CA1 specifically, higher levels of GFAP staining compared to the cortex were observed in control mice and the staining in diseased rTG4510 appeared to be more pronounced (Figure 4.7). Statistical analyses showed that GFAP levels were higher in diseased compared to control rTG4510 mice that had been treated with vehicle ($p = 0.0001$) or VU0486846 ($p = 0.0478$) in the cortex and in vehicle-treated diseased compared to control mice in the CA1 ($p = 0.0022$), but not in the general hippocampal area ($p > 0.6060$), suggesting that inflammation might be specific to a certain area of

the hippocampal formation. No effect of VU0486846 treatment was found (Figure 4.7). In summary, changes in GFAP levels were caused by genotype in the cortex regardless of treatment and in the CA1 area of the hippocampus in vehicle-treated animals, with no effect of VU0486846 treatment being observed.

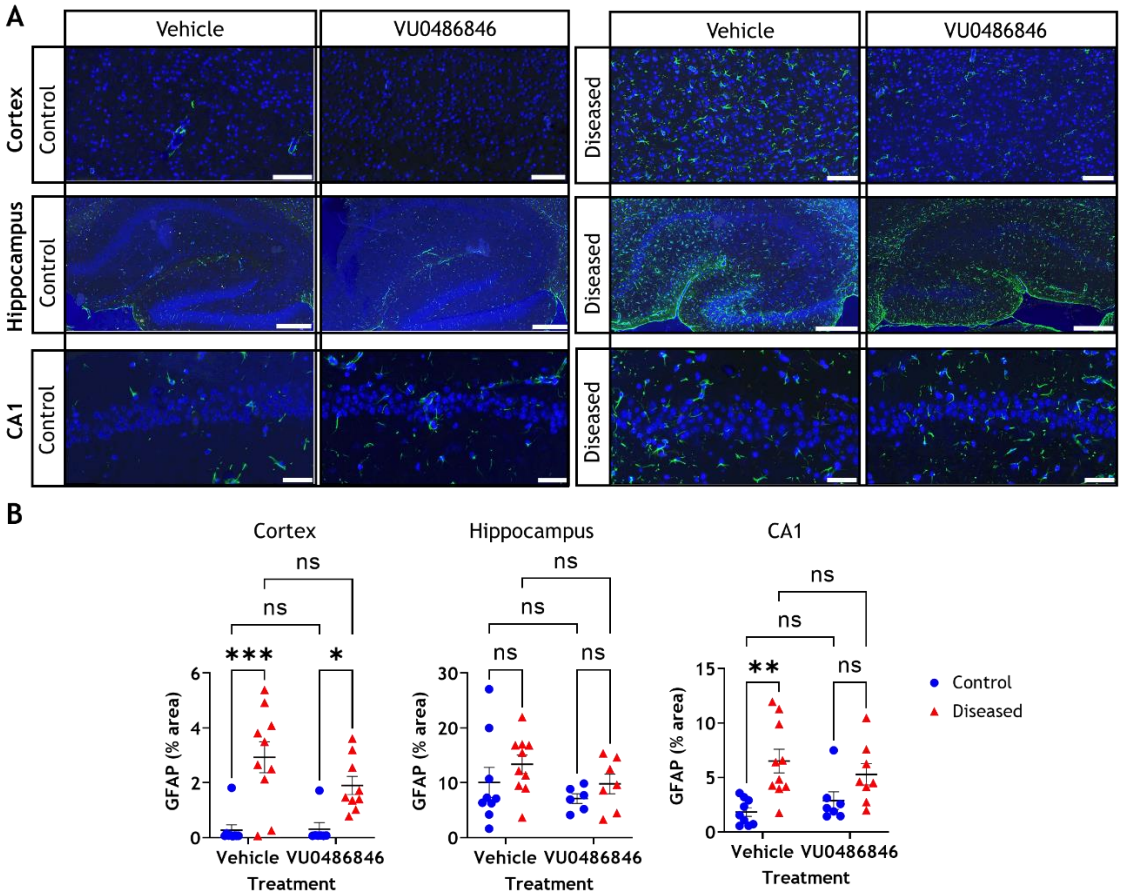

Figure 4.7 Immunostaining for GFAP indicates that genotype, but not drug treatment, affects protein levels. Representative images of GFAP staining (green) in the cortex, hippocampus and CA1 in vehicle- and VU0486846-treated control and diseased rTG4510 mice (A) and quantification of this staining (B) are shown. Nuclei have been stained with DAPI (blue). Staining was performed on 5 µm thick coronal sections and images acquired using a NanoZoomer S60 digital slide scanner with the fluorescence imaging module at 40x magnification. Images shown are representative of n = 6-10 mice per group. Scale bars represent 100 µm in the cortex, 250 µm in the hippocampus and 50 µm in the CA1. For the quantification, data are shown as means ± SEM with data points representing individual mice. For statistical analysis of the quantification, two-way ANOVA for genotype and treatment were used, followed by a Tukey's multiple comparison test; * $p < 0.05$, ** $p < 0.01$, *** $p < 0.001$.

In western blot analysis, a range of other proteins in addition to GFAP and pTau was assessed. Many of these were based on proteomic changes observed in a murine prion model of neurodegeneration upon treatment with VU0486846 (Dwomoh et al., 2022a). Levels of tau were analysed using the Tau12 and Tau46 antibodies, which detect human, and mouse and human tau isoforms, respectively in addition to pTau. In both the cortex (Figure 4.8) and the

hippocampus (Figure 4.9), all tau species, namely pTau, Tau12 and Tau46 were upregulated in the diseased compared to control rTG4510 mice, with no effect of VU0486846 treatment observed.

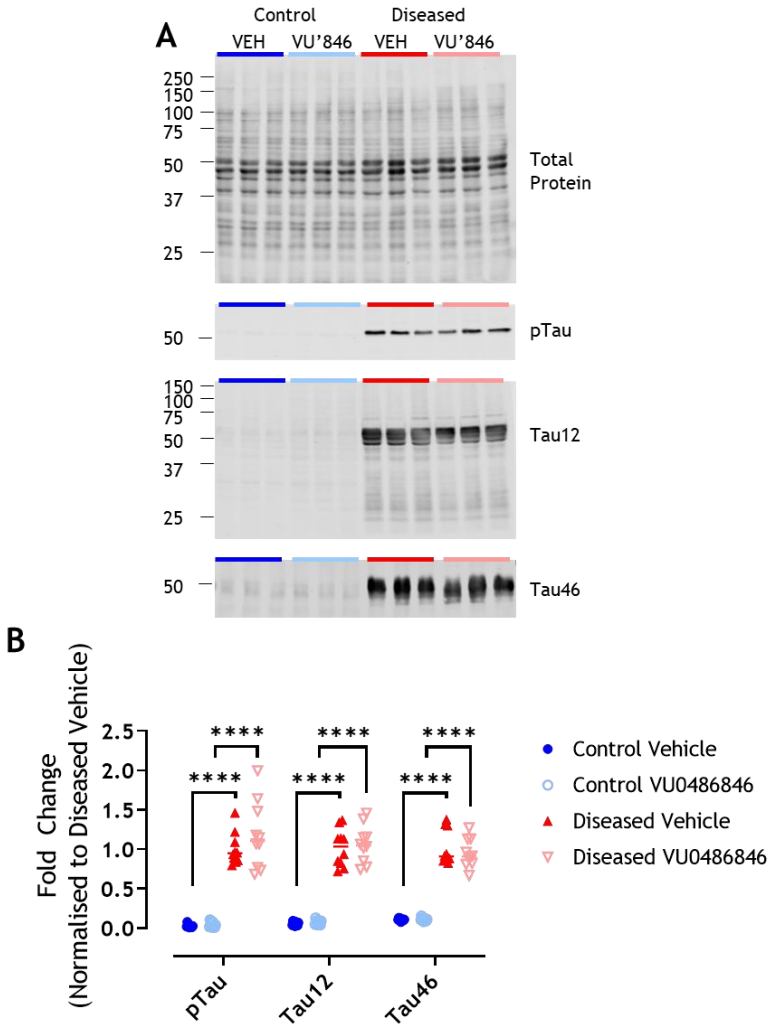

Figure 4.8 VU0486846 has no effect on protein levels of the tau species pTau, Tau12 and Tau46 in the cortex in rTG4510 mice. Representative blots (A) and quantification (B) of relative tau protein levels found in samples from vehicle (VEH)- (blue) and VU0486846 (VU'846)-treated control (light blue) as well as vehicle- (red) and VU0486846-treated (rose) diseased rTG4510 mice are shown. Blots were analysed using Image Studio Lite Version 5.2. Protein levels were normalised to signal obtained from corresponding REVERT Total Protein Stain, followed by normalisation to the average protein level of the vehicle-treated diseased rTG4510 group expressed as fold change, n = 10. For the quantification, data are shown as means ± SEM with data points representing individual mice. Data for each protein were analysed using two-way ANOVA for genotype and treatment, followed by Tukey's multiple comparison tests; **** $p < 0.0001$. pTau: phosporylated Tau.

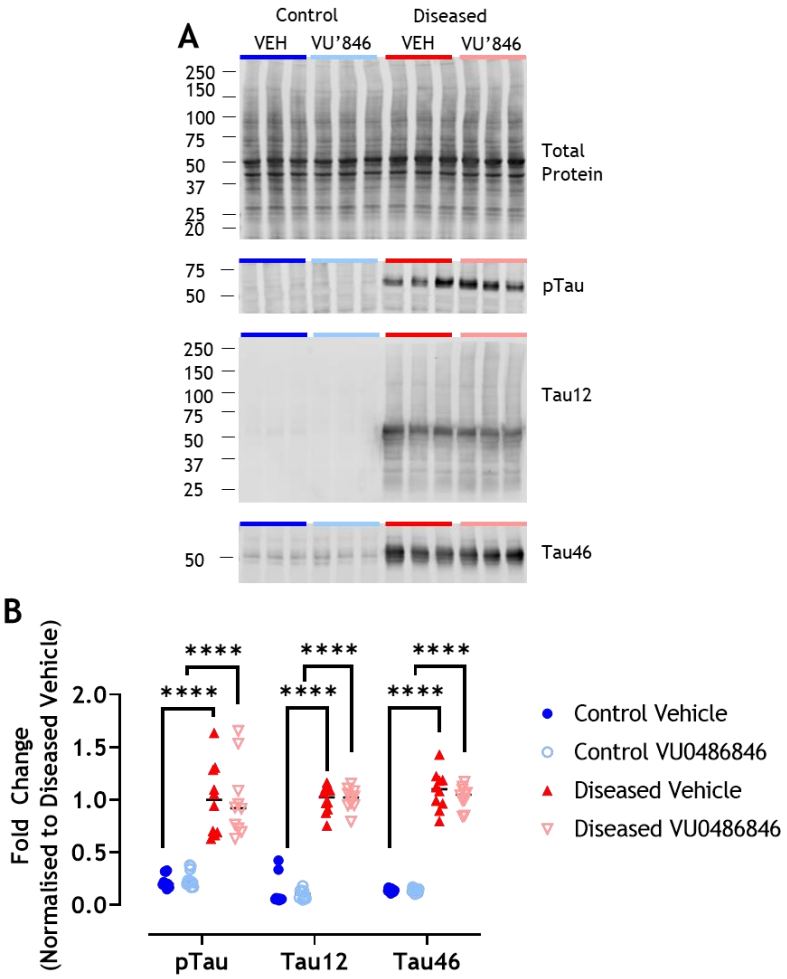

Figure 4.9 VU0486846 has no effect on protein levels of the tau species pTau, Tau12 and Tau46 in the hippocampus in rTG4510 mice. Representative blots (A) and quantification (B) of relative tau protein levels found in samples from vehicle (VEH)- (blue) and VU0486846 (VU'846)-treated control (light blue) as well as vehicle- (red) and VU0486846-treated (rose) diseased rTG4510 mice are shown. Tau12 detects human tau isoforms only, while Tau46 detects both mouse and human tau. Blots were analysed using Image Studio Lite Version 5.2. Protein levels were normalised to signal obtained from corresponding REVERT Total Protein Stain, followed by normalisation to the average protein level of the vehicle-treated diseased rTG4510 group expressed as fold change, n = 10. Data for each protein were analysed using two-way ANOVA for genotype and treatment, followed by Tukey's multiple comparison tests; **** $p < 0.0001$. pTau: phosporylated Tau.

M_1 mAChR protein levels were analysed to control for an effect of disease or treatment on the protein levels of M_1 mAChR. In the cortex, no difference between control and diseased mice were found (Figure 4.10), whereas in the hippocampus, M_1 mAChR levels were reduced in diseased compared to control rTG4510 mice regardless of treatment (both $p \leq 0.0412$, Figure 4.11). Nevertheless, in both the cortex and the hippocampus, VU0486846 treatment did not affect M_1 mAChR levels (Figure 4.10, Figure 4.11). A representative blot of M_1 mAChR staining including a negative control can be found in Appendix Figure 1.

Since neuroinflammation, including astrogliosis and microgliosis, have been reported to play an important role in AD pathology (Middeldorp and Hol, 2011, Heneka et al., 2015, Dansokho and Heneka, 2018, Kumar et al., 2021), the astrocyte markers, GFAP and vimentin, and the microglial marker IBA1 were analysed. Interestingly, in the murine prion model of neurodegeneration, chronic treatment with the M_1 mAChR PAM VU0486846 normalised elevated level of neuroinflammatory markers to levels observed in control (Dwomoh et al., 2022a). In both the cortex and hippocampus, GFAP levels were upregulated in diseased rTG4510 mice compared to control regardless of treatment (all $p < 0.0001$), whereas only in the hippocampus an upregulation of vimentin levels in diseased compared to control mice was found (both $p < 0.0001$, Figure 4.10, Figure 4.11). For the microglial marker IBA1, no changes were observed in the cortex (Figure 4.10), or hippocampus (Figure 4.11). Treatment had no effect on any of the analysed markers of neuroinflammation. Interestingly, however, strong correlations were found between pTau and GFAP levels in control mice ($r = 0.7042$, $p = 0.0005$) and diseased mice ($r = 0.7741$, $p < 0.0001$) in the cortex (Figure 4.12 A) as well as control ($r = 0.9268$, $p < 0.0001$) and diseased mice ($r = 0.7774$, $p < 0.0001$) in the hippocampus (Figure 4.12 B), regardless of treatment.

ApoE was assessed, since polymorphisms in the *ApoE* gene are a major genetic risk factor for AD (Coon et al., 2007, Yamazaki et al., 2019) and an upregulation of ApoE mRNA was observed in the cortex of diseased compared to control rTG4510 mice at 8.0 months (Appendix Figure 2). While in the cortex no changes were found (Figure 4.10), in the hippocampus a significant difference between control and diseased vehicle-treated rTG4510 mice only ($p = 0.0099$, Figure 4.11 B) was observed.

Due to the atrophy phenotype in rTG4510 mice, the expression levels of the neuronal marker NeuN were also assessed to determine whether any changes in neuronal counts could be detected following chronic administration of VU0486846. No changes in NeuN levels in the cortex (Figure 4.10) or hippocampus (Figure 4.11) were observed. A representative blot of NeuN staining including a negative control can be found in Appendix Figure 1.

Finally, SerpinA3N, a regulator of proteolysis (Nielsen et al., 2007), was analysed, as upregulation of this protein in the murine prion model of neurodegeneration was recovered to control levels by chronic administration of VU0486846 (Dwomoh et al., 2022a), and it would therefore be interesting to see whether this effect is prion-specific or a more general neurodegenerative phenomenon. No changes in SerpinA3N could be observed in the cortex (Figure 4.10), whereas an upregulation in SerpinA3N levels vehicle-treated diseased compared to control rTG4510 mice was found in the hippocampus ($p = 0.0069$, Figure 4.11). Overall, protein levels evaluated were, if at all, only affected by the genotype of the mice, but not treatment with the M_1 mAChR PAM U0486846.

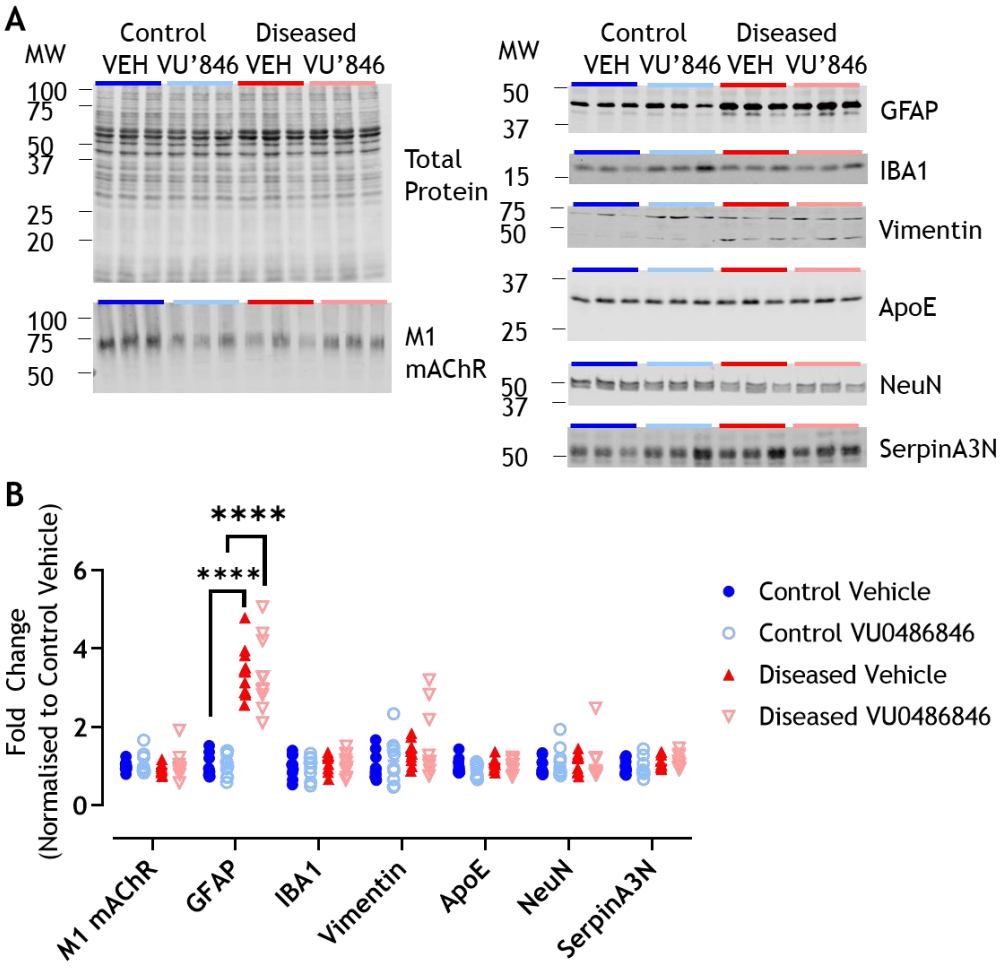

Figure 4.10 VU0486846 has no effect on neuroinflammation in the cortex in rTG4510 mice
Representative blots (A) and quantification (B) of relative protein levels found in samples from vehicle (VEH)- (blue) and VU0486846 (VU'846)-treated control (light blue) as well as vehicle- (red) and VU0486846-treated (rose) diseased rTG4510 mice are shown. Blots were analysed using Image Studio Lite Version 5.2. Protein levels were normalised to signal obtained from corresponding REVERT Total Protein Stain, followed by normalisation to the average protein level of the vehicle-treated control group expressed as fold change, n = 10. Data for each protein were analysed using two-way ANOVA for genotype and treatment followed by Tukey's multiple comparison tests; **** $p < 0.0001$.

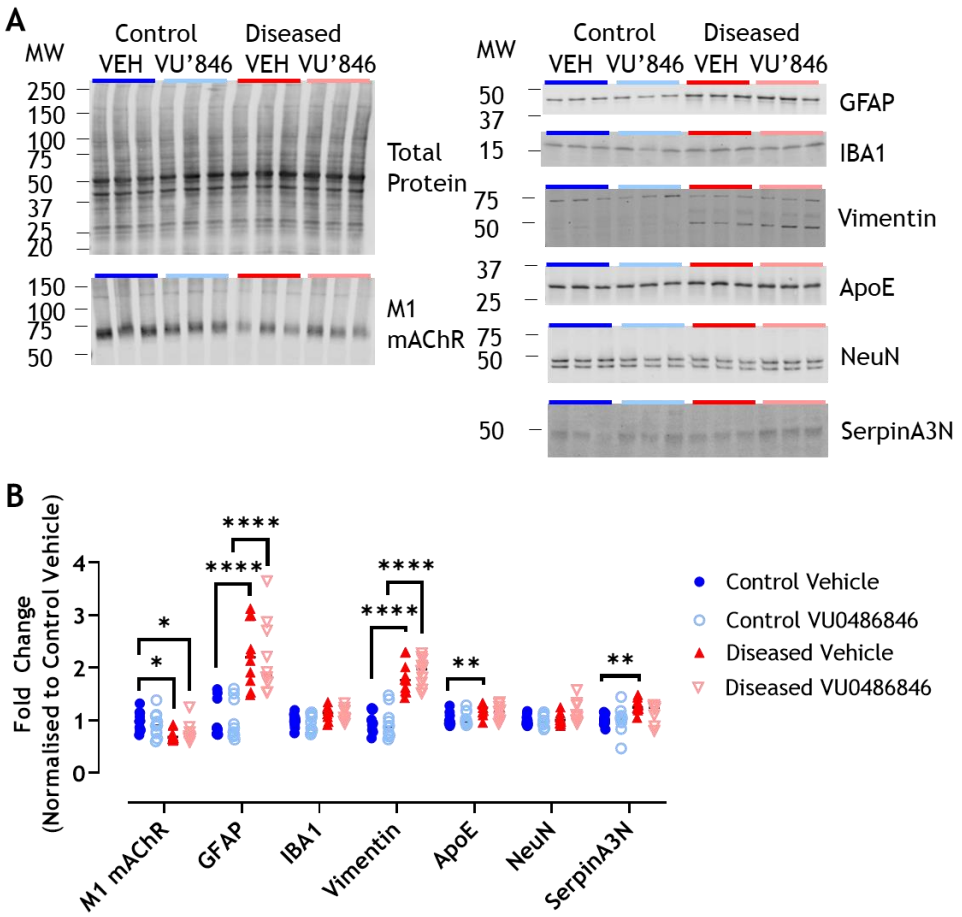

Figure 4.11 VU0486846 does not affect neuroinflammation in the hippocampus in rTG4510 mice. Representative blots (A) and quantification (B) of relative protein levels found in samples from vehicle (VEH)- (blue) and VU0486846 (VU'846)-treated control (light blue) as well as vehicle- (red) and VU0486846-treated (rose) diseased rTG4510 mice are shown. Blots were analysed using Image Studio Lite Version 5.2. Protein levels were normalised to signal obtained from corresponding REVERT Total Protein Stain, followed by normalisation to the average protein level of the vehicle-treated control group expressed as fold change, n = 10. Data for each protein were analysed using two-way ANOVA for genotype and treatment followed by Tukey's multiple comparison tests; * $p < 0.05$, ** $p < 0.01$, **** $p < 0.0001$.

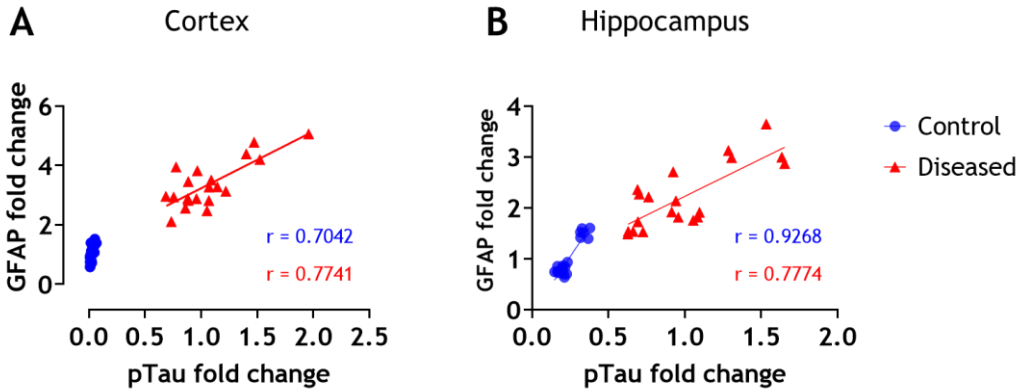

Figure 4.12 Correlation of pTau and GFAP protein levels in cortical and hippocampal samples. Plotting the GFAP and pTau protein levels observed in immunoblotting in the cortex (A) and hippocampus (B) for control (blue) and diseased (red) rTG4510 mice regardless of treatment, strong correlations could be observed. The relevant Pearson correlation coefficients (r) are indicated in the respective colours in each graph; n = 20.

4.2.3 Chronic administration of VU0486846 normalises expression of several proteins involved in inflammatory responses

Since effects of M_1 mAChR activation on neuroinflammatory responses, including but not limited to astrogliosis and microgliosis, have been reported in the murine prion model of terminal neurodegeneration (Dwomoh et al., 2022a), the effect of VU0486846 treatment on inflammatory responses in rTG4510 mice was investigated using a Proteome Profiler cytokine array. This cytokine array allows for the determination and analysis of 111 mouse cytokines and chemokines of interest using a membrane-based immunoassay. In the rTG4510 mice, three analytes out of the 111 tested were upregulated in diseased compared to control mice (Figure 4.13 A). The markedly upregulated analytes in the vehicle-treated diseased rTG4510 mice, which are reversed to control-like levels with drug treatment, are acidic FGF, coagulation factor III and cystatin C (Figure 4.13 B). Acidic FGF and coagulation factor III are involved in angiogenesis (Siedlak et al., 1991, Jefferies et al., 2013), while cystatin C is a cysteine protease inhibitor (Levy et al., 2006) The analyte showing higher levels in the vehicle-treated control mice only is interleukin (IL)-28A/B, which is a cytokine typically activated in response to viral or bacterial infections (Witte et al., 2010). Since the lysates were pooled from 10 mice per group, no statistical analysis could be performed, and further experiments should be conducted to confirm whether this is a true effect of VU0486846 treatment.

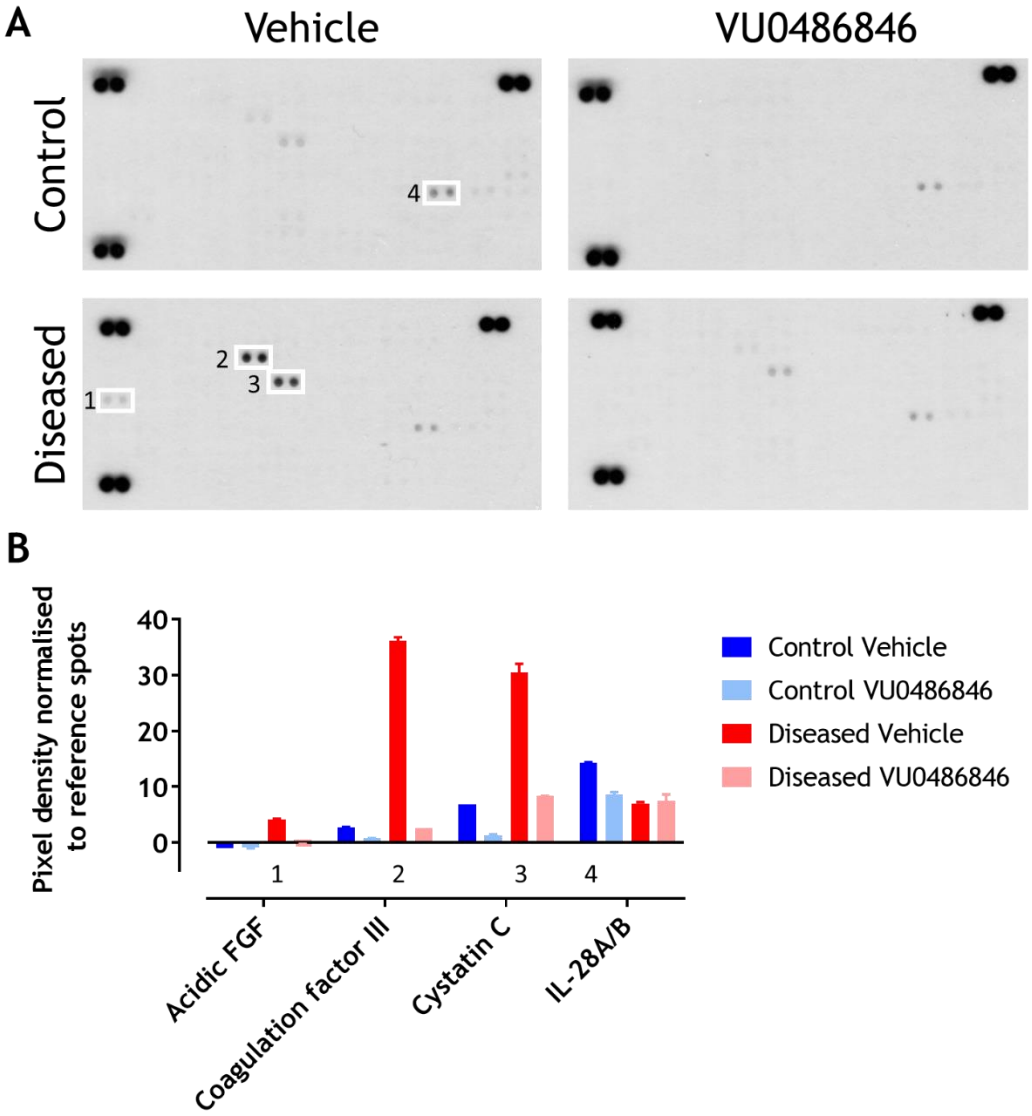

Figure 4.13 Changes in inflammatory markers upon chronic treatment with VU0486846 in rTG4510 mice. Cortical samples were obtained after conclusion of the efficacy study with VU0486846, and brain homogenates were analysed using a Mouse XL Cytokine Array Kit (A). Bar graphs show altered analytes (B). Numbers show analytes (A) corresponding to the most increased condition of the altered analytes (B). Pooled cortical brain homogenates from 10 mice per group were used. Data is shown as means ± SEM.

Next, experiments were designed to validate changes in the analytes identified from the cytokine array using RT-qPCR. In both the hippocampus and cortex, coagulation factor III and cystatin C were upregulated in diseased compared to control rTG4510 mice, whereas no difference in levels of acidic FGF was found (Figure 4.14). Therefore, the results from the RT-qPCR analysis validate the results observed for coagulation factor III and cystatin C in the cytokine array, but not for acidic FGF.

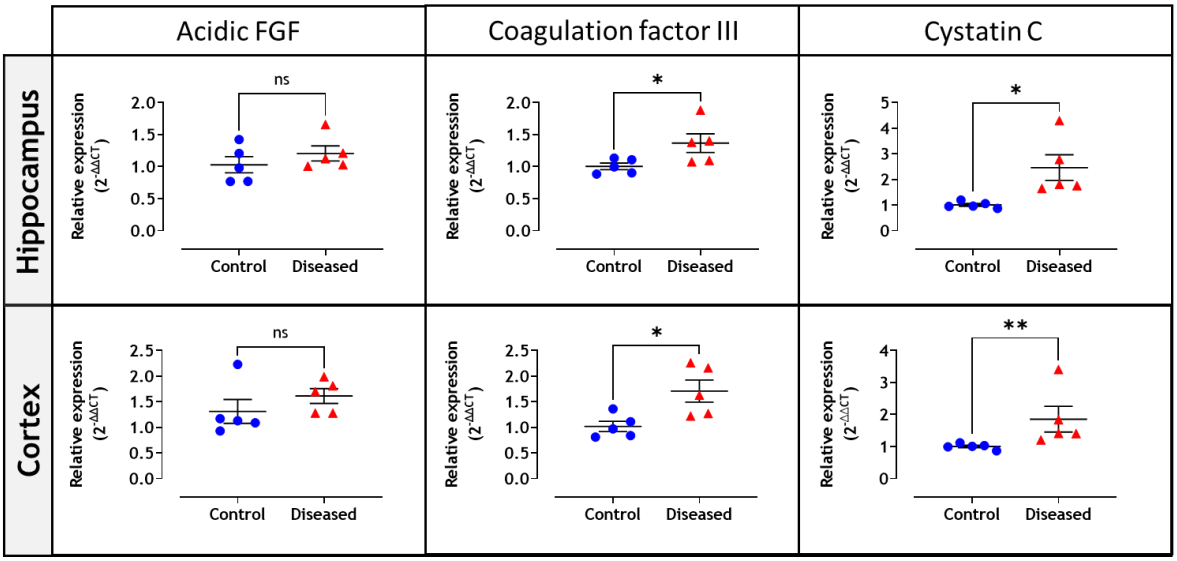

Figure 4.14 Coagulation factor III and cystatin C are upregulated in diseased compared to control rTG4510. Gene expression of acidic FGF, coagulation factor III and cystatin C, in hippocampal (upper panel) and cortical samples (lower panel) determined using RT-qPCR analysis is shown. Samples were obtained from 8.0 months old mice used for telemetry measurements in Chapter 4. To assess relative expression levels, data was analysed using the ΔΔCT method, normalising first to α-tubulin and then the mean of the control values for each gene of interest. Data are expressed as means ± SEM and each data point corresponds to an individual mouse. Data for each gene were analysed using unpaired t-tests, or when failing the Shapiro-Wilk normality test Mann-Whitney tests were used; * $p < 0.05$, ** $p < 0.01$.

4.3 Discussion

Specific targeting of the M_1 mAChR has been suggested to confer benefits in neurodegenerative diseases in human (Burford et al., 2011, Conn et al., 2014) and mouse models of AD (Caccamo et al., 2006, Fisher et al., 2016, Lebois et al., 2017). In the murine prion mouse model of terminal neurodegeneration, targeting the M_1 mAChR with PAMs has been shown to exert disease-modifying effects. More specifically, a rescue of learning and memory deficits, normalisation of markers of neuroinflammation and neurodegeneration, and an extended life span have been observed (Bradley et al., 2017, Dwomoh et al., 2022a). Therefore, to explore the potential of M_1 mAChR PAMs as a therapeutic option for symptomatic and disease-modifying treatment in other neurodegenerative models, including AD models, the effects of targeting the M_1 mAChR with PAMs were assessed in the AD-relevant rTG4510 tauopathy mouse model. Administration of VU0486846 was safe. Contrary to the hypothesis, chronic treatment with VU0486846 did not affect biochemical markers of disease, indicating that the M_1 mAChR PAM may not have a disease-modifying effect in this model of AD. Interestingly, the results indicate that dosing with VU0486846 does influence some inflammatory markers, namely coagulation factor III and cystatin C.

The absense of an effect of chronic treatment with VU0486846 in the rTG4510 mouse model could be due to several reasons. First, the start of the efficacy study could have been too late to allow for recovery of neuropathology. As the doxycycline studies suggest that partial suppression of pTau in the rTG4510 model up until 4.1 months can still affect disease progression (Santacruz et al., 2005, Spires et al., 2006, Blackmore et al., 2017), it is unlikely that the absence of an effect is due to the dosing time window. Nevertheless, future work could include pilot studies starting from different time-points, based on the appearance of key disease markers in the rTG4510 model. Second, the observed results could be due to the M_1 mAChR PAM VU0486846 not affecting pathologically relevant processes in this tau model. In the APP_{Swe} model, chronic treatment with VU0486846, starting after the onset of pathology, was found to reduce amyloid pathology and cognitive deficits (Abd-Elrahman et al., 2022). A range of *in vitro* and *in vivo* studies have elucidated the effect of M_1 mAChR

activation on APP processing and amyloid pathology (Nitsch et al., 1992, Buxbaum et al., 1992, Buxbaum et al., 1993, Haring et al., 1998, Forlenza et al., 2000, Canet-Aviles et al., 2002, Caccamo et al., 2006). In the murine prion mouse model of terminal neurodegeneration, chronic treatment with VU0486846 ameliorated memory and learning deficits, while also restoring levels of neuroinflammatory markers, including GFAP, and proteins involved in the clearance of misfolded proteins (Dwomoh et al., 2022a). While this was the first study investigating the effect of M_1 mAChR modulation in the rTG4510 mouse model, studies in the dual amyloid-tau 3xTg AD model suggest that M_1 mAChR activation is important for controlling phosphorylation of tau by inhibiting activation of the tau kinase GSK-3β (Caccamo et al., 2006, Medeiros et al., 2011b). Here, activity of GSK-3β was not measured and therefore, it is unclear whether chronic dosing with VU0486846 inhibited GSK-3β. Phosphorylated tau is in turn more likely to form tangles (Medeiros et al., 2011a). Here, administration of the M_1 mAChR PAM VU0486846 did not seem to affect levels of tau phosphorylation observed. In this study, however, only the AT8 antibody, which mostly detects phosphorylated tau in intra- and extracellular NFTs, was used to detect tau phosphorylation and no other tau phosphorylation antibodies detecting pre-tangle or specific NFT stages were applied (Augustinack et al., 2002). Additionally, unlike in a range of models including the prion mouse model and the 3xTg AD model (Medeiros et al., 2011b, Dwomoh et al., 2022a), neuroinflammatory markers such as GFAP were not affected by chronic dosing in the rTG4510 model. It is still unclear from previous studies how M_1 mAChR activation modulates neuroinflammation (Medeiros et al., 2011b, Abd-Elrahman et al., 2022, Dwomoh et al., 2022a), however, it is possible that the effect is indirect via modulation of prion or amyloid and tau levels, respectively. If this were true, the absence of an effect of VU0486846 treatment on tau pathology would consequently then result in no effect of treatment on neuroinflammation. Third, like many AD mouse model, the rTG4510 model is based on overexpression of human mutant tau, but in this model, overexpression of the human tau mutant has been found to affect development (Caouette et al., 2013, Helboe and Volbracht, 2013). One study found that adult-onset tau overexpression (suppressing tau expression with doxycycline up until 2.5 months of age) leads to alterations compared to perinatal overexpression: reduced brain atrophy and neuronal loss as well as lower levels of phosphorylated tau and glia were found

until at least 10 months of age (Caouette et al., 2013). Based on their magnetic resonance imaging and IHC analysis the authors suggest that the severe pathological events associated with human mutant tau overexpression in this model occur during the perinatal and early postnatal stages of development. In humans, neuropathological processes associated with AD usually do not unfold until mid- to late adulthood (Caouette et al., 2013). It is therefore possible, that results in this model could be affected by developmental alterations caused by the mutant tau overexpression leading to long-lasting alterations unrelated to the AD phenotype. Therefore, if further pilot studies at different time-points are conducted as discussed above, these should be performed in mice, in which the pTau transgene expression is suppressed until the onset of adulthood to avoid confounding effects of overexpression during development.

One further factor that could have affected these results are reported binding of tau, but not pTau, to muscarinic receptors, including the M_1 mAChR, leading to tau-induced increases in intracellular calcium levels in neuronal cultures *in vitro* as well as in rabbit tear secretion experiments *in vivo* (Gomez-Ramos et al., 2008, Gómez-Ramos et al., 2009, Martinez-Aguila et al., 2014). In this study, the AT8 antibody was used for detecting phosphorylated tau, whereas Tau12 and Tau46 antibodies detect epitopes not affected by phosphorylation, hence reflecting total tau levels (Petry et al., 2014, Song et al., 2015). Therefore, due to the nature of the tau antibodies utilised, the amount of unphosphorylated and phosphorylated tau present could not be determined. ELISA immunoassays for total and phosphorylated tau could have been used to investigate protein levels, however, other studies have suggested increases in total and phosphorylated tau levels with age (Song et al., 2015). While it was also suggested that tau binds to a site distinct to the orthosteric binding site (Gómez-Ramos et al., 2009), this has not been investigated further. Therefore, it is unclear whether tau could compete with VU0486846 for the same binding site, and thereby interfere with the drug's activity.

Additionally, since no robust behavioural indicators of disease progression were observed in the rTG4510 model (Chapter 4), it was more difficult to assess efficacies of a drug candidate. Even if a change in pTau levels would have been

found to be reduced, the benefit would have potentially been unclear in the absence of a behavioural readout.

In this study, the only proteins increased in vehicle-treated diseased rTG4510 mice compared to control mice and restored to normal levels in the VU0486846-treated diseased mice are acidic FGF, coagulation factor III and cystatin C. These results are interesting as both acidic FGF and coagulation factor III are involved in angiogenesis and overexpression of angiogenic factors in areas of tissue damage associated with plaques and tangles has been reported (Siedlak et al., 1991, Jefferies et al., 2013). There is also evidence for a role of the cysteine protease inhibitor cystatin C in AD (Wang et al., 1997, Deng et al., 2001, Levy et al., 2001, Levy et al., 2006). Cystatin C levels in the cerebrospinal fluid were found to be positively correlated with pTau in AD patients (Sundelöf et al., 2010), and overexpression of human cystatin C in APP transgenic mice has been shown to reduce Aß deposition (Mi et al., 2007, Kaeser et al., 2007). Contrary to the observed decrease in IL-28A/B in diseased mice compared to vehicle treated controls, Weeraratna et al. (2007) reported an increase in IL-28A gene expression in samples taken from inferior parietal lobes of late onset AD compared to non-demented controls. Overall, several of the identified analytes have been linked to AD pathology and it would be interesting to investigate these changes further using more quantitative assays, such as ELISAs and Bio-Plex Multiplex Immunoassays. Since no further samples from this dosing study were available, these assays were not possible at this time, however, samples from the 8.0 months old mice used for telemetry (Chapter 4) were available for gene expression analysis. Since the results from the RT-qPCR suggest that coagulation factor III and cystatin C are significantly higher in diseased rTG4510 mice compared to controls in both the hippocampus and cortex, the results from the cytokine assay could represent a normalising effect of VU0486846 treatment on these factors in the rTG4510 mouse model.

Finally, studies have shown that not only overexpression of the mutant human tau, but also disruption of endogenous mouse genes caused by the random insertion of the $MAPT^{P301L}$ and the CaMKIIα-tTA transgenes contribute to the neuropathological phenotypes observed in the rTG4510 model (Gamache et al., 2019, Goodwin et al., 2019). More specifically, the CaMKIIα-tTA transgene was

found to result in a 508 kb deletion on chromosome 12 disrupting five mouse genes and the MAPT^{P301L} inserted within the fibroblast growth factor 14 gene on chromosome 14, leading to a deletion of 244 kb. Gamache et al. (2019) then created a mouse line using a targeted insertion strategy to ensure that no mouse genes would be disrupted. Interestingly, when crossed with the CaMKIIα-tTA activator line used to breed diseased rTG4510 mice, the resulting mice exhibited higher levels of MAPT^{P301L} compared to rTG4510 mice, but neurodegeneration and tau pathology occurred later (Gamache et al., 2019). Since this study, therefore, suggests that a significant portion of the neuropathology observed in this model is not linked to overexpression of MAPT^{P301L} itself, but rather the disruption of endogenous mouse genes (Gamache et al., 2019), this could provide a further explanation as to why chronic administration of VU0486846 did not have an effect on selected markers of neuropathology in this tauopathy model, despite significant beneficial effects having been reported in other taupathy models. Therefore, studying the effect of chronic treatment with M_1 mAChR PAM VU0486846 in a different tau pathology model would be beneficial.

Similar to in Chapter 3, it should be noted that the current study used male mice only, as this was a trial to assess the effect of the M_1 mAChR PAM VU0486846 in the rTG4510 tauopathy mouse model. Funders and researchers increasingly appreciate the importance of using both sexes in *in vivo* therapeutic studies (Lee, 2018, Karp and Reavey, 2019), however, the characterisation in Chapter 4 was performed in male mice only to exclude the effect of the oestrous cycle on behavioural results particularly and due to a lower availability of female mice from our supplier. Therefore, as neuropathological and behavioural changes has not been characterised in female rTG4510 mice including known sex-dependent differences, such as an earlier onset of tau pathology and associated behavioural impairments in females (Yue et al., 2011, Song et al., 2015), this efficacy study was performed in male rTG4510 mice only.

As discussed a range of factors other than the drug could have affected the results of the efficacy study with the M_1 mAChR PAM VU0486846 in the rTG4510 mouse model. It remains to be seen whether the absence of an effect of VU0486846 treatment was due to the drug not working in this particular model or other factors. Nevertheless, this compound has shown no adverse effects and

showed promise in both the APP_{Swe} model and the murine prion model of terminal neurodegeneration (Abd-Elrahman et al., 2022, Dwomoh et al., 2022a). In addition to M_1 mAChR-based therapeutics, a range of other potentially disease-modifting candidates are in various stages of drug development, such as the Aß-targeted immunotherapy lecanamab achieving promising results in Phase 3 clinical trials (Eisai, 2020, Cummings et al., 2022, van Dyck et al., 2022) or the immuno-modulatory small molecule lenalidomide, which is approved as an anti-cancer treatment, in Phase 2 trials (Decourt et al., 2020, Cummings et al., 2022). Overall, targeting the M_1 mAChR remains an avenue of interest in the treatment of AD, especially with compounds leading to limited adverse effects, such as VU0486846.

Chapter 5 M_1 mAChR localisation in the brain

5.1 Introduction

As discussed previously, the M_1 mAChR is widely expressed in brain regions associated with memory and learning, such as the hippocampus and cortex (see 1.3.4) and targeting the M_1 mAChR results in symptomatic and potentially disease-modifying effects in some disease models (see 4.1.1). Another important factor to consider when assessing the potential of the M1 mAChR as a drug target in neurodegeneration is receptor localisation and whether neurodegeneration affects this. Previous studies (for more details see 1.2.3.1) and the availability of the Human Protein Atlas (proteinatlas.org; Sjöstedt et al., 2020) have vastly contributed to our general understanding of M_1 mAChR distribution in the brain, however, it is vital to study the distribution of the receptor at a higher anatomical resolution and especially at a whole systems level (Lebois et al., 2018), as well as in neurodegeneration and in response to M_1 mAChR activation. Since reporter mouse lines may provide a useful tool to map the expression profile of M_1 mAChRs throughout the entire brain, a knock-in transgenic mouse model was generated to constitutively express a variant of the M_1 mAChR containing a *C*-terminal meGFP tag (M_1-meGFP; 2D sequence diagram in Figure 5.1) in cells that would normally express the M_1 mAChR (Marsango et al., 2022, von Stetten et al., 2012).

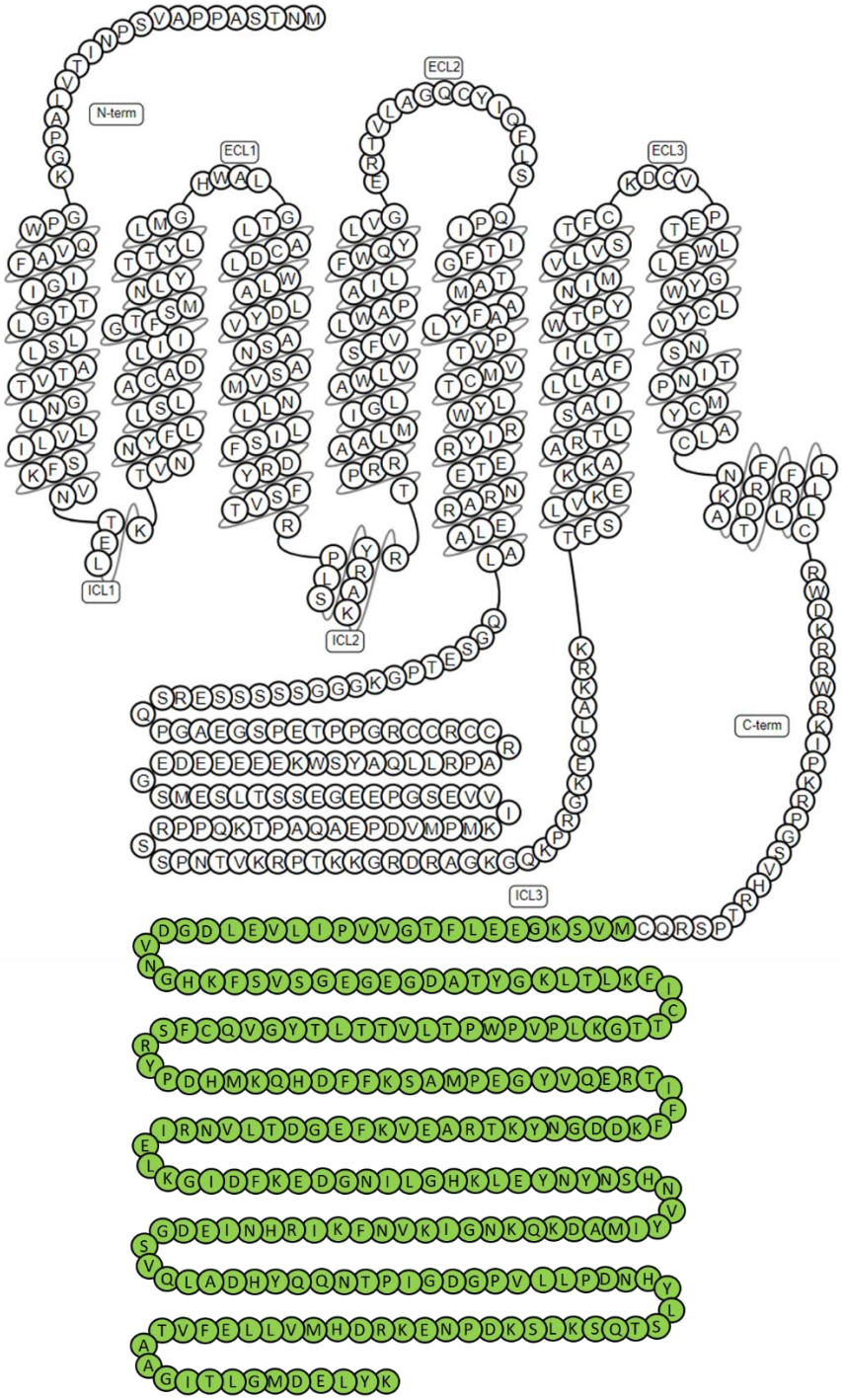

Figure 5.1 2D snake plot diagram of the M_1 mAChR with a meGFP tag on the *C* terminus. Sequence diagram of the human M_1 mAChR was obtained from the GPCR database (GPCRdb.org) and combined with the sequence of meGFP obtained from the fluorescent protein database (FPbase.org).

5.1.1 Studying receptor populations using reporter mouse lines

As discussed, most studies in the past investigating receptor localisation have relied on quantitative autoradiography, immunohistochemistry or in situ hybridisation (see 1.2.3.1). However, these methods are dependent on the specificity of the antibody, which is difficult to achieve due to the conserved

nature of the muscarinic receptors, used as well as the sectioning method used. As an alternative, a range of mouse lines utilising reporter proteins have been developed in the last three decades to label specific cell types or proteins *in vivo* and *ex vivo* (Daigle et al., 2018).

The most commonly used non-fluorescent marker is the *LacZ* gene, but others such as chloramphenicol acetyltransferase are also utilised (Gebhard et al., 2007, Jay and Schneider, 2014, Li et al., 2018, Krämer et al., 2021). The *LacZ* gene encodes the ß-galactosidase protein (ß-gal) (Krämer et al., 2021), and its enzymatic activity is utilised in histochemical assays to convert the colourless 5-bromo-4-chloro-3-indolyl-ß-D-galactopyranoside, also known as X-gal, into indoxyl, which is then rapidly oxidised into a blue product (Horwitz et al., 1964, Krämer et al., 2021). The first *LacZ* reporter mouse was generated in 1987 (Goring et al., 1987) and non-fluorescent markers, such as *LacZ,* have since been used widely in cell lineage tracing and gene expression studies (Krämer et al., 2021). However, while in recent years various fluorescent probes have been developed to detect *LacZ* positive cells, these probes, similar to the conventional histochemical assays required for visualising the signal in non-fluorescent reporter gene lines, have only been successful in *ex vivo* visualisation at present (Gebhard et al., 2007, Abe and Fujimori, 2013, Ito et al., 2018).

Since the discovery of GFP from jellyfish *Aequorea Victoria* (Shimomura et al., 1962), fluorescent proteins have become a useful tool for high resolution imaging of cells and tissues in real time. Over the years, a range of fluorescent proteins for the use in reporter mouse lines have been discovered and developed. These include yellow and cyan fluorescent protein, as well as red fluorescent protein (RFP) variants, including DsRed variants, monomeric RFP 1, tandem dimer Tomato and monomeric Cherry (Feng et al., 2000, Vintersten et al., 2004, Long et al., 2005, Muzumdar et al., 2007, Fink et al., 2010).

The most commonly used fluorescent reporter gene is *GFP*. Successful cloning of the *GFP* gene (Prasher et al., 1992) quickly led to its first reported expression in *E. coli* and *C. elegans* (Chalfie et al., 1994). The first enhanced GFP (eGFP) reporter mouse line was generated in 1997 (Okabe et al., 1997). This mouse line expressed eGFP cDNA driven by a chicken beta-actin promoter and

cytomegalovirus enhancer leading to all tissues, except erythrocytes and hair, fluorescing green under excitation light. The ubiquitous expression of *eGFP* in these mice from a 4-cell prenatal stage throughout life suggested that this expression was not detrimental to the health of the mice (Li et al., 2018). GFP and its variants expressing a stronger signal, such as eGFP, and the monomeric eGFP (meGFP), a A206K mutant of eGFP reducing the tendency of the fluorescent protein to dimerise, have been used in a range of studies (Kain et al., 1995, von Stetten et al., 2012, Faget et al., 2012, Renda and Nashmi, 2012, Mani et al., 2014, Herrick et al., 2017, Marsango et al., 2022).

These reporter genes strains are established by genetically altering the mouse genome. One approach to genetically alter a gene of interest is gene targeting by homologous recombination in ES cells. These ES cells are then injected into blastocytes, which can be transplanted into pseudo-pregnant female mice resulting in the generation of genetically altered chimeric mice (Folger et al., 1982, Evans and Kaufman, 1981, Thomas and Capecchi, 1987, Mansour et al., 1988, Bouabe and Okkenhaug, 2013). Furthermore, recombination systems, such as the Cre/loxP system, can be used to generate mouse lines with specific temporal and spatial patterns of gene expression (Kühn et al., 1995, Sauer, 1998, Metzger and Chambon, 2001, Schnütgen et al., 2003, Bouabe and Okkenhaug, 2013, McLellan et al., 2017). In constitutive knock-in models, the gene of interest is inserted into a gene locus of interest, which could for example mean that the gene for a specific receptor is replaced by a variant of the same receptor but with a fluorescent protein tag.

Due to the highly conserved structure of the five muscarinic receptors, there are very few suitable antibodies for the M_1 mAChR and reporter mouse lines are likely to give a better overview of the receptor distribution. Therefore, as discussed above a novel knock-in mouse line was generated in our laboratory, which expresses a M_1 mAChR variant that has been *C*-terminally tagged with meGFP, an intrinsically fluorescent protein (Marsango et al., 2022).

5.1.2 Advances in tissue clearing and microscopy to visualise proteins of interest on a whole systems level

Fluorescent reporter mouse lines have been utilised extensively in *in vivo* imaging studies. These imaging studies, however, are often still performed in optically transparent tissues and model systems, such as embryos. However, organs in mature animals are not transparent, making fluorescent *in vivo* imaging challenging. However, in the last decade, concurrent advances in tissue clearing and microscopy have made it possible to visualise proteins of interest, either through the use of a reporter line or antibody staining, in cleared intact organs such as the brain.

A range of clearing techniques based on different approaches have been developed. Broadly these can be categorised as solvent-based (hydrophobic tissue clearing), aqueous-based (hydrophilic tissue-clearing), and hydrogel-based methods (Seo et al., 2016, Ueda et al., 2020, Richardson et al., 2021). Generally, these protocols include steps to remove lipids, and possibly pigments and calcium phosphate from bones to match the refractive index (RI) of the cleared tissue to that of the RI matching solution used with the aim of achieving an apparently transparent tissue for imaging (Ueda et al., 2020, Richardson et al., 2021).

Solvent-based clearing techniques, such as the DISCO methods, namely 3DISCO (3D imaging of solvent-cleared organs) (Ertürk et al., 2012), iDISCO (immunolabeling-enabled imaging of solvent cleared organs) (Renier et al., 2014) or vDISCO (nanobody(V_HH)-boosted 3D imaging of solvent-cleared organs) (Cai et al., 2019), include a dehydration step to remove water from the tissue, as water scatters light due to different RI, followed by an organic solvent step to remove lipids and match the RI of the tissue (Susaki and Ueda, 2016, Liebmann et al., 2016, Cai et al., 2019, Molbay et al., 2021). These solvent-based clearing methods allow for rapid clearing of tissues within days, and preservation of the tissue, including signal from immunolabelling, for months (Renier et al., 2014, Cai et al., 2019, Ueda et al., 2020).

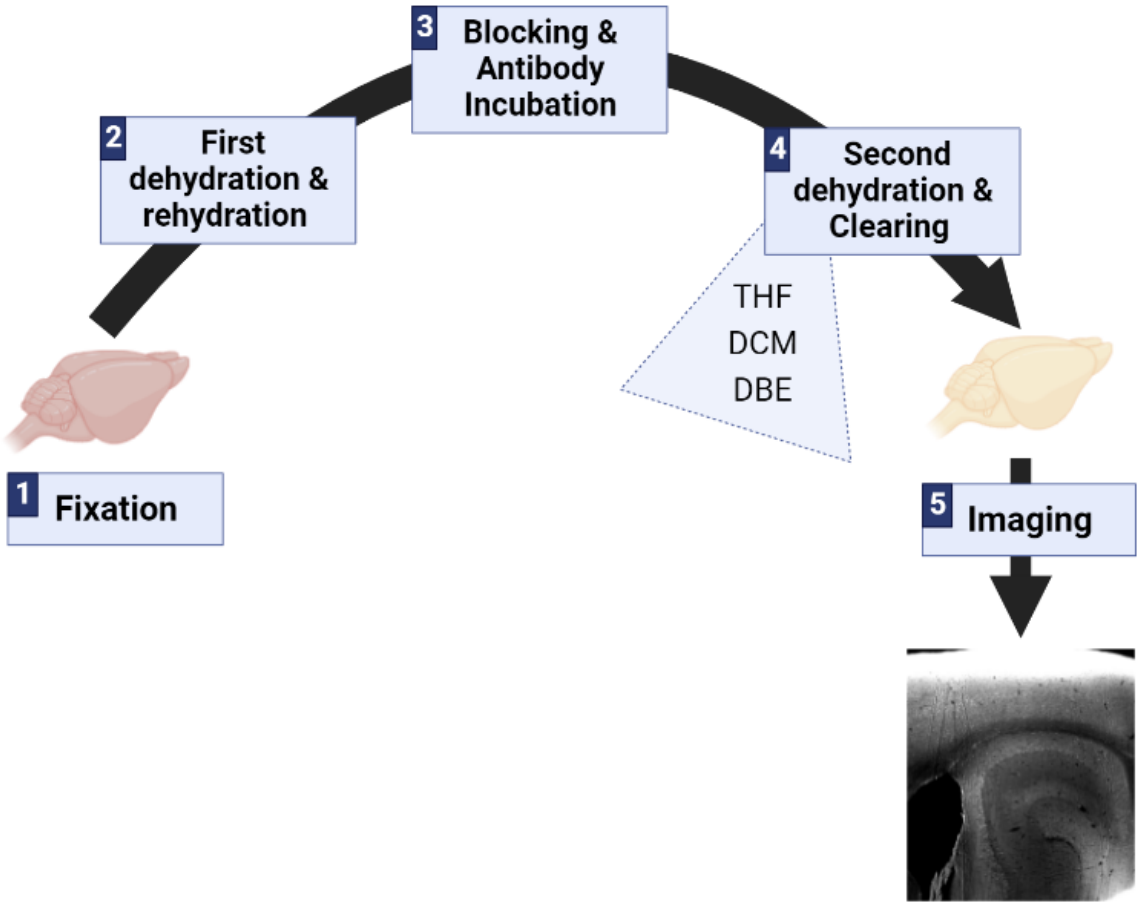

Figure 5.2 Basic steps of the adapted iDISCO protocol. After perfusion with DBPS and 4% PFA, dissected brains were post-fixed in 4% PFA (1), followed by dehydration and rehydration in methanol to reduce autofluorescence and improve antibody diffusion (2). Then, the tissue was blocked, and primary and secondary antibody incubations were performed (3). Samples were dehydrated and cleared in increasing concentrations of tetrahydrofuran (THF), dichloromethane (DCM) and dibenzyl-ether (DBE) (4) and finally the protein of interest could be imaged in ethyl cinnamate using a light sheet microscope (5). Protocol provided by CM Gonzalez. Illustration created using BioRender.com.

Aqueous-based clearing methods, such as Sca*l*e, SeeDB and CUBIC, use water-based reagents, which can bind to proteins, other biomolecules and adjacent water molecules and thereby preserve the macrostructure of the tissue (Ueda et al., 2020). In Sca*l*e, urea is utilised as a clearing agent, whereas in Sca*l*eS, a variation of Sca*l*e, sorbitol is used to enhance the tissue clearing seen with urea (Hirshburg et al., 2007, Hama et al., 2011, Hama et al., 2015). Compared to other clearing techniques including CUBIC, 3DISCO, and SeeDB, the endogenous fluorescence from reporter mice in brain tissue from adult mice has been reported to be preserved the most in Sca*l*eS (Hama et al., 2015). In SeeDB, sucrose is used as an RI matching solution (Ke et al., 2013), whereas in CUBIC, amino alcohol reagents are used for removing lipids and pigments and aromatic amides are used as RI matching reagents (Tainaka et al., 2014, Susaki et al., 2015, Susaki and Ueda, 2016, Tainaka et al., 2018).

In hydrogel-based methods, such as CLARITY (Clear Lipid-exchanged Acrylamide-hybridized Rigid Imaging/ Immunostaining/ in situ-hybridization-compatible Tissue hYdrogel), proteins and other molecules are bound to a hydrogel and thereby preserved, followed by removal of lipids either by passive clearing using detergents or electrophoretic active clearing (Figure 5.3) (Chung et al., 2013, Tomer et al., 2014, Epp et al., 2015). Several variations of CLARITY have been developed to increase tissue permeability, speed up passive clearing and immunolabeling or utilise tissue expansion for super-resolution imaging (Yang et al., 2014, Treweek et al., 2015, Ku et al., 2016, Gradinaru et al., 2018).

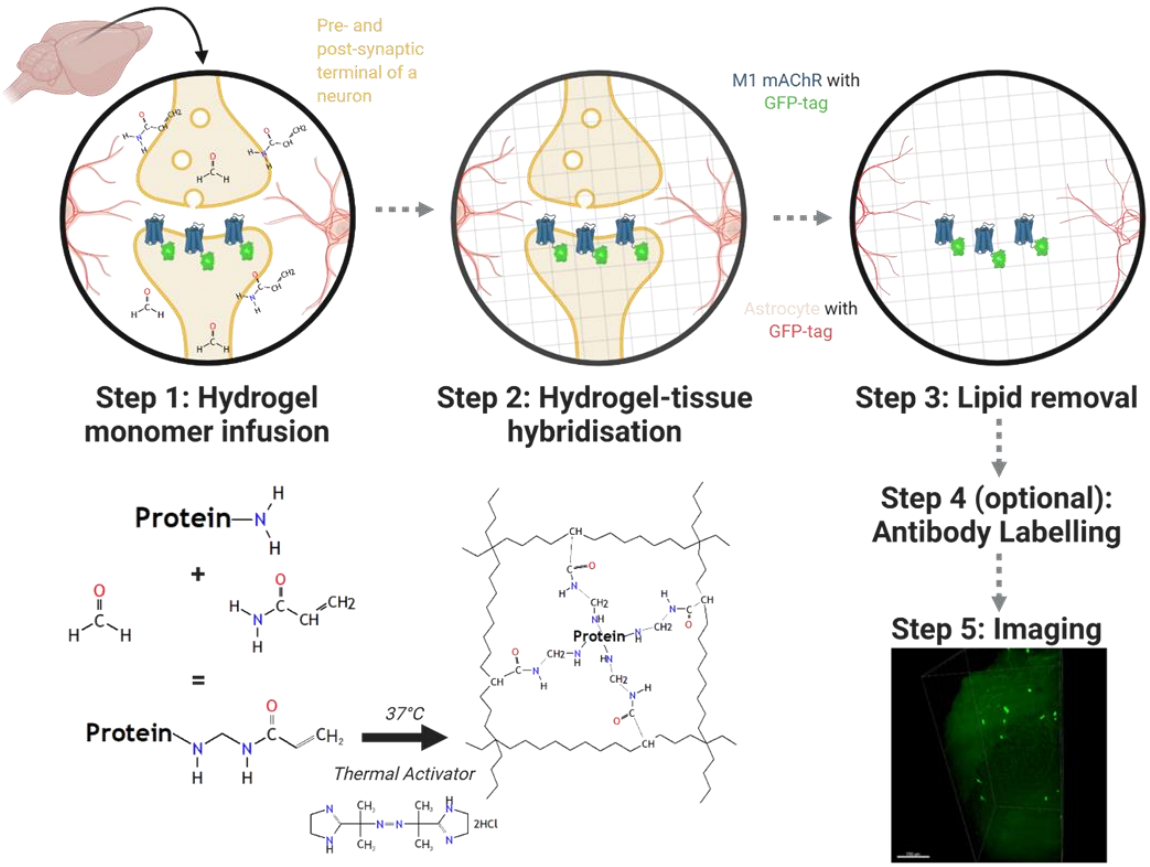

Figure 5.3 Basic steps of the CLARITY protocol. After perfusion, dissected brains are incubated in hydrogel monomer solution (1), followed by thermal activation at 37°C of these leading to formation of a hydrogel-tissue mesh binding to all cell contents (e.g. proteins, DNA, RNA) other than lipids (2). Then tissue is cleared by removing lipids from the brain (3), target proteins can be antibody labelled (4) and finally the protein of interest can be imaged. Adapted from Chung et al. (2013). Illustration created using BioRender.com.

The clearing techniques mentioned above, or variations thereof, have previously been used to prepare thick slices or whole-brain samples for visualising of a target protein with different microscopy techniques (Renier et al., 2016, Ke et al., 2016). Some studies, especially in thick slices, use confocal and two-photon microscopy, and for whole brain samples, light sheet microscopy is most

commonly used. One of the main advantages of confocal and two-photon microscopy is the capability to perform optical sectioning of samples, however the use of these approaches in large samples is generally limited by speed and photobleaching (Richardson et al., 2021). In light sheet fluorescence microscopy (LSFM) a small layer of the sample is illuminated by a light sheet, which is then detected at a perpendicular angle via a detection objective and attached camera (Figure 5.4). This basic setup minimises photobleaching of the surrounding tissue significantly and large samples can comparatively quickly be captured due to the large field-of-view and the high acquisition rate (Reynaud et al., 2008, Hillman et al., 2019, Corsetti et al., 2019, Richardson et al., 2021). A range of more complex LSFM setups have been developed over the years including those specifically for imaging cleared samples using specialised objectives to achieve rapid volumetric imaging with subcellular resolution in cleared samples (Reynaud et al., 2008, Daetwyler and Huisken, 2016, Corsetti et al., 2019, Hillman et al., 2019, Richardson et al., 2021). For these reasons, LSFM has largely become the method of choice for imaging large, cleared samples such as mouse brain (Hillman et al., 2019).

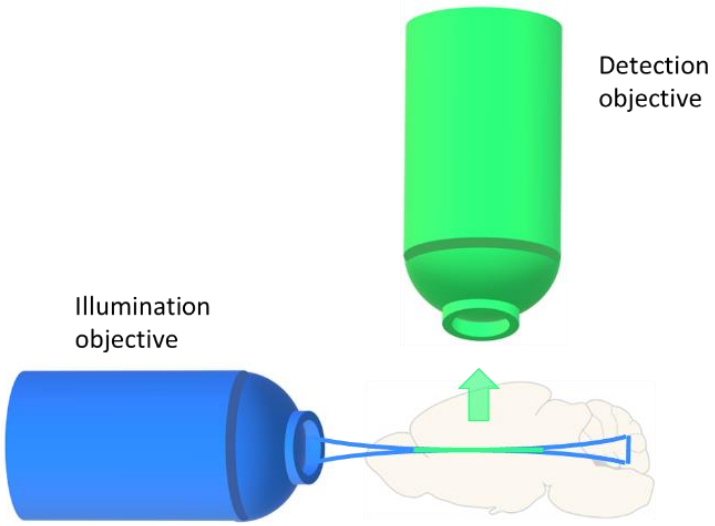

Figure 5.4 Basic principle of light sheet microscopy. An excitatory sheet of light focused through the illumination objective illuminates a layer of the sample and is detected perpendicularly via the detection objective.

5.1.3 Aims

As summarised in 4.1.1, previous studies have suggested a potential therapeutic effect of M_1 mAChR activation in neurodegeneration. However, the M_1 mAChR distribution in the brain remains understudied at high anatomical detail (Lebois

et al., 2018) and there is a lack of knowledge on how this distribution is affected by neurodegeneration. With the availability of a meGFP reporter mouse line for the M_1 mAChR in our laboratory, the aims of this chapter were to

- Characterise the signalling and function of the meGFP tagged M_1 mAChR
- Study the distribution of the M_1 mAChR *in situ*

Since the tagged receptor, replaces the WT receptor in its endogenous locus, it was hypothesised that the expression and function of M_1-meGFP would not differ from that of the M_1 mAChR. While in rTG4510 a reduction in M_1 mAChR especially at 10.0 months of age was found (see 893.2.1.2), in the murine prion model of terminal neurodegeneration and in AD in human the post-synaptic M_1 mAChR population remained intact (Bartus et al., 1982, Mash et al., 1985, Bradley et al., 2017). Therefore, a further hypothesis was that neurodegeneration in the form of murine prion disease would not affect the M_1 mAChR distribution.

5.2 Results

5.2.1 Signalling and function of the M_1-meGFP is similar to M_1-WT control

Initial experiments were designed to determine the effect of the addition of meGFP to the *C* terminal of M_1 mAChR (Figure 5.1) on expression or function of the receptor. Using immunoblotting to detect both the M_1 mAChR and the GFP tag, the M_1-meGFP was found to be upregulated both in hippocampal and cortical samples, as well as in lysates prepared from neuronal cultures, compared to controls (Figure 5.5). In western blots detecting the M_1 mAChR, a single band corresponding to the calculated molecular weight of 55 kDa was detected in the M_1-WT samples (marked in black), while in samples from homozygous M_1-meGFP mice (marked in pink) a band at approximately 80 kDa, corresponding to the size of the M_1-meGFP construct, was found. Samples from heterozygous M_1-meGFP mice (marked in green) yielded both bands at 55- and 80 kDa, suggesting that both M_1-WT and M_1-meGFP receptor forms were present. GFP antisera detected only the 80 kDa receptor variant corresponding to the size of the M_1-meGFP construct. Qualitative assessment shows that M_1-meGFP expression in heterozygous mice was weaker compared to that of the homozygous mice (Figure 5.5 A, B), reflecting the fact that only half of the receptors in the heterozygous mice were the M_1-meGFP variant compared to all in the homozygous mice. Since no corresponding bands were detected in the M_1-KO samples, it is likely that the bands observed in the other samples are indeed variants of the M_1 mAChR. Furthermore, no other bands corresponding to lower molecular weights could be found in any of the blots suggesting that the transgene only exists as the full-length version and no cleaved or degraded fragments are produced (Figure 5.5 A-C). Although, immunoblotting is a semi-quantitative technique and results are only indicative, the quantification suggests that the receptor is significantly upregulated in homozygous M_1-meGFP mice compared to the M_1-WT mice in the hippocampus (2-fold, $p < 0.0001$, Figure 5.5 D), cortex (2-fold, $p < 0.0001$, Figure 5.5 E) and neuronal cultures ($p = 0.0228$, Figure 5.5 F). In samples from heterozygous M_1-meGFP mice, M_1 mAChR receptor levels were significantly upregulated around 1.6-fold in the hippocampus ($p = 0.0004$, Figure 5.5 D) and the cortex ($p = 0.0002$, Figure 5.5 E).

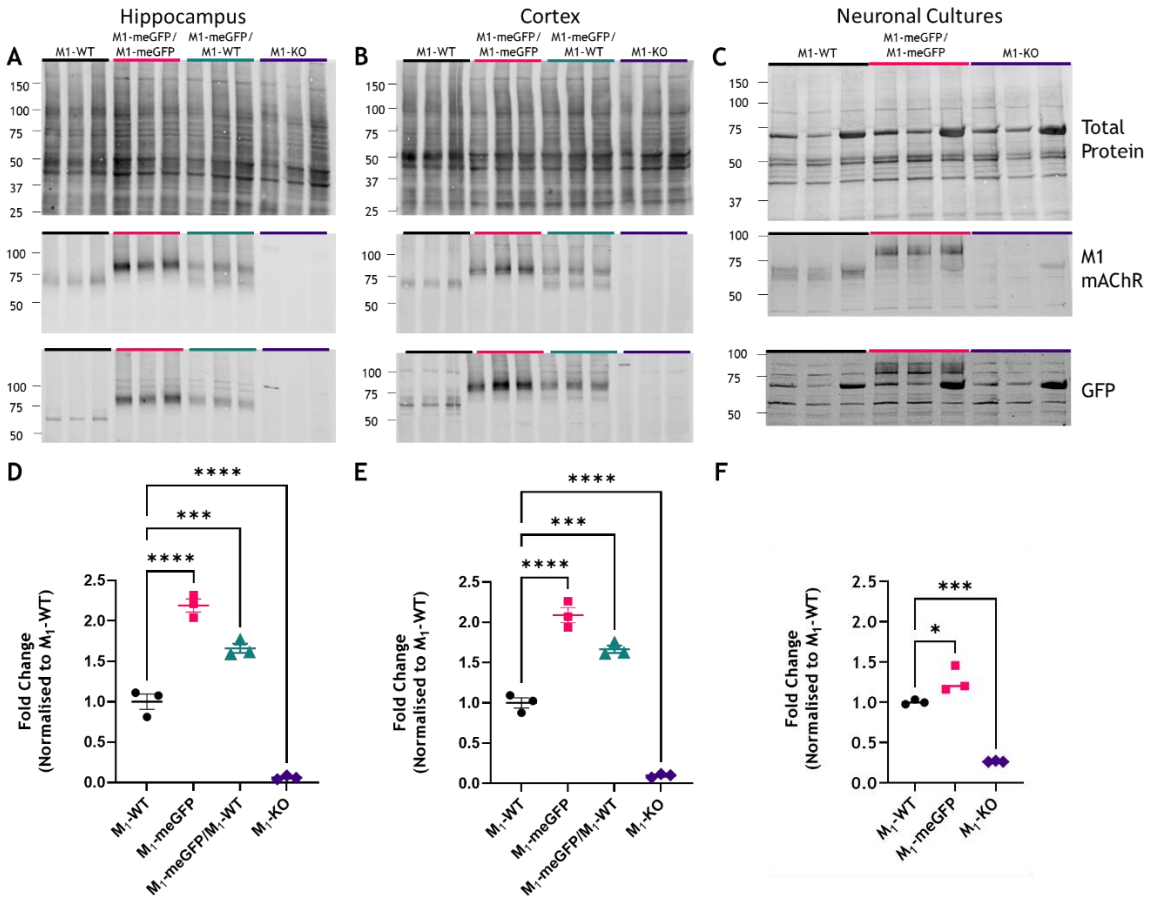

Figure 5.5 Immunoblotting for M_1 mAChR and GFP in lysates from hippocampal and cortical tissues, and neuronal cultures. Representative blots of the REVERT Total Protein stain, M_1 mAChR and GFP in hippocampal (A) and cortical samples (B) as well as neuronal cultures (C) are shown. Blots show M_1-wild-type (WT) control, homozygous M_1-meGFP (M_1-meGFP/M_1-meGFP), heterozygous M_1-meGFP (M_1-meGFP/WT) and M_1-knockout (KO) samples as indicated. Relative protein levels for M_1 mAChR were calculated for hippocampus (D), cortex (E), and neuronal cultures (F). For this, blots were quantified using Image Studio Lite Version 5.2. Protein levels were normalised to signal obtained from corresponding REVERT Total Protein Stain, followed by normalisation to the average protein level of the M_1-WT levels, expressed as fold change, n = 3. Data were analysed using one-way ANOVA for genotype followed by Dunnett's multiple comparison tests; *** $p < 0.001$ **** $p < 0.0001$.

Expression levels of the M_1 mAChR in samples from control M_1-WT, M_1-meGFP and M_1-KO mice were further assessed using quantitative [^{3}H]-NMS binding studies to explore any effects of the meGFP tag on receptor expression. For all samples, total- and non-specific binding, in the presence of the muscarinic antagonist atropine, were measured and specific binding for samples from the different mouse strains in the hippocampus (Figure 5.6 A) and cortex (Figure 5.6 B) was calculated. From the specific binding curves in turn, the muscarinic receptor densities (B_{max}) and dissociation constants (K_D) were calculated. Statistical analysis showed that the muscarinic receptor density is equivalent in tissues from M_1-WT and M_1-meGFP mice (Figure 5.6 C). Whereas the B_{max} in both

M_1-WT (hippocampus p = 0.0352, cortex p = 0.0427) and M_1-meGFP (hippocampus p = 0.0049) samples was significantly higher than in M_1-KO samples, K_D values were not significantly different between M_1-WT, M_1-meGFP, and M_1-KO mice in either hippocampal or cortical samples (Figure 5.6 C).

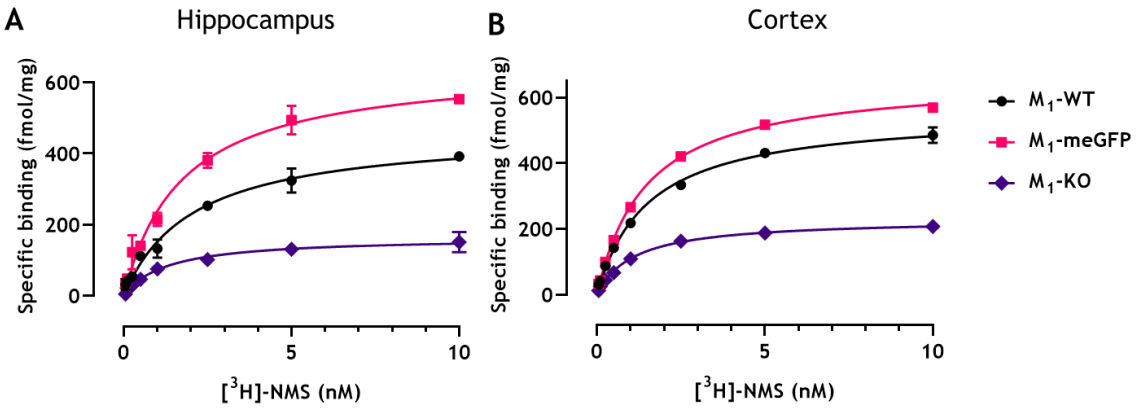

C

	Genotype	B_{max} (fmol/mg)	K_D (nM)
Hippocampus	M_1-WT	502.8 ± 85.7 *	0.9 ± 0.4
	M_1-meGFP	625.3 ± 71.4 **	0.8 ± 0.3
	M_1-KO	221.4 ± 24.6	0.6 ± 0.2
Cortex	M_1-WT	495.5 ± 61.9 *	0.8 ± 0.3
	M_1-meGFP	438.1 ± 85.0	1.1 ± 0.1
	M_1-KO	226.5 ± 32.2	0.7 ± 0.2

Figure 5.6 Expression levels of the M_1-meGFP is equivalent to M_1-WT in cortical and hippocampal samples as assessed using [^{3}H]-NMS saturation binding. Representative graphs of specific binding in hippocampal (A) and cortical (B) membranes prepared from M_1-wild-type (WT) control, M_1-meGFP and M_1-knockout (KO) mice are shown. The calculated muscarinic receptor densities, B_{max}, and dissociation constants, K_D, for experiments in hippocampal and cortical samples are shown (C). Data is shown as means ± SEM, n = 4. For statistical analysis, one-way ANOVA for genotype, followed by Tukey's multiple comparisons tests were used, except for B_{max} in cortical samples. Due to the M_1-WT data failing in the Shapiro-Wilk normality test, for the statistical analysis of the B_{max} in cortical samples, the non-parametric Kruskal-Wallis test and Dunnett's multiple comparison test were used, ** p <0.01 and ** p <0.5 for the indicated strain compared to M_1-KO.

Since all muscarinic receptors bind [^{3}H]-NMS with similar affinity, the M_1 mAChR-KO control was also included to allow for the calculation of M_1 mAChR expression by subtracting the specific binding measured for the M_1-KO control from that measured in control M_1-WT and M_1-meGFP samples. While in cortical samples, M_1 mAChR expression levels were similar in M_1-WT and M_1-meGFP samples (211-269 fmol/mg), in hippocampal samples M_1 mAChR expression levels were higher in M_1-meGFP (404 fmol/mg) compared to M_1-WT samples (281 fmol/mg). Therefore, higher expression levels of M_1-meGFP compared M_1-WT in hippocampal tissue were observed.

Subsequent experiments were performed to investigate a possible effect of the observed raised M_1-meGFP expression levels on G protein functionality (Figure 5.7). In neuronal cultures, an IP-One assay was used to assess carbachol-induced receptor activation. Addition of carbachol to neuronal cultures led to a concentration-dependent accumulation of IP1, which was similar in cultures prepared from M_1-WT and M_1-meGFP animals as shown by pEC50 values of 5.12 ± 0.19 and 4.78 ± 0.29 respectively (Figure 5.7 A). In cortical membrane preparations, a [^{35}S]-GTPγS assay was used to assess basal and carbachol-induced $G\alpha_q$-protein activation. At a basal state around 23 to 32% of [^{35}S]-GTPγS was bound in all samples. Upon agonist stimulation, a four-fold increase in bound [^{35}S]-GTPγS was measured, normalised to M_1-WT levels, at 100% and 117% in samples from M_1-WT and M_1-meGFP, respectively (both $p < 0.0001$). No statistical difference between M_1-WT and M_1-meGFP samples was found (Figure 5.7 B). Stimulation with carbachol in membranes prepared from M_1-KO mice led to no increase in bound [^{35}S]-GTPγS over basal levels indicating that the carbachol response is driven entirely by M_1 mAChR in the M_1-WT and M_1-meGFP membranes. Therefore, while there is an indication that M_1 mAChR levels in the M_1-meGFP mice may be higher compared to M_1-WT, this does not lead to a significant increase in G protein coupling to the receptor.

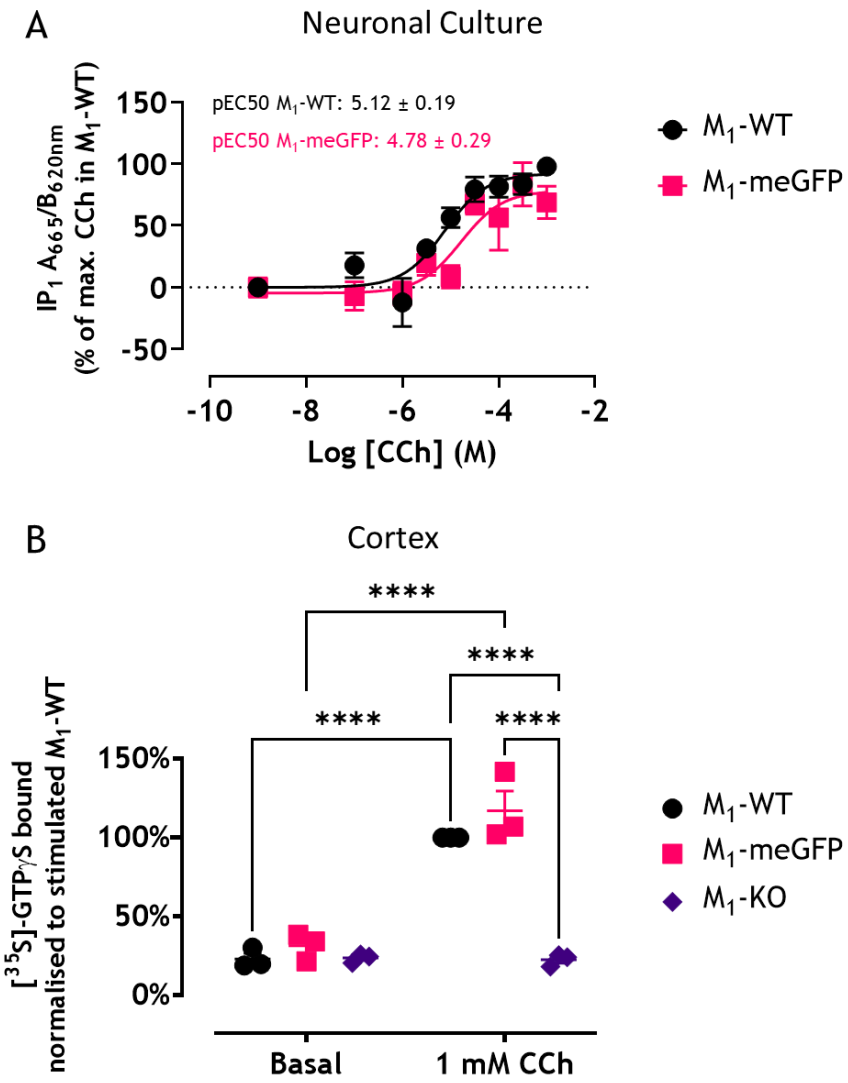

Figure 5.7 Signalling at the M_1-meGFP is equivalent to M_1-WT in neuronal cultures and cortical membranes. Neuronal cultures prepared from M_1-wild-type (WT) and M_1-meGFP mice were stimulating with increasing concentrations of carbachol (CCh) in IP-One Assay (A). For the IP-One assay, data was analysed using a log(agonist) vs. response (three parameters) analysis of non-linear regression. Data are expressed as means ± SEM and pEC50 values are indicated in the figure. In the [^{35}S]-GTPγS assays, G protein activation was measured in cortical membranes prepared from M_1-WT, M_1-meGFP and M_1-knockout (KO) samples under basal and CCh-induced conditions (B). For analysis of the [^{35}S]-GTPγS assay, results were normalised to the stimulated control membranes and a two-way ANOVA for genotype and treatment followed by a Tukey's multiple comparison test was performed for statistical analysis. Data is expressed as means ± SEM, with individual data points representing membranes prepared from individual mice. For the [^{35}S]-GTPγS assay, n = 3, and for the IP1 assay, data from 3-4 independent experiments is shown.

Next, behavioural experiments were performed to determine whether the addition of the meGFP affects *in vivo* behavioural phenotypes. In an open field test, locomotor activity was assessed (Figure 5.8). In agreement with previous studies, M_1-KO mice exhibit a hyperactive phenotype, showing a significant increase in total distance travelled compared to M_1-WT ($p = 0.0003$) and M_1-meGFP mice ($p = 0.0008$) (Miyakawa et al., 2001, Gerber et al., 2001, Bradley et al., 2020). No difference was observed in activity levels between M_1-WT and

M_1-meGFP (p = 0.8663, Figure 5.8), suggesting that addition of the meGFP tag to the M_1 mAChR does not induce a hyperactivity phenotype indicative of disrupted M_1 mAChR signalling.

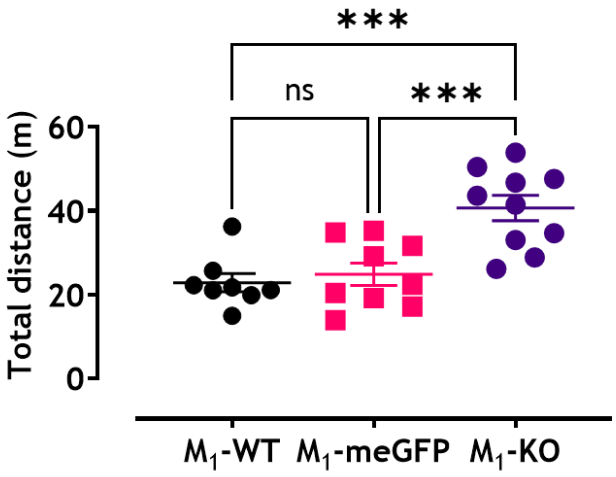

Figure 5.8 Locomotor activity of M_1-meGFP mice is equivalent to M_1-WT mice in an open field test. Total distance travelled by M_1-wild-type (WT), M_1-meGFP and M_1-knockout (KO) mice was determined during a 10 min interval in the open field test. Data was analysed using a one-way ANOVA for genotype followed by a Tukey's multiple comparisons test. Behavioural data is shown as means ± SEM of n = 8-10 mice. This experiment was performed by SJ Bradley and is being used with permission.

A fear-conditioning paradigm was performed to evaluate the impact of the meGFP addition to the M_1 mAChR on learning and memory processes. In fear conditioning (described in 2.10.2), associative learning and memory is assessed by measuring freezing response to either the fear conditioning context environment or conditioned stimulus (tone) (Fanselow and Poulos, 2005).

Baseline levels for all strains were similar for both the context (Figure 5.9 A) and cued tone responses (Figure 5.9 B). For the context and cued responses, all strains exhibited associative learning shown by a significantly increased freezing response during context retrieval compared to baseline context measurements ($p < 0.0001$, Figure 5.9 A, B). For context ($p > 0.1133$) and tone retrieval ($p > 0.8198$), no difference between M_1-WT, M_1-meGFP mice and M_1-KO mice were observed. Overall, no behavioural differences between M_1-WT and M_1-meGFP mice could be found suggesting that the addition of the meGFP tag to the M_1 mAChR does not affect complex function of the receptor.

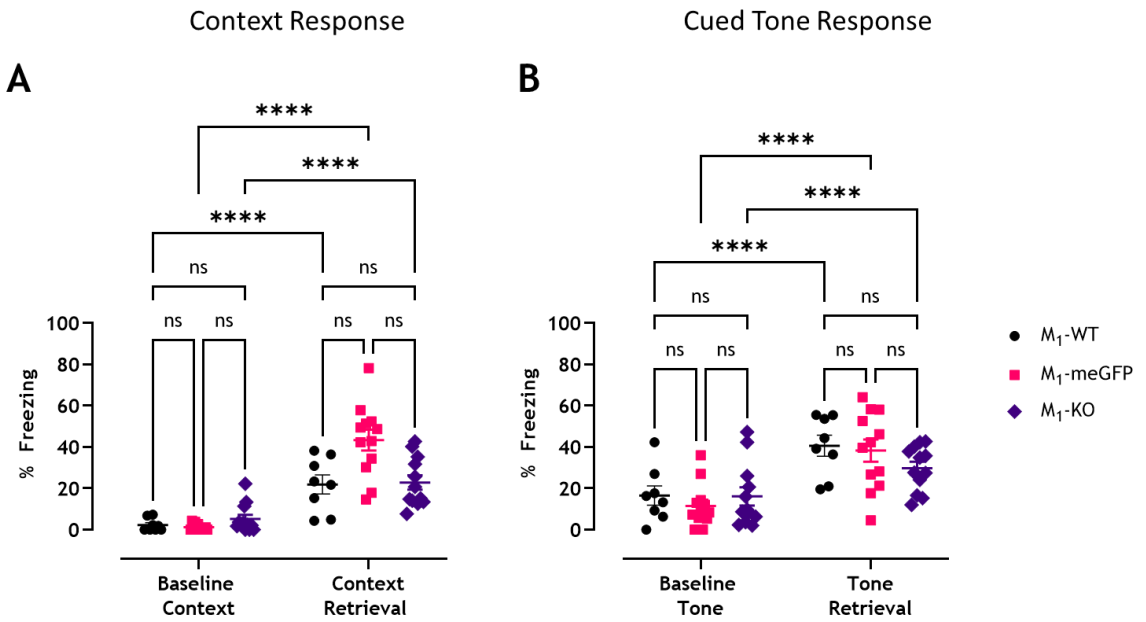

Figure 5.9 M_1-meGFP mice show similar responses to M_1-WT control mice in fear conditioning experiments. Contextual (A) and cued (tone, B) fear conditioning response were assessed in M_1-wild-type (WT) control, M_1-meGFP and M_1-knockout (KO) mice. Data are shown as means ± SEM, n = 8-12. For statistical analysis, the main effects only model of the two-way ANOVA for genotype and time-point (baseline vs. retrieval) was used followed by Tukey's multiple comparison tests, where **** p <0.0001.

5.2.2 Visualisation of the intrinsic meGFP fluorescence

The meGFP tagged M_1 mAChR was first visualised in neuronal cultures. Cultures were stained with a GFP antibody to enable the comparison of signal achieved by antibody staining with the fluorescence obtained from the endogenous meGFP (Figure 5.10). When imaging the intrinsic meGFP signal, no specific staining could be detected due to high levels of autofluorescence in both the M_1-WT control and the M_1-meGFP samples. Staining with the GFP antibody resulted in specific signal in the M_1-meGFP samples in the membrane of the neuronal cell body and along some axons (Figure 5.10).

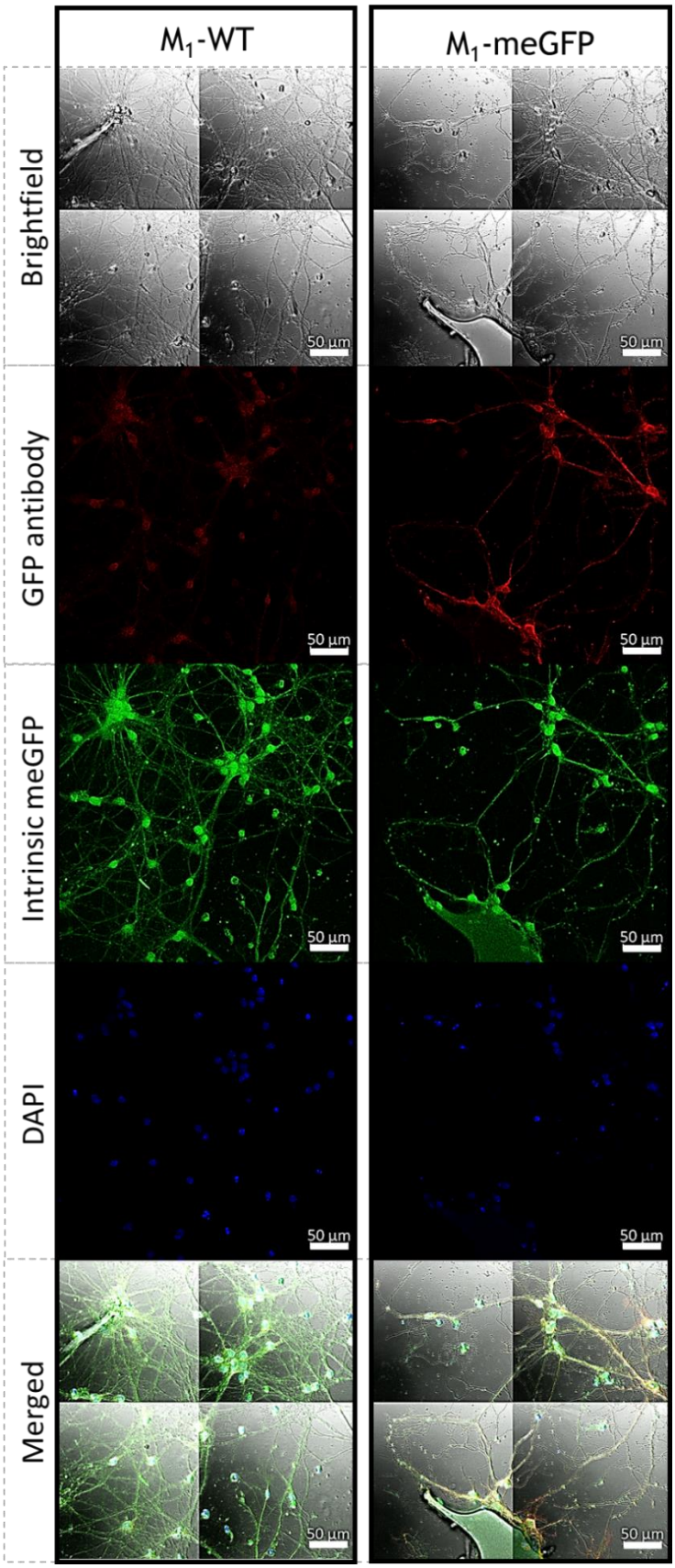

Figure 5.10 Specific staining in M_1-meGFP neuronal cultures can be seen using a GFP antibody. When comparing GFP antibody staining (red) and the meGFP signal (green) in cultures prepared from control- and M_1-meGFP mice, no difference in intrinsic meGFP signal was found. Specific staining was observed when using the GFP antibody. Brightfield images, DAPI staining, and the merged images are also shown for both control and M_1-meGFP samples as indicated. Images were acquired using an LSM 880 confocal microscope with 40x magnification. Scale bars represent 50 µm.

Four perfusion and fixation protocols were then assessed for their ability to preserve the intrinsic meGFP signal and to reduce autofluorescence in brain sections (details in Table 5.1).

Table 5.1 Details of four perfusion and fixation protocols assessed for the preservation of the endogenous meGFP signal. For each of the protocols, a specific feature of the protocol is highlighted, as well as the expected outcome of this feature and relevant references.

Protocol Number	Specific feature	Reasoning	Reference
1	„Standard protocol“ + 15% sucrose step	Cryoprotection	(Bourgognon et al., 2021)
2	Perfusion with 9.25% sucrose in PB first, rest same as in 1	Prevent cell shrinkage	(Faget et al., 2012, Scouten et al., 2006)
3	1% periodate–lysine–PFA	Reducing autofluorescence and PFA-induced quenching of GFP fluorescence	(Zukor et al., 2010, Herrick et al., 2017)
4	1% PFA	Reduce PFA-induced quenching of GFP fluorescence	(Renda and Nashmi, 2012)

Brains fixed using Protocols 3 and 4 were too fragile for processing and therefore disregarded. Brains prepared using Protocols 1 and 2 could successfully be cut into 30 µm thick coronal sections. When assessing the level of endogenous fluorescence observable in the M_1-meGFP tagged mice compared to controls with these two perfusion and fixation protocols it became apparent that Protocol 1 and 2 preserved the fluorescence of the endogenous tag (Figure 5.11). When comparing the fluorescence in the hippocampus, a brain region that expresses high levels of the M_1 mAChR, in these two protocols, the signal appears to be stronger in the M_1-meGFP sample prepared using the Protocol 2 (Figure 5.11 D) compared to Protocol 1(Figure 5.11 B). In M_1-WT controls the level of autofluorescence of the tissue appears to be the same for Protocol 1 (Figure 5.11 A) and Protocol 2 (Figure 5.11 C).

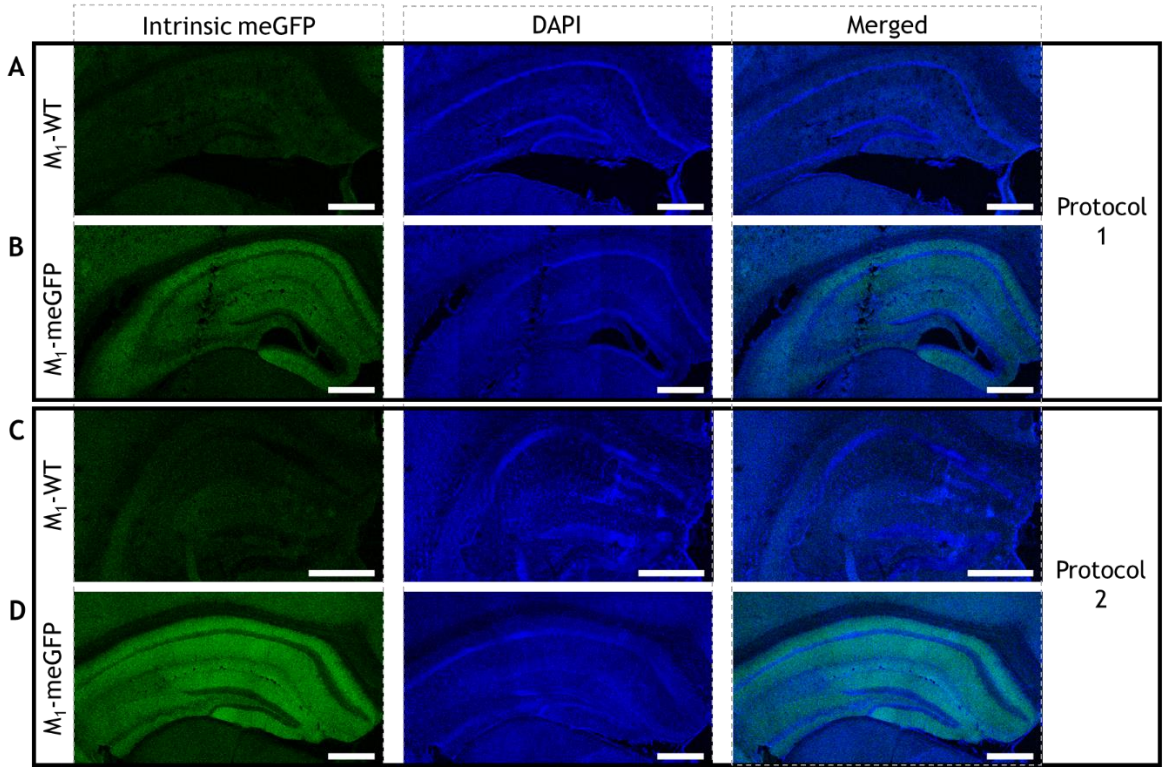

Figure 5.11 Comparison of meGFP fluorescence preserved by different fixation protocols in the hippocampal regions in cryosectioned 30µm thick coronal sections. Samples processed using Protocol 1 in M_1-wild-type (WT) control mice (A) and mice expressing M_1-meGFP receptors (B), as well as using Protocol 2 in M_1-WT control (C) and M_1-meGFP mice (D) are shown. Images were acquired using the same settings on a LSM 880 confocal microscope at 10x magnification. Scale bars represent 500µm.

5.2.3 Assessing chromogenic staining targeting the meGFP tag

Since one aim of this chapter was to assess the distribution of the M_1 mAChR in the whole brain and it is difficult to prepare serial sections through the whole brain using a cryostat, chromogenic staining protocols were tested with the aim of visualising the meGFP tag in sections through the whole brain.

Using chromogenic IHC protocol 1, the staining observed in samples from M_1-WT and M_1-meGFP mice was similar with all antibody dilutions tested indicating non-specific staining (1:500-1:5000, Figure 5.12).

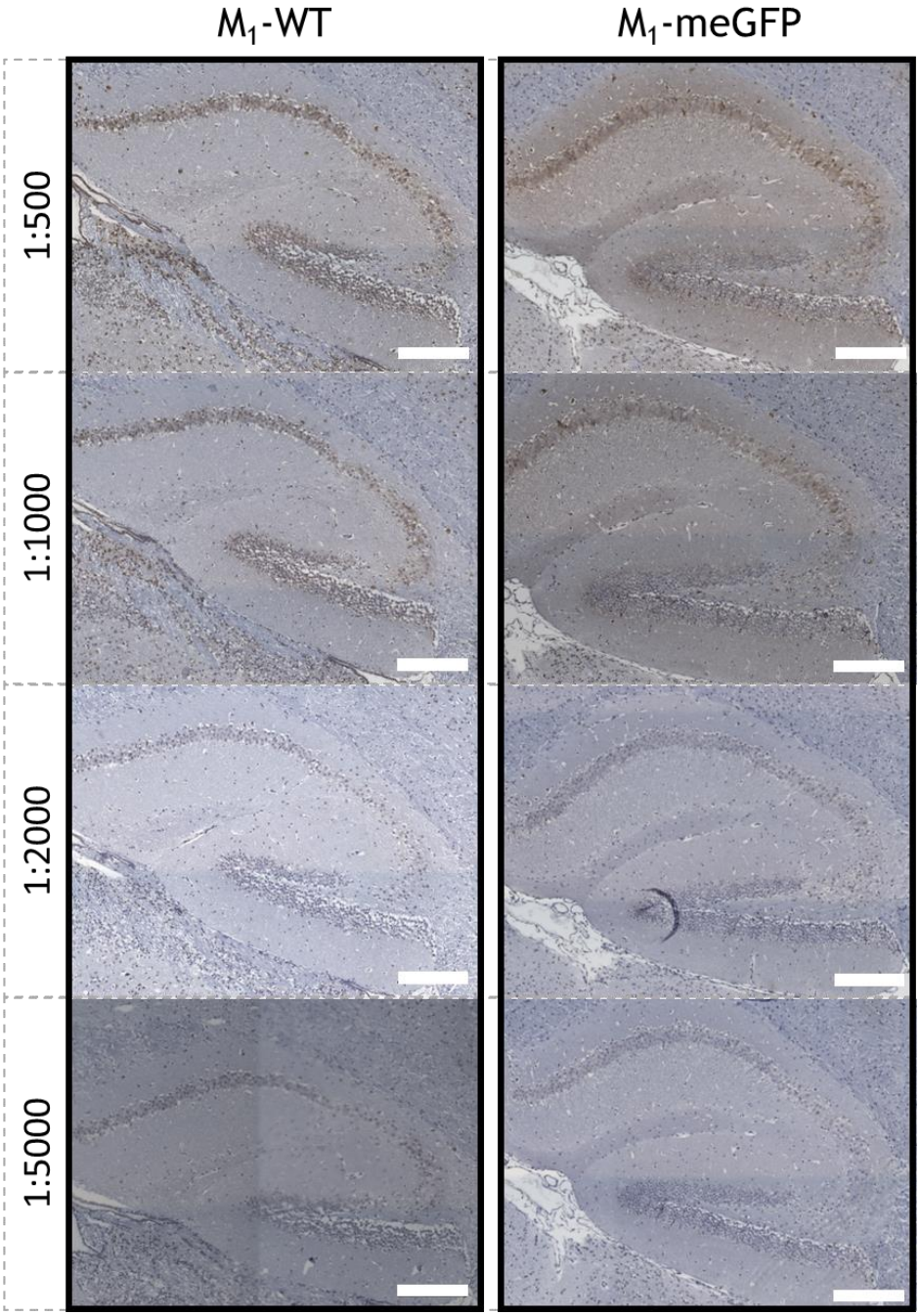

Figure 5.12 Staining with a rabbit anti-GFP antibody in control M_1-WT and M_1-meGFP mice using chromogenic IHC protocol 1 is unspecific. Images show the staining observed in the hippocampal area in 5 µm thick sagittal sections from control M_1-wild-type (WT) and M_1-meGFP mice. Sections were incubated with DAB for 5 min resulting in brown staining. Sections were then also dipped in haematoxylin for counterstaining nuclei in blue. Antibody incubations used are indicated at the side for both control M_1-WT and M_1-meGFP samples. Images were acquired using the EVOS FL Auto 2 Imaging System at 20x magnification. Scale bar represents 200 µm.

A second chromogenic IHC protocol was then used, which includes several modifications compared to the first protocol to improve blocking and epitope-retrieval to reduce non-specific interactions and enhance specific staining (see 2.8). However, despite these adjustments the staining observed in M_1-WT and M_1-meGFP mice was similar at all primary antibody dilutions (1:500 and 1:1000) and DAB incubation times (30 sec and 2 min) tested (Figure 5.13 A).

There is potentially some specific staining in the M_1-meGFP mice samples, at a 1:1000 dilution incubated with DAB for 30 sec, particularly in the pyramidal layer in the CA areas (black arrow) and the granular layer of the DG (red arrows, Figure 5.13 A), however, further optimisation is needed. This need for further optimisation is highlighted by the observation that comparable staining was found in both M_1-WT and M_1-meGFP mice in the isotype control at the same conditions (Figure 5.13 B) indicating significant non-specific binding of the rabbit anti-GFP antibody is likely to take place. While the chromogenic staining protocol could be optimised further, brain clearing techniques in combination with light sheet microscopy were optimised instead to assess meGFP signal in an intact brain hemisphere on a systems level.

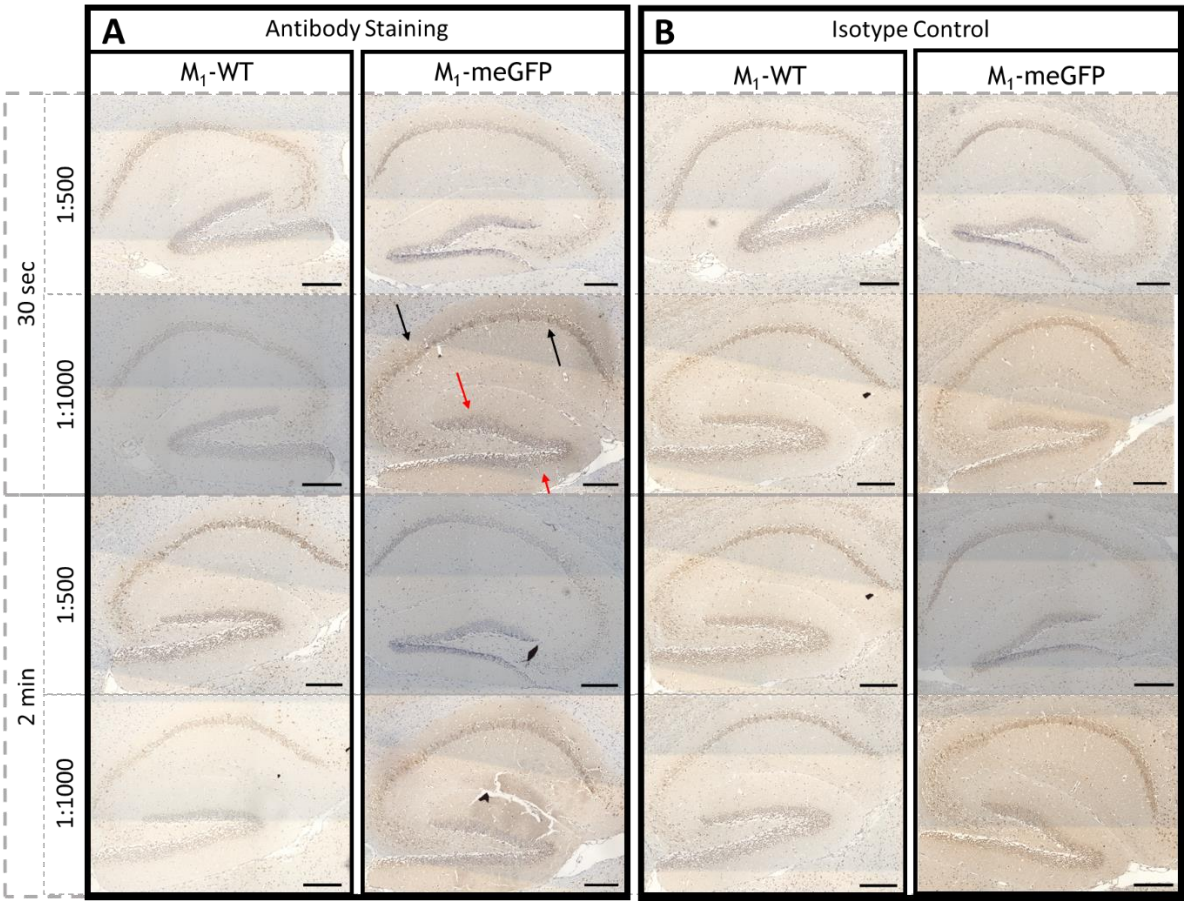

Figure 5.13 Staining with a GFP antibody in control M_1-WT and M_1-meGFP mice using chromogenic IHC protocol 2 is non-specific. Images show the staining observed using the GFP antibody (A) or the isotype control (B) in the hippocampal area in 5 µm thick sagittal sections from control M_1-wild-type (WT) and M_1-meGFP mice. Sections were incubated with DAB for 30 sec to 2 min as indicated resulting in brown staining. Sections were then also dipped in haematoxylin for counterstaining nuclei in blue. Antibody incubations used are indicated along the side for both control M_1-WT and M_1-meGFP samples. Black and red arrows highlight the pyramidal layer of the cornu ammonis regions and the granular layer of the dentate gyrus, respectively. Images were acquired using the EVOS FL Auto 2 Imaging System at 20x magnification. Scale bar represents 200 µm.

5.2.4 Visualisation of M_1-meGFP using light sheet microscopy in clarified samples

While it is useful to examine the distribution of M_1 mAChR based on the fluorescence of the meGFP tag in sections using confocal microscopy, an approach that allows the mapping of the receptor population in the intact brain would allow for a more comprehensive understanding of receptor distribution on a systems level. Therefore, CLARITY, a tissue-clearing protocol previously used for endogenously fluorescent proteins (Figure 5.3) (Chung et al., 2013, Tomer et al., 2014), was used to assess the endogenous M_1-meGFP signal in brain blocks. Brain blocks containing the hippocampal region were passively cleared. While the transparency of the samples increasing with longer incubations, the tissue integrity decreased (Figure 5.14) making handling of the tissue more difficult.

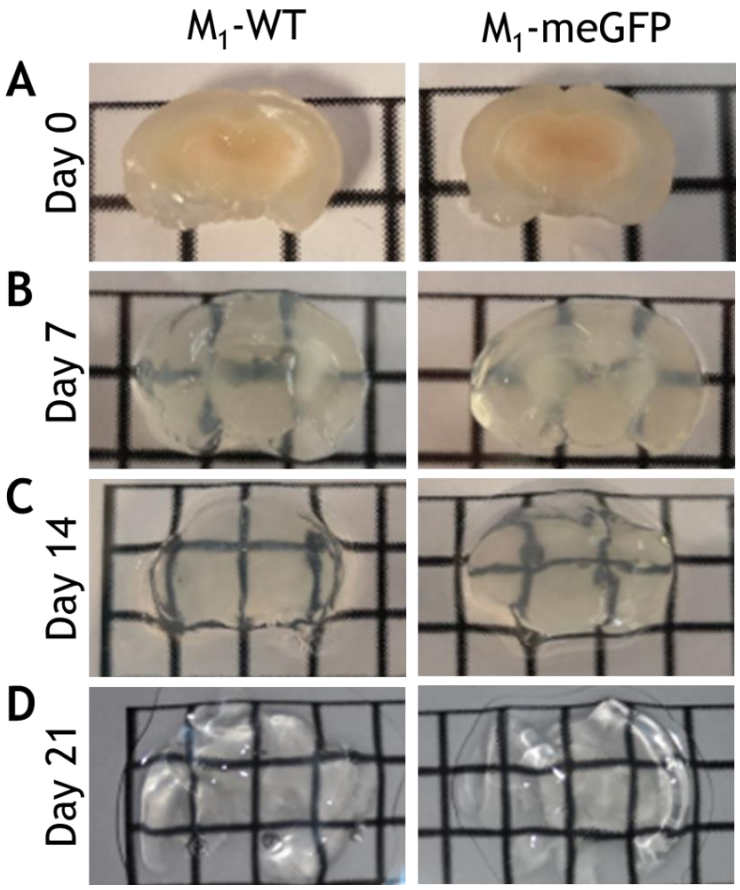

Figure 5.14 Gradual clearing of brain samples processed using CLARITY. Images show brain samples containing the hippocampal region from M_1-wild-type (WT) and M_1-meGFP mice before the start of passive clearing (A), after one (B), two (C) and three weeks (D) of passive clearing at 37°C.

Brain blocks that had been cleared for 2 weeks were used for visualisation utilising light sheet microscopy. This time-point was a compromise to achieve

the clearest samples, before the tissue integrity started to become compromised from over-clearing. In the M_1-meGFP sample (Figure 5.15 B, D) more nuances in signal intensity could be found compared to the control sample (Figure 5.15 A, C). However, similarly to the problem observed in neuronal cultures, a high level of autofluorescence could be observed in both M_1-WT and M_1-meGFP samples both when looking at a coronal view of the sections (Figure 5.15 A, B) as well as from a sagittal view (Figure 5.15 C, D), therefore no clear specific signal could be observed.

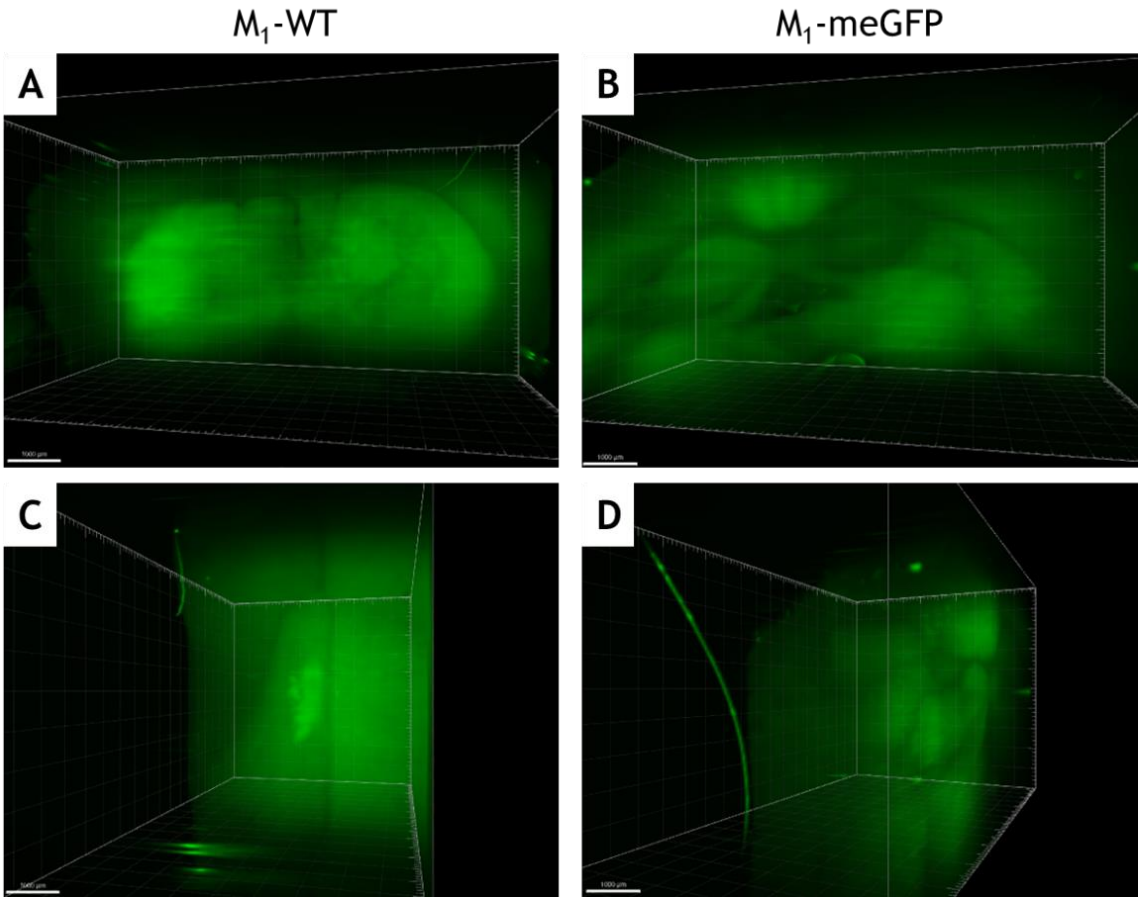

Figure 5.15 Light sheet microscopy of CLARITY-cleared 3 mm-thick coronal brain blocks containing the hippocampal region obtained from control and M_1-meGFP mice. Coronal sections were passively cleared for 2 weeks using the CLARITY protocol and imaged on a Zeiss Lightsheet Z.1. 3D images of the brain blocks were rendered using IMARIS Software. Frontal and lateral side views of the 3D reconstruction of the coronal brain block in M_1-wild-type (WT) control (A and C, respectively) and M_1-meGFP (B and D, respectively) samples are shown. Images were acquired using a 20x cleared tissue Zeiss objective. Scale bars represent 1000 µm.

It was challenging to locate the hippocampal area in samples consisting of a whole hemisphere using the Zeiss Lightsheet Z.1, therefore, an Ultramicroscope II Light Sheet Microscope was used to assess the intrinsic meGFP signal in a hemisphere from a M_1-meGFP mouse (Figure 5.16). Figure 5.16 shows optical sagittal sections through a brain hemisphere moving laterally (A-D). Lighter

regions indicate more signal, however, the signal observed does not appear to be specific and is mostly likely caused by autofluorescence as no signal could be found in the hippocampus (Figure 5.16, highlighted by white arrows).

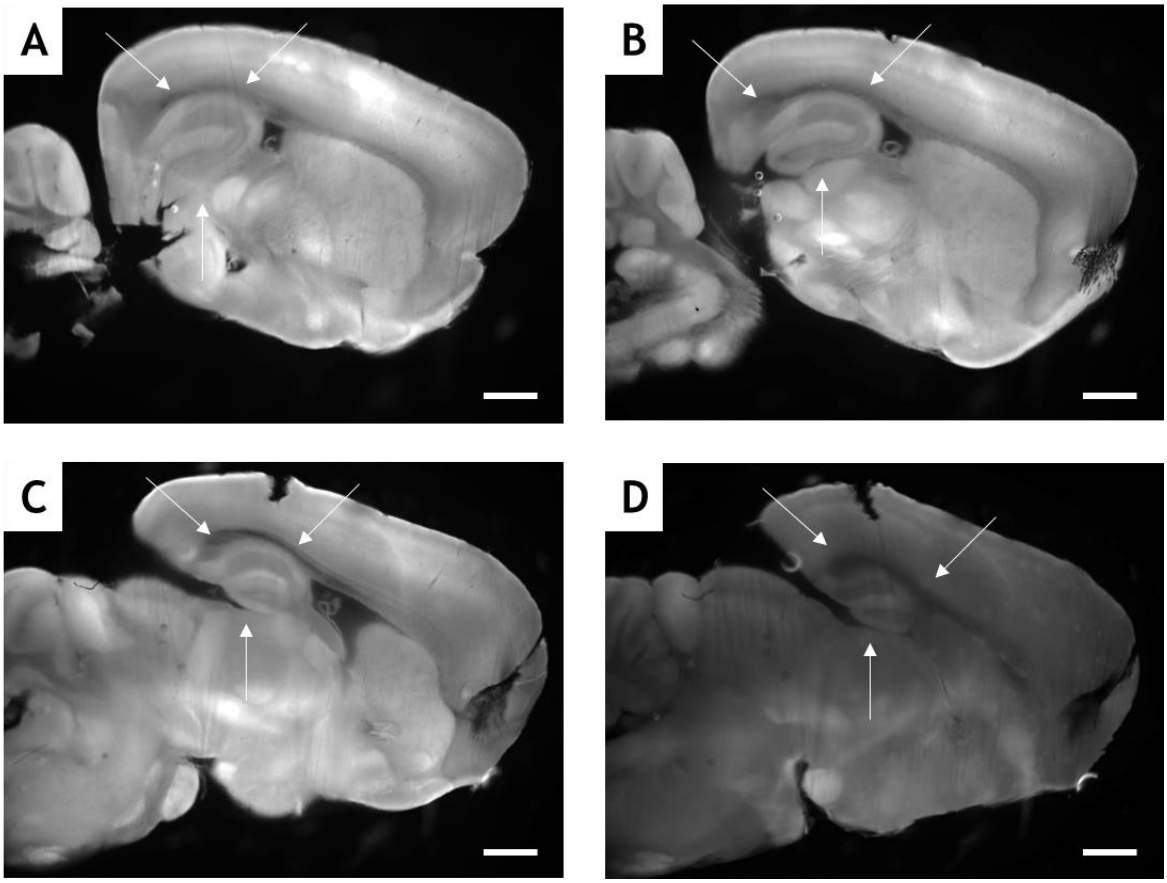

Figure 5.16 Sagittal views at different levels through the hippocampus in a CLARITY-cleared brain hemisphere from a M_1-meGFP mouse. Images show the shape of the hippocampus (indicated by arrows) moving from a more lateral to increasingly medial views (A to D). Lighter areas indicate potential detection of the intrinsic GFP signal. Images were acquired on an UltraMicroscope II Light Sheet Microscope (LaVision) using the 2x objective lens with manually adjustable zoom, resulting in a final magnification of 0.8x. Scale bars represent 1,000 µm.

As Figures 5.10, 5.15 and 5.16 show, the endogenous signal of the meGFP tag does not appear to be strong enough to be distinguishable from the autofluorescence observed in neuronal cultures, cleared brain blocks and whole hemispheres. Therefore, an adapted iDISCO protocol for brain clearing (Figure 5.2), which is known to quench endogenous fluorescence (Renier et al., 2014), was used in combination with antibody staining.

Using the iDISCO protocol, some specific GFP antibody staining in the M_1-meGFP (Figure 5.17 B) compared to the M_1-KO sample (Figure 5.17 A) could be observed, particularly in the hippocampus (Figure 5.17 B, white arrows) and

cortex (Figure 5.17 B, white arrows). In the hippocampus, the staining appears to be mostly in the pyramidal layer of the CA1-3 and the dorsal subiculum.

Strong staining was observed at the top of the cortex in both the M_1-KO and M_1-meGFP brain (Figure 5.17), potentially due to some of the secondary antibody failing to penetrate beyond the surface of the cortex.

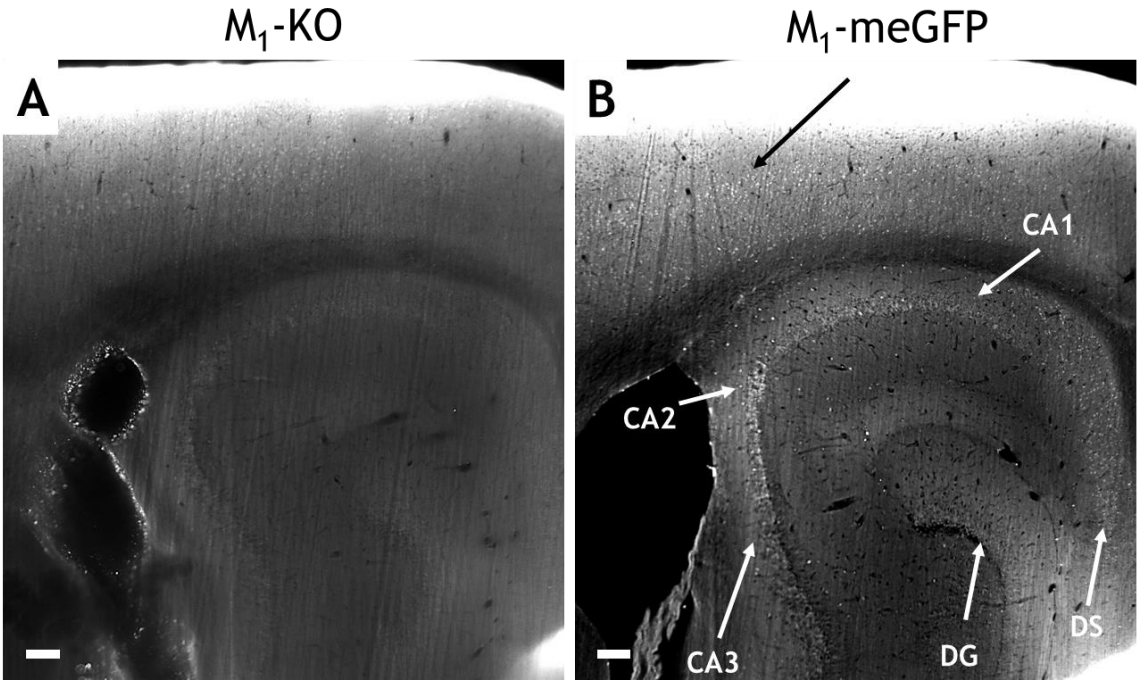

Figure 5.17 Optical sagittal section through the hippocampus and cortex in GFP-stained iDISCO cleared brain hemispheres. Brain hemispheres from M_1-knockout (KO) (A) and M_1-meGFP (B) mice were cleared using the adapted iDISCO protocol, stained with a chicken anti-GFP antibody followed by an Alexa Fluor-647 anti-chicken antibody and then imaged in ethidium cinnamate using an UltraMicroscope II Light Sheet Microscope (LaVision). Lighter areas in the M_1-meGFP sample indicate areas stained for the GFP-tag on the M_1 mAChR in the hippocampus (white arrows) and cortex (black arrow). Images were acquired at the same hippocampal level (3.12 mm lateral to Bregma) using the same setting and a 2x objective lens with manually adjusted zoom leading to a final magnification of 6.88x. DG: dentate gyrus, DS: dorsal subiculum. Scale bars represent 100 µm.

These results suggest that brain clearing in combination with light sheet microscopy is a promising approach for assessing localisation of the M_1 mAChR in the M_1-meGFP reporter mouse line, however, due to time constraints further optimisation and progress was not possible.

5.3 Discussion

The M_1 mAChR has shown pro-cognitive and potential disease-modifying effects in preclinical studies (Lebois et al., 2018, Scarpa et al., 2020). Currently, therapeutics targeting the M_1 mAChR are being developed to improve cognition, reduce neuroinflammation and potentially have disease-modifying effects without causing adverse effects commonly seen with current treatments. Several studies using radioligands and antibodies have reported M_1 mAChR localisation in brain sections (Buckley et al., 1988, Weiner et al., 1990, Levey et al., 1991, Levey, 1993, Hersch et al., 1994), however, the use of reporter mouse lines combined with advanced microscopy techniques could be exploited to study M_1 mAChR distribution in the brain at a high anatomical detail on a systems level. Therefore, the effect of the meGFP tag addition to the M_1 mAChR on receptor signalling and function was investigated and while in line with the hypothesis little effect of the meGFP tag addition to the M_1 mAChR on receptor function was found, contradictory to the hypothesis some effect of the tag on receptor expression was observed. In addition, several techniques were utilities to assess distribution of the M_1-meGFP receptor, ranging from chromogenic staining to clearing tissue combined with light sheet microscopy, demonstrating that the receptor is challenging to visualise. Due to time constraints, the second hypothesis of this chapter could unfortunately not be assessed here.

M_1-WT and M_1-meGFP mice displayed similar results in [^{3}H]-NMS saturation binding, [^{35}S]-GTPγS assays in brain samples, in IP1 assays in neuronal cultures and in the locomotor and fear conditioning paradigms. However, immunoblotting suggested increased receptor expression in the M_1-meGFP compared to M_1-WT samples. While this observation could be caused by the addition of the meGFP tag to the M_1 mAChR, it should also be noted that the M_1-WT and M_1-meGFP mice have C57BL/6J and C57BL/6N backgrounds, respectively, and the M_1-meGFP mice were bred in-house, while the M_1-WT mice were purchased commercially. While there are no studies investigating muscarinic receptors specifically, C57BL/6 strain-specific genetic and phenotype difference have been reported and could have influenced the results (Bothe et al., 2004, Bryant et al., 2008, Mulligan et al., 2008, Bourdi et al., 2011).

While no significant differences were found in the fear conditioning experiment, several considerations are important to note. Freezing levels during context retrieval were non-significantly reduced in M_1-WT and M_1-KO compared to M_1-meGFP mice. While the cause is unclear, at the time of the experiment (November 2021) relatively low contextual responses were recorded in untreated, commercially purchased M_1-WT mice, which has since returned to more normal levels of around 60% freezing (see Appendix Figure 3). Furthermore, while studies in our laboratory (Bradley et al., 2017) have shown deficits in the hippocampus-dependent, contextual fear response (Phillips and LeDoux, 1992, Anagnostaras et al., 2001, Wiltgen et al., 2006) in M_1-KO compared to M_1-WT mice, other groups have reported an enhanced response (Anagnostaras et al., 2003). Slightly different fear conditioning paradigms were used, which could account for some of the differences described. While the characteristics of the tone in the tone-foot shock pairings were the same and the shock was given for the same amount of time, Anagnostaras et al. (2003) used a shock of 0.75 mA compared to 0.4 mA used in our laboratory (Bradley et al., 2017). Anagnostaras et al. (2003) also only used two tone-foot shock pairings and assessed the freezing response for 4 min on the following day compared to three tone-foot shock pairings for training and a 3 min assessment interval used by our laboratory (Bradley et al., 2017). The M_1-KO mice used were backcrossed for at least 5 generations (Anagnostaras et al., 2003) or at least 10 generations onto the black C57BL/6N background (Bradley et al., 2017). In this study, an inducible M_1 mAChR strain on a C57BL/6J background was used as M_1-KO mice and as discussed M_1-WT and M_1-meGFP mice had C57BL/6J and C57BL/6N backgrounds, respectively. Additionally, the hyperactive phenotype observed in M_1-KO mice could confound results (Figure 5.8). As highlighted a range of factors could have influence the fear conditioning results reported in the literature (Anagnostaras et al., 2003, Bradley et al., 2017) and in this chapter. Cued fear conditioning is thought to dependent on the auditory cortex and amygdala (LeDoux et al., 1984, Quirk et al., 1997) and no difference between M_1-KO and M_1-WT mice in the cued response was reported (Anagnostaras et al., 2003, Young and Thomas, 2014). Similar to above, C57BL/6 strain-specific differences could also have contributed to the results observed. At the time of the study, it was difficult to acquire C57BL/6N mice, however, if this study was to be continued, mice with the same substrain background should be used as well as bred and housed in the same way

to rule out an effect of these factors. At this time, some of the experiments assessing the effect of the meGFP tag on M_1 mAChR signalling and function should be repeated. Unfortunately, this was not presently possible due to time constraints.

When comparing the images obtained from the range of immunostaining and microscopy techniques used here, it appears that there is a difference in the distribution depending on the technique used. In the samples prepared using the cryostat and assessing the endogenous fluorescence of the meGFP tag, a signal can be observed in all layers of the hippocampus except for the pyramidal layer. In the preliminary data from the iDISCO -cleared and immunostained samples, however, signal seemed to be mainly distributed along the pyramidal layers of the CA1, CA2 and CA3 regions as well as in the dorsal subiculum. It is unclear why imaging the signal of the intrinsic tag or the immunostained tag would lead to such different results except for the possibility that one of the methods results in unspecific staining. Previous studies in rat tissue suggest that the M_1 mAChR is expressed widely in the hippocampus including the pyramidal layers, stratum oriens and radiatum, particularly in the CA1 region, and decreasing through the CA areas to the CA3 (Levey et al., 1995, Lebois et al., 2018). In the DG, the stratum moleculare and granulosum showed immunostaining for the M_1 mAChR (Levey et al., 1995, Lebois et al., 2018). Since the signal in the iDISCO samples also includes the pyramidal layer across the CA areas similar to results demonstrated by others (Buckley et al., 1988), this method is likely to be the more accurate and appropriate method of detection.

While an optimal combination of immunostaining and microscopy could not be achieved within this project, the results suggest that a form of the DISCO protocols combined with the Ultramicroscope II may to be the most suitable technique for receptor localisation studies on a systems level in the M_1-meGFP mouse model. Due to insufficient brain penetration of the secondary antibody, incubation times would have to be optimised and a different antibody or even a nanobody should be considered for labelling. Nanobodies generally allow for better immunostaining due to the smaller molecular weight and size and therefore, allow more rapid brain penetration and improve resolution by reducing the distance to the target protein (Ries et al., 2012, Deschout et al.,

2014, Beghein and Gettemans, 2017, Cai et al., 2019, Dong et al., 2019). A new variation of DISCO, called vDISCO, which uses nanobodies for boosting the intrinsic signal of tagged proteins, has shown much improved staining in whole brains compared to the use of conventional antibodies or using the iDISCO protocol with nanobodies (Cai et al., 2019). Therefore, vDISCO should be considered for further studies. With LSFM being used increasingly more in academic settings, it will also become more easily accessible. However, this technique not only requires the availability of the specialised microscope, but also the computational power and expertise to acquire, store and process large files. The handling of large complex data sets has previously been identified as a bottleneck for tissue clearing and some specific software packages have been developed for this (Vigouroux et al., 2017, Hörl et al., 2019).

Overall, the results in this chapter demonstrate the feasibility of using the M_1-meGFP reporter line and the proposed clearing and imaging techniques to allow detailed localisation studies of the M_1 mAChR at higher resolutions across the whole brain. This would be beneficial for diseases that have a cholinergic component, such as AD, and should therefore be pursued further.

Chapter 6 Final Discussion

AD is the most common form of dementia. However, despite decades of research, no disease-modifying treatments exist. Due to its pro-cognitive effects and potential for disease-modification, the M_1 mAChR has been proposed as a therapeutic target to address this unmet clinical need (Lebois et al., 2018, Scarpa et al., 2020). Drug candidates targeting the M_1 mAChR, such as the orthosteric ligand xanomeline, have failed to date in clinical trials partially due to their non-specific nature. However, allosteric compounds targeting the M_1 mAChR have the potential to convey subtype specific effects with a lessened side effect profile (Kruse et al., 2014, Dwomoh et al., 2022b).

In our laboratory, M_1 mAChR PAMs have shown pro-cognitive and disease-modifying effects in a murine prion model of terminal neurodegeneration (Bradley et al., 2017, Dwomoh et al., 2022a). This model shows significant correlation with human neurodegenerative disease, including human AD. These similarities include molecular changes associated with neuroinflammation, synaptic dysfunction and mitochondrial dysregulation. However, this is not an AD model, and therefore these mice do not present the classical pathological hallmarks of AD, namely Aß and tau pathology. Therefore, potential approaches to target the M_1 mAChR need to be assessed in more AD-relevant mouse models to understand whether targeting this receptor is a plausible way to influence pathology.

A recent study in the Aß-based APP_{Swe} model of AD showed improvements in Aß pathology and cognitive deficits following treatment with VU0486846 (Abd-Elrahman et al., 2022). In this thesis, a tauopathy mouse model (rTG4510) was characterised prior to assessing disease-modifying effects of the M_1 mAChR PAM VU0486846. The rTG4510 mouse model is a commonly used AD model as demonstrated by a wealth of studies, including dosing studies with tau-based immunotherapies amongst others (see 3.1.1) (Sankaranarayanan et al., 2015, Schroeder et al., 2017). Characterisation of the rTG4510 model suggested that elevated GFAP and pTau protein expression could serve as markers of neuropathology and neurodegeneration, while no abnormal behavioural phenotypes could be established at the time-points assessed (Chapter 3). In contrast to results in the prion model of terminal neurodegenerative disease or

the APP_{Swe} model (Abd-Elrahman et al., 2022, Dwomoh et al., 2022a), targeting the M_1 mAChR using the M_1 mAChR PAM VU0486846 did not affect markers of pathology, such as pTau and GFAP, in the rTG4510 model. Interestingly, however, chronic dosing with M_1 mAChR PAM VU0486846 returned the elevated levels of two proteins, namely coagulation factor III and cystatin C, to those observed in control rTG4510 mice. Both proteins have been shown to be dysregulated in brains of AD patients (McComb et al., 1991, Deng et al., 2001, Levy et al., 2001). While cystatin C is generally thought to play a protective role in AD (Mi et al., 2007), elevated levels of cystatin C and co-immunoreactivity with Aß and tau aggregates have also been observed (Wang et al., 1997, Deng et al., 2001). Studies suggested that the deposition of the protease inhibitor cystatin C might cause an imbalance between proteases and protease inhibitors in the walls of blood vessels contributing to the degeneration of micro vessels in the brain (Wang et al., 1997, Levy et al., 2001). Coagulation factor III initiates the coagulation cascade and has also been found to accumulate in Aß aggregates, but it is unclear if this contributes to pathology in AD (McComb et al., 1991). However, a possible contribution of these proteins on AD pathology has not been studied in detail. It would be interesting to assess the levels of coagulation factor III and cystatin C in tau aggregates in the dosed rTG4510 mice, for example using immunohistochemistry, to determine whether this relates to neuronal cell loss or GFAP expression levels as markers of neurodegeneration. Lastly, another observation was significant variability between rTG4510 mice of the same genotype, which will be discussed below in relation to variability observed in AD patients (Chapter 4).

The results highlight two important issues AD researchers are facing. Firstly, no comprehensive AD model recapitulating all neuropathological hallmarks and molecular changes that are observed in human patients exists, thereby hindering progress in the development of effective clinical candidates. However, until the underlying neuropathology is fully understood, more appropriate models cannot be developed. Secondly, substantial variation between rTG4510 mice could be observed despite exhibiting the same genotype and being exposed to the same environmental factors. AD, however, is a complex, multi-factorial disease, which can be caused by dominant, fully penetrant genetic mutations, but in most cases is caused by sporadic disease. Since the variation in neuropathology and

symptoms is consequently much more pronounced in patients, the identification of AD subtypes is crucial in the development of new therapeutics. This identification of AD subtypes would be invaluable in informing patient stratification in clinical trials, and in the development of models for the preclinical drug development aimed at specific patient subgroups. For example, while the spread of tau pathology was classically thought to follow one stereotypical trajectory (Braak and Braak, 1991), a recent study observed four distinct patterns (Vogel et al., 2021), suggesting that four AD subgroups could be identified based on this observation alone. Additionally, different subtypes of AD with varying levels of atrophy and cholinergic dysfunction have been identified, which may result in subtype-specific responses when treated with AChEIs (Machado et al., 2020). Additionally, the identification and stratification of cholinergic subgroups is crucial when assessing therapeutic candidates targeting the cholinergic system (Machado et al., 2020) including M_1 mAChR PAMs, which rely on endogenous stimulation.

Due to the therapeutic potential of M_1 mAChR activation in AD, another important factor to consider is the localisation of the M_1 mAChR in the brain and whether neurodegeneration causes dysregulation of M_1 mAChR distribution. To this end, an M_1-meGFP tagged mouse line was created in our laboratory. Characterisation of the model suggested that addition of the meGFP tag does not affect receptor function or signalling. Due to time constraints, the distribution and localisation in situ could not be determined and neurodegeneration-based alterations could not be explored. Nevertheless, preliminary results suggest that particularly a DISCO-based brain clearing technique in combination with light sheet microscopy, such as the Ultramicroscope II, could be used for this investigation (Chapter 5). Findings from such a study would significantly enhance knowledge of the impact of neurodegeneration on the M_1 mAChR distribution in the whole brain. This knowledge in turn could have significant impact on future drug strategies.

Since AD and some other neurodegenerative disorders are classified as proteinopathies with prion-like spread of misfolded protein aggregates (Golde and Miller, 2009, Brundin et al., 2010, Duyckaerts et al., 2019), the potential to identify pathological mechanisms common to these diseases, rather than

targeting the accumulations of disease-specific proteins, such as Aß and tau, is an important alternative strategy. For example, a recent study has suggested a role of cellular prion protein in contributing to the toxicity of Aß, α-synuclein and tau. Hence, regulating the levels of cellular prion could therefore be a therapeutic target for neurodegenerative diseases displaying these types of inclusions, such as AD and PD (Corbett et al., 2020).

The research presented in this thesis could have been improved by several changes and additions. For the characterisation and efficacy studies, the use of both male and female mice would have potentially been able to reveal sex-dependent differences in response to the drug. Additionally, pilot studies would have been useful to determine the best time-point for the start of an efficacy study with the M_1 mAChR PAM. Since the rTG4510 mouse model is a tauopathy model and changes in tau processing following M_1 mAChR activation have been reported in other models (see 1114.1.1), it would have been useful to measure GSK-3ß levels as well as use a range of tau antibodies indicative of different tau phosphorylation and NFT stages to elucidate any potential effect of VU0486846 on tau pathology. In retrospect, it would also have been interesting to use control- and patient-derived iPSCs of EOAD and LOAD cases, possibly in 3D co-culture models for example of neurons and glial cells, to assess the effect of M_1 mAChR PAM treatments on Aß and tau pathology, inflammatory processes, and endosomal and mitochondrial dysfunction (Barak et al., 2022) to complement the efficacy study in the rTG4510 mice. This could potentially have helped to unravel the effect of M_1 mAChR activation on AD pathology in different subtypes in more detail.

Building on the results from this thesis, future directions are two-fold: Firstly, based on the VU0486846 efficacy study in rTG4510, a further efficacy study should be conducted in another AD mouse model, such as the 3xTg AD model, which exhibits both tau and Aß pathology, since synergetic effects of Aß and tau pathology have been suggested to drive pathology in human AD (Miller et al., 2011, Sherman et al., 2016, Busche and Hyman, 2020). Using pilot studies to establish an optimal starting time-point for a dosing study with VU0486846 in female and male mice, an efficacy study could evaluate the effect of the M_1 mAChR PAM on markers of APP and tau processing, such as BACE1 and GSK-3ß

expression and activity, neuroinflammatory and ideally behavioural markers, as well as coagulation factor III and cystatin C, which were affected by drug administration here. GFAP levels in blood could also be measured longitudinally, as these have been found to correlate with pathology in human, and compared to histology at the end point of the study. Secondly, a DISCO-based clearing protocol in combination with light sheet imaging of whole cleared brains could be used to assess whether neurodegeneration in the form of murine prion disease affects distribution of the meGFP-M_1 mAChR informing future drug studies in neurodegeneration.

While no disease-modifying treatments currently exist, there have been significant advances in the field which increase confidence that the trajectory of AD may be altered by targeting the pathological hallmarks of AD. Recently, aducanumab was approved by the FDA (Cummings et al., 2021, Thomas et al., 2021) and promising Phase 3 results were published for lecanemab (Eisai, 2020, van Dyck et al., 2022). These two drugs are the first promising therapeutics targeting the underlying pathology of AD, namely Aß in these cases, to have been approved or with an approval expected in early 2023. These drugs have been shown to lower Aß levels and improve cognitive scores in early AD, but also lead to significant side effects in some cases (Salloway et al., 2022, van Dyck et al., 2022). Therefore, the post-approval study for aducanumab to be concluded in 2030 will determine whether the drug does indeed have disease-modifying effects (Walsh et al., 2021). Additionally, results from a small first human trial using gene therapy to express *ApoE* ε2, which is thought to have protective effects (Genin et al., 2011), in homozygous *ApoE* ε4 carriers show some promising results with *ApoE* ε2 still being expressed in the CSF at the one-year follow-up and possible small reductions in $Aß_{42}$, pTau and total tau levels in the lowest-dose group of LX1001 (Shugart, 2022, Rosenberg et al., 2018). While these results were from a very small cohort (n = 3) and cognitive function was not reported, this study could hold promise for disease-modifying interventions particularly in patients with a genetic predisposition for AD caused by *ApoE* ε4 (Coon et al., 2007, Yamazaki et al., 2019). Other modes of actions, such as targeting neuroinflammation and proteostasis, are also being tested in clinical trials (Cummings et al., 2022) and it remains to be seen, whether these could lead to disease-modifying effects on their own or as complementary strategies.

In this thesis, novel changes in coagulation factor III and cystatin C were identified in the rTG4510 mouse model, which were responsive to treatment with a M_1 mAChR PAM. These changes could contribute to a disease-modifying effect of M_1 mAChR activation, however, more research is needed. Additionally, this thesis explored a novel way of visualising receptor distribution in cleared, whole brains with the goal of analysing changes in response to neurodegeneration. Overall, a multitude of promising approaches, not just targeting the pathological hallmarks of AD, but also other mechanisms such as inflammation, are currently in different stages of clinical testing and post-approval studies, providing hope for disease-modifying treatments for AD patients and their carers.

Appendices

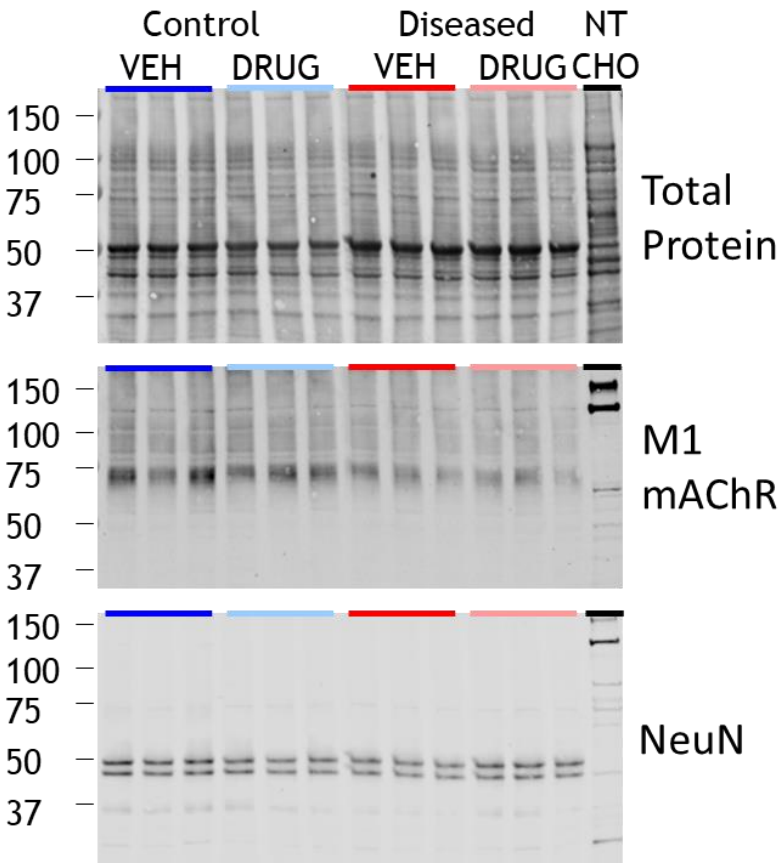

Appendix Figure 1 Antibodies for M_1 mAChR and NeuN resulted in specific staining in immunoblotting. Representative immunoblots for and vehicle- and VU0486846-treated control (dark blue and light blue) and diseased (red and pink) rTG4510 mice and a control lysate from non-transfected (NT) Chinese hamster ovary (CHO) cells (black) are shown. The first blot shows observations from the REVERT Total Protein Stain, and the second and third immunoblots show staining with a M_1 mAChR and NeuN antibody, respectively.

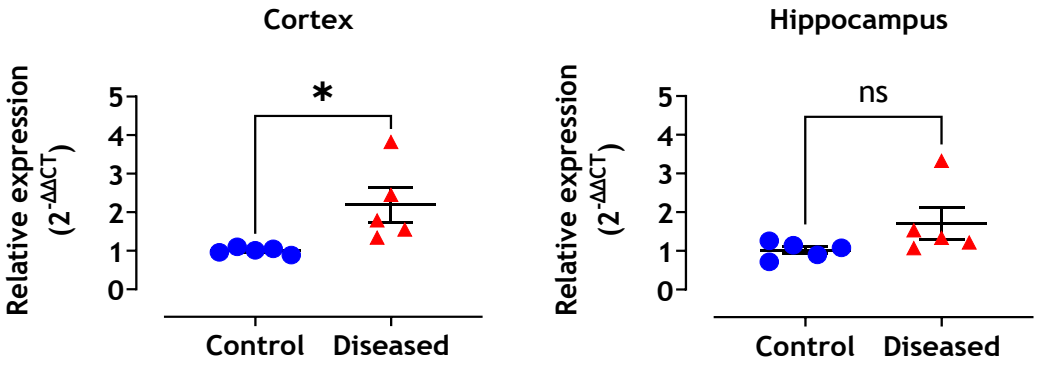

Appendix Figure 2 Gene expression levels of ApoE in control and diseased rTG4510 mice at 8.0 months of age. RT-qPCR analysis of Apolipoprotein E (ApoE) levels was performed in cortical and hippocampal samples collected from control and diseased rTG4510 mice following telemetry experiments at 8.0 months of age. To assess relative expression levels, data was analysed using the ΔΔCT method, normalising first to α-tubulin and then the mean of the control values for ApoE. Data are shown as means ± SEM and data points represent individual mice. Statistical analysis was performed using unpaired t-tests, * $p < 0.05$.

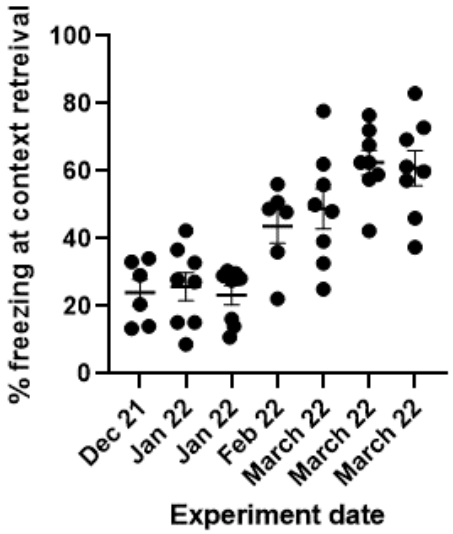

Appendix Figure 3 Freezing responses of commercially purchased M_1-WT C57BL/6J during context retrieval from December 2021 to March 2022. Data was provided by A McFall. N = 6-8 mice per time-point.

List of References

ABD-ELRAHMAN, K. S., SARASIJA, S., COLSON, T.-L. L. & FERGUSON, S. S. G. 2022. A positive allosteric modulator for the muscarinic receptor (M1 mAChR) improves pathology and cognitive deficits in female APPswe/PSEN1ΔE9 mice. *British Journal of Pharmacology,* 179**,** 1769-1783.

ABE, T. & FUJIMORI, T. 2013. Reporter Mouse Lines for Fluorescence Imaging. *Development, Growth & Differentiation,* 55**,** 390-405.

ADLER, E., HOON, M. A., MUELLER, K. L., CHANDRASHEKAR, J., RYBA, N. J. & ZUKER, C. S. 2000. A novel family of mammalian taste receptors. *Cell,* 100**,** 693-702.

AGCA, C., KLAKOTSKAIA, D., SCHACHTMAN, T. R., CHAN, A. W., LAH, J. J. & AGCA, Y. 2016. Presenilin 1 transgene addition to amyloid precursor protein overexpressing transgenic rats increases amyloid beta 42 levels and results in loss of memory retention. *BMC Neurosci,* 17**,** 46.

ALFONSO-PRIETO, M., GIORGETTI, A. & CARLONI, P. 2019. Multiscale simulations on human Frizzled and Taste2 GPCRs. *Current Opinion in Structural Biology,* 55**,** 8-16.

ALONSO, J. R., U, H. S. & AMARAL, D. G. 1996. Cholinergic innervation of the primate hippocampal formation: II. Effects of fimbria/fornix transection. *Journal of Comparative Neurology,* 375**,** 527-551.

ALZFORUM. 2022. *Research Models* [Online]. Alzforum. Available: https://www.alzforum.org/research-models/search?species%5B%5D=319&diseases%5B%5D=145&genes=&types=&keywords-entry=&keywords=#results [Accessed May 5, 2022 2022].

ALZHEIMER, A. 1907. Über eine eigenartige Erkrankung der Hirnrinde. *Zentralbl. Nervenh. Psych.,* 18**,** 177-179.

ANAGNOSTARAS, S. G., GALE, G. D. & FANSELOW, M. S. 2001. Hippocampus and contextual fear conditioning: recent controversies and advances. *Hippocampus,* 11**,** 8-17.

ANAGNOSTARAS, S. G., MURPHY, G. G., HAMILTON, S. E., MITCHELL, S. L., RAHNAMA, N. P., NATHANSON, N. M. & SILVA, A. J. 2003. Selective cognitive dysfunction in acetylcholine M1 muscarinic receptor mutant mice. *Nature neuroscience,* 6**,** 51-58.

ANAND, R., GILL, K. D. & MAHDI, A. A. 2014. Therapeutics of Alzheimer's disease: Past, present and future. *Neuropharmacology,* 76**,** 27-50.

ANDERSON, L. & SEILHAMER, J. 1997. A comparison of selected mRNA and protein abundances in human liver. *ELECTROPHORESIS,* 18**,** 533-537.

ANISUZZAMAN, A. S. M., UWADA, J., MASUOKA, T., YOSHIKI, H., NISHIO, M., IKEGAYA, Y., TAKAHASHI, N., MATSUKI, N., FUJIBAYASHI, Y., YONEKURA, Y., MOMIYAMA, T. & MURAMATSU, I. 2013. Novel contribution of cell surface and intracellular M1-muscarinic acetylcholine receptors to synaptic plasticity in hippocampus. *Journal of Neurochemistry,* 126**,** 360-371.

ARAÇ, D., BOUCARD, A. A., BOLLIGER, M. F., NGUYEN, J., SOLTIS, S. M., SÜDHOF, T. C. & BRUNGER, A. T. 2012. A novel evolutionarily conserved domain of cell‐adhesion GPCRs mediates autoproteolysis. *The EMBO journal,* 31**,** 1364-1378.

ARAUJO, J. A., NOBREGA, J. N., RAYMOND, R. & MILGRAM, N. W. 2011. Aged dogs demonstrate both increased sensitivity to scopolamine impairment and decreased

muscarinic receptor density. *Pharmacology Biochemistry and Behavior,* 98**,** 203-209.

ARDILES, Á. O., TAPIA-ROJAS, C. C., MANDAL, M., ALEXANDRE, F., KIRKWOOD, A., INESTROSA, N. C. & PALACIOS, A. G. 2012. Postsynaptic dysfunction is associated with spatial and object recognition memory loss in a natural model of Alzheimer's disease. *Proceedings of the National Academy of Sciences,* 109**,** 13835-13840.

AREA-GOMEZ, E. & SCHON, E. A. 2017. On the pathogenesis of Alzheimer's disease: the MAM hypothesis. *The FASEB Journal,* 31**,** 864-867.

ARMSTRONG, R. A. 2009. The molecular biology of senile plaques and neurofibrillary tangles in Alzheimer's disease. *Folia Neuropathologica,* 47**,** 289-299.

ARRAJ, M. & LEMMER, B. 2006. Circadian rhythms in heart rate, motility, and body temperature of wild‐type C57 and eNOS knock‐out mice under light‐dark, free‐run, and after time zone transition. *Chronobiology international,* 23**,** 795-812.

ATTWOOD, T. & FINDLAY, J. 1994. Fingerprinting G-protein-coupled receptors. *Protein Engineering, Design and Selection,* 7**,** 195-203.

AUGUSTINACK, J. C., SCHNEIDER, A., MANDELKOW, E.-M. & HYMAN, B. T. 2002. Specific tau phosphorylation sites correlate with severity of neuronal cytopathology in Alzheimer's disease. *Acta Neuropathologica,* 103**,** 26-35.

BAINS, R. S., WELLS, S., SILLITO, R. R., ARMSTRONG, J. D., CATER, H. L., BANKS, G. & NOLAN, P. M. 2018. Assessing mouse behaviour throughout the light/dark cycle using automated in-cage analysis tools. *Journal of Neuroscience Methods,* 300**,** 37-47.

BALDWIN, J. M. 1994. Structure and function of receptors coupled to G proteins. *Current Opinion in Cell Biology,* 6**,** 180-190.

BALLESTEROS, J. A. & WEINSTEIN, H. 1995. Integrated methods for the construction of three-dimensional models and computational probing of structure-function relations in G protein-coupled receptors. *Methods in neurosciences.* Elsevier.

BARAK, M., FEDOROVA, V., POSPISILOVA, V., RASKA, J., VOCHYANOVA, S., SEDMIK, J., HRIBKOVA, H., KLIMOVA, H., VANOVA, T. & BOHACIAKOVA, D. 2022. Human iPSC-Derived Neural Models for Studying Alzheimer's Disease: from Neural Stem Cells to Cerebral Organoids. *Stem Cell Reviews and Reports,* 18**,** 792-820.

BARKER, W. W., LUIS, C. A., KASHUBA, A., LUIS, M., HARWOOD, D. G., LOEWENSTEIN, D., WATERS, C., JIMISON, P., SHEPHERD, E. & SEVUSH, S. 2002. Relative frequencies of Alzheimer disease, Lewy body, vascular and frontotemporal dementia, and hippocampal sclerosis in the State of Florida Brain Bank. *Alzheimer Disease & Associated Disorders,* 16**,** 203-212.

BARTLETT, S. E., ENQUIST, J., HOPF, F. W., LEE, J. H., GLADHER, F., KHARAZIA, V., WALDHOER, M., MAILLIARD, W. S., ARMSTRONG, R. & BONCI, A. 2005. Dopamine responsiveness is regulated by targeted sorting of D2 receptors. *Proceedings of the National Academy of Sciences,* 102**,** 11521-11526.

BARTOLOMEO, A. C., MORRIS, H., BUCCAFUSCO, J. J., KILLE, N., ROSENZWEIG-LIPSON, S., HUSBANDS, M. G., SABB, A. L., ABOU-GHARBIA, M., MOYER, J. A. & BOAST, C. A. 2000. The Preclinical Pharmacological Profile of WAY-132983, a Potent M1 Preferring Agonist. *Journal of Pharmacology and Experimental Therapeutics,* 292**,** 584.

BARTUS, R. T., DEAN III, R. L., BEER, B. & LIPPA, A. S. 1982. The cholinergic hypothesis of geriatric memory dysfunction. *Science,* 217**,** 408-414.

BATEMAN, R. J., AISEN, P. S., DE STROOPER, B., FOX, N. C., LEMERE, C. A., RINGMAN, J. M., SALLOWAY, S., SPERLING, R. A., WINDISCH, M. & XIONG, C. 2011. Autosomal-dominant Alzheimer's disease: a review and proposal for the prevention of Alzheimer's disease. *Alzheimer's Research & Therapy,* 3**,** 1.

BEACH, T. G., WALKER, D. G., POTTER, P. E., SUE, L. I. & FISHER, A. 2001. Reduction of cerebrospinal fluid amyloid β after systemic administration of M1 muscarinic agonists. *Brain research,* 905**,** 220-223.

BECKER, K., JÄHRLING, N., SAGHAFI, S., WEILER, R. & DODT, H.-U. 2012. Chemical Clearing and Dehydration of GFP Expressing Mouse Brains. *PLOS ONE,* 7**,** e33916.

BEGHEIN, E. & GETTEMANS, J. 2017. Nanobody technology: a versatile toolkit for microscopic imaging, protein–protein interaction analysis, and protein function exploration. *Frontiers in immunology,* 8**,** 771.

BELLE, M., GODEFROY, D., COULY, G., MALONE, S. A., COLLIER, F., GIACOBINI, P. & CHÉDOTAL, A. 2017. Tridimensional visualization and analysis of early human development. *Cell,* 169**,** 161-173. e12.

BENFATO, I. D., QUINTANILHA, A. C. S., HENRIQUE, J. S., SOUZA, M. A., ROSÁRIO, B. D. A., BESERRA FILHO, J. I. A., SANTOS, R. L. O., RIBEIRO, A. M., LE SUEUR MALUF, L. & DE OLIVEIRA, C. A. M. 2022. Effects of long-term social isolation on central, behavioural and metabolic parameters in middle-aged mice. *Behavioural Brain Research,* 417**,** 113630.

BENNETT, D. A., SCHNEIDER, J. A., WILSON, R. S., BIENIAS, J. L. & ARNOLD, S. E. 2004. Neurofibrillary tangles mediate the association of amyloid load with clinical Alzheimer disease and level of cognitive function. *Archives of neurology,* 61**,** 378-384.

BENNETT, R. E., BRYANT, A., HU, M., ROBBINS, A. B., HOPP, S. C. & HYMAN, B. T. 2018. Partial reduction of microglia does not affect tau pathology in aged mice. *Journal of Neuroinflammation,* 15**,** 311.

BENOVIC, J., KÜHN, H., WEYAND, I., CODINA, J., CARON, M. & LEFKOWITZ, R. 1987. Functional desensitization of the isolated beta-adrenergic receptor by the beta-adrenergic receptor kinase: potential role of an analog of the retinal protein arrestin (48-kDa protein). *Proceedings of the National Academy of Sciences,* 84**,** 8879-8882.

BENOVIC, J. L., STRASSER, R. H., CARON, M. G. & LEFKOWITZ, R. J. 1986. Beta-adrenergic receptor kinase: identification of a novel protein kinase that phosphorylates the agonist-occupied form of the receptor. *Proceedings of the National Academy of Sciences,* 83**,** 2797-2801.

BERNARDINI, N., ROZA, C., SAUER, S. K., GOMEZA, J., WESS, J. & REEH, P. W. 2002. Muscarinic M2 receptors on peripheral nerve endings: a molecular target of antinociception. *Journal of Neuroscience,* 22**,** RC229-RC229.

BERSTEIN, G., BLANK, J. L., JHON, D.-Y., EXTON, J. H., RHEE, S. G. & ROSS, E. M. 1992. Phospholipase C-β1 is a GTPase-activating protein for Gq/11, its physiologic regulator. *Cell,* 70**,** 411-418.

BERTRON, J. L., CHO, H. P., GARCIA-BARRANTES, P. M., PANARESE, J. D., SALOVICH, J. M., NANCE, K. D., ENGERS, D. W., ROOK, J. M., BLOBAUM, A. L. & NISWENDER, C. M. 2018. The discovery of VU0486846: steep SAR from a series of M1 PAMs based on a novel benzomorpholine core. *Bioorganic & medicinal chemistry letters,* 28**,** 2175-2179.

BEYER, L., STOCKER, H., RUJESCU, D., HOLLECZEK, B., STOCKMANN, J., NABERS, A., BRENNER, H. & GERWERT, K. 2022. Amyloid-beta misfolding and GFAP predict risk of clinical Alzheimer's disease diagnosis within 17 years. *Alzheimer's & Dementia,* n/a.

BHANOT, P., BRINK, M., SAMOS, C. H., HSIEH, J.-C., WANG, Y., MACKE, J. P., ANDREW, D., NATHANS, J. & NUSSE, R. 1996. A new member of the frizzled family from Drosophila functions as a Wingless receptor. *Nature,* 382**,** 225-230.

BIASTRE, K. & BURNAKIS, T. 2009. Trospium chloride treatment of overactive bladder. *Ann Pharmacother,* 43**,** 283-95.

BIRDSALL, N. & LAZARENO, S. 2005. Allosterism at muscarinic receptors: ligands and mechanisms. *Mini reviews in medicinal chemistry,* 5**,** 523-543.

BJARNADÓTTIR, T. K., FREDRIKSSON, R., HÖGLUND, P. J., GLORIAM, D. E., LAGERSTRÖM, M. C. & SCHIÖTH, H. B. 2004. The human and mouse repertoire of the adhesion family of G-protein-coupled receptors. *Genomics,* 84**,** 23-33.

BLACKMORE, T., MEFTAH, S., MURRAY, T. K., CRAIG, P. J., BLOCKEEL, A., PHILLIPS, K., EASTWOOD, B., O'NEILL, M. J., MARSTON, H., AHMED, Z., GILMOUR, G. & GASTAMBIDE, F. 2017. Tracking progressive pathological and functional decline in the rTg4510 mouse model of tauopathy. *Alzheimer's Research & Therapy,* 9**,** 77.

BLANCHARD, J. W., VICTOR, M. B. & TSAI, L.-H. 2022. Dissecting the complexities of Alzheimer disease with in vitro models of the human brain. *Nature Reviews Neurology,* 18**,** 25-39.

BOCKAERT, J. & PIN, J. P. 1999. Molecular tinkering of G protein‐coupled receptors: an evolutionary success. *The EMBO journal,* 18**,** 1723-1729.

BODICK, N., OFFEN, W., SHANNON, H., SATTERWHITE, J., LUCAS, R., VAN LIER, R. & PAUL, S. 1997a. The selective muscarinic agonist xanomeline improves both the cognitive deficits and behavioral symptoms of Alzheimer disease. *Alzheimer disease and associated disorders*.

BODICK, N. C., OFFEN, W. W., LEVEY, A. I., CUTLER, N. R., GAUTHIER, S. G., SATLIN, A., SHANNON, H. E., TOLLEFSON, G. D., RASMUSSEN, K. & BYMASTER, F. P. 1997b. Effects of xanomeline, a selective muscarinic receptor agonist, on cognitive function and behavioral symptoms in Alzheimer disease. *Archives of neurology,* 54**,** 465-473.

BOMBERGER, J. M., SPIELMAN, W. S., HALL, C. S., WEINMAN, E. J. & PARAMESWARAN, N. 2005. Receptor activity-modifying protein (RAMP) isoform-specific regulation of adrenomedullin receptor trafficking by NHERF-1. *Journal of Biological Chemistry,* 280**,** 23926-23935.

BONNER, T., BUCKLEY, N., YOUNG, A. & BRANN, M. 1987. Identification of a family of muscarinic acetylcholine receptor genes. *Science,* 237**,** 527-532.

BORSON, S. & RASKIND, M. A. 1997. Clinical features and pharmacologic treatment of behavioral symptoms of Alzheimer's disease. *Neurology,* 48**,** 17S.

BOTHE, G. W. M., BOLIVAR, V. J., VEDDER, M. J. & GEISTFELD, J. G. 2004. Genetic and behavioral differences among five inbred mouse strains commonly used in the production of transgenic and knockout mice. *Genes, Brain and Behavior,* 3**,** 149-157.

BOUABE, H. & OKKENHAUG, K. 2013. Gene Targeting in Mice: A Review. *In:* BAILER, S. M. & LIEBER, D. (eds.) *Virus-Host Interactions: Methods and Protocols.* Totowa, NJ: Humana Press.

BOURDI, M., DAVIES, J. S. & POHL, L. R. 2011. Mispairing C57BL/6 Substrains of Genetically Engineered Mice and Wild-Type Controls Can Lead to Confounding Results as It Did in Studies of JNK2 in Acetaminophen and Concanavalin A Liver Injury. *Chemical Research in Toxicology,* 24**,** 794-796.

BOURGOGNON, J.-M., SPIERS, J. G., ROBINSON, S. W., SCHEIBLICH, H., GLYNN, P., ORTORI, C., BRADLEY, S. J., TOBIN, A. B. & STEINERT, J. R. 2021. Inhibition of neuroinflammatory nitric oxide signaling suppresses glycation and prevents

neuronal dysfunction in mouse prion disease. *Proceedings of the National Academy of Sciences,* 118**,** e2009579118.

BOUSCHET, T., MARTIN, S. & HENLEY, J. M. 2005. Receptor-activity-modifying proteins are required for forward trafficking of the calcium-sensing receptor to the plasma membrane. *Journal of cell science,* 118**,** 4709-4720.

BOWEN, D. M., SMITH, C. B., WHITE, P. & DAVISON, A. N. 1976. Neurotransmitter-related enzymes and indices of hypoxia in senile dementia and other abiotrophies. *Brain: a journal of neurology,* 99**,** 459-496.

BRAAK, H. & BRAAK, E. 1991. Neuropathological stageing of Alzheimer-related changes. *Acta neuropathologica,* 82**,** 239-259.

BRAAK, H., BRAAK, E. & STROTHJOHANN, M. 1994. Abnormally phosphorylated tau protein related to the formation of neurofibrillary tangles and neuropil threads in the cerebral cortex of sheep and goat. *Neuroscience letters,* 171**,** 1-4.

BRADLEY, S. J., BOURGOGNON, J. M., SANGER, H. E., VERITY, N., MOGG, A. J., WHITE, D. J., BUTCHER, A. J., MORENO, J. A., MOLLOY, C., MACEDO-HATCH, T., EDWARDS, J. M., WESS, J., PAWLAK, R., READ, D. J., SEXTON, P. M., BROAD, L. M., STEINERT, J. R., MALLUCCI, G. R., CHRISTOPOULOS, A., FELDER, C. C. & TOBIN, A. B. 2017. M1 muscarinic allosteric modulators slow prion neurodegeneration and restore memory loss. *J Clin Invest,* 127**,** 487-499.

BRADLEY, S. J., MOLLOY, C., BUNDGAARD, C., MOGG, A. J., THOMPSON, K. J., DWOMOH, L., SANGER, H. E., CRABTREE, M., BROOKE, S. M., SEXTON, P. M., FELDER, C. C., CHRISTOPOULOS, A., BROAD, L. M., TOBIN, A. B. & LANGMEAD, C. J. 2018. Bitopic binding mode of an M1 muscarinic acetylcholine receptor agonist associated with adverse clinical trial outcomes. *Mol Pharmacol*.

BRADLEY, S. J., MOLLOY, C., VALUSKOVA, P., DWOMOH, L., SCARPA, M., ROSSI, M., FINLAYSON, L., SVENSSON, K. A., CHERNET, E., BARTH, V. N., GHERBI, K., SYKES, D. A., WILSON, C. A., MISTRY, R., SEXTON, P. M., CHRISTOPOULOS, A., MOGG, A. J., ROSETHORNE, E. M., SAKATA, S., JOHN CHALLISS, R. A., BROAD, L. M. & TOBIN, A. B. 2020. Biased M1-muscarinic-receptor-mutant mice inform the design of next-generation drugs. *Nature Chemical Biology,* 16**,** 240-249.

BRADLEY, S. R., LAMEH, J., OHRMUND, L., SON, T., BAJPAI, A., NGUYEN, D., FRIBERG, M., BURSTEIN, E. S., SPALDING, T. A., OTT, T. R., SCHIFFER, H. H., TABATABAEI, A., MCFARLAND, K., DAVIS, R. E. & BONHAUS, D. W. 2010. AC-260584, an orally bioavailable M(1) muscarinic receptor allosteric agonist, improves cognitive performance in an animal model. *Neuropharmacology,* 58**,** 365-73.

BRANDT, R., LÉGER, J. & LEE, G. 1995. Interaction of tau with the neural plasma membrane mediated by tau's amino-terminal projection domain. *The Journal of cell biology,* 131**,** 1327-1340.

BRANNAN, S., MILLER, A., PAUL, S. & BREIER, A. KarXT, a combination of the M1/M4 cholinergic receptor agonist xanomeline and trospium for the treatment of psychosis and cognitive impairment in schizophrenia: phase I studies. NEUROPSYCHOPHARMACOLOGY, 2018. NATURE PUBLISHING GROUP MACMILLAN BUILDING, 4 CRINAN ST, LONDON N1 9XW, ENGLAND, S174-S175.

BRANNAN, S. K., SAWCHAK, S., MILLER, A. C., LIEBERMAN, J. A., PAUL, S. M. & BREIER, A. 2021. Muscarinic cholinergic receptor agonist and peripheral antagonist for schizophrenia. *New England Journal of Medicine,* 384**,** 717-726.

BRIER, M. R., GORDON, B., FRIEDRICHSEN, K., MCCARTHY, J., STERN, A., CHRISTENSEN, J., OWEN, C., ALDEA, P., SU, Y., HASSENSTAB, J., CAIRNS NIGEL, J., HOLTZMAN DAVID, M., FAGAN ANNE, M., MORRIS JOHN, C.,

BENZINGER TAMMIE, L. S. & ANCES BEAU, M. 2016. Tau and Aβ imaging, CSF measures, and cognition in Alzheimer's disease. *Science Translational Medicine,* 8**,** 338ra66-338ra66.

BROWN, A. J. H., BRADLEY, S. J., MARSHALL, F. H., BROWN, G. A., BENNETT, K. A., BROWN, J., CANSFIELD, J. E., CROSS, D. M., DE GRAAF, C., HUDSON, B. D., DWOMOH, L., DIAS, J. M., ERREY, J. C., HURRELL, E., LIPTROT, J., MATTEDI, G., MOLLOY, C., NATHAN, P. J., OKRASA, K., OSBORNE, G., PATEL, J. C., PICKWORTH, M., ROBERTSON, N., SHAHABI, S., BUNDGAARD, C., PHILLIPS, K., BROAD, L. M., GOONAWARDENA, A. V., MORAIRTY, S. R., BROWNING, M., PERINI, F., DAWSON, G. R., DEAKIN, J. F. W., SMITH, R. T., SEXTON, P. M., WARNECK, J., VINSON, M., TASKER, T., TEHAN, B. G., TEOBALD, B., CHRISTOPOULOS, A., LANGMEAD, C. J., JAZAYERI, A., COOKE, R. M., RUCKTOOA, P., CONGREVE, M. S., WEIR, M. & TOBIN, A. B. 2021. From structure to clinic: Design of a muscarinic M1 receptor agonist with the potential to treat Alzheimer's disease. *Cell,* 184**,** 5886-5901.e22.

BROWNLOW, M. L., BENNER, L., D'AGOSTINO, D., GORDON, M. N. & MORGAN, D. 2013. Ketogenic Diet Improves Motor Performance but Not Cognition in Two Mouse Models of Alzheimer's Pathology. *PLOS ONE,* 8**,** e75713.

BRUNDIN, P., MELKI, R. & KOPITO, R. 2010. Prion-like transmission of protein aggregates in neurodegenerative diseases. *Nature reviews. Molecular cell biology,* 11**,** 301-307.

BRYANT, C. D., ZHANG, N. N., SOKOLOFF, G., FANSELOW, M. S., ENNES, H. S., PALMER, A. A. & MCROBERTS, J. A. 2008. Behavioral differences among C57BL/6 substrains: implications for transgenic and knockout studies. *Journal of neurogenetics,* 22**,** 315-331.

BUCCITELLI, C. & SELBACH, M. 2020. mRNAs, proteins and the emerging principles of gene expression control. *Nature Reviews Genetics,* 21**,** 630-644.

BUCHANAN, K. A., PETROVIC, M. M., CHAMBERLAIN, S. E., MARRION, N. V. & MELLOR, J. R. 2010. Facilitation of long-term potentiation by muscarinic M(1) receptors is mediated by inhibition of SK channels. *Neuron,* 68**,** 948-63.

BUCKLEY, N. J., BONNER, T. & BRANN, M. 1988. Localization of a family of muscarinic receptor mRNAs in rat brain. *Journal of Neuroscience,* 8**,** 4646-4652.

BÜNEMANN, M. & HOSEY, M. M. 1998. Regulators of G protein signaling (RGS) proteins constitutively activate Gβγ-gated potassium channels. *Journal of Biological Chemistry,* 273**,** 31186-31190.

BURFORD, N. T., WATSON, J., BERTEKAP, R. & ALT, A. 2011. Strategies for the identification of allosteric modulators of G-protein-coupled receptors. *Biochemical Pharmacology,* 81**,** 691-702.

BURNS, T. C., LI, M. D., MEHTA, S., AWAD, A. J. & MORGAN, A. A. 2015. Mouse models rarely mimic the transcriptome of human neurodegenerative diseases: A systematic bioinformatics-based critique of preclinical models. *European Journal of Pharmacology,* 759**,** 101-117.

BUSCHE, M. A. & HYMAN, B. T. 2020. Synergy between amyloid-β and tau in Alzheimer's disease. *Nature Neuroscience,* 23**,** 1183-1193.

BUXBAUM, J. D., KOO, E. H. & GREENGARD, P. 1993. Protein phosphorylation inhibits production of Alzheimer amyloid beta/A4 peptide. *Proceedings of the National Academy of Sciences,* 90**,** 9195-9198.

BUXBAUM, J. D., OISHI, M., CHEN, H. I., PINKAS-KRAMARSKI, R., JAFFE, E. A., GANDY, S. E. & GREENGARD, P. 1992. Cholinergic agonists and interleukin 1 regulate processing and secretion of the Alzheimer beta/A4 amyloid protein precursor. *Proceedings of the National Academy of Sciences,* 89**,** 10075-10078.

BYMASTER, F. P., CARTER, P. A., YAMADA, M., GOMEZA, J., WESS, J., HAMILTON, S. E., NATHANSON, N. M., MCKINZIE, D. L. & FELDER, C. C. 2003a. Role of specific muscarinic receptor subtypes in cholinergic parasympathomimetic responses, in vivo phosphoinositide hydrolysis, and pilocarpine‐induced seizure activity. *European journal of neuroscience,* 17**,** 1403-1410.

BYMASTER, F. P., MCKINZIE, D. L., FELDER, C. C. & WESS, J. 2003b. Use of M1–M5 Muscarinic Receptor Knockout Mice as Novel Tools to Delineate the Physiological Roles of the Muscarinic Cholinergic System. *Neurochemical Research,* 28**,** 437-442.

CABRERA-VERA, T. M., VANHAUWE, J., THOMAS, T. O., MEDKOVA, M., PREININGER, A., MAZZONI, M. R. & HAMM, H. E. 2003. Insights into G protein structure, function, and regulation. *Endocr Rev,* 24**,** 765-81.

CACCAMO, A., FISHER, A. & LAFERLA, F. M. 2009. M1 agonists as a potential disease-modifying therapy for Alzheimer's disease. *Current Alzheimer Research,* 6**,** 112-117.

CACCAMO, A., ODDO, S., BILLINGS, L. M., GREEN, K. N., MARTINEZ-CORIA, H., FISHER, A. & LAFERLA, F. M. 2006. M1 receptors play a central role in modulating AD-like pathology in transgenic mice. *Neuron,* 49**,** 671-682.

CAI, H., WANG, Y., MCCARTHY, D., WEN, H., BORCHELT, D. R., PRICE, D. L. & WONG, P. C. 2001. BACE1 is the major β-secretase for generation of Aβ peptides by neurons. *Nature Neuroscience,* 4**,** 233-234.

CAI, R., PAN, C., GHASEMIGHARAGOZ, A., TODOROV, M. I., FÖRSTERA, B., ZHAO, S., BHATIA, H. S., PARRA-DAMAS, A., MROWKA, L. & THEODOROU, D. 2019. Panoptic imaging of transparent mice reveals whole-body neuronal projections and skull–meninges connections. *Nature neuroscience,* 22**,** 317-327.

CANALS, M., LANE, J. R., WEN, A., SCAMMELLS, P. J., SEXTON, P. M. & CHRISTOPOULOS, A. 2012. A Monod-Wyman-Changeux mechanism can explain G protein-coupled receptor (GPCR) allosteric modulation. *Journal of Biological Chemistry,* 287**,** 650-659.

CANET-AVILES, R.-M., ANDERTON, M., HOOPER, N. M., TURNER, A. J. & VAUGHAN, P. F. 2002. Muscarine enhances soluble amyloid precursor protein secretion in human neuroblastoma SH-SY5Y by a pathway dependent on protein kinase Cα, src-tyrosine kinase and extracellular signal-regulated kinase but not phospholipase C. *Molecular brain research,* 102**,** 62-72.

CAOUETTE, D., XIE, Z., MILICI, A., KUHN, M., BOCAN, T. & YANG, D. 2013. Perinatal suppression of Tau P301L has a long lasting preventive effect against neurodegeneration. *International Journal of Neuropathology,* 1**,** 53-69.

CARMONA-ROSAS, G., ALCÁNTARA-HERNÁNDEZ, R. & HERNÁNDEZ-ESPINOSA, D. A. 2019. Chapter 12 - The role of β-arrestins in G protein-coupled receptor heterologous desensitization: A brief story. *In:* SHUKLA, A. K. (ed.) *Methods in Cell Biology.* Academic Press.

CASTELLANO, J. M., KIM, J., STEWART, F. R., JIANG, H., DEMATTOS, R. B., PATTERSON, B. W., FAGAN, A. M., MORRIS, J. C., MAWUENYEGA, K. G. & CRUCHAGA, C. 2011. Human apoE isoforms differentially regulate brain amyloid-β peptide clearance. *Science translational medicine,* 3**,** 89ra57-89ra57.

CAULFIELD, M. P. & BIRDSALL, N. J. M. 1998. International Union of Pharmacology. XVII. Classification of Muscarinic Acetylcholine Receptors. *Pharmacological Reviews,* 50**,** 279-290.

CECCARELLI, B. & HURLBUT, W. 1980. Vesicle hypothesis of the release of quanta of acetylcholine. *Physiological Reviews,* 60**,** 396-441.

CHALFIE, M., TU, Y., EUSKIRCHEN, G., WARD WILLIAM, W. & PRASHER DOUGLAS, C. 1994. Green Fluorescent Protein as a Marker for Gene Expression. *Science,* 263**,** 802-805.

CHAMBERS, N. E., MEADOWS, S. M., TAYLOR, A., SHEENA, E., LANZA, K., CONTI, M. M. & BISHOP, C. 2019. Effects of Muscarinic Acetylcholine m1 and m4 Receptor Blockade on Dyskinesia in the Hemi-Parkinsonian Rat. *Neuroscience,* 409**,** 180-194.

CHAN, W., MCKINZIE, D., BOSE, S., MITCHELL, S., WITKIN, J., THOMPSON, R., CHRISTOPOULOS, A., LAZARENO, S., BIRDSALL, N. & BYMASTER, F. 2008. Allosteric modulation of the muscarinic M4 receptor as an approach to treating schizophrenia. *Proceedings of the National Academy of Sciences,* 105**,** 10978-10983.

CHEN, Y. & STRUHL, G. 1996. Dual Roles for Patched in Sequestering and Transducing Hedgehog. *Cell,* 87**,** 553-563.

CHEREZOV, V., ROSENBAUM, D. M., HANSON, M. A., RASMUSSEN, S. G., THIAN, F. S., KOBILKA, T. S., CHOI, H.-J., KUHN, P., WEIS, W. I. & KOBILKA, B. K. 2007. High-resolution crystal structure of an engineered human β2-adrenergic G protein–coupled receptor. *science,* 318**,** 1258-1265.

CHIARINI, A., ARMATO, U., GARDENAL, E., GUI, L. & DAL PRÀ, I. 2017. Amyloid β-exposed human astrocytes overproduce phospho-tau and overrelease it within exosomes, effects suppressed by calcilytic NPS 2143—further implications for Alzheimer's therapy. *Frontiers in neuroscience,* 11**,** 217.

CHRISTOPOULOS, A. 2000. Quantification of allosteric interactions at G protein coupled receptors using radioligand binding assays. *Current Protocols in Pharmacology,* 11**,** 1.22. 1-1.22. 40.

CHRISTOPOULOS, A. 2002. Allosteric binding sites on cell-surface receptors: novel targets for drug discovery. *Nat Rev Drug Discov,* 1**,** 198-210.

CHRISTOPOULOS, A., CHANGEUX, J.-P., CATTERALL, W. A., FABBRO, D., BURRIS, T. P., CIDLOWSKI, J. A., OLSEN, R. W., PETERS, J. A., NEUBIG, R. R. & PIN, J.-P. 2014. International Union of Basic and Clinical Pharmacology. XC. multisite pharmacology: recommendations for the nomenclature of receptor allosterism and allosteric ligands. *Pharmacological reviews,* 66**,** 918-947.

CHROMIŃSKI, K. & TKACZ, M. 2010. Comparison of outlier detection methods in biomedical data. *Journal of Medical Informatics & Technologies,* 16**,** 89--94.

CHUN, H., MARRIOTT, I., LEE, C. J. & CHO, H. 2018. Elucidating the Interactive Roles of Glia in Alzheimer's Disease Using Established and Newly Developed Experimental Models. *Frontiers in Neurology,* 9.

CHUNG, K., WALLACE, J., KIM, S.-Y., KALYANASUNDARAM, S., ANDALMAN, A. S., DAVIDSON, T. J., MIRZABEKOV, J. J., ZALOCUSKY, K. A., MATTIS, J. & DENISIN, A. K. 2013. Structural and molecular interrogation of intact biological systems. *Nature,* 497**,** 332-337.

CICOGNOLA, C., JANELIDZE, S., HERTZE, J., ZETTERBERG, H., BLENNOW, K., MATTSSON-CARLGREN, N. & HANSSON, O. 2021. Plasma glial fibrillary acidic protein detects Alzheimer pathology and predicts future conversion to Alzheimer dementia in patients with mild cognitive impairment. *Alzheimer's Research & Therapy,* 13**,** 68.

CLAVAGUERA, F., BOLMONT, T., CROWTHER, R. A., ABRAMOWSKI, D., FRANK, S., PROBST, A., FRASER, G., STALDER, A. K., BEIBEL, M. & STAUFENBIEL, M. 2009. Transmission and spreading of tauopathy in transgenic mouse brain. *Nature cell biology,* 11**,** 909-913.

COHEN-MANSFIELD, J. & BILLIG, N. 1986. Agitated behaviors in the elderly: I. A conceptual review. *Journal of the American Geriatrics Society,* 34**,** 711-721.

COHEN, R. M., REZAI-ZADEH, K., WEITZ, T. M., RENTSENDORJ, A., GATE, D., SPIVAK, I., BHOLAT, Y., VASILEVKO, V., GLABE, C. G., BREUNIG, J. J., RAKIC, P., DAVTYAN, H., AGADJANYAN, M. G., KEPE, V., BARRIO, J. R., BANNYKH, S., SZEKELY, C. A., PECHNICK, R. N. & TOWN, T. 2013. A transgenic Alzheimer rat with plaques, tau pathology, behavioral impairment, oligomeric aβ, and frank neuronal loss. *J Neurosci,* 33**,** 6245-56.

CONDELLO, C., LEMMIN, T., STÖHR, J., NICK, M., WU, Y., MAXWELL, A. M., WATTS, J. C., CARO, C. D., OEHLER, A. & KEENE, C. D. 2018. Structural heterogeneity and intersubject variability of Aβ in familial and sporadic Alzheimer's disease. *Proceedings of the National Academy of Sciences,* 115**,** E782-E791.

CONGDON, E. E. & SIGURDSSON, E. M. 2018. Tau-targeting therapies for Alzheimer disease. *Nature Reviews Neurology,* 14**,** 399-415.

CONGREVE, M., OSWALD, C. & MARSHALL, F. H. 2017. Applying Structure-Based Drug Design Approaches to Allosteric Modulators of GPCRs. *Trends in Pharmacological Sciences,* 38**,** 837-847.

CONN, P. J., CHRISTOPOULOS, A. & LINDSLEY, C. W. 2009a. Allosteric modulators of GPCRs: a novel approach for the treatment of CNS disorders. *Nature reviews Drug discovery,* 8**,** 41-54.

CONN, P. J., JONES, C. K. & LINDSLEY, C. W. 2009b. Subtype-selective allosteric modulators of muscarinic receptors for the treatment of CNS disorders. *Trends in pharmacological sciences,* 30**,** 148-155.

CONN, P. J., LINDSLEY, C. W., MEILER, J. & NISWENDER, C. M. 2014. Opportunities and challenges in the discovery of allosteric modulators of GPCRs for treating CNS disorders. *Nat Rev Drug Discov,* 13**,** 692-708.

COOK, C., DUNMORE, J. H., MURRAY, M. E., SCHEFFEL, K., SHUKOOR, N., TONG, J., CASTANEDES-CASEY, M., PHILLIPS, V., ROUSSEAU, L. & PENULIAR, M. S. 2014. Severe amygdala dysfunction in a MAPT transgenic mouse model of frontotemporal dementia. *Neurobiology of aging,* 35**,** 1769-1777.

COON, K. D., MYERS, A. J., CRAIG, D. W., WEBSTER, J. A., PEARSON, J. V., LINCE, D. H., ZISMANN, V. L., BEACH, T. G., LEUNG, D. & BRYDEN, L. 2007. A high-density whole-genome association study reveals that APOE is the major susceptibility gene for sporadic late-onset Alzheimer's disease. *The Journal of clinical psychiatry,* 68**,** 8183.

CORBETT, G. T., WANG, Z., HONG, W., COLOM-CADENA, M., ROSE, J., LIAO, M., ASFAW, A., HALL, T. C., DING, L., DESOUSA, A., FROSCH, M. P., COLLINGE, J., HARRIS, D. A., PERKINTON, M. S., SPIRES-JONES, T. L., YOUNG-PEARSE, T. L., BILLINTON, A. & WALSH, D. M. 2020. PrP is a central player in toxicity mediated by soluble aggregates of neurodegeneration-causing proteins. *Acta Neuropathologica,* 139**,** 503-526.

CORDER, E. H., SAUNDERS, A. M., STRITTMATTER, W. J., SCHMECHEL, D. E., GASKELL, P. C., SMALL, G., ROSES, A., HAINES, J. & PERICAK-VANCE, M. A. 1993. Gene dose of apolipoprotein E type 4 allele and the risk of Alzheimer's disease in late onset families. *Science,* 261**,** 921-923.

CORSETTI, S., GUNN-MOORE, F. & DHOLAKIA, K. 2019. Light sheet fluorescence microscopy for neuroscience. *Journal of Neuroscience Methods,* 319**,** 16-27.

CROOK, J. M., TOMASKOVIC-CROOK, E., COPOLOV, D. L. & DEAN, B. 2000. Decreased muscarinic receptor binding in subjects with schizophrenia: a study of the human hippocampal formation. *Biological psychiatry,* 48**,** 381-388.

CUMMINGS, B. J., HEAD, E., RUEHL, W., MILGRAM, N. W. & COTMAN, C. W. 1996. The canine as an animal model of human aging and dementia. *Neurobiology of aging,* 17**,** 259-268.

CUMMINGS, J., AISEN, P., LEMERE, C., ATRI, A., SABBAGH, M. & SALLOWAY, S. 2021. Aducanumab produced a clinically meaningful benefit in association with amyloid lowering. *Alzheimer's Research & Therapy,* 13**,** 98.

CUMMINGS, J., LEE, G., NAHED, P., KAMBAR, M. E. Z. N., ZHONG, K., FONSECA, J. & TAGHVA, K. 2022. Alzheimer's disease drug development pipeline: 2022. *Alzheimer's & Dementia: Translational Research & Clinical Interventions,* 8**,** e12295.

DAAKA, Y., LUTTRELL, L. M. & LEFKOWITZ, R. J. 1997. Switching of the coupling of the β2-adrenergic receptor to different G proteins by protein kinase A. *Nature,* 390**,** 88-91.

DAETWYLER, S. & HUISKEN, J. 2016. Fast fluorescence microscopy with light sheets. *The Biological Bulletin,* 231**,** 14-25.

DAIGLE, T. L., MADISEN, L., HAGE, T. A., VALLEY, M. T., KNOBLICH, U., LARSEN, R. S., TAKENO, M. M., HUANG, L., GU, H., LARSEN, R., MILLS, M., BOSMA-MOODY, A., SIVERTS, L. A., WALKER, M., GRAYBUCK, L. T., YAO, Z., FONG, O., NGUYEN, T. N., GARREN, E., LENZ, G. H., CHAVARHA, M., PENDERGRAFT, J., HARRINGTON, J., HIROKAWA, K. E., HARRIS, J. A., NICOVICH, P. R., MCGRAW, M. J., OLLERENSHAW, D. R., SMITH, K. A., BAKER, C. A., TING, J. T., SUNKIN, S. M., LECOQ, J., LIN, M. Z., BOYDEN, E. S., MURPHY, G. J., DA COSTA, N. M., WATERS, J., LI, L., TASIC, B. & ZENG, H. 2018. A Suite of Transgenic Driver and Reporter Mouse Lines with Enhanced Brain-Cell-Type Targeting and Functionality. *Cell,* 174**,** 465-480.e22.

DANSOKHO, C. & HENEKA, M. T. 2018. Neuroinflammatory responses in Alzheimer's disease. *Journal of Neural Transmission,* 125**,** 771-779.

DASARI, S. & GULLEDGE, A. T. 2010. M1 and M4 Receptors Modulate Hippocampal Pyramidal Neurons. *Journal of Neurophysiology,* 105**,** 779-792.

DAVIES, P. & MALONEY, A. 1976. Selective loss of central cholinergic neurons in Alzheimer's disease. *The Lancet,* 308**,** 1403.

DAVIS, A. A., FRITZ, J. J., WESS, J., LAH, J. J. & LEVEY, A. I. 2010. Deletion of M1 muscarinic acetylcholine receptors increases amyloid pathology in vitro and in vivo. *Journal of Neuroscience,* 30**,** 4190-4196.

DAVOREN, J. E., LEE, C.-W., GARNSEY, M., BRODNEY, M. A., CORDES, J., DLUGOLENSKI, K., EDGERTON, J. R., HARRIS, A. R., HELAL, C. J. & JENKINSON, S. 2016. Discovery of the potent and selective M1 PAM-agonist N-[(3 R, 4 S)-3-hydroxytetrahydro-2 H-pyran-4-yl]-5-methyl-4-[4-(1, 3-thiazol-4-yl) benzyl] pyridine-2-carboxamide (PF-06767832): Evaluation of efficacy and cholinergic side effects. *Journal of medicinal chemistry,* 59**,** 6313-6328.

DE LIGT, R. A. F., KOUROUNAKIS, A. P. & IJZERMAN, A. P. 2000. Inverse agonism at G protein-coupled receptors: (patho)physiological relevance and implications for drug discovery. *British Journal of Pharmacology,* 130**,** 1-12.

DE MEDEIROS, L. M., DE BASTIANI, M. A., RICO, E. P., SCHONHOFEN, P., PFAFFENSELLER, B., WOLLENHAUPT-AGUIAR, B., GRUN, L., BARBÉ-TUANA, F., ZIMMER, E. R., CASTRO, M. A. A., PARSONS, R. B. & KLAMT, F. 2019. Cholinergic Differentiation of Human Neuroblastoma SH-SY5Y Cell Line and Its Potential Use as an In vitro Model for Alzheimer's Disease Studies. *Molecular Neurobiology,* 56**,** 7355-7367.

DEALMEIDA, V. I. & MAYO, K. E. 1998. Identification of Binding Domains of the Growth Hormone-Releasing Hormone Receptor by Analysis of Mutant and Chimeric Receptor Proteins. *Molecular Endocrinology,* 12**,** 750-765.

DEAN, B., HOPPER, S., CONN, P. J. & SCARR, E. 2016. Changes in BQCA allosteric modulation of [3H] NMS binding to human cortex within schizophrenia and by divalent cations. *Neuropsychopharmacology,* 41**,** 1620-1628.

DEAN, B., MCLEOD, M., KERIAKOUS, D., MCKENZIE, J. & SCARR, E. 2002. Decreased muscarinic1 receptors in the dorsolateral prefrontal cortex of subjects with schizophrenia. *Molecular psychiatry,* 7**,** 1083-1091.

DEAN, B. & SCARR, E. 2020. Muscarinic M1 and M4 receptors: Hypothesis driven drug development for schizophrenia. *Psychiatry Research,* 288**,** 112989.

DECOURT, B., WILSON, J., RITTER, A., DARDIS, C., DIFILIPPO, F. P., ZHUANG, X., CORDES, D., LEE, G., FULKERSON, N. D., ST ROSE, T., HARTLEY, K. & SABBAGH, M. N. 2020. MCLENA-1: A Phase II Clinical Trial for the Assessment of Safety, Tolerability, and Efficacy of Lenalidomide in Patients with Mild Cognitive Impairment Due to Alzheimer's Disease. *Open Access J Clin Trials,* 12**,** 1-13.

DENG, A., IRIZARRY, M. C., NITSCH, R. M., GROWDON, J. H. & REBECK, G. W. 2001. Elevation of Cystatin C in Susceptible Neurons in Alzheimer's Disease. *The American Journal of Pathology,* 159**,** 1061-1068.

DENNIS, S. H., PASQUI, F., COLVIN, E. M., SANGER, H., MOGG, A. J., FELDER, C. C., BROAD, L. M., FITZJOHN, S. M., ISAAC, J. T. & MELLOR, J. R. 2016. Activation of Muscarinic M1 Acetylcholine Receptors Induces Long-Term Potentiation in the Hippocampus. *Cereb Cortex,* 26**,** 414-26.

DESCHOUT, H., ZANACCHI, F. C., MLODZIANOSKI, M., DIASPRO, A., BEWERSDORF, J., HESS, S. T. & BRAECKMANS, K. 2014. Precisely and accurately localizing single emitters in fluorescence microscopy. *Nature methods,* 11**,** 253-266.

DESIKAN, R. S., MCEVOY, L. K., THOMPSON, W. K., HOLLAND, D., RODDEY, J. C., BLENNOW, K., AISEN, P. S., BREWER, J. B., HYMAN, B. T. & DALE, A. M. 2011. Amyloid‐β associated volume loss occurs only in the presence of phospho‐tau. *Annals of neurology,* 70**,** 657-661.

DICKEY, C., KRAFT, C., JINWAL, U., KOREN, J., JOHNSON, A., ANDERSON, L., LEBSON, L., LEE, D., DICKSON, D. & DE SILVA, R. 2009. Aging analysis reveals slowed tau turnover and enhanced stress response in a mouse model of tauopathy. *The American journal of pathology,* 174**,** 228-238.

DIGBY, G. J., UTLEY, T. J., LAMSAL, A., SEVEL, C., SHEFFLER, D. J., LEBOIS, E. P., BRIDGES, T. M., WOOD, M. R., NISWENDER, C. M., LINDSLEY, C. W. & CONN, P. J. 2012. Chemical Modification of the M1 Agonist VU0364572 Reveals Molecular Switches in Pharmacology and a Bitopic Binding Mode. *ACS Chemical Neuroscience,* 3**,** 1025-1036.

DOMINGUES, C., AB DA CRUZ E SILVA, O. & HENRIQUES, A. 2017. Impact of cytokines and chemokines on Alzheimer's disease neuropathological hallmarks. *Current Alzheimer Research,* 14**,** 870-882.

DONG, J.-X., LEE, Y., KIRMIZ, M., PALACIO, S., DUMITRAS, C., MORENO, C. M., SANDO, R., SANTANA, L. F., SÜDHOF, T. C., GONG, B., MURRAY, K. D. & TRIMMER, J. S. 2019. A toolbox of nanobodies developed and validated for use as intrabodies and nanoscale immunolabels in mammalian brain neurons. *eLife,* 8**,** e48750.

DROR, R. O., GREEN, H. F., VALANT, C., BORHANI, D. W., VALCOURT, J. R., PAN, A. C., ARLOW, D. H., CANALS, M., LANE, J. R. & RAHMANI, R. 2013. Structural basis for modulation of a G-protein-coupled receptor by allosteric drugs. *Nature,* 503**,** 295-299.

DROR, R. O., MILDORF, T. J., HILGER, D., MANGLIK, A., BORHANI, D. W., ARLOW, D. H., PHILIPPSEN, A., VILLANUEVA, N., YANG, Z. & LERCH, M. T. 2015.

Structural basis for nucleotide exchange in heterotrimeric G proteins. *Science,* 348**,** 1361-1365.

DRUMMOND, E., NAYAK, S., FAUSTIN, A., PIRES, G., HICKMAN, R. A., ASKENAZI, M., COHEN, M., HALDIMAN, T., KIM, C., HAN, X., SHAO, Y., SAFAR, J. G., UEBERHEIDE, B. & WISNIEWSKI, T. 2017. Proteomic differences in amyloid plaques in rapidly progressive and sporadic Alzheimer's disease. *Acta Neuropathologica,* 133**,** 933-954.

DRUMMOND, E. & WISNIEWSKI, T. 2017. Alzheimer's disease: experimental models and reality. *Acta neuropathologica,* 133**,** 155-175.

DU, L. Y., CHANG, L. Y., ARDILES, A. O., TAPIA-ROJAS, C., ARAYA, J., INESTROSA, N. C., PALACIOS, A. G. & ACOSTA, M. L. 2015. Alzheimer's disease-related protein expression in the retina of Octodon degus. *PLoS one,* 10**,** e0135499.

DUFF, K., ECKMAN, C., ZEHR, C., YU, X., PRADA, C. M., PEREZ-TUR, J., HUTTON, M., BUEE, L., HARIGAYA, Y., YAGER, D., MORGAN, D., GORDON, M. N., HOLCOMB, L., REFOLO, L., ZENK, B., HARDY, J. & YOUNKIN, S. 1996. Increased amyloid-beta42(43) in brains of mice expressing mutant presenilin 1. *Nature,* 383**,** 710-3.

DUYCKAERTS, C., CLAVAGUERA, F. & POTIER, M.-C. 2019. The prion-like propagation hypothesis in Alzheimer's and Parkinson's disease. *Current Opinion in Neurology,* 32.

DWOMOH, L., ROSSI, M., SCARPA, M., KHAJEHALI, E., MOLLOY, C., HERZYK, P., MISTRY, S. N., BOTTRILL, A. R., SEXTON, P. M., CHRISTOPOULOS, A., CONN, J., LINDSLEY, C. W., BRADLEY, S. J. & TOBIN, A. B. 2022a. M1 muscarinic receptor activation reduces the molecular pathology and slows the progression of prion-mediated neurodegenerative disease. *Science Signaling,* 15**,** eabm3720.

DWOMOH, L., TEJEDA, G. S. & TOBIN, A. B. 2022b. Targeting the M1 muscarinic acetylcholine receptor in Alzheimer's disease. *Neuronal Signal,* 6**,** Ns20210004.

EBERT, U. & KIRCH, W. 1998. Scopolamine model of dementia: electroencephalogram findings and cognitive performance. *European journal of clinical investigation,* 28**,** 944-949.

EID, A., MHATRE, I. & RICHARDSON, J. R. 2019. Gene-environment interactions in Alzheimer's disease: A potential path to precision medicine. *Pharmacology & Therapeutics,* 199**,** 173-187.

EISAI 2020. Lecanemab confirmatory phase 3 CLARITY AD study met primary endpoint, showing highly statistically significant reduction of clinical decline in large global clinical study of 1,795 participants with early Alzheimer's Fisease.

ELDER, G. A., GAMA SOSA, M. A. & DE GASPERI, R. 2010. Transgenic mouse models of Alzheimer's disease. *The Mount Sinai journal of medicine, New York,* 77**,** 69-81.

ELLAITHY, A., GONZALEZ-MAESO, J., LOGOTHETIS, D. A. & LEVITZ, J. 2020. Structural and Biophysical Mechanisms of Class C G Protein-Coupled Receptor Function. *Trends in Biochemical Sciences,* 45**,** 1049-1064.

ENGERS, J. L., CHILDRESS, E. S., LONG, M. F., CAPSTICK, R. A., LUSCOMBE, V. B., CHO, H. P., DICKERSON, J. W., ROOK, J. M., BLOBAUM, A. L., NISWENDER, C. M., ENGERS, D. W., CONN, P. J. & LINDSLEY, C. W. 2018. VU6007477, a Novel M1 PAM Based on a Pyrrolo[2,3-b]pyridine Carboxamide Core Devoid of Cholinergic Adverse Events. *ACS Medicinal Chemistry Letters,* 9**,** 917-922.

EPP, J. R., NIIBORI, Y., LIZ HSIANG, H.-L., MERCALDO, V., DEISSEROTH, K., JOSSELYN, S. A. & FRANKLAND, P. W. 2015. Optimization of CLARITY for Clearing Whole-Brain and Other Intact Organs. *eNeuro,* 2**,** ENEURO.0022-15.2015.

ERLANDSON, S. C., MCMAHON, C. & KRUSE, A. C. 2018. Structural Basis for G Protein–Coupled Receptor Signaling. *Annual review of biophysics,* 47**,** 1-18.

ERSKINE, D., TAYLOR, J.-P., BAKKER, G., BROWN, A. J., TASKER, T. & NATHAN, P. J. 2019. Cholinergic muscarinic M1 and M4 receptors as therapeutic targets for cognitive, behavioural, and psychological symptoms in psychiatric and neurological disorders. *Drug Discovery Today,* 24**,** 2307-2314.

ERTEKIN-TANER, N. 2007. Genetics of Alzheimer's disease: a centennial review. *Neurologic clinics,* 25**,** 611-667.

ERTÜRK, A., BECKER, K., JÄHRLING, N., MAUCH, C. P., HOJER, C. D., EGEN, J. G., HELLAL, F., BRADKE, F., SHENG, M. & DODT, H.-U. 2012. Three-dimensional imaging of solvent-cleared organs using 3DISCO. *Nature Protocols,* 7**,** 1983-1995.

ESCH, F., KEIM, P., BEATTIE, E., BLACHER, R., CULWELL, A., OLTERSDORF, T., MCCLURE, D. & WARD, P. 1990. Cleavage of amyloid beta peptide during constitutive processing of its precursor. *Science,* 248**,** 1122-1124.

EVANS, M. J. & KAUFMAN, M. H. 1981. Establishment in culture of pluripotential cells from mouse embryos. *nature,* 292**,** 154-156.

FAGET, L., ERBS, E., LE MERRER, J., SCHERRER, G., MATIFAS, A., BENTURQUIA, N., NOBLE, F., DECOSSAS, M., KOCH, M., KESSLER, P., VONESCH, J. L., SCHWAB, Y., KIEFFER, B. L. & MASSOTTE, D. 2012. In Vivo Visualization of Delta Opioid Receptors upon Physiological Activation Uncovers a Distinct Internalization Profile. *Journal of Neuroscience,* 32**,** 7301-7310.

FANSELOW, M. S. & POULOS, A. M. 2005. The neuroscience of mammalian associative learning. *Annual review of psychology,* 56**,** 207-234.

FELDER, C. C. 1995. Muscarinic acetylcholine receptors: signal transduction through multiple effectors. *The FASEB Journal,* 9**,** 619-625.

FELDER, C. C., BYMASTER, F. P., WARD, J. & DELAPP, N. 2000. Therapeutic Opportunities for Muscarinic Receptors in the Central Nervous System. *Journal of Medicinal Chemistry,* 43**,** 4333-4353.

FELDER, C. C., GOLDSMITH, P. J., JACKSON, K., SANGER, H. E., EVANS, D. A., MOGG, A. J. & BROAD, L. M. 2018. Current status of muscarinic M1 and M4 receptors as drug targets for neurodegenerative diseases. *Neuropharmacology,* 136**,** 449-458.

FENG, G., MELLOR, R. H., BERNSTEIN, M., KELLER-PECK, C., NGUYEN, Q. T., WALLACE, M., NERBONNE, J. M., LICHTMAN, J. W. & SANES, J. R. 2000. Imaging neuronal subsets in transgenic mice expressing multiple spectral variants of GFP. *Neuron,* 28**,** 41-51.

FERRARI, A., HOERNDLI, F., BAECHI, T., NITSCH, R. M. & GÖTZ, J. R. 2003. β-Amyloid induces paired helical filament-like tau filaments in tissue culture. *Journal of Biological Chemistry,* 278**,** 40162-40168.

FINK, D., WOHRER, S., PFEFFER, M., TOMBE, T., ONG, C. J. & SORENSEN, P. H. 2010. Ubiquitous expression of the monomeric red fluorescent protein mCherry in transgenic mice. *genesis,* 48**,** 723-729.

FISCHER, R. & MAIER, O. 2015. Interrelation of Oxidative Stress and Inflammation in Neurodegenerative Disease: Role of TNF. *Oxidative Medicine and Cellular Longevity,* 2015**,** 610813.

FISHER, A., BEZPROZVANNY, I., WU, L., RYSKAMP, D. A., BAR-NER, N., NATAN, N., BRANDEIS, R., ELKON, H., NAHUM, V. & GERSHONOV, E. 2016. AF710B, a novel M1/σ1 agonist with therapeutic efficacy in animal models of Alzheimer's disease. *Neurodegenerative Diseases,* 16**,** 95-110.

FISHER, A., PITTEL, Z., HARING, R., BAR-NER, N., KLIGER-SPATZ, M., NATAN, N., EGOZI, I., SONEGO, H., MARCOVITCH, I. & BRANDEIS, R. 2003. M1 muscarinic agonists can modulate some of the hallmarks in Alzheimer's disease. *Journal of Molecular Neuroscience,* 20**,** 349-356.

FLICKER, C., SERBY, M. & FERRIS, S. H. 1990. Scopolamine effects on memory, language, visuospatial praxis and psychomotor speed. *Psychopharmacology,* 100**,** 243-250.

FLOOD, J. F. & CHERKIN, A. 1986. Scopolamine effects on memory retention in mice: a model of dementia? *Behavioral and neural biology,* 45**,** 169-184.

FLYNN, D. D., FERRARI-DILEO, G., MASH, D. C. & LEVEY, A. I. 1995. Differential Regulation of Molecular Subtypes of Muscarinic Receptors in Alzheimer's Disease. *Journal of Neurochemistry,* 64**,** 1888-1891.

FOLGER, K. R., WONG, E. A., WAHL, G. & CAPECCHI, M. R. 1982. Patterns of integration of DNA microinjected into cultured mammalian cells: evidence for homologous recombination between injected plasmid DNA molecules. *Molecular and cellular biology,* 2**,** 1372-1387.

FORLENZA, O., SPINK, J., DAYANANDAN, R., ANDERTON, B., OLESEN, O. & LOVESTONE, S. 2000. Muscarinic agonists reduce tau phosphorylation in non-neuronal cells via GSK-3β inhibition and in neurons. *Journal of neural transmission,* 107**,** 1201-1212.

FOSTER, D. J., CHOI, D. L., CONN, P. J. & ROOK, J. M. 2014. Activation of M_1 and M_4 muscarinic receptors as potential treatments for Alzheimer's disease and schizophrenia. *Neuropsychiatric disease and treatment*.

FRANCIS, P. T., PALMER, A. M., SNAPE, M. & WILCOCK, G. K. 1999. The cholinergic hypothesis of Alzheimer's disease: a review of progress. *Journal of Neurology, Neurosurgery & Psychiatry,* 66**,** 137.

FREDRIKSSON, R., LAGERSTRÖM, M. C., LUNDIN, L.-G. & SCHIÖTH, H. B. 2003. The G-Protein-Coupled Receptors in the Human Genome Form Five Main Families. Phylogenetic Analysis, Paralogon Groups, and Fingerprints. *Molecular Pharmacology,* 63**,** 1256-1272.

FREDRIKSSON, R. & SCHIÖTH, H. B. 2005. The repertoire of G-protein–coupled receptors in fully sequenced genomes. *Molecular pharmacology,* 67**,** 1414-1425.

FREEDMAN, N. J. & LEFKOWITZ, R. J. 1996. Desensitization of G protein-coupled receptors. *Recent progress in hormone research,* 51**,** 319-51; discussion 352.

FROST, B., JACKS, R. L. & DIAMOND, M. I. 2009. Propagation of tau misfolding from the outside to the inside of a cell. *Journal of Biological Chemistry,* 284**,** 12845-12852.

GALLO, M. P., ALLOATTI, G., EVA, C., OBERTO, A. & LEVI, R. C. 1993. M1 muscarinic receptors increase calcium current and phosphoinositide turnover in guinea-pig ventricular cardiocytes. *J Physiol,* 471**,** 41-60.

GAMACHE, J., BENZOW, K., FORSTER, C., KEMPER, L., HLYNIALUK, C., FURROW, E., ASHE, K. H. & KOOB, M. D. 2019. Factors other than hTau overexpression that contribute to tauopathy-like phenotype in rTg4510 mice. *Nat Commun,* 10**,** 2479.

GAMES, D., ADAMS, D., ALESSANDRINI, R., BARBOUR, R., BORTHELETTE, P., BLACKWELL, C., CARR, T., CLEMENS, J., DONALDSON, T. & GILLESPIE, F. 1995. Alzheimer-type neuropathology in transgenic mice overexpressing V717F β-amyloid precursor protein. *Nature,* 373**,** 523-527.

GEBHARD, S., HATTORI, T., BAUER, E., BÖSL, M. R., SCHLUND, B., PÖSCHL, E., ADAM, N., DE CROMBRUGGHE, B. & VON DER MARK, K. 2007. BAC constructs in transgenic reporter mouse lines control efficient and specific LacZ

expression in hypertrophic chondrocytes under the complete Col10a1 promoter. *Histochemistry and Cell Biology,* 127**,** 183-194.

GENIN, E., HANNEQUIN, D., WALLON, D., SLEEGERS, K., HILTUNEN, M., COMBARROS, O., BULLIDO, M. J., ENGELBORGHS, S., DE DEYN, P., BERR, C., PASQUIER, F., DUBOIS, B., TOGNONI, G., FIÉVET, N., BROUWERS, N., BETTENS, K., AROSIO, B., COTO, E., DEL ZOMPO, M., MATEO, I., EPELBAUM, J., FRANK-GARCIA, A., HELISALMI, S., PORCELLINI, E., PILOTTO, A., FORTI, P., FERRI, R., SCARPINI, E., SICILIANO, G., SOLFRIZZI, V., SORBI, S., SPALLETTA, G., VALDIVIESO, F., VEPSÄLÄINEN, S., ALVAREZ, V., BOSCO, P., MANCUSO, M., PANZA, F., NACMIAS, B., BOSSÙ, P., HANON, O., PICCARDI, P., ANNONI, G., SERIPA, D., GALIMBERTI, D., LICASTRO, F., SOININEN, H., DARTIGUES, J. F., KAMBOH, M. I., VAN BROECKHOVEN, C., LAMBERT, J. C., AMOUYEL, P. & CAMPION, D. 2011. APOE and Alzheimer disease: a major gene with semi-dominant inheritance. *Molecular Psychiatry,* 16**,** 903-907.

GERBER, D. J., SOTNIKOVA, T. D., GAINETDINOV, R. R., HUANG, S. Y., CARON, M. G. & TONEGAWA, S. 2001. Hyperactivity, elevated dopaminergic transmission, and response to amphetamine in M1 muscarinic acetylcholine receptor-deficient mice. *Proceedings of the National Academy of Sciences,* 98**,** 15312-15317.

GHOSAL, K., VOGT, D. L., LIANG, M., SHEN, Y., LAMB, B. T. & PIMPLIKAR, S. W. 2009. Alzheimer's disease-like pathological features in transgenic mice expressing the APP intracellular domain. *Proceedings of the National Academy of Sciences,* 106**,** 18367-18372.

GIACOBINI, E. & GOLD, G. 2013. Alzheimer disease therapy—moving from amyloid-β to tau. *Nature Reviews Neurology,* 9**,** 677-686.

GIANNAKOPOULOS, P., HERRMANN, F., BUSSIÈRE, T., BOURAS, C., KÖVARI, E., PERL, D., MORRISON, J., GOLD, G. & HOF, P. 2003. Tangle and neuron numbers, but not amyloid load, predict cognitive status in Alzheimer's disease. *Neurology,* 60**,** 1495-1500.

GIL-BEA, F. J., GARCÍA-ALLOZA, M., DOMÍNGUEZ, J., MARCOS, B. & RAMÍREZ, M. J. 2005. Evaluation of cholinergic markers in Alzheimer's disease and in a model of cholinergic deficit. *Neuroscience Letters,* 375**,** 37-41.

GILMAN, S., KOLLER, M., BLACK, R. S., JENKINS, L., GRIFFITH, S. G., FOX, N. C., EISNER, L., KIRBY, L., ROVIRA, M. B., FORETTE, F. & ORGOGOZO, J.-M. 2005. Clinical effects of Aβ immunization (AN1792) in patients with AD in an interrupted trial. *Neurology,* 64**,** 1553-1562.

GIUNTI, S., ANDERSEN, N., RAYES, D. & DE ROSA, M. J. 2021. Drug discovery: Insights from the invertebrate Caenorhabditis elegans. *Pharmacology Research & Perspectives,* 9**,** e00721.

GLENN, M. J., NESBITT, C. & MUMBY, D. G. 2003. Perirhinal cortex lesions produce variable patterns of retrograde amnesia in rats. *Behavioural brain research,* 141**,** 183-193.

GLUSMAN, G., YANAI, I., RUBIN, I. & LANCET, D. 2001. The complete human olfactory subgenome. *Genome research,* 11**,** 685-702.

GOEDERT, M. & SPILLANTINI MARIA, G. 2006. A Century of Alzheimer's Disease. *Science,* 314**,** 777-781.

GOLDBERG, R. J. 2007. Alzheimer's Disease. *Comprehensive Therapy,* 33**,** 58-64.

GOLDE, T. E. & MILLER, V. M. 2009. Proteinopathy-induced neuronal senescence: a hypothesis for brain failure in Alzheimer's and other neurodegenerative diseases. *Alzheimers Res Ther,* 1**,** 1-12.

GÓMEZ-RAMOS, A., DÍAZ-HERNÁNDEZ, M., RUBIO, A., DÍAZ-HERNÁNDEZ, J. I., MIRAS-PORTUGAL, M. T. & AVILA, J. 2009. Characteristics and consequences of muscarinic receptor activation by tau protein. *European Neuropsychopharmacology,* 19**,** 708-717.

GOMEZ-RAMOS, A., DIAZ-HERNANDEZ, M., RUBIO, A., MIRAS-PORTUGAL, M. & AVILA, J. 2008. Extracellular tau promotes intracellular calcium increase through M1 and M3 muscarinic receptors in neuronal cells. *Molecular and Cellular Neuroscience,* 37**,** 673-681.

GOMEZA, J., SHANNON, H., KOSTENIS, E., FELDER, C., ZHANG, L., BRODKIN, J., GRINBERG, A., SHENG, H. & WESS, J. 1999. Pronounced pharmacologic deficits in M2 muscarinic acetylcholine receptor knockout mice. *Proceedings of the National Academy of Sciences,* 96**,** 1692-1697.

GONG, Y., CHANG, L., VIOLA, K. L., LACOR, P. N., LAMBERT, M. P., FINCH, C. E., KRAFFT, G. A. & KLEIN, W. L. 2003. Alzheimer's disease-affected brain: presence of oligomeric Aβ ligands (ADDLs) suggests a molecular basis for reversible memory loss. *Proceedings of the National Academy of Sciences,* 100**,** 10417-10422.

GOODMAN, O. B., KRUPNICK, J. G., SANTINI, F., GUREVICH, V. V., PENN, R. B., GAGNON, A. W., KEEN, J. H. & BENOVIC, J. L. 1996. β-Arrestin acts as a clathrin adaptor in endocytosis of the β2-adrenergic receptor. *nature,* 383**,** 447-450.

GOODWIN, L. O., SPLINTER, E., DAVIS, T. L., URBAN, R., HE, H., BRAUN, R. E., CHESLER, E. J., KUMAR, V., VAN MIN, M., NDUKUM, J., PHILIP, V. M., REINHOLDT, L. G., SVENSON, K., WHITE, J. K., SASNER, M., LUTZ, C. & MURRAY, S. A. 2019. Large-scale discovery of mouse transgenic integration sites reveals frequent structural variation and insertional mutagenesis. *Genome Res,* 29**,** 494-505.

GORING, D., ROSSANT, J., CLAPOFF, S., BREITMAN, M. & TSUI, L.-C. 1987. In situ detection of β-galactosidase in lenses of transgenic mice with a γ-crystallin/lacZ gene. *Science,* 235**,** 456-458.

GOSENS, R. & GROSS, N. 2018. The mode of action of anticholinergics in asthma. *European Respiratory Journal,* 52**,** 1701247.

GÖTZ, J. & ITTNER, L. M. 2008. Animal models of Alzheimer's disease and frontotemporal dementia. *Nature Reviews Neuroscience,* 9**,** 532-544.

GRACE, C. R. R., PERRIN, M. H., DIGRUCCIO, M. R., MILLER, C. L., RIVIER, J. E., VALE, W. W. & RIEK, R. 2004. NMR structure and peptide hormone binding site of the first extracellular domain of a type B1 G protein-coupled receptor. *Proceedings of the National Academy of Sciences,* 101**,** 12836-12841.

GRADINARU, V., TREWEEK, J., OVERTON, K. & DEISSEROTH, K. 2018. Hydrogel-Tissue Chemistry: Principles and Applications. *Annu Rev Biophys,* 47**,** 355-376.

GRAY, J. A. & MCNAUGHTON, N. 1983. Comparison between the behavioural effects of septal and hippocampal lesions: a review. *Neuroscience & Biobehavioral Reviews,* 7**,** 119-188.

GREENFIELD, J. P., TSAI, J., GOURAS, G. K., HAI, B., THINAKARAN, G., CHECLER, F., SISODIA, S. S., GREENGARD, P. & XU, H. 1999. Endoplasmic reticulum and trans-Golgi network generate distinct populations of Alzheimer β-amyloid peptides. *Proceedings of the National Academy of Sciences,* 96**,** 742-747.

GREGORY, K. J., SEXTON, P. M. & CHRISTOPOULOS, A. 2007. Allosteric modulation of muscarinic acetylcholine receptors. *Current neuropharmacology,* 5**,** 157-167.

GRIECO, F., BERNSTEIN, B. J., BIEMANS, B., BIKOVSKI, L., BURNETT, C. J., CUSHMAN, J. D., VAN DAM, E. A., FRY, S. A., RICHMOND-HACHAM, B.,

HOMBERG, J. R., KAS, M. J. H., KESSELS, H. W., KOOPMANS, B., KRASHES, M. J., KRISHNAN, V., LOGAN, S., LOOS, M., MCCANN, K. E., PARDUZI, Q., PICK, C. G., PREVOT, T. D., RIEDEL, G., ROBINSON, L., SADIGHI, M., SMIT, A. B., SONNTAG, W., ROELOFS, R. F., TEGELENBOSCH, R. A. J. & NOLDUS, L. P. J. J. 2021. Measuring Behavior in the Home Cage: Study Design, Applications, Challenges, and Perspectives. *Frontiers in Behavioral Neuroscience,* 15.

GROTHE, M., HEINSEN, H. & TEIPEL, S. J. 2012. Atrophy of the Cholinergic Basal Forebrain Over the Adult Age Range and in Early Stages of Alzheimer's Disease. *Biological Psychiatry,* 71**,** 805-813.

GRUNDKE-IQBAL, I., IQBAL, K., TUNG, Y.-C., QUINLAN, M., WISNIEWSKI, H. M. & BINDER, L. I. 1986. Abnormal phosphorylation of the microtubule-associated protein tau (tau) in Alzheimer cytoskeletal pathology. *Proceedings of the National Academy of Sciences,* 83**,** 4913-4917.

GUELA, C., WU, C.-K., SAROFF, D., LORENZO, A., YUAN, M. & YANKNER, B. A. 1998. Aging renders the brain vulnerable to amyloid β-protein neurotoxicity. *Nature medicine,* 4**,** 827-831.

GUERREIRO, R., WOJTAS, A., BRAS, J., CARRASQUILLO, M., ROGAEVA, E., MAJOUNIE, E., CRUCHAGA, C., SASSI, C., KAUWE, J. S. & YOUNKIN, S. 2013. TREM2 variants in Alzheimer's disease. *New England Journal of Medicine,* 368**,** 117-127.

GUNN-MOORE, D. A., MCVEE, J., BRADSHAW, J. M., PEARSON, G. R., HEAD, E. & GUNN-MOORE, F. J. 2006. Ageing changes in cat brains demonstrated by β-amyloid and AT8-immunoreactive phosphorylated tau deposits. *Journal of Feline Medicine & Surgery,* 8**,** 234-242.

GUO, J.-P., ARAI, T., MIKLOSSY, J. & MCGEER, P. L. 2006. Aβ and tau form soluble complexes that may promote self aggregation of both into the insoluble forms observed in Alzheimer's disease. *Proceedings of the National Academy of Sciences,* 103**,** 1953-1958.

GUPTA, M. K., MOHAN, M. L. & NAGA PRASAD, S. V. 2018. Chapter Three - G Protein-Coupled Receptor Resensitization Paradigms. *In:* SHUKLA, A. K. (ed.) *International Review of Cell and Molecular Biology.* Academic Press.

GUREVICH, V. V., DION, S. B., ONORATO, J. J., PTASIENSKI, J., KIM, C. M., STERNE-MARR, R., HOSEY, M. M. & BENOVIC, J. L. 1995. Arrestin Interactions with G Protein-coupled Receptors: Direct binding studies of wild type and mutant arrestins with rhodopsin, β2-adrenergic, and M2 muscarinic cholinergic receptors. *Journal of Biological Chemistry,* 270**,** 720-731.

GUREVICH, V. V. & GUREVICH, E. V. 2003. The new face of active receptor bound arrestin attracts new partners. *Structure,* 11**,** 1037-1042.

GUREVICH, V. V. & GUREVICH, E. V. 2006. The structural basis of arrestin-mediated regulation of G-protein-coupled receptors. *Pharmacology & therapeutics,* 110**,** 465-502.

GUREVICH, V. V. & GUREVICH, E. V. 2019. GPCR Signaling Regulation: The Role of GRKs and Arrestins. *Frontiers in Pharmacology,* 10.

GUTTIKONDA, S. R., SIKKEMA, L., TCHIEU, J., SAURAT, N., WALSH, R. M., HARSCHNITZ, O., CICERI, G., SNEEBOER, M., MAZUTIS, L., SETTY, M., ZUMBO, P., BETEL, D., DE WITTE, L. D., PE'ER, D. & STUDER, L. 2021. Fully defined human pluripotent stem cell-derived microglia and tri-culture system model C3 production in Alzheimer's disease. *Nature Neuroscience,* 24**,** 343-354.

HAAM, J. & YAKEL, J. L. 2017. Cholinergic modulation of the hippocampal region and memory function. *Journal of neurochemistry,* 142**,** 111-121.

HAASS, C., HUNG, A. Y., SCHLOSSMACHER, M. G., TEPLOW, D. B. & SELKOE, D. J. 1993. beta-Amyloid peptide and a 3-kDa fragment are derived by distinct cellular mechanisms. *Journal of Biological Chemistry,* 268**,** 3021-3024.

HAASS, C., KAETHER, C., THINAKARAN, G. & SISODIA, S. 2012. Trafficking and Proteolytic Processing of APP. *Cold Spring Harbor Perspectives in Medicine,* 2.

HAGA, K. & HAGA, T. 1992. Activation by G protein beta gamma subunits of agonist- or light-dependent phosphorylation of muscarinic acetylcholine receptors and rhodopsin. *Journal of Biological Chemistry,* 267**,** 2222-2227.

HAGA, K., KRUSE, A. C., ASADA, H., YURUGI-KOBAYASHI, T., SHIROISHI, M., ZHANG, C., WEIS, W. I., OKADA, T., KOBILKA, B. K. & HAGA, T. 2012. Structure of the human M2 muscarinic acetylcholine receptor bound to an antagonist. *Nature,* 482**,** 547-551.

HALLINAN, G. I., VARGAS-CABALLERO, M., WEST, J. & DEINHARDT, K. 2019. Tau Misfolding Efficiently Propagates between Individual Intact Hippocampal Neurons. *The Journal of Neuroscience,* 39**,** 9623.

HAMA, H., HIOKI, H., NAMIKI, K., HOSHIDA, T., KUROKAWA, H., ISHIDATE, F., KANEKO, T., AKAGI, T., SAITO, T. & SAIDO, T. 2015. ScaleS: an optical clearing palette for biological imaging. *Nature neuroscience,* 18**,** 1518-1529.

HAMA, H., KUROKAWA, H., KAWANO, H., ANDO, R., SHIMOGORI, T., NODA, H., FUKAMI, K., SAKAUE-SAWANO, A. & MIYAWAKI, A. 2011. Scale: a chemical approach for fluorescence imaging and reconstruction of transparent mouse brain. *Nature neuroscience,* 14**,** 1481-1488.

HAMM, H. E. 1998. The many faces of G protein signaling. *Journal of Biological Chemistry,* 273**,** 669-672.

HARDY, J. 1997. Amyloid, the presenilins and Alzheimer's disease. *Trends in Neurosciences,* 20**,** 154-159.

HARDY, J. & SELKOE, D. J. 2002. The amyloid hypothesis of Alzheimer's disease: progress and problems on the road to therapeutics. *Science,* 297**,** 353-356.

HARING, R., FISHER, A., MARCIANO, D., PITTEL, Z., KLOOG, Y., ZUCKERMAN, A., ESHHAR, N. & HELDMAN, E. 1998. Mitogen‐activated protein kinase‐dependent and protein kinase C‐dependent pathways link the m1 muscarinic receptor to β‐amyloid precursor protein secretion. *Journal of neurochemistry,* 71**,** 2094-2103.

HARKANY, T., ABRAHAM, I., TIMMERMAN, W., LASKAY, G., TOTH, B., SASVARI, M., KONYA, C., SEBENS, J., KORF, J. & NYAKAS, C. 2000. β‐Amyloid neurotoxicity is mediated by a glutamate‐triggered excitotoxic cascade in rat nucleus basalis. *European Journal of Neuroscience,* 12**,** 2735-2745.

HARKANY, T., O'MAHONY, S., KELLY, J., SOOS, K., TÖRÕ, I., PENKE, B., LUITEN, P., NYAKAS, C., GULYA, K. & LEONARD, B. 1998. β-Amyloid (Phe (SO3H) 24) 25–35 in rat nucleus basalis induces behavioral dysfunctions, impairs learning and memory and disrupts cortical cholinergic innervation. *Behavioural brain research,* 90**,** 133-145.

HASSELMO, M. E. & WYBLE, B. P. 1997. Free recall and recognition in a network model of the hippocampus: simulating effects of scopolamine on human memory function. *Behavioural Brain Research,* 89**,** 1-34.

HAUSER, A. S., ATTWOOD, M. M., RASK-ANDERSEN, M., SCHIÖTH, H. B. & GLORIAM, D. E. 2017. Trends in GPCR drug discovery: new agents, targets and indications. *Nature reviews Drug discovery,* 16**,** 829.

HAUSER, A. S., GLORIAM, D. E., BRÄUNER-OSBORNE, H. & FOSTER, S. R. 2020. Novel approaches leading towards peptide GPCR de-orphanisation. *British Journal of Pharmacology,* 177**,** 961-968.

HEAD, E., CALLAHAN, H., MUGGENBURG, B., COTMAN, C. & MILGRAM, N. 1998. Visual-discrimination learning ability and β-amyloid accumulation in the dog. *Neurobiology of aging,* 19**,** 415-425.

HELBOE, L., EGEBJERG, J., BARKHOLT, P. & VOLBRACHT, C. 2017. Early depletion of CA1 neurons and late neurodegeneration in a mouse tauopathy model. *Brain Research,* 1665**,** 22-35.

HELBOE, L. & VOLBRACHT, C. 2013. Late neurodegeneration in the Tau transgenic mouse model rTg4510. *Molecular Neurodegeneration,* 8**,** P58.

HELLSTRÖM-LINDAHL, E., VIITANEN, M. & MARUTLE, A. 2009. Comparison of Aβ levels in the brain of familial and sporadic Alzheimer's disease. *Neurochemistry International,* 55**,** 243-252.

HENEKA, M. T., CARSON, M. J., KHOURY, J. E., LANDRETH, G. E., BROSSERON, F., FEINSTEIN, D. L., JACOBS, A. H., WYSS-CORAY, T., VITORICA, J., RANSOHOFF, R. M., HERRUP, K., FRAUTSCHY, S. A., FINSEN, B., BROWN, G. C., VERKHRATSKY, A., YAMANAKA, K., KOISTINAHO, J., LATZ, E., HALLE, A., PETZOLD, G. C., TOWN, T., MORGAN, D., SHINOHARA, M. L., PERRY, V. H., HOLMES, C., BAZAN, N. G., BROOKS, D. J., HUNOT, S., JOSEPH, B., DEIGENDESCH, N., GARASCHUK, O., BODDEKE, E., DINARELLO, C. A., BREITNER, J. C., COLE, G. M., GOLENBOCK, D. T. & KUMMER, M. P. 2015. Neuroinflammation in Alzheimer's disease. *The Lancet Neurology,* 14**,** 388-405.

HENSTRIDGE, C. M. & SPIRES-JONES, T. L. 2018. Modeling Alzheimer's disease brains in vitro. *Nature Neuroscience,* 21**,** 899-900.

HEPLER, J. R. 1999. Emerging roles for RGS proteins in cell signalling. *Trends in Pharmacological Sciences,* 20**,** 376-382.

HERLITZE, S., GARCIA, D., MACKIE, K., HILLE, B., SCHEUER, T. & CATTERALL, W. A. 1996. Modulation of Ca2 channels by G-protein ß subunits. *Nature,* 380**,** 258-262.

HERRICK, D. B., LIN, B., PETERSON, J., SCHNITTKE, N. & SCHWOB, J. E. 2017. Notch1 maintains dormancy of olfactory horizontal basal cells, a reserve neural stem cell. *Proceedings of the National Academy of Sciences,* 114**,** E5589.

HERSCH, S. M., GUTEKUNST, C. A., REES, H. D., HEILMAN, C. J. & LEVEY, A. I. 1994. Distribution of m1-m4 muscarinic receptor proteins in the rat striatum: light and electron microscopic immunocytochemistry using subtype- specific antibodies. *The Journal of Neuroscience,* 14**,** 3351.

HILLMAN, E. M. C., VOLETI, V., LI, W. & YU, H. 2019. Light-Sheet Microscopy in Neuroscience. *Annual Review of Neuroscience,* 42**,** 295-313.

HIRSHBURG, J., CHOI, B., NELSON, J. S. & YEH, A. T. 2007. Correlation between collagen solubility and skin optical clearing using sugars. *Lasers in Surgery and Medicine,* 39**,** 140-144.

HOLCOMB, L., GORDON, M. N., MCGOWAN, E., YU, X., BENKOVIC, S., JANTZEN, P., WRIGHT, K., SAAD, I., MUELLER, R., MORGAN, D., SANDERS, S., ZEHR, C., O'CAMPO, K., HARDY, J., PRADA, C. M., ECKMAN, C., YOUNKIN, S., HSIAO, K. & DUFF, K. 1998. Accelerated Alzheimer-type phenotype in transgenic mice carrying both mutant amyloid precursor protein and presenilin 1 transgenes. *Nat Med,* 4**,** 97-100.

HOLLINGSWORTH, S. A., KELLY, B., VALANT, C., MICHAELIS, J. A., MASTROMIHALIS, O., THOMPSON, G., VENKATAKRISHNAN, A. J., HERTIG, S., SCAMMELLS, P. J., SEXTON, P. M., FELDER, C. C., CHRISTOPOULOS, A.

& DROR, R. O. 2019. Cryptic pocket formation underlies allosteric modulator selectivity at muscarinic GPCRs. *Nature Communications,* 10**,** 3289.

HOLTZMAN, D. M., MORRIS, J. C. & GOATE, A. M. 2011. Alzheimer's disease: the challenge of the second century. *Science translational medicine,* 3**,** 77sr1-77sr1.

HÖRL, D., ROJAS RUSAK, F., PREUSSER, F., TILLBERG, P., RANDEL, N., CHHETRI, R. K., CARDONA, A., KELLER, P. J., HARZ, H., LEONHARDT, H., TREIER, M. & PREIBISCH, S. 2019. BigStitcher: reconstructing high-resolution image datasets of cleared and expanded samples. *Nature Methods,* 16**,** 870-874.

HORWITZ, J. P., CHUA, J., CURBY, R. J., TOMSON, A. J., DA ROOGE, M. A., FISHER, B. E., MAURICIO, J. & KLUNDT, I. 1964. Substrates for cytochemical demonstration of enzyme activity. I. Some substituted 3-indolyl-β-D-glycopyranosides1a. *Journal of medicinal chemistry,* 7**,** 574-575.

HOYT, K. R. & OBRIETAN, K. 2022. Circadian clocks, cognition, and Alzheimer's disease: synaptic mechanisms, signaling effectors, and chronotherapeutics. *Molecular Neurodegeneration,* 17**,** 35.

HSIA, J. A., MOSS, J., HEWLETT, E. L. & VAUGHAN, M. 1984. ADP-ribosylation of adenylate cyclase by pertussis toxin. Effects on inhibitory agonist binding. *Journal of Biological Chemistry,* 259**,** 1086-1090.

HSIAO, K., CHAPMAN, P., NILSEN, S., ECKMAN, C., HARIGAYA, Y., YOUNKIN, S., YANG, F. & COLE, G. 1996. Correlative memory deficits, Aβ elevation, and amyloid plaques in transgenic mice. *Science,* 274**,** 99-103.

HUANG, L.-K., CHAO, S.-P. & HU, C.-J. 2020. Clinical trials of new drugs for Alzheimer disease. *Journal of biomedical science,* 27**,** 1-13.

HUANG, Y. & MAHLEY, R. W. 2014. Apolipoprotein E: Structure and function in lipid metabolism, neurobiology, and Alzheimer's diseases. *Neurobiology of Disease,* 72**,** 3-12.

HULME, E., BIRDSALL, N. & BUCKLEY, N. 1990. Muscarinic receptor subtypes. *Annual review of pharmacology and toxicology,* 30**,** 633-673.

HULME, E., LU, Z., SALDANHA, J. & BEE, M. 2003. Structure and activation of muscarinic acetylcholine receptors. *Biochemical Society Transactions,* 31**,** 29-34.

HUNG, A., HAASS, C., NITSCH, R., QIU, W. Q., CITRON, M., WURTMAN, R., GROWDON, J. & SELKOE, D. 1993. Activation of protein kinase C inhibits cellular production of the amyloid beta-protein. *Journal of Biological Chemistry,* 268**,** 22959-22962.

HURLEY, M. J., DEACON, R. M. J., BEYER, K., IOANNOU, E., IBÁÑEZ, A., TEELING, J. L. & COGRAM, P. 2018. The long-lived Octodon degus as a rodent drug discovery model for Alzheimer's and other age-related diseases. *Pharmacology & Therapeutics,* 188**,** 36-44.

INESTROSA, N. C., REYES, A. E., CHACÓN, M. A., CERPA, W., VILLALÓN, A., MONTIEL, J., MERABACHVILI, G., ALDUNATE, R., BOZINOVIC, F. & ABOITIZ, F. 2005. Human-like rodent amyloid-β-peptide determines Alzheimer pathology in aged wild-type Octodon degu. *Neurobiology of aging,* 26**,** 1023-1028.

INGELSSON, M., FUKUMOTO, H., NEWELL, K., GROWDON, J., HEDLEY–WHYTE, E., FROSCH, M., ALBERT, M., HYMAN, B. & IRIZARRY, M. 2004. Early Aβ accumulation and progressive synaptic loss, gliosis, and tangle formation in AD brain. *Neurology,* 62**,** 925-931.

INGLESE, J., KOCH, W. J., TOUHARA, K. & LEFKOWITZ, R. J. 1995. Gβγ interactions with PH domains and Ras-MAPK signaling pathways. *Trends in Biochemical Sciences,* 20**,** 151-156.

INGLIS, F. 2002. The tolerability and safety of cholinesterase inhibitors in the treatment of dementia. *International journal of clinical practice. Supplement*, 45-63.

IQBAL, K., ALONSO, A. D. C., CHEN, S., CHOHAN, M. O., EL-AKKAD, E., GONG, C.-X., KHATOON, S., LI, B., LIU, F. & RAHMAN, A. 2005. Tau pathology in Alzheimer disease and other tauopathies. *Biochimica et Biophysica Acta (BBA)-Molecular Basis of Disease,* 1739, 198-210.

IRIZARRY, M. C., MCNAMARA, M., FEDORCHAK, K., HSIAO, K. & HYMAN, B. T. 1997a. APPSw transgenic mice develop age-related Aβ deposits and neuropil abnormalities, but no neuronal loss in CA1. *Journal of Neuropathology & Experimental Neurology,* 56, 965-973.

IRIZARRY, M. C., SORIANO, F., MCNAMARA, M., PAGE, K. J., SCHENK, D., GAMES, D. & HYMAN, B. T. 1997b. Aβ deposition is associated with neuropil changes, but not with overt neuronal loss in the human amyloid precursor protein V717F (PDAPP) transgenic mouse. *Journal of Neuroscience,* 17, 7053-7059.

ISING, C., VENEGAS, C., ZHANG, S., SCHEIBLICH, H., SCHMIDT, S. V., VIEIRA-SAECKER, A., SCHWARTZ, S., ALBASSET, S., MCMANUS, R. M. & TEJERA, D. 2019. NLRP3 inflammasome activation drives tau pathology. *Nature,* 575, 669-673.

ISRAEL, M. A., YUAN, S. H., BARDY, C., REYNA, S. M., MU, Y., HERRERA, C., HEFFERAN, M. P., VAN GORP, S., NAZOR, K. L. & BOSCOLO, F. S. 2012. Probing sporadic and familial Alzheimer's disease using induced pluripotent stem cells. *Nature,* 482, 216-220.

ITO, H., KAWAMATA, Y., KAMIYA, M., TSUDA-SAKURAI, K., TANAKA, S., UENO, T., KOMATSU, T., HANAOKA, K., OKABE, S., MIURA, M. & URANO, Y. 2018. Red-Shifted Fluorogenic Substrate for Detection of lacZ-Positive Cells in Living Tissue with Single-Cell Resolution. *Angewandte Chemie International Edition,* 57, 15702-15706.

IWATSUBO, T. 2004. The γ-secretase complex: machinery for intramembrane proteolysis. *Current opinion in neurobiology,* 14, 379-383.

IYO, M., NAMBA, H., FUKUSHI, K., SHINOTOH, H., NAGATSUKA, S., SUHARA, T., SUDO, Y., SUZUKI, K. & IRIE, T. 1997. Measurement of acetylcholinesterase by positron emission tomography in the brains of healthy controls and patients with Alzheimer's disease. *The Lancet,* 349, 1805-1809.

JACK JR, C. R., KNOPMAN, D. S., JAGUST, W. J., PETERSEN, R. C., WEINER, M. W., AISEN, P. S., SHAW, L. M., VEMURI, P., WISTE, H. J. & WEIGAND, S. D. 2013. Tracking pathophysiological processes in Alzheimer's disease: an updated hypothetical model of dynamic biomarkers. *The Lancet Neurology,* 12, 207-216.

JACOBSEN, J. S., WU, C.-C., REDWINE, J. M., COMERY, T. A., ARIAS, R., BOWLBY, M., MARTONE, R., MORRISON, J. H., PANGALOS, M. N. & REINHART, P. H. 2006. Early-onset behavioral and synaptic deficits in a mouse model of Alzheimer's disease. *Proceedings of the National Academy of Sciences,* 103, 5161-5166.

JAKUBÍK, J., RANDÁKOVÁ, A., CHETVERIKOV, N., EL-FAKAHANY, E. E. & DOLEŽAL, V. 2020. The operational model of allosteric modulation of pharmacological agonism. *Sci Rep,* 10, 14421.

JANDA, C. Y., WAGHRAY, D., LEVIN, A. M., THOMAS, C. & GARCIA, K. C. 2012. Structural Basis of Wnt Recognition by Frizzled. *Science,* 337, 59-64.

JANKOWSKY, J. L. & ZHENG, H. 2017. Practical considerations for choosing a mouse model of Alzheimer's disease. *Molecular Neurodegeneration,* 12, 89.

JAY, F. F. & SCHNEIDER, M. R. 2014. A reporter mouse line with doxycyclin-inducible expression of β-glucosidase. *Histochemistry and Cell Biology,* 142, 721-724.

JEFFERIES, W. A., PRICE, K. A., BIRON, K. E., FENNINGER, F., PFEIFER, C. G. & DICKSTEIN, D. L. 2013. Adjusting the compass: new insights into the role of angiogenesis in Alzheimer's disease. *Alzheimer's Research & Therapy,* 5**,** 64.

JIANG, S., LI, Y., ZHANG, C., ZHAO, Y., BU, G., XU, H. & ZHANG, Y.-W. 2014. M1 muscarinic acetylcholine receptor in Alzheimer's disease. *Neuroscience Bulletin,* 30**,** 295-307.

JOLY-AMADO, A., SERRANEAU, K. S., BROWNLOW, M., MARÍN DE EVSIKOVA, C., SPEAKMAN, J. R., GORDON, M. N. & MORGAN, D. 2016. Metabolic changes over the course of aging in a mouse model of tau deposition. *Neurobiology of Aging,* 44**,** 62-73.

JONES, C. K., BRADY, A. E., DAVIS, A. A., XIANG, Z., BUBSER, M., TANTAWY, M. N., KANE, A. S., BRIDGES, T. M., KENNEDY, J. P. & BRADLEY, S. R. 2008. Novel selective allosteric activator of the M1 muscarinic acetylcholine receptor regulates amyloid processing and produces antipsychotic-like activity in rats. *Journal of Neuroscience,* 28**,** 10422-10433.

JUL, P., VOLBRACHT, C., DE JONG, I. E., HELBOE, L., ELVANG, A. B. & PEDERSEN, J. T. 2016. Hyperactivity with agitative-like behavior in a mouse tauopathy model. *Journal of Alzheimer's Disease,* 49**,** 783-795.

JURGA, A. M., PALECZNA, M. & KUTER, K. Z. 2020. Overview of general and discriminating markers of differential microglia phenotypes. *Frontiers in cellular neuroscience,* 14**,** 198.

KABIR, M. T., SUFIAN, M. A., UDDIN, M., BEGUM, M., AKHTER, S., ISLAM, A., MATHEW, B., ISLAM, M. & AMRAN, M. 2019. NMDA receptor antagonists: repositioning of memantine as a multitargeting agent for Alzheimer's therapy. *Current Pharmaceutical Design,* 25**,** 3506-3518.

KAESER, S. A., HERZIG, M. C., COOMARASWAMY, J., KILGER, E., SELENICA, M.-L., WINKLER, D. T., STAUFENBIEL, M., LEVY, E., GRUBB, A. & JUCKER, M. 2007. Cystatin C modulates cerebral β-amyloidosis. *Nature Genetics,* 39**,** 1437.

KAIN, S. R., ADAMS, M., KONDEPUDI, A., YANG, T. T., WARD, W. W. & KITTS, P. 1995. Green fluorescent protein as a reporter of gene expression and protein localization. *Biotechniques,* 19**,** 650-5.

KALBACK, W., WATSON, M. D., KOKJOHN, T. A., KUO, Y.-M., WEISS, N., LUEHRS, D. C., LOPEZ, J., BRUNE, D., SISODIA, S. S. & STAUFENBIEL, M. 2002. APP transgenic mice Tg2576 accumulate Aβ peptides that are distinct from the chemically modified and insoluble peptides deposited in Alzheimer's disease senile plaques. *Biochemistry,* 41**,** 922-928.

KAMBOH, M. I. 2004. Molecular genetics of late‐onset Alzheimer's disease. *Annals of human genetics,* 68**,** 381-404.

KAMPHUIS, W., MIDDELDORP, J., KOOIJMAN, L., SLUIJS, J. A., KOOI, E.-J., MOETON, M., FRERIKS, M., MIZEE, M. R. & HOL, E. M. 2014. Glial fibrillary acidic protein isoform expression in plaque related astrogliosis in Alzheimer's disease. *Neurobiology of Aging,* 35**,** 492-510.

KARCH, C. M. & GOATE, A. M. 2015. Alzheimer's disease risk genes and mechanisms of disease pathogenesis. *Biological psychiatry,* 77**,** 43-51.

KARP, N. A. & REAVEY, N. 2019. Sex bias in preclinical research and an exploration of how to change the status quo. *British Journal of Pharmacology,* 176**,** 4107-4118.

KARUNA THERAPEUTICS 2022. Karuna Therapeutics Announces Positive Results from Phase 3 EMERGENT-2 Trial of KarXT in Schizophrenia.

KAUSHAL, A., WANI, W. Y., ANAND, R. & GILL, K. D. 2013. Spontaneous and induced nontransgenic animal models of AD: modeling AD using combinatorial approach. *American Journal of Alzheimer's Disease & Other Dementias®,* 28**,** 318-326.

KE, M.-T., FUJIMOTO, S. & IMAI, T. 2013. SeeDB: a simple and morphology-preserving optical clearing agent for neuronal circuit reconstruction. *Nature neuroscience,* 16**,** 1154-1161.

KE, M.-T., NAKAI, Y., FUJIMOTO, S., TAKAYAMA, R., YOSHIDA, S., KITAJIMA, T. S., SATO, M. & IMAI, T. 2016. Super-resolution mapping of neuronal circuitry with an index-optimized clearing agent. *Cell reports,* 14**,** 2718-2732.

KENAKIN, T. 2002a. Drug Efficacy at G Protein–Coupled Receptors. *Annual Review of Pharmacology and Toxicology,* 42**,** 349-379.

KENAKIN, T. 2002b. Efficacy at G-protein-coupled receptors. *Nature Reviews Drug Discovery,* 1**,** 103-110.

KENAKIN, T. 2004. Allosteric modulators: the new generation of receptor antagonist. *Molecular interventions,* 4**,** 222.

KENT, S. A., SPIRES-JONES, T. L. & DURRANT, C. S. 2020. The physiological roles of tau and Aβ: implications for Alzheimer's disease pathology and therapeutics. *Acta Neuropathologica,* 140**,** 417-447.

KEOV, P., SEXTON, P. M. & CHRISTOPOULOS, A. 2011. Allosteric modulation of G protein-coupled receptors: A pharmacological perspective. *Neuropharmacology,* 60**,** 24-35.

KHAJEHALI, E., BRADLEY, S., VAN DER WESTHUIZEN, E. T., MOLLOY, C., VALANT, C., FINLAYSON, L., LINDSLEY, C. W., SEXTON, P. M., TOBIN, A. B. & CHRISTOPOULOS, A. 2020. Restoring Agonist Function at a Chemogenetically Modified M1 Muscarinic Acetylcholine Receptor. *ACS Chemical Neuroscience,* 11**,** 4270-4279.

KLINGBERG, A., HASENBERG, A., LUDWIG-PORTUGALL, I., MEDYUKHINA, A., MÄNN, L., BRENZEL, A., ENGEL, D. R., FIGGE, M. T., KURTS, C. & GUNZER, M. 2017. Fully Automated Evaluation of Total Glomerular Number and Capillary Tuft Size in Nephritic Kidneys Using Lightsheet Microscopy. *Journal of the American Society of Nephrology,* 28**,** 452.

KLUG, J., SNYDER, J. M., DARVAS, M., IMAI, D. M., CHURCH, M., LATIMER, C., KEENE, C. D. & LADIGES, W. 2020. Aging pet cats develop neuropathology similar to human Alzheimer's disease. *Aging Pathobiology and Therapeutics,* 2**,** 120-125.

KOHOUT, T. A., LIN, F.-T., PERRY, S. J., CONNER, D. A. & LEFKOWITZ, R. J. 2001. β-Arrestin 1 and 2 differentially regulate heptahelical receptor signaling and trafficking. *Proceedings of the National Academy of Sciences,* 98**,** 1601-1606.

KOLAKOWSKI, J. L. 1994. GCRDb: a G-protein-coupled receptor database. *Receptors & channels,* 2**,** 1-7.

KONDO, T., ASAI, M., TSUKITA, K., KUTOKU, Y., OHSAWA, Y., SUNADA, Y., IMAMURA, K., EGAWA, N., YAHATA, N. & OKITA, K. 2013. Modeling Alzheimer's disease with iPSCs reveals stress phenotypes associated with intracellular Aβ and differential drug responsiveness. *Cell stem cell,* 12**,** 487-496.

KOOISTRA, A. J., MORDALSKI, S., PÁNDY-SZEKERES, G., ESGUERRA, M., MAMYRBEKOV, A., MUNK, C., KESERŰ, G. M. & GLORIAM, DAVID E. 2021. GPCRdb in 2021: integrating GPCR sequence, structure and function. *Nucleic Acids Research,* 49**,** D335-D343.

KOTREDES, K. P., OBLAK, A. L., PREUSS, C., PANDEY, R. S., TERRITO, P. R., RIZZO, S. J. S., CARTER, G. W., SASNER, M., HOWELL, G. R. & LAMB, B. T. 2021. LOAD2: A late‐onset Alzheimer's disease mouse model expressing APOE ε4, Trem2* R47H, and humanized amyloid‐beta. *Alzheimer's & Dementia,* 17**,** e056017.

KRÄMER, M. S., FEIL, R. & SCHMIDT, H. 2021. Analysis of Gene Expression Using lacZ Reporter Mouse Lines. *In:* SINGH, S. R., HOFFMAN, R. M. & SINGH, A. (eds.) *Mouse Genetics : Methods and Protocols.* New York, NY: Springer US.

KRASNOPEROV, V. G., BITTNER, M. A., BEAVIS, R., KUANG, Y., SALNIKOW, K. V., CHEPURNY, O. G., LITTLE, A. R., PLOTNIKOV, A. N., WU, D. & HOLZ, R. W. 1997. α-Latrotoxin stimulates exocytosis by the interaction with a neuronal G-protein-coupled receptor. *Neuron,* 18**,** 925-937.

KRISHNAN, A., NIJMEIJER, S., GRAAF, C. D. & SCHIÖTH, H. B. 2016. Classification, nomenclature, and structural aspects of adhesion GPCRs. *Adhesion G Protein-Coupled Receptors***,** 15-41.

KRISTIANSEN, K. 2004. Molecular mechanisms of ligand binding, signaling, and regulation within the superfamily of G-protein-coupled receptors: molecular modeling and mutagenesis approaches to receptor structure and function. *Pharmacology & Therapeutics,* 103**,** 21-80.

KRUPNICK, J. G. & BENOVIC, J. L. 1998. The role of receptor kinases and arrestins in G protein-coupled receptor regulation. *Annual review of pharmacology and toxicology,* 38**,** 289.

KRUSE, A. C., HU, J., PAN, A. C., ARLOW, D. H., ROSENBAUM, D. M., ROSEMOND, E., GREEN, H. F., LIU, T., CHAE, P. S. & DROR, R. O. 2012. Structure and dynamics of the M3 muscarinic acetylcholine receptor. *Nature,* 482**,** 552.

KRUSE, A. C., KOBILKA, B. K., GAUTAM, D., SEXTON, P. M., CHRISTOPOULOS, A. & WESS, J. 2014. Muscarinic acetylcholine receptors: novel opportunities for drug development. *Nature Reviews Drug Discovery,* 13**,** 549-560.

KRUSE, A. C., RING, A. M., MANGLIK, A., HU, J., HU, K., EITEL, K., HÜBNER, H., PARDON, E., VALANT, C. & SEXTON, P. M. 2013. Activation and allosteric modulation of a muscarinic acetylcholine receptor. *Nature,* 504**,** 101-106.

KU, T., SWANEY, J., PARK, J.-Y., ALBANESE, A., MURRAY, E., CHO, J. H., PARK, Y.-G., MANGENA, V., CHEN, J. & CHUNG, K. 2016. Multiplexed and scalable super-resolution imaging of three-dimensional protein localization in size-adjustable tissues. *Nature biotechnology,* 34**,** 973-981.

KUBO, T., FUKUDA, K., MIKAMI, A., MAEDA, A., TAKAHASHI, H., MISHINA, M., HAGA, T., HAGA, K., ICHIYAMA, A. & KANGAWA, K. 1986. Cloning, sequencing and expression of complementary DNA encoding the muscarinic acetylcholine receptor. *Nature,* 323**,** 411-416.

KÜHN, H. & DREYER, W. J. 1972. Light dependent phosphorylation of rhodopsin by ATP. *FEBS letters,* 20**,** 1-6.

KÜHN, R., SCHWENK, F., AGUET, M. & RAJEWSKY, K. 1995. Inducible Gene Targeting in Mice. *Science,* 269**,** 1427-1429.

KUMAR, A., FONTANA, I. C. & NORDBERG, A. 2021. Reactive astrogliosis: A friend or foe in the pathogenesis of Alzheimer's disease. *Journal of Neurochemistry,* n/a.

KUO, Y.-M., KOKJOHN, T. A., BEACH, T. G., SUE, L. I., BRUNE, D., LOPEZ, J. C., KALBACK, W. M., ABRAMOWSKI, D., STURCHLER-PIERRAT, C. & STAUFENBIEL, M. 2001. Comparative analysis of amyloid-β chemical structure and amyloid plaque morphology of transgenic mouse and Alzheimer's disease brains. *Journal of Biological Chemistry,* 276**,** 12991-12998.

KUPERSTEIN, I., BROERSEN, K., BENILOVA, I., ROZENSKI, J., JONCKHEERE, W., DEBULPAEP, M., VANDERSTEEN, A., SEGERS‐NOLTEN, I., VAN DER WERF, K. & SUBRAMANIAM, V. 2010. Neurotoxicity of Alzheimer's disease Aβ peptides is induced by small changes in the Aβ42 to Aβ40 ratio. *The EMBO journal,* 29**,** 3408-3420.

LAFERLA, F. M. & GREEN, K. N. 2012. Animal models of Alzheimer disease. *Cold Spring Harbor perspectives in medicine,* 2**,** a006320.

LAGERSTRÖM, M. C. & SCHIÖTH, H. B. 2008. Structural diversity of G protein-coupled receptors and significance for drug discovery. *Nature reviews Drug discovery,* 7**,** 339-357.

LAMBRIGHT, D. G., SONDEK, J., BOHM, A., SKIBA, N. P., HAMM, H. E. & SIGLER, P. B. 1996. The 2.0 Å crystal structure of a heterotrimeric G protein. *Nature,* 379**,** 311-319.

LANE, J. R., SEXTON, P. M. & CHRISTOPOULOS, A. 2013. Bridging the gap: bitopic ligands of G-protein-coupled receptors. *Trends in pharmacological sciences,* 34**,** 59-66.

LANGE, H. S., CANNON, C. E., DROTT, J. T., KUDUK, S. D. & USLANER, J. M. 2015. The M1 muscarinic positive allosteric modulator PQCA improves performance on translatable tests of memory and attention in rhesus monkeys. *Journal of Pharmacology and Experimental Therapeutics,* 355**,** 442-450.

LANOISELÉE, H.-M., NICOLAS, G., WALLON, D., ROVELET-LECRUX, A., LACOUR, M., ROUSSEAU, S., RICHARD, A.-C., PASQUIER, F., ROLLIN-SILLAIRE, A. & MARTINAUD, O. 2017. APP, PSEN1, and PSEN2 mutations in early-onset Alzheimer disease: A genetic screening study of familial and sporadic cases. *PLoS medicine,* 14**,** e1002270.

LAPORTE, S. A., OAKLEY, R. H., ZHANG, J., HOLT, J. A., FERGUSON, S. S., CARON, M. G. & BARAK, L. S. 1999. The β2-adrenergic receptor/βarrestin complex recruits the clathrin adaptor AP-2 during endocytosis. *Proceedings of the National Academy of Sciences,* 96**,** 3712-3717.

LASCHET, C., DUPUIS, N. & HANSON, J. 2018. The G protein-coupled receptors deorphanization landscape. *Biochemical Pharmacology,* 153**,** 62-74.

LAU, C., NG, L., THOMPSON, C., PATHAK, S., KUAN, L., JONES, A. & HAWRYLYCZ, M. 2008. Exploration and visualization of gene expression with neuroanatomy in the adult mouse brain. *BMC Bioinformatics,* 9**,** 153.

LAWLOR, P. A. & YOUNG, D. 2011. Aβ infusion and related models of Alzheimer dementia. *Animal models of Dementia.* Springer.

LEBOIS, E. P., DIGBY, G. J., SHEFFLER, D. J., MELANCON, B. J., TARR, J. C., CHO, H. P., MILLER, N. R., MORRISON, R., BRIDGES, T. M. & XIANG, Z. 2011. Development of a highly selective, orally bioavailable and CNS penetrant M1 agonist derived from the MLPCN probe ML071. *Bioorganic & medicinal chemistry letters,* 21**,** 6451-6455.

LEBOIS, E. P., SCHROEDER, J. P., ESPARZA, T. J., BRIDGES, T. M., LINDSLEY, C. W., CONN, P. J., BRODY, D. L., DANIELS, J. S. & LEVEY, A. I. 2017. Disease-modifying effects of M1 muscarinic acetylcholine receptor activation in an Alzheimer's disease mouse model. *ACS chemical neuroscience,* 8**,** 1177-1187.

LEBOIS, E. P., THORN, C., EDGERTON, J. R., POPIOLEK, M. & XI, S. 2018. Muscarinic receptor subtype distribution in the central nervous system and relevance to aging and Alzheimer's disease. *Neuropharmacology,* 136**,** 362-373.

LEBOIS, E. P., TRIMPER, J. B., HU, C., LEVEY, A. I. & MANNS, J. R. 2016. Effects of Selective M1 Muscarinic Receptor Activation on Hippocampal Spatial Representations and Neuronal Oscillations. *ACS Chemical Neuroscience,* 7**,** 1393-1405.

LEBON, G., LANGMEAD, C. J., TEHAN, B. G. & HULME, E. C. 2009. Mutagenic Mapping Suggests a Novel Binding Mode for Selective Agonists of M1 Muscarinic Acetylcholine Receptors. *Molecular Pharmacology,* 75**,** 331.

LEDOUX, J. E., SAKAGUCHI, A. & REIS, D. J. 1984. Subcortical efferent projections of the medial geniculate nucleus mediate emotional responses conditioned to acoustic stimuli. *Journal of Neuroscience,* 4**,** 683-698.

LEE, D. A. & HIGGINBOTHAM, E. J. 2005. Glaucoma and its treatment: A review. *American Journal of Health-System Pharmacy,* 62**,** 691-699.

LEE, S. K. 2018. Sex as an important biological variable in biomedical research. *BMB Rep,* 51**,** 167-173.

LEE, Y., BASITH, S. & CHOI, S. 2018. Recent Advances in Structure-Based Drug Design Targeting Class A G Protein-Coupled Receptors Utilizing Crystal Structures and Computational Simulations. *Journal of Medicinal Chemistry,* 61**,** 1-46.

LEFKOWITZ, R. 2007. Seven transmembrane receptors: something old, something new. *Acta physiologica,* 190**,** 9-19.

LEVEY, A. I. 1993. Immunological localization of m1–m5 muscarinic acetylcholine receptors in peripheral tissues and brain. *Life Sciences,* 52**,** 441-448.

LEVEY, A. I., EDMUNDS, S. M., KOLIATSOS, V., WILEY, R. G. & HEILMAN, C. J. 1995. Expression of m1-m4 muscarinic acetylcholine receptor proteins in rat hippocampus and regulation by cholinergic innervation. *Journal of Neuroscience,* 15**,** 4077-4092.

LEVEY, A. I., KITT, C., SIMONDS, W., PRICE, D. & BRANN, M. 1991. Identification and localization of muscarinic acetylcholine receptor proteins in brain with subtype-specific antibodies. *Journal of Neuroscience,* 11**,** 3218-3226.

LEVY, E., JASKOLSKI, M. & GRUBB, A. 2006. The Role of Cystatin C in Cerebral Amyloid Angiopathy and Stroke: Cell Biology and Animal Models. *Brain Pathology,* 16**,** 60-70.

LEVY, E., SASTRE, M., KUMAR, A., GALLO, G., PICCARDO, P., GHETTI, B. & TAGLIAVINI, F. 2001. Codeposition of Cystatin C with Amyloid-β Protein in the Brain of Alzheimer Disease Patients. *Journal of Neuropathology & Experimental Neurology,* 60**,** 94-104.

LEWIS, J., MCGOWAN, E., ROCKWOOD, J., MELROSE, H., NACHARAJU, P., VAN SLEGTENHORST, M., GWINN-HARDY, K., MURPHY, M. P., BAKER, M. & YU, X. 2000. Neurofibrillary tangles, amyotrophy and progressive motor disturbance in mice expressing mutant (P301L) tau protein. *Nature genetics,* 25**,** 402-405.

LI, J., XIANG, B., SU, W., ZHANG, X., HUANG, Y. & MA, L. 2003. Agonist-induced formation of opioid receptor-G protein-coupled receptor kinase (GRK)-Gβγ complex on membrane is required for GRK2 function in vivo. *Journal of Biological Chemistry,* 278**,** 30219-30226.

LI, S., CHEN, L.-X., PENG, X.-H., WANG, C., QIN, B.-Y., TAN, D., HAN, C.-X., YANG, H., REN, X.-N., LIU, F., XU, C.-H. & ZHOU, X.-H. 2018. Overview of the reporter genes and reporter mouse models. *Animal Models and Experimental Medicine,* 1**,** 29-35.

LI, Y., STERNWEIS, P. M., CHARNECKI, S., SMITH, T. F., GILMAN, A. G., NEER, E. J. & KOZASA, T. 1998. Sites for Gα binding on the G protein β subunit overlap with sites for regulation of phospholipase Cβ and adenylyl cyclase. *Journal of Biological Chemistry,* 273**,** 16265-16272.

LIEBMANN, T., RENIER, N., BETTAYEB, K., GREENGARD, P., TESSIER-LAVIGNE, M. & FLAJOLET, M. 2016. Three-dimensional study of Alzheimer's disease hallmarks using the iDISCO clearing method. *Cell reports,* 16**,** 1138-1152.

LIN, H.-H., STACEY, M., SAXBY, C., KNOTT, V., CHAUDHRY, Y., EVANS, D., GORDON, S., MCKNIGHT, A. J., HANDFORD, P. & LEA, S. 2001. Molecular analysis of the epidermal growth factor-like short consensus repeat domain-

mediated protein-protein interactions: dissection of the CD97-CD55 complex. *Journal of Biological Chemistry,* 276**,** 24160-24169.

LIN, L., GEORGIEVSKA, B., MATTSSON, A. & ISACSON, O. 1999. Cognitive changes and modified processing of amyloid precursor protein in the cortical and hippocampal system after cholinergic synapse loss and muscarinic receptor activation. *Proceedings of the National Academy of Sciences,* 96**,** 12108-12113.

LIU, Y., BEYER, A. & AEBERSOLD, R. 2016. On the Dependency of Cellular Protein Levels on mRNA Abundance. *Cell,* 165**,** 535-550.

LOGOTHETIS, D. E., KURACHI, Y., GALPER, J., NEER, E. J. & CLAPHAM, D. E. 1987. The βγ subunits of GTP-binding proteins activate the muscarinic K+ channel in heart. *Nature,* 325**,** 321-326.

LONG, J. Z., LACKAN, C. S. & HADJANTONAKIS, A.-K. 2005. Genetic and spectrally distinct in vivoimaging: embryonic stem cells and mice with widespread expression of a monomeric red fluorescent protein. *BMC biotechnology,* 5**,** 1-11.

LUTTRELL, L. M. 2008. Reviews in Molecular Biology and Biotechnology: Transmembrane Signaling by G Protein-Coupled Receptors. *Molecular Biotechnology,* 39**,** 239-264.

LYTHGOE, M. P., JENEI, K. & PRASAD, V. 2022. Regulatory decisions diverge over aducanumab for Alzheimer's disease. British Medical Journal Publishing Group.

MA, L., SEAGER, M. A., WITTMANN, M., JACOBSON, M., BICKEL, D., BURNO, M., JONES, K., GRAUFELDS, V. K., XU, G. & PEARSON, M. 2009. Selective activation of the M1 muscarinic acetylcholine receptor achieved by allosteric potentiation. *Proceedings of the National Academy of Sciences,* 106**,** 15950-15955.

MACHADO, A., FERREIRA, D., GROTHE, M. J., EYJOLFSDOTTIR, H., ALMQVIST, P. M., CAVALLIN, L., LIND, G., LINDEROTH, B., SEIGER, Å., TEIPEL, S., WAHLBERG, L. U., WAHLUND, L.-O., WESTMAN, E., ERIKSDOTTER, M. & FOR THE ALZHEIMER'S DISEASE NEUROIMAGING, I. 2020. The cholinergic system in subtypes of Alzheimer's disease: an in vivo longitudinal MRI study. *Alzheimer's Research & Therapy,* 12**,** 51.

MAEDA, S., QU, Q., ROBERTSON, M. J., SKINIOTIS, G. & KOBILKA, B. K. 2019. Structures of the M1 and M2 muscarinic acetylcholine receptor/G-protein complexes. *Science,* 364**,** 552-557.

MALITSCHEK, B., SCHWEIZER, C., KEIR, M., HEID, J., FROESTL, W., MOSBACHER, J., KUHN, R., HENLEY, J., JOLY, C., PIN, J. P., KAUPMANN, K. & BETTLER, B. 1999. The N-terminal domain of γ-aminobutyric acid(B) receptors is sufficient to specify agonist and antagonist binding. *Molecular Pharmacology,* 56**,** 448-454.

MALLUCCI, G. R., WHITE, M. D., FARMER, M., DICKINSON, A., KHATUN, H., POWELL, A. D., BRADNER, S., JEFFERYS, J. G. R. & COLLINGE, J. 2007. Targeting cellular prion protein reverses early cognitive deficits and neurophysiological dysfunction in prion-infected mice. *Neuron*, 53(3), 325-335.

MALLUCCI, G. R. 2009. Prion neurodegeneration: starts and stops at the synapse. *Prion*, 3(4), 195-201.

MANI, B. K., WALKER, A. K., LOPEZ SOTO, E. J., RAINGO, J., LEE, C. E., PERELLÓ, M., ANDREWS, Z. B. & ZIGMAN, J. M. 2014. Neuroanatomical characterization of a growth hormone secretagogue receptor-green fluorescent protein reporter mouse. *Journal of Comparative Neurology,* 522**,** 3644-3666.

MANSOUR, S. L., THOMAS, K. R. & CAPECCHI, M. R. 1988. Disruption of the proto-oncogene int-2 in mouse embryo-derived stem cells: a general strategy for targeting mutations to non-selectable genes. *Nature,* 336**,** 348-352.

MARINO, M. J., ROUSE, S. T., LEVEY, A. I., POTTER, L. T. & CONN, P. J. 1998. Activation of the genetically defined m1 muscarinic receptor potentiates N-methyl-D-aspartate (NMDA) receptor currents in hippocampal pyramidal cells. *Proc Natl Acad Sci U S A,* 95**,** 11465-70.

MARSANGO, S., JENKINS, L., PEDIANI, J. D., BRADLEY, S. J., WARD, R. J., HESSE, S., BIENER, G., STONEMAN, M. R., TOBIN, A. B. & RAICU, V. 2022. The M 1 muscarinic receptor is present in situ as a ligand-regulated mixture of monomers and oligomeric complexes. *Proceedings of the National Academy of Sciences of the United States of America,* 119**,** e2201103119.

MARTINEZ-AGUILA, A., FONSECA, B., HERNANDEZ, F., DÍAZ-HERNANDEZ, M., AVILA, J. & PINTOR, J. 2014. Tau triggers tear secretion by interacting with muscarinic acetylcholine receptors in New Zealand white rabbits. *Journal of Alzheimer's disease : JAD,* 40 Suppl 1**,** S71-7.

MARTINI-STOICA, H., COLE, A. L., SWARTZLANDER, D. B., CHEN, F., WAN, Y.-W., BAJAJ, L., BADER, D. A., LEE, V. M., TROJANOWSKI, J. Q. & LIU, Z. 2018. TFEB enhances astroglial uptake of extracellular tau species and reduces tau spreading. *Journal of Experimental Medicine,* 215**,** 2355-2377.

MARUCCI, G., BUCCIONI, M., BEN, D. D., LAMBERTUCCI, C., VOLPINI, R. & AMENTA, F. 2021. Efficacy of acetylcholinesterase inhibitors in Alzheimer's disease. *Neuropharmacology,* 190**,** 108352.

MASH, D. & POTTER, L. 1986. Autoradiographic localization of M1 and M2 muscarine receptors in the rat brain. *Neuroscience,* 19**,** 551-564.

MASH, D. C., FLYNN, D. D. & POTTER, L. T. 1985. Loss of M2 muscarine receptors in the cerebral cortex in Alzheimer's disease and experimental cholinergic denervation. *Science,* 228**,** 1115-1117.

MASH, D. C., WHITE, W. F. & MESULAM, M. M. 1988. Distribution of muscarinic receptor subtypes within architectonic subregions of the primate cerebral cortex. *Journal of Comparative Neurology,* 278**,** 265-274.

MATSUNAMI, H., MONTMAYEUR, J.-P. & BUCK, L. B. 2000. A family of candidate taste receptors in human and mouse. *Nature,* 404**,** 601-604.

MCCOMB, R. D., MILLER, K. A. & CARSON, S. D. 1991. Tissue factor antigen in senile plaques of Alzheimer's disease. *Am J Pathol,* 139**,** 491-4.

MCCUDDEN, C. R., HAINS, M. D., KIMPLE, R. J., SIDEROVSKI, D. P. & WILLARD, F. S. 2005. G-protein signaling: back to the future. *Cellular and Molecular Life Sciences,* 62**,** 551-577.

MCDONALD, P. H., CHOW, C.-W., MILLER, W. E., LAPORTE, S. A., FIELD, M. E., LIN, F.-T., DAVIS, R. J. & LEFKOWITZ, R. J. 2000. β-Arrestin 2: a receptor-regulated MAPK scaffold for the activation of JNK3. *Science,* 290**,** 1574-1577.

MCLATCHIE, L. M., FRASER, N. J., MAIN, M. J., WISE, A., BROWN, J., THOMPSON, N., SOLARI, R., LEE, M. G. & FOORD, S. M. 1998. RAMPs regulate the transport and ligand specificity of the calcitonin-receptor-like receptor. *Nature,* 393**,** 333-339.

MCLELLAN, M. A., ROSENTHAL, N. A. & PINTO, A. R. 2017. Cre-loxP-Mediated Recombination: General Principles and Experimental Considerations. *Current Protocols in Mouse Biology,* 7**,** 1-12.

MEDEIROS, R., BAGLIETTO‐VARGAS, D. & LAFERLA, F. M. 2011a. The role of tau in Alzheimer's disease and related disorders. *CNS neuroscience & therapeutics,* 17**,** 514-524.

MEDEIROS, R., KITAZAWA, M., CACCAMO, A., BAGLIETTO-VARGAS, D., ESTRADA-HERNANDEZ, T., CRIBBS, D. H., FISHER, A. & LAFERLA, F. M. 2011b. Loss of Muscarinic M1 Receptor Exacerbates Alzheimer's Disease–Like Pathology and Cognitive Decline. *The American journal of pathology,* 179**,** 980-991.

MELANCON, B. J., TARR, J. C., PANARESE, J. D., WOOD, M. R. & LINDSLEY, C. W. 2013. Allosteric modulation of the M1 muscarinic acetylcholine receptor: improving cognition and a potential treatment for schizophrenia and Alzheimer's disease. *Drug Discovery Today,* 18**,** 1185-1199.

MESULAM, M.-M. 2004. The cholinergic innervation of the human cerebral cortex. *Progress in brain research,* 145**,** 67-78.

MESULAM, M., MUFSON, E., WAINER, B. & LEVEY, A. 1983a. Central cholinergic pathways in the rat: an overview based on an alternative nomenclature (Ch1–Ch6). *Neuroscience,* 10**,** 1185-1201.

MESULAM, M., MUFSON, E. J., LEVEY, A. I. & WAINER, B. H. 1983b. Cholinergic innervation of cortex by the basal forebrain: cytochemistry and cortical connections of the septal area, diagonal band nuclei, nucleus basalis (substantia innominata), and hypothalamus in the rhesus monkey. *Journal of Comparative Neurology,* 214**,** 170-197.

METZGER, D. & CHAMBON, P. 2001. Site-and time-specific gene targeting in the mouse. *Methods,* 24**,** 71-80.

MEYER-LUEHMANN, M., COOMARASWAMY, J., BOLMONT, T., KAESER, S., SCHAEFER, C., KILGER, E., NEUENSCHWANDER, A., ABRAMOWSKI, D., FREY, P. & JATON, A. L. 2006. Exogenous induction of cerebral ß-amyloidogenesis is governed by agent and host. *Science,* 313**,** 1781-1784.

MI, W., PAWLIK, M., SASTRE, M., JUNG, S. S., RADVINSKY, D. S., KLEIN, A. M., SOMMER, J., SCHMIDT, S. D., NIXON, R. A., MATHEWS, P. M. & LEVY, E. 2007. Cystatin C inhibits amyloid-β deposition in Alzheimer's disease mouse models. *Nature Genetics,* 39**,** 1440.

MIDDELDORP, J. & HOL, E. M. 2011. GFAP in health and disease. *Progress in Neurobiology,* 93**,** 421-443.

MILGRAM, N. W., HEAD, E., WEINER, E. & THOMAS, E. 1994. Cognitive functions and aging in the dog: acquisition of nonspatial visual tasks. *Behavioral neuroscience,* 108**,** 57.

MILLER, S. G. & KENNEDY, M. B. 1985. Distinct forebrain and cerebellar isozymes of type II Ca2+/calmodulin-dependent protein kinase associate differently with the postsynaptic density fraction. *Journal of Biological Chemistry,* 260**,** 9039-9046.

MILLER, Y., MA, B. & NUSSINOV, R. 2011. Synergistic interactions between repeats in tau protein and Aβ amyloids may be responsible for accelerated aggregation via polymorphic states. *Biochemistry,* 50**,** 5172-5181.

MILLIGAN, G. & KOSTENIS, E. 2006. Heterotrimeric G-proteins: a short history. *British Journal of Pharmacology,* 147**,** S46-S55.

MINTER, M. R., TAYLOR, J. M. & CRACK, P. J. 2016. The contribution of neuroinflammation to amyloid toxicity in Alzheimer's disease. *Journal of neurochemistry,* 136**,** 457-474.

MIYAKAWA, T., YAMADA, M., DUTTAROY, A. & WESS, J. 2001. Hyperactivity and intact hippocampus-dependent learning in mice lacking the M1 muscarinic acetylcholine receptor. *Journal of Neuroscience,* 21**,** 5239-5250.

MJ DEACON, R., J ALTIMIRAS, F., A BAZAN-LEON, E., D PYARASANI, R., M NACHTIGALL, F., S SANTOS, L., G TSOLAKI, A., PEDNEKAR, L., KISHORE, U. & R BIEKOFSKY, R. 2015. Natural AD-Like neuropathology in Octodon degus: impaired burrowing and neuroinflammation. *Current Alzheimer Research,* 12**,** 314-322.

MOLBAY, M., KOLABAS, Z. I., TODOROV, M. I., OHN, T.-L. & ERTÜRK, A. 2021. A guidebook for DISCO tissue clearing. *Molecular Systems Biology,* 17**,** e9807.

MOLCHAN, S. E., MARTINEZ, R. A., HILL, J. L., WEINGARTNER, H. J., THOMPSON, K., VITIELLO, B. & SUNDERLAND, T. 1992. Increased cognitive sensitivity to scopolamine with age and a perspective on the scopolamine model. *Brain Research Reviews,* 17**,** 215-226.

MORAN, P. 1993. Differential effects of scopolamine and mecamylamine on working and reference memory in the rat. *Pharmacology Biochemistry and Behavior,* 45**,** 533-538.

MORAN, S. P., DICKERSON, J. W., CHO, H. P., XIANG, Z., MAKSYMETZ, J., REMKE, D. H., LV, X., DOYLE, C. A., RAJAN, D. H. & NISWENDER, C. M. 2018. M1-positive allosteric modulators lacking agonist activity provide the optimal profile for enhancing cognition. *Neuropsychopharmacology,* 43**,** 1763-1771.

MOREIRA, P. I., CARVALHO, C., ZHU, X., SMITH, M. A. & PERRY, G. 2010. Mitochondrial dysfunction is a trigger of Alzheimer's disease pathophysiology. *Biochimica et Biophysica Acta (BBA) - Molecular Basis of Disease,* 1802**,** 2-10.

MOUSSA-PACHA, N. M., ABDIN, S. M., OMAR, H. A., ALNISS, H. & AL-TEL, T. H. 2020. BACE1 inhibitors: Current status and future directions in treating Alzheimer's disease. *Medicinal Research Reviews,* 40**,** 339-384.

MULLIGAN, M. K., PONOMAREV, I., BOEHM, S., OWEN, J. A., LEVIN, P. S., BERMAN, A. E., BLEDNOV, Y. A., CRABBE, J., WILLIAMS, R. & MILES, M. 2008. Alcohol trait and transcriptional genomic analysis of C57BL/6 substrains. *Genes, Brain and Behavior,* 7**,** 677-689.

MURATORE, C. R., RICE, H. C., SRIKANTH, P., CALLAHAN, D. G., SHIN, T., BENJAMIN, L. N., WALSH, D. M., SELKOE, D. J. & YOUNG-PEARSE, T. L. 2014. The familial Alzheimer's disease APPV717I mutation alters APP processing and Tau expression in iPSC-derived neurons. *Human molecular genetics,* 23**,** 3523-3536.

MUZUMDAR, M. D., TASIC, B., MIYAMICHI, K., LI, L. & LUO, L. 2007. A global double‐fluorescent Cre reporter mouse. *genesis,* 45**,** 593-605.

NAKAMURA, S., MURAYAMA, N., NOSHITA, T., ANNOURA, H. & OHNO, T. 2001. Progressive brain dysfunction following intracerebroventricular infusion of beta1–42-amyloid peptide. *Brain research,* 912**,** 128-136.

NARAYAN, P., HOLMSTRÖM, K. M., KIM, D.-H., WHITCOMB, D. J., WILSON, M. R., ST. GEORGE-HYSLOP, P., WOOD, N. W., DOBSON, C. M., CHO, K. & ABRAMOV, A. Y. 2014. Rare individual amyloid-β oligomers act on astrocytes to initiate neuronal damage. *Biochemistry,* 53**,** 2442-2453.

NATHAN, P. J., WATSON, J., LUND, J., DAVIES, C. H., PETERS, G., DODDS, C. M., SWIRSKI, B., LAWRENCE, P., BENTLEY, G. D. & O'NEILL, B. V. 2013. The potent M1 receptor allosteric agonist GSK1034702 improves episodic memory in humans in the nicotine abstinence model of cognitive dysfunction. *International Journal of Neuropsychopharmacology,* 16**,** 721-731.

NEUGROSCHL, J. & WANG, S. 2011. Alzheimer's disease: diagnosis and treatment across the spectrum of disease severity. *The Mount Sinai journal of medicine, New York,* 78**,** 596-612.

NGUYEN, M. L., COX, G. D. & PARSONS, S. M. 1998. Kinetic parameters for the vesicular acetylcholine transporter: two protons are exchanged for one acetylcholine. *Biochemistry,* 37**,** 13400-13410.

NIEBERLER, M., KITTEL, R. J., PETRENKO, A. G., LIN, H.-H. & LANGENHAN, T. 2016. Control of Adhesion GPCR Function Through Proteolytic Processing. *In:* LANGENHAN, T. & SCHÖNEBERG, T. (eds.) *Adhesion G Protein-coupled Receptors: Molecular, Physiological and Pharmacological Principles in Health and Disease.* Cham: Springer International Publishing.

NIELSEN, H. M., MINTHON, L., LONDOS, E., BLENNOW, K., MIRANDA, E., PEREZ, J., CROWTHER, D., LOMAS, D. & JANCIAUSKIENE, S. 2007. Plasma and CSF serpins in Alzheimer disease and dementia with Lewy bodies. *Neurology,* 69**,** 1569-1579.

NITSCH, R. M., DENG, M., TENNIS, M., SCHOENFELD, D. & GROWDON, J. H. 2000. The selective muscarinic M1 agonist AF102B decreases levels of total Aβ in cerebrospinal fluid of patients with Alzheimer's disease. *Annals of neurology,* 48**,** 913-918.

NITSCH, R. M., SLACK, B. E., WURTMAN, R. J. & GROWDON, J. H. 1992. Release of Alzheimer amyloid precursor derivatives stimulated by activation of muscarinic acetylcholine receptors. *Science,* 258**,** 304-307.

NORMAN, C. L., GOULD, R. W., BRAGG, C., LINDSLEY, C. W., JONES, C. K. & NADER, M. A. 2020. The Effects of the M1 Muscarinic Acetylcholine Receptor Positive Allosteric Modulator VU0486846 on Cognitive Performance in Aged Nonhuman Primates. *The FASEB Journal,* 34**,** 1-1.

NØRSKOV-LAURITSEN, L., THOMSEN, A. R. B. & BRÄUNER-OSBORNE, H. 2014. G Protein-Coupled Receptor Signaling Analysis Using Homogenous Time-Resolved Förster Resonance Energy Transfer (HTRF®) Technology. *International Journal of Molecular Sciences,* 15**,** 2554-2572.

NUNOMURA, A., PERRY, G., ALIEV, G., HIRAI, K., TAKEDA, A., BALRAJ, E. K., JONES, P. K., GHANBARI, H., WATAYA, T. & SHIMOHAMA, S. 2001. Oxidative damage is the earliest event in Alzheimer disease. *Journal of Neuropathology & Experimental Neurology,* 60**,** 759-767.

O'HARA, P. J., SHEPPARD, P. O., THÓGERSEN, H., VENEZIA, D., HALDEMAN, B. A., MCGRANE, V., HOUAMED, K. M., THOMSEN, C., GILBERT, T. L. & MULVIHILL, E. R. 1993. The ligand-binding domain in metabotropic glutamate receptors is related to bacterial periplasmic binding proteins. *Neuron,* 11**,** 41-52.

OAKLEY, R. H., LAPORTE, S. A., HOLT, J. A., BARAK, L. S. & CARON, M. G. 1999. Association of β-Arrestin with G Protein-coupled Receptors during Clathrin-mediated Endocytosis Dictates the Profile of Receptor Resensitization. *Journal of Biological Chemistry,* 274**,** 32248-32257.

ODDO, S., CACCAMO, A., KITAZAWA, M., TSENG, B. P. & LAFERLA, F. M. 2003a. Amyloid deposition precedes tangle formation in a triple transgenic model of Alzheimer's disease. *Neurobiology of aging,* 24**,** 1063-1070.

ODDO, S., CACCAMO, A., SHEPHERD, J. D., MURPHY, M. P., GOLDE, T. E., KAYED, R., METHERATE, R., MATTSON, M. P., AKBARI, Y. & LAFERLA, F. M. 2003b. Triple-transgenic model of Alzheimer's disease with plaques and tangles: intracellular Aβ and synaptic dysfunction. *Neuron,* 39**,** 409-421.

OECKL, P., ANDERL-STRAUB, S., VON ARNIM, C. A. F., BALDEIRAS, I., DIEHL-SCHMID, J., GRIMMER, T., HALBGEBAUER, S., KORT, A. M., LIMA, M., MARQUES, T. M., ORTNER, M., SANTANA, I., STEINACKER, P., VERBEEK, M. M., VOLK, A. E., LUDOLPH, A. C. & OTTO, M. 2022. Serum GFAP differentiates Alzheimer's disease from frontotemporal dementia and predicts MCI-to-dementia conversion. *Journal of Neurology, Neurosurgery & Psychiatry,* 93**,** 659.

OKABE, M., IKAWA, M., KOMINAMI, K., NAKANISHI, T. & NISHIMUNE, Y. 1997. Green mice'as a source of ubiquitous green cells. *FEBS letters,* 407**,** 313-319.

OKAMOTO, T., SEKIYAMA, N., OTSU, M., SHIMADA, Y., SATO, A., NAKANISHI, S. & JINGAMI, H. 1998. Expression and purification of the extracellular ligand binding region of metabotropic glutamate receptor subtype 1. *Journal of Biological Chemistry,* 273**,** 13089-13096.

OKUDA, T., HAGA, T., KANAI, Y., ENDOU, H., ISHIHARA, T. & KATSURA, I. 2000. Identification and characterization of the high-affinity choline transporter. *Nature neuroscience,* 3**,** 120-125.

OLDHAM, W. M. & HAMM, H. E. 2006. Structural basis of function in heterotrimeric G proteins. *Quarterly reviews of biophysics,* 39**,** 117-166.

OTERO-GARCIA, M., MAHAJANI, S. U., WAKHLOO, D., TANG, W., XUE, Y.-Q., MORABITO, S., PAN, J., OBERHAUSER, J., MADIRA, A. E., SHAKOURI, T., DENG, Y., ALLISON, T., HE, Z., LOWRY, W. E., KAWAGUCHI, R., SWARUP, V. & COBOS, I. 2022. Molecular signatures underlying neurofibrillary tangle susceptibility in Alzheimer's disease. *Neuron,* 110**,** 2929-2948.e8.

OTSU, N. 1979. A threshold selection method from gray-level histograms. *IEEE transactions on systems, man, and cybernetics,* 9**,** 62-66.

PALCZEWSKI, K., KUMASAKA, T., HORI, T., BEHNKE, C. A., MOTOSHIMA, H., FOX, B. A., LE TRONG, I., TELLER, D. C., OKADA, T. & STENKAMP, R. E. 2000. Crystal structure of rhodopsin: AG protein-coupled receptor. *science,* 289**,** 739-745.

PANDEY, R. S., KOTREDES, K., PREUSS, C., OBLAK, A. L., LAMB, B. T., HOWELL, G. R., SASNER, M. & CARTER, G. W. Transcriptomic Profiling of APOE4/Trem2* R47H Mouse Models for Late Onset Alzheimer's Disease. 2020 Alzheimer's Association International Conference, 2020. ALZ.

PANZA, F., SOLFRIZZI, V., SERIPA, D., IMBIMBO, B. P., LOZUPONE, M., SANTAMATO, A., ZECCA, C., BARULLI, M. R., BELLOMO, A., PILOTTO, A., DANIELE, A., GRECO, A. & LOGROSCINO, G. 2016. Tau-Centric Targets and Drugs in Clinical Development for the Treatment of Alzheimer's Disease. *BioMed Research International,* 2016**,** 3245935.

PAPAIOANNOU, N., TOOTEN, P. C., VAN EDEREN, A. M., BOHL, J. R., ROFINA, J., TSANGARIS, T. & GRUYS, E. 2001. Immunohistochemical investigation of the brain of aged dogs. I. Detection of neurofibrillary tangles and of 4-hydroxynonenal protein, an oxidative damage product, in senile plaques. *Amyloid,* 8**,** 11-21.

PARK, J., WETZEL, I., MARRIOTT, I., DRÉAU, D., D'AVANZO, C., KIM, D. Y., TANZI, R. E. & CHO, H. 2018. A 3D human triculture system modeling neurodegeneration and neuroinflammation in Alzheimer's disease. *Nature Neuroscience,* 21**,** 941-951.

PASCOAL, T. A., BENEDET, A. L., ASHTON, N. J., KANG, M. S., THERRIAULT, J., CHAMOUN, M., SAVARD, M., LUSSIER, F. Z., TISSOT, C. & KARIKARI, T. K. 2021. Microglial activation and tau propagate jointly across Braak stages. *Nature medicine,* 27**,** 1592-1599.

PEREA, J. R., LÓPEZ, E., DÍEZ-BALLESTEROS, J. C., ÁVILA, J., HERNÁNDEZ, F. & BOLÓS, M. 2019. Extracellular monomeric tau is internalized by astrocytes. *Frontiers in neuroscience,* 13**,** 442.

PEREIRA, J. B., JANELIDZE, S., SMITH, R., MATTSSON-CARLGREN, N., PALMQVIST, S., TEUNISSEN, C. E., ZETTERBERG, H., STOMRUD, E., ASHTON, N. J., BLENNOW, K. & HANSSON, O. 2021. Plasma GFAP is an early marker of amyloid-β but not tau pathology in Alzheimer's disease. *Brain,* 144**,** 3505-3516.

PÉREZ, M., HERNÁNDEZ, F., GÓMEZ‐RAMOS, A., SMITH, M., PERRY, G. & AVILA, J. 2002. Formation of aberrant phosphotau fibrillar polymers in neural cultured cells. *European Journal of Biochemistry,* 269**,** 1484-1489.

PERRETT, S. & JONES, G. W. 2008. Insights into the mechanism of prion propagation. *Current Opinion in Structural Biology,* 18**,** 52-59.

PERRY, E. K., SMITH, C. J., COURT, J. A. & PERRY, R. H. 1990. Cholinergic nicotinic and muscarinic receptors in dementia of Alzheimer, Parkinson and Lewy body types. *Journal of Neural Transmission - Parkinson's Disease and Dementia Section,* 2**,** 149-158.

PERRY, N. A., KAOUD, T. S., ORTEGA, O. O., KAYA, A. I., MARCUS, D. J., PLEINIS, J. M., BERNDT, S., CHEN, Q., ZHAN, X. & DALBY, K. N. 2019. Arrestin-3 scaffolding of the JNK3 cascade suggests a mechanism for signal amplification. *Proceedings of the National Academy of Sciences,* 116**,** 810-815.

PETRY, F. R., PELLETIER, J., BRETTEVILLE, A., MORIN, F., CALON, F., HÉBERT, S. S., WHITTINGTON, R. A. & PLANEL, E. 2014. Specificity of Anti-Tau Antibodies when Analyzing Mice Models of Alzheimer's Disease: Problems and Solutions. *PLOS ONE,* 9**,** e94251.

PHILLIPS, R. & LEDOUX, J. 1992. Differential contribution of amygdala and hippocampus to cued and contextual fear conditioning. *Behavioral neuroscience,* 106**,** 274.

PIERCE, K. L. & LEFKOWITZ, R. J. 2001. Classical and new roles of β-arrestins in the regulation of G-PROTEIN-COUPLED receptors. *Nature Reviews Neuroscience,* 2**,** 727-733.

PIN, J.-P., GALVEZ, T. & PRÉZEAU, L. 2003. Evolution, structure, and activation mechanism of family 3/C G-protein-coupled receptors. *Pharmacology & therapeutics,* 98**,** 325-354.

PITCHER, J., LOHSE, M. J., CODINA, J., CARON, M. G. & LEFKOWITZ, R. J. 1992. Desensitization of the isolated. beta. 2-adrenergic receptor by. beta.-adrenergic receptor kinase, cAMP-dependent protein kinase, and protein kinase C occurs via distinct molecular mechanisms. *Biochemistry,* 31**,** 3193-3197.

PITTEL, Z., HELDMAN, E., BARG, J., HARING, R. & FISHER, A. 1996. Muscarinic control of amyloid precursor protein secretion in rat cerebral cortex and cerebellum. *Brain research,* 742**,** 299-304.

POOLER, A. M., NOBLE, W. & HANGER, D. P. 2014. A role for tau at the synapse in Alzheimer's disease pathogenesis. *Neuropharmacology,* 76**,** 1-8.

PRADO, M. A. M., REIS, R. A. M., PRADO, V. F., DE MELLO, M. C., GOMEZ, M. V. & DE MELLO, F. G. 2002. Regulation of acetylcholine synthesis and storage. *Neurochemistry International,* 41**,** 291-299.

PRASHER, D. C., ECKENRODE, V. K., WARD, W. W., PRENDERGAST, F. G. & CORMIER, M. J. 1992. Primary structure of the Aequorea victoria green-fluorescent protein. *Gene,* 111**,** 229-233.

PRICE, J. L. & MORRIS, J. C. 1999. Tangles and plaques in nondemented aging and “preclinical” Alzheimer's disease. *Annals of Neurology: Official Journal of the American Neurological Association and the Child Neurology Society,* 45**,** 358-368.

PRINCE, M., ALI, G.-C., GUERCHET, M., PRINA, A. M., ALBANESE, E. & WU, Y.-T. 2016. Recent global trends in the prevalence and incidence of dementia, and survival with dementia. *Alzheimer's research & therapy,* 8**,** 1-13.

PRÜßING, K., VOIGT, A. & SCHULZ, J. B. 2013. Drosophila melanogaster as a model organism for Alzheimer’s disease. *Molecular Neurodegeneration,* 8**,** 35.

PURCELL, R. H. & HALL, R. A. 2018. Adhesion G Protein-Coupled Receptors as Drug Targets. *Annu Rev Pharmacol Toxicol,* 58**,** 429-449.

QUIRK, G. J., ARMONY, J. L. & LEDOUX, J. E. 1997. Fear conditioning enhances different temporal components of tone-evoked spike trains in auditory cortex and lateral amygdala. *Neuron,* 19**,** 613-624.

RAEDLER, T. J., KNABLE, M. B., JONES, D. W., URBINA, R. A., GOREY, J. G., LEE, K. S., EGAN, M. F., COPPOLA, R. & WEINBERGER, D. R. 2003. In Vivo Determination of Muscarinic Acetylcholine Receptor Availability in Schizophrenia. *American Journal of Psychiatry,* 160**,** 118-127.

RAGOZZINO, M. E., ARTIS, S., SINGH, A., TWOSE, T. M., BECK, J. E. & MESSER, W. S. 2012. The Selective M1 Muscarinic Cholinergic Agonist CDD-0102A Enhances

Working Memory and Cognitive Flexibility. *Journal of Pharmacology and Experimental Therapeutics,* 340**,** 588.

RAJA, W. K., MUNGENAST, A. E., LIN, Y.-T., KO, T., ABDURROB, F., SEO, J. & TSAI, L.-H. 2016. Self-organizing 3D human neural tissue derived from induced pluripotent stem cells recapitulate Alzheimer's disease phenotypes. *PloS one,* 11**,** e0161969.

RAMSDEN, M., KOTILINEK, L., FORSTER, C., PAULSON, J., MCGOWAN, E., SANTACRUZ, K., GUIMARAES, A., YUE, M., LEWIS, J. & CARLSON, G. 2005. Age-dependent neurofibrillary tangle formation, neuron loss, and memory impairment in a mouse model of human tauopathy (P301L). *Journal of Neuroscience,* 25**,** 10637-10647.

RANJAN, R., DWIVEDI, H., BAIDYA, M., KUMAR, M. & SHUKLA, A. K. 2017. Novel Structural Insights into GPCR–β-Arrestin Interaction and Signaling. *Trends in Cell Biology,* 27**,** 851-862.

RANSOHOFF, R. M. & BROWN, M. A. 2012. Innate immunity in the central nervous system. *The Journal of clinical investigation,* 122**,** 1164-1171.

RENDA, A. & NASHMI, R. 2012. Spectral confocal imaging of fluorescently tagged nicotinic receptors in knock-in mice with chronic nicotine administration. *JoVE (Journal of Visualized Experiments)***,** e3516.

RENIER, N., ADAMS, E. L., KIRST, C., WU, Z., AZEVEDO, R., KOHL, J., AUTRY, A. E., KADIRI, L., VENKATARAJU, K. U. & ZHOU, Y. 2016. Mapping of brain activity by automated volume analysis of immediate early genes. *Cell,* 165**,** 1789-1802.

RENIER, N., WU, Z., SIMON, DAVID J., YANG, J., ARIEL, P. & TESSIER-LAVIGNE, M. 2014. iDISCO: A Simple, Rapid Method to Immunolabel Large Tissue Samples for Volume Imaging. *Cell,* 159**,** 896-910.

REUVENY, E., SLESINGER, P. A., INGLESE, J., MORALES, J. M., IÑIGUEZ-LLUHI, J. A., LEFKOWITZ, R. J., BOURNE, H. R., JAN, Y. N. & JAN, L. Y. 1994. Activation of the cloned muscarinic potassium channel by G protein βγ subunits. *Nature,* 370**,** 143-146.

REYNAUD, E. G., KRŽIČ, U., GREGER, K. & STELZER, E. H. K. 2008. Light sheet‐based fluorescence microscopy: More dimensions, more photons, and less photodamage. *HFSP Journal,* 2**,** 266-275.

RHEE, S. G. 2001. Regulation of phosphoinositide-specific phospholipase C. *Annual review of biochemistry,* 70**,** 281-312.

RICHARDSON, D. S., GUAN, W., MATSUMOTO, K., PAN, C., CHUNG, K., ERTÜRK, A., UEDA, H. R. & LICHTMAN, J. W. 2021. Tissue clearing. *Nature Reviews Methods Primers,* 1**,** 1-24.

RIES, J., KAPLAN, C., PLATONOVA, E., EGHLIDI, H. & EWERS, H. 2012. A simple, versatile method for GFP-based super-resolution microscopy via nanobodies. *Nature methods,* 9**,** 582-584.

ROERTGEN, K. E., PARISI, J. E., CLARK, H. B., BARNES, D. L., O'BRIEN, T. D. & JOHNSON, K. H. 1996. Aβ-associated cerebral angiopathy and senile plaques with neurofibrillary tangles and cerebral hemorrhage in an aged wolverine (Gulo gulo). *Neurobiology of aging,* 17**,** 243-247.

ROFINA, J., VAN EDEREN, A., TOUSSAINT, M., SECREVE, M., VAN DER SPEK, A., VAN DER MEER, I., VAN EERDENBURG, F. & GRUYS, E. 2006. Cognitive disturbances in old dogs suffering from the canine counterpart of Alzheimer's disease. *Brain research,* 1069**,** 216-226.

ROJAS-GUTIERREZ, E., MUÑOZ-ARENAS, G., TREVIÑO, S., ESPINOSA, B., CHAVEZ, R., ROJAS, K., FLORES, G., DÍAZ, A. & GUEVARA, J. 2017. Alzheimer's disease

and metabolic syndrome: A link from oxidative stress and inflammation to neurodegeneration. *Synapse,* 71**,** e21990.

ROOK, J. M., ABE, M., CHO, H. P., NANCE, K. D., LUSCOMBE, V. B., ADAMS, J. J., DICKERSON, J. W., REMKE, D. H., GARCIA-BARRANTES, P. M., ENGERS, D. W., ENGERS, J. L., CHANG, S., FOSTER, J. J., BLOBAUM, A. L., NISWENDER, C. M., JONES, C. K., CONN, P. J. & LINDSLEY, C. W. 2017. Diverse Effects on M1 Signaling and Adverse Effect Liability within a Series of M1 Ago-PAMs. *ACS Chemical Neuroscience,* 8**,** 866-883.

ROOK, J. M., BERTRON, J. L., CHO, H. P., GARCIA-BARRANTES, P. M., MORAN, S. P., MAKSYMETZ, J. T., NANCE, K. D., DICKERSON, J. W., REMKE, D. H., CHANG, S., HARP, J. M., BLOBAUM, A. L., NISWENDER, C. M., JONES, C. K., STAUFFER, S. R., CONN, P. J. & LINDSLEY, C. W. 2018. A Novel M1 PAM VU0486846 Exerts Efficacy in Cognition Models without Displaying Agonist Activity or Cholinergic Toxicity. *ACS Chemical Neuroscience,* 9**,** 2274-2285.

ROSENBAUM, D. M., RASMUSSEN, S. G. F. & KOBILKA, B. K. 2009. The structure and function of G-protein-coupled receptors. *Nature,* 459**,** 356-363.

ROSENBERG, J. B., KAPLITT, M. G., DE, B. P., CHEN, A., FLAGIELLO, T., SALAMI, C., PEY, E., ZHAO, L., RICART ARBONA, R. J., MONETTE, S., DYKE, J. P., BALLON, D. J., KAMINSKY, S. M., SONDHI, D., PETSKO, G. A., PAUL, S. M. & CRYSTAL, R. G. 2018. AAVrh.10-Mediated APOE2 Central Nervous System Gene Therapy for APOE4-Associated Alzheimer's Disease. *Hum Gene Ther Clin Dev,* 29**,** 24-47.

ROSS, E. & GILMAN, A. 1977. Resolution of some components of adenylate cyclase necessary for catalytic activity. *Journal of Biological Chemistry,* 252**,** 6966-6969.

ROSS, E. M. & WILKIE, T. M. 2000. GTPase-activating proteins for heterotrimeric G proteins: Regulators of G proteins: Regulators of G protein signaling (RGS) and RGS-like proteins. *Annual review of biochemistry,* 69**,** 795.

ROY, S. M., MINASOV, G., ARANCIO, O., CHICO, L. W., VAN ELDIK, L. J., ANDERSON, W. F., PELLETIER, J. C. & WATTERSON, D. M. 2019. A Selective and Brain Penetrant p38αMAPK Inhibitor Candidate for Neurologic and Neuropsychiatric Disorders That Attenuates Neuroinflammation and Cognitive Dysfunction. *Journal of Medicinal Chemistry,* 62**,** 5298-5311.

RUSH, D. K. 1988. Scopolamine amnesia of passive avoidance: a deficit of information acquisition. *Behavioral and neural biology,* 50**,** 255-274.

RUSS, A. P. & LAMPEL, S. 2005. The druggable genome: an update. *Drug Discovery Today,* 10**,** 1607-1610.

RUSTED, J. M. & WARBURTON, D. M. 1988. The effects of scopolamine on working memory in healthy young volunteers. *Psychopharmacology,* 96**,** 145-152.

SADOT, E., GURWITZ, D., BARG, J., BEHAR, L., GINZBURG, I. & FISHER, A. 1996. Activation of m1 muscarinic acetylcholine receptor regulates τ phosphorylation in transfected PC12 cells. *Journal of neurochemistry,* 66**,** 877-880.

SAH, V. P., SEASHOLTZ, T. M., SAGI, S. A. & BROWN, J. H. 2000. The Role of Rho in G Protein-Coupled Receptor Signal Transduction. *Annual Review of Pharmacology and Toxicology,* 40**,** 459-489.

SAITOH, O., KUBO, Y., MIYATANI, Y., ASANO, T. & NAKATA, H. 1997. RGS8 accelerates G-protein-mediated modulation of K+ currents. *Nature,* 390**,** 525-529.

SALAH-UDDIN, H., SCARR, E., PAVEY, G., HARRIS, K., HAGAN, J. J., DEAN, B., CHALLISS, R. & WATSON, J. M. 2009. Altered M1 muscarinic acetylcholine receptor (CHRM1)-Gαq/11 coupling in a schizophrenia endophenotype. *Neuropsychopharmacology,* 34**,** 2156-2166.

SALEEM, S. & KANNAN, R. R. 2018. Zebrafish: an emerging real-time model system to study Alzheimer's disease and neurospecific drug discovery. *Cell death discovery,* 4**,** 1-13.

SALLOWAY, S., CHALKIAS, S., BARKHOF, F., BURKETT, P., BARAKOS, J., PURCELL, D., SUHY, J., FORRESTAL, F., TIAN, Y., UMANS, K., WANG, G., SINGHAL, P., BUDD HAEBERLEIN, S. & SMIRNAKIS, K. 2022. Amyloid-Related Imaging Abnormalities in 2 Phase 3 Studies Evaluating Aducanumab in Patients With Early Alzheimer Disease. *JAMA Neurology,* 79**,** 13-21.

SALON, J. A., LODOWSKI, D. T. & PALCZEWSKI, K. 2011. The Significance of G Protein-Coupled Receptor Crystallography for Drug Discovery. *Pharmacological Reviews,* 63**,** 901.

SANABRIA-CASTRO, A., ALVARADO-ECHEVERRÍA, I. & MONGE-BONILLA, C. 2017. Molecular Pathogenesis of Alzheimer's Disease: An Update. *Annals of Neurosciences,* 24**,** 46-54.

SANKARANARAYANAN, S., BARTEN, D. M., VANA, L., DEVIDZE, N., YANG, L., CADELINA, G., HOQUE, N., DECARR, L., KEENAN, S. & LIN, A. 2015. Passive immunization with phospho-tau antibodies reduces tau pathology and functional deficits in two distinct mouse tauopathy models. *PloS one,* 10**,** e0125614.

SANTACRUZ, K., LEWIS, J., SPIRES, T., PAULSON, J., KOTILINEK, L., INGELSSON, M., GUIMARAES, A., DETURE, M., RAMSDEN, M. & MCGOWAN, E. 2005. Tau suppression in a neurodegenerative mouse model improves memory function. *Science,* 309**,** 476-481.

SANTOS, R., URSU, O., GAULTON, A., BENTO, A. P., DONADI, R. S., BOLOGA, C. G., KARLSSON, A., AL-LAZIKANI, B., HERSEY, A. & OPREA, T. I. 2017. A comprehensive map of molecular drug targets. *Nature reviews Drug discovery,* 16**,** 19.

SASNER, M., OBLAK, A. L., GARCEAU, D., KOTREDES, K. P., SONI, D., LIN, P. B. C., PREUSS, C., UYAR, A., PANDEY, R. S. & CARTER, G. W. 2021. Evaluation of late‐onset Alzheimer's disease risk variants in mouse models. *Alzheimer's & Dementia,* 17**,** e055629.

SAUER, B. 1998. Inducible Gene Targeting in Mice Using the Cre/loxSystem. *Methods,* 14**,** 381-392.

SCARMEAS, N., BRANDT, J., BLACKER, D., ALBERT, M., HADJIGEORGIOU, G., DUBOIS, B., DEVANAND, D., HONIG, L. & STERN, Y. 2007. Disruptive Behavior as a Predictor in Alzheimer Disease. *Archives of Neurology,* 64**,** 1755-1761.

SCARPA, M., HESSE, S. & BRADLEY, S. J. 2020. M1 muscarinic acetylcholine receptors: A therapeutic strategy for symptomatic and disease-modifying effects in Alzheimer's disease? *In:* LANGMEAD, C. J. (ed.) *Advances in Pharmacology.* Academic Press.

SCARR, E., COWIE, T., KANELLAKIS, S., SUNDRAM, S., PANTELIS, C. & DEAN, B. 2009. Decreased cortical muscarinic receptors define a subgroup of subjects with schizophrenia. *Molecular psychiatry,* 14**,** 1017-1023.

SCHEUNER, D., ECKMAN, C., JENSEN, M., SONG, X., CITRON, M., SUZUKI, N., BIRD, T., HARDY, J., HUTTON, M. & KUKULL, W. 1996. Secreted amyloid β–protein similar to that in the senile plaques of Alzheimer's disease is increased in vivo by the presenilin 1 and 2 and APP mutations linked to familial Alzheimer's disease. *Nature medicine,* 2**,** 864-870.

SCHIÖTH, H. B. & FREDRIKSSON, R. 2005. The GRAFS classification system of G-protein coupled receptors in comparative perspective. *General and Comparative Endocrinology,* 142**,** 94-101.

SCHNÜTGEN, F., DOERFLINGER, N., CALLÉJA, C., WENDLING, O., CHAMBON, P. & GHYSELINCK, N. B. 2003. A directional strategy for monitoring Cre-mediated recombination at the cellular level in the mouse. *Nature Biotechnology,* 21**,** 562-565.

SCHROEDER, S., JOLY-AMADO, A., SOLIMAN, A., SENGUPTA, U., KAYED, R., GORDON, M. N. & MORGAN, D. 2017. Oligomeric tau-targeted immunotherapy in Tg4510 mice. *Alzheimer's Research & Therapy,* 9**,** 46.

SCOUTEN, C. W., O'CONNOR, R. & CUNNINGHAM, M. 2006. Perfusion Fixation of Research Animals. *Microscopy Today,* 14**,** 26-33.

SELKOE, D. J. 2011. Resolving controversies on the path to Alzheimer's therapeutics. *Nature Medicine,* 17**,** 1060-1065.

SELKOE, D. J. & HARDY, J. 2016. The amyloid hypothesis of Alzheimer's disease at 25 years. *EMBO Molecular Medicine,* 8**,** 595-608.

SELKOE, D. J. & WOLFE, M. S. 2007. Presenilin: running with scissors in the membrane. *Cell,* 131**,** 215-221.

SENTE, A., PEER, R., SRIVASTAVA, A., BAIDYA, M., LESK, A. M., BALAJI, S., SHUKLA, A. K., BABU, M. M. & FLOCK, T. 2018. Molecular mechanism of modulating arrestin conformation by GPCR phosphorylation. *Nature Structural & Molecular Biology,* 2*5***,** 538-545.

SEO, J., CHOE, M. & KIM, S. Y. 2016. Clearing and Labeling Techniques for Large-Scale Biological Tissues. *Mol Cells,* 39**,** 439-46.

SERRANO-POZO, A., FROSCH, M. P., MASLIAH, E. & HYMAN, B. T. 2011. Neuropathological Alterations in Alzheimer Disease. *Cold Spring Harbor Perspectives in Medicine,* 1.

SHEKHAR, A., POTTER, W. Z., LIGHTFOOT, J., LIENEMANN D PHARM, J., DUBÉ, S., MALLINCKRODT, C., BYMASTER, F. P., MCKINZIE, D. L. & FELDER, C. C. 2008. Selective muscarinic receptor agonist xanomeline as a novel treatment approach for schizophrenia. *American Journal of Psychiatry,* 165**,** 1033-1039.

SHEN, W., HAMILTON, S. E., NATHANSON, N. M. & SURMEIER, D. J. 2005. Cholinergic suppression of KCNQ channel currents enhances excitability of striatal medium spiny neurons. *Journal of Neuroscience,* 25**,** 7449-7458.

SHEN, W., TIAN, X., DAY, M., ULRICH, S., TKATCH, T., NATHANSON, N. M. & SURMEIER, D. J. 2007. Cholinergic modulation of Kir2 channels selectively elevates dendritic excitability in striatopallidal neurons. *Nature neuroscience,* 10**,** 1458-1466.

SHENOY, S. K., DRAKE, M. T., NELSON, C. D., HOUTZ, D. A., XIAO, K., MADABUSHI, S., REITER, E., PREMONT, R. T., LICHTARGE, O. & LEFKOWITZ, R. J. 2006. β-Arrestin-dependent, G Protein-independent ERK1/2 Activation by the β2 Adrenergic Receptor*. *Journal of Biological Chemistry,* 281**,** 1261-1273.

SHERMAN, M. A., LACROIX, M., AMAR, F., LARSON, M. E., FORSTER, C., AGUZZI, A., BENNETT, D. A., RAMSDEN, M. & LESNÉ, S. E. 2016. Soluble conformers of Aβ and tau alter selective proteins governing axonal transport. *Journal of Neuroscience,* 36**,** 9647-9658.

SHI, P., ZHANG, J., YANG, H. & ZHANG, Y.-P. 2003. Adaptive diversification of bitter taste receptor genes in Mammalian evolution. *Molecular biology and evolution,* 20**,** 805-814.

SHIMOMURA, O., JOHNSON, F. H. & SAIGA, Y. 1962. Extraction, purification and properties of aequorin, a bioluminescent protein from the luminous hydromedusan, Aequorea. *Journal of cellular and comparative physiology,* 59**,** 223-239.

SHIN, Y., CHOI, S. H., KIM, E., BYLYKBASHI, E., KIM, J. A., CHUNG, S., KIM, D. Y., KAMM, R. D. & TANZI, R. E. 2019. Blood–Brain Barrier Dysfunction in a 3D In Vitro Model of Alzheimer's Disease. *Advanced Science,* 6**,** 1900962.

SHINOE, T., MATSUI, M., TAKETO, M. M. & MANABE, T. 2005. Modulation of Synaptic Plasticity by Physiological Activation of M₁ Muscarinic Acetylcholine Receptors in the Mouse Hippocampus. *The Journal of Neuroscience,* 25**,** 11194.

SHINOHARA, M., FUJIOKA, S., MURRAY, M. E., WOJTAS, A., BAKER, M., ROVELET-LECRUX, A., RADEMAKERS, R., DAS, P., PARISI, J. E. & GRAFF-RADFORD, N. R. 2014. Regional distribution of synaptic markers and APP correlate with distinct clinicopathological features in sporadic and familial Alzheimer's disease. *Brain,* 137**,** 1533-1549.

SHIREY, J. K., BRADY, A. E., JONES, P. J., DAVIS, A. A., BRIDGES, T. M., KENNEDY, J. P., JADHAV, S. B., MENON, U. N., XIANG, Z., WATSON, M. L., CHRISTIAN, E. P., DOHERTY, J. J., QUIRK, M. C., SNYDER, D. H., LAH, J. J., LEVEY, A. I., NICOLLE, M. M., LINDSLEY, C. W. & CONN, P. J. 2009. A Selective Allosteric Potentiator of the M1 Muscarinic Acetylcholine Receptor Increases Activity of Medial Prefrontal Cortical Neurons and Restores Impairments in Reversal Learning. *The Journal of Neuroscience,* 29**,** 14271-86.

SHUGART, J. 2022. *In Small Trial, Gene Therapy Spurs ApoE2 Production* [Online]. Alzforum. Available: https://www.alzforum.org/news/conference-coverage/small-trial-gene-therapy-spurs-apoe2-production [Accessed 16/12/2022 2022].

SIEDLAK, S. L., CRAS, P., KAWAI, M., RICHEY, P. & PERRY, G. 1991. Basic fibroblast growth factor binding is a marker for extracellular neurofibrillary tangles in Alzheimer disease. *Journal of Histochemistry & Cytochemistry,* 39**,** 899-904.

SIMON, M. I., STRATHMANN, M. P. & GAUTAM, N. 1991. Diversity of G proteins in signal transduction. *Science,* 252**,** 802-808.

SIPOS, E., KURUNCZI, A., KASZA, A., HORVÁTH, J., FELSZEGHY, K., LAROCHE, S., TOLDI, J., PARDUCZ, A., PENKE, B. & PENKE, Z. 2007. β-Amyloid pathology in the entorhinal cortex of rats induces memory deficits: implications for Alzheimer's disease. *Neuroscience,* 147**,** 28-36.

SJÖSTEDT, E., ZHONG, W., FAGERBERG, L., KARLSSON, M., MITSIOS, N., ADORI, C., OKSVOLD, P., EDFORS, F., LIMISZEWSKA, A., HIKMET, F., HUANG, J., DU, Y., LIN, L., DONG, Z., YANG, L., LIU, X., JIANG, H., XU, X., WANG, J., YANG, H., BOLUND, L., MARDINOGLU, A., ZHANG, C., VON FEILITZEN, K., LINDSKOG, C., PONTÉN, F., LUO, Y., HÖKFELT, T., UHLÉN, M. & MULDER, J. 2020. An atlas of the protein-coding genes in the human, pig, and mouse brain. *Science,* 367**,** eaay5947.

SKOVRONSKY, D. M., MOORE, D. B., MILLA, M. E., DOMS, R. W. & LEE, V. M.-Y. 2000. Protein Kinase C-dependent α-Secretase Competes with β-Secretase for Cleavage of Amyloid-β Precursor Protein in the Trans-Golgi Network. *Journal of Biological Chemistry,* 275**,** 2568-2575.

SLOAN, H. L., GOOD, M. & DUNNETT, S. B. 2006. Double dissociation between hippocampal and prefrontal lesions on an operant delayed matching task and a water maze reference memory task. *Behavioural brain research,* 171**,** 116-126.

SNOW, B. E., KRUMINS, A. M., BROTHERS, G. M., LEE, S.-F., WALL, M. A., CHUNG, S., MANGION, J., ARYA, S., GILMAN, A. G. & SIDEROVSKI, D. P. 1998. AG protein γ subunit-like domain shared between RGS11 and other RGS proteins specifies binding to Gβ5 subunits. *Proceedings of the National Academy of Sciences,* 95**,** 13307-13312.

SOFRONIEW, M. V. & VINTERS, H. V. 2010. Astrocytes: biology and pathology. *Acta neuropathologica,* 119**,** 7-35.

SONG, L., LU, S. X., OUYANG, X., MELCHOR, J., LEE, J., TERRACINA, G., WANG, X., HYDE, L., HESS, J. F., PARKER, E. M. & ZHANG, L. 2015. Analysis of tau post-translational modifications in rTg4510 mice, a model of tau pathology. *Mol Neurodegener,* 10**,** 14.

SORDO, L., MARTINI, A. C., HOUSTON, E. F., HEAD, E. & GUNN-MOORE, D. 2021. Neuropathology of Aging in Cats and its Similarities to Human Alzheimer's Disease. *Frontiers in Aging,* 2**,** 18.

SOREQ, H. & SEIDMAN, S. 2001. Acetylcholinesterase — new roles for an old actor. *Nature Reviews Neuroscience,* 2**,** 294-302.

SOUTHAN, C., SHARMAN, J. L., BENSON, H. E., FACCENDA, E., PAWSON, A. J., ALEXANDER, S. P., BUNEMAN, O. P., DAVENPORT, A. P., MCGRATH, J. C. & PETERS, J. A. 2016. The IUPHAR/BPS Guide to PHARMACOLOGY in 2016: towards curated quantitative interactions between 1300 protein targets and 6000 ligands. *Nucleic acids research,* 44**,** D1054-D1068.

SPERLING, R. A., MORMINO, E. C., SCHULTZ, A. P., BETENSKY, R. A., PAPP, K. V., AMARIGLIO, R. E., HANSEEUW, B. J., BUCKLEY, R., CHHATWAL, J. & HEDDEN, T. 2019. The impact of amyloid‐beta and tau on prospective cognitive decline in older individuals. *Annals of neurology,* 85**,** 181-193.

SPIRES, T. L., ORNE, J. D., SANTACRUZ, K., PITSTICK, R., CARLSON, G. A., ASHE, K. H. & HYMAN, B. T. 2006. Region-specific dissociation of neuronal loss and neurofibrillary pathology in a mouse model of tauopathy. *The American journal of pathology,* 168**,** 1598-1607.

SRIRAM, K. & INSEL, P. A. 2018. G Protein-Coupled Receptors as Targets for Approved Drugs: How Many Targets and How Many Drugs? *Molecular Pharmacology,* 93**,** 251.

STASKIN, D., KAY, G., TANNENBAUM, C., GOLDMAN, H., BHASHI, K., LING, J. & OEFELEIN, M. 2010. Trospium chloride has no effect on memory testing and is assay undetectable in the central nervous system of older patients with overactive bladder. *International journal of clinical practice,* 64**,** 1294-1300.

STEFFEN, J., KROHN, M., PAARMANN, K., SCHWITLICK, C., BRÜNING, T., MARREIROS, R., MÜLLER-SCHIFFMANN, A., KORTH, C., BRAUN, K. & PAHNKE, J. 2016. Revisiting rodent models: Octodon degus as Alzheimer's disease model? *Acta Neuropathologica Communications,* 4**,** 1-11.

STEWART, A. & FISHER, R. A. 2015. Chapter One - Introduction: G Protein-coupled Receptors and RGS Proteins. *In:* FISHER, R. A. (ed.) *Progress in Molecular Biology and Translational Science.* Academic Press.

STIRLING, D. R., SWAIN-BOWDEN, M. J., LUCAS, A. M., CARPENTER, A. E., CIMINI, B. A. & GOODMAN, A. 2021. CellProfiler 4: improvements in speed, utility and usability. *BMC Bioinformatics,* 22**,** 433.

STOFFEL, R., PITCHER, J. & LEFKOWITZ, R. 1997. Targeting G protein-coupled receptor kinases to their receptor substrates. *The Journal of membrane biology,* 157**,** 1-8.

STURCHLER-PIERRAT, C., ABRAMOWSKI, D., DUKE, M., WIEDERHOLD, K.-H., MISTL, C., ROTHACHER, S., LEDERMANN, B., BÜRKI, K., FREY, P. & PAGANETTI, P. A. 1997. Two amyloid precursor protein transgenic mouse models with Alzheimer disease-like pathology. *Proceedings of the National Academy of Sciences,* 94**,** 13287-13292.

SUN, Y.-Y., WANG, Z., ZHOU, H.-Y. & HUANG, H.-C. 2022. Sleep–Wake Disorders in Alzheimer's Disease: A Review. *ACS Chemical Neuroscience,* 13**,** 1467-1478.

SUNDELÖF, J., SUNDSTRÖM, J., HANSSON, O., ERIKSDOTTER-JÖNHAGEN, M., GIEDRAITIS, V., LARSSON, A., DEGERMAN-GUNNARSSON, M., INGELSSON,

M., MINTHON, L. & BLENNOW, K. 2010. Cystatin C levels are positively correlated with both Aβ 42 and tau levels in cerebrospinal fluid in persons with Alzheimer's disease, mild cognitive impairment, and healthy controls. *Journal of Alzheimer's Disease,* 21**,** 471-478.

SUNDERLAND, T., TARIOT, P. N., WEINGARTNER, H., MURPHY, D. L., NEWHOUSE, P. A., MUELLER, E. A. & COHEN, R. M. 1986. Pharmacologic modelling of Alzheimer's disease. *Progress in Neuro-Psychopharmacology and Biological Psychiatry,* 10**,** 599-610.

SUSAKI, E. A., TAINAKA, K., PERRIN, D., YUKINAGA, H., KUNO, A. & UEDA, H. R. 2015. Advanced CUBIC protocols for whole-brain and whole-body clearing and imaging. *Nature protocols,* 10**,** 1709-1727.

SUSAKI, E. A. & UEDA, H. R. 2016. Whole-body and whole-organ clearing and imaging techniques with single-cell resolution: toward organism-level systems biology in mammals. *Cell chemical biology,* 23**,** 137-157.

TAINAKA, K., KUBOTA, S. I., SUYAMA, T. Q., SUSAKI, E. A., PERRIN, D., UKAI-TADENUMA, M., UKAI, H. & UEDA, H. R. 2014. Whole-body imaging with single-cell resolution by tissue decolorization. *Cell,* 159**,** 911-924.

TAINAKA, K., MURAKAMI, T. C., SUSAKI, E. A., SHIMIZU, C., SAITO, R., TAKAHASHI, K., HAYASHI-TAKAGI, A., SEKIYA, H., ARIMA, Y. & NOJIMA, S. 2018. Chemical landscape for tissue clearing based on hydrophilic reagents. *Cell reports,* 24**,** 2196-2210. e9.

TAMBINI, M. D., NORRIS, K. A. & D'ADAMIO, L. 2020. Opposite changes in APP processing and human Aβ levels in rats carrying either a protective or a pathogenic APP mutation. *Elife,* 9.

TANG, W.-J. & GILMAN, A. G. 1991. Type-specific regulation of adenylyl cyclase by G protein βγ subunits. *Science,* 254**,** 1500-1503.

TANZI, R. E. 2012. The Genetics of Alzheimer Disease. *Cold Spring Harbor Perspectives in Medicine,* 2.

TASHKIN, D. P., CELLI, B., SENN, S., BURKHART, D., KESTEN, S., MENJOGE, S. & DECRAMER, M. 2008. A 4-year trial of tiotropium in chronic obstructive pulmonary disease. *New England Journal of Medicine,* 359**,** 1543-1554.

TAUSSIG, R., TANG, W.-J., HEPLER, J. R. & GILMAN, A. G. 1994. Distinct patterns of bidirectional regulation of mammalian adenylyl cyclases. *Journal of Biological Chemistry,* 269**,** 6093-6100.

TEKIRIAN, T. L., COLE, G. M., RUSSELL, M. J., YANG, F., WEIKSTEIN, D. R., PATEL, E., SNOWDON, D. A., MARKESBERY, W. R. & GEDDES, J. W. 1996. Carboxy terminal of β-amyloid deposits in aged human, canine, and polar bear brains. *Neurobiology of aging,* 17**,** 249-257.

TERRY, R. D., MASLIAH, E., SALMON, D. P., BUTTERS, N., DETERESA, R., HILL, R., HANSEN, L. A. & KATZMAN, R. 1991. Physical basis of cognitive alterations in Alzheimer's disease: synapse loss is the major correlate of cognitive impairment. *Annals of Neurology: Official Journal of the American Neurological Association and the Child Neurology Society,* 30**,** 572-580.

THAL, D. M., SUN, B., FENG, D., NAWARATNE, V., LEACH, K., FELDER, C. C., BURES, M. G., EVANS, D. A., WEIS, W. I. & BACHHAWAT, P. 2016. Crystal structures of the M1 and M4 muscarinic acetylcholine receptors. *Nature,* 531**,** 335-340.

THOMAS, E., WASUNNA-SMITH, B. & KURUVILLA, T. 2021. Aducanumab and disease modifying treatments for Alzheimer's disease. *Progress in Neurology and Psychiatry,* 25**,** 4-6.

THOMAS, K. R. & CAPECCHI, M. R. 1987. Site-directed mutagenesis by gene targeting in mouse embryo-derived stem cells. *Cell,* 51**,** 503-512.

THOMPSON, S., LANCTÔT, K. L. & HERRMANN, N. 2004. The benefits and risks associated with cholinesterase inhibitor therapy in Alzheimer's disease. *Expert opinion on drug safety,* 3**,** 425-440.

THOMSEN, A. R. B., HAHN, H. & BUNNETT, N. W. 2022. Chapter 2 - Arrestin-mediated trafficking and compartmentalized biology of GPCRs. *In:* GUREVICH, V. V. (ed.) *Arrestins.* Academic Press.

THOMSEN, M., CONN, P. J., LINDSLEY, C., WESS, J., BOON, J. Y., FULTON, B. S., FINK-JENSEN, A. & CAINE, S. B. 2010. Attenuation of Cocaine's Reinforcing and Discriminative Stimulus Effects via Muscarinic M1 Acetylcholine Receptor Stimulation. *Journal of Pharmacology and Experimental Therapeutics,* 332**,** 959.

TOBIN, A. B. 2008. G-protein-coupled receptor phosphorylation: where, when and by whom. *British Journal of Pharmacology,* 153**,** S167-S176.

TOHGO, A., CHOY, E. W., GESTY-PALMER, D., PIERCE, K. L., LAPORTE, S., OAKLEY, R. H., CARON, M. G., LEFKOWITZ, R. J. & LUTTRELL, L. M. 2003. The Stability of the G Protein-coupled Receptor-β-Arrestin Interaction Determines the Mechanism and Functional Consequence of ERK Activation*. *Journal of Biological Chemistry,* 278**,** 6258-6267.

TOMER, R., YE, L., HSUEH, B. & DEISSEROTH, K. 2014. Advanced CLARITY for rapid and high-resolution imaging of intact tissues. *Nature Protocols,* 9**,** 1682-1697.

TREWEEK, J. B., CHAN, K. Y., FLYTZANIS, N. C., YANG, B., DEVERMAN, B. E., GREENBAUM, A., LIGNELL, A., XIAO, C., CAI, L. & LADINSKY, M. S. 2015. Whole-body tissue stabilization and selective extractions via tissue-hydrogel hybrids for high-resolution intact circuit mapping and phenotyping. *Nature protocols,* 10**,** 1860-1896.

TRINCZEK, B., EBNETH, A., MANDELKOW, E. & MANDELKOW, E. 1999. Tau regulates the attachment/detachment but not the speed of motors in microtubule-dependent transport of single vesicles and organelles. *Journal of cell science,* 112**,** 2355-2367.

TYNDALL, J. D. & SANDILYA, R. 2005. GPCR agonists and antagonists in the clinic. *Medicinal chemistry,* 1**,** 405-421.

UDDIN, M. S., AL MAMUN, A., KABIR, M. T., ASHRAF, G. M., BIN-JUMAH, M. N. & ABDEL-DAIM, M. M. 2021. Multi-Target Drug Candidates for Multifactorial Alzheimer's Disease: AChE and NMDAR as Molecular Targets. *Molecular Neurobiology,* 58**,** 281-303.

UEDA, H. R., ERTÜRK, A., CHUNG, K., GRADINARU, V., CHÉDOTAL, A., TOMANCAK, P. & KELLER, P. J. 2020. Tissue clearing and its applications in neuroscience. *Nature Reviews Neuroscience,* 21**,** 61-79.

USLANER, J. M., EDDINS, D., PURI, V., CANNON, C. E., SUTCLIFFE, J., CHEW, C. S., PEARSON, M., VIVIAN, J. A., CHANG, R. K. & RAY, W. J. 2013. The muscarinic M1 receptor positive allosteric modulator PQCA improves cognitive measures in rat, cynomolgus macaque, and rhesus macaque. *Psychopharmacology,* 225**,** 21-30.

VAGNUCCI, A. H. & LI, W. W. 2003. Alzheimer's disease and angiogenesis. *The Lancet,* 361**,** 605-608.

VALANT, C., FELDER, C. C., SEXTON, P. M. & CHRISTOPOULOS, A. 2012. Probe dependence in the allosteric modulation of a G protein-coupled receptor: implications for detection and validation of allosteric ligand effects. *Molecular pharmacology,* 81**,** 41-52.

VALANT, C., SEXTON, P. M. & CHRISTOPOULOS, A. 2009. Orthosteric/allosteric bitopic ligands. *Molecular interventions,* 9**,** 125.

VAN DAM, D. & DE DEYN, P. P. 2011. Animal models in the drug discovery pipeline for Alzheimer's disease. *British Journal of Pharmacology,* 164**,** 1285-1300.

VAN DER WESTHUIZEN, E. T., CHOY, K. C., VALANT, C., MCKENZIE-NICKSON, S., BRADLEY, S. J., TOBIN, A. B., SEXTON, P. M. & CHRISTOPOULOS, A. 2021. Fine tuning muscarinic acetylcholine receptor signaling through allostery and bias. *Frontiers in Pharmacology,* 11**,** 606656.

VAN DYCK, C. H., SWANSON, C. J., AISEN, P., BATEMAN, R. J., CHEN, C., GEE, M., KANEKIYO, M., LI, D., REYDERMAN, L., COHEN, S., FROELICH, L., KATAYAMA, S., SABBAGH, M., VELLAS, B., WATSON, D., DHADDA, S., IRIZARRY, M., KRAMER, L. D. & IWATSUBO, T. 2022. Lecanemab in Early Alzheimer's Disease. *New England Journal of Medicine*.

VARDIGAN, J. D., CANNON, C. E., PURI, V., DANCHO, M., KOSER, A., WITTMANN, M., KUDUK, S. D., RENGER, J. J. & USLANER, J. M. 2015. Improved cognition without adverse effects: novel M1 muscarinic potentiator compares favorably to donepezil and xanomeline in rhesus monkey. *Psychopharmacology,* 232**,** 1859-1866.

VARNUM, M. M. & IKEZU, T. 2012. The classification of microglial activation phenotypes on neurodegeneration and regeneration in Alzheimer's disease brain. *Archivum immunologiae et therapiae experimentalis,* 60**,** 251-266.

VELAZQUEZ-MOCTEZUMA, J., GILLIN, J. C. & SHIROMANI, P. J. 1989. Effect of specific M1, M2 muscarinic receptor agonists on REM sleep generation. *Brain Research,* 503**,** 128-131.

VENKATAKRISHNAN, A., DEUPI, X., LEBON, G., TATE, C. G., SCHERTLER, G. F. & BABU, M. M. 2013. Molecular signatures of G-protein-coupled receptors. *Nature,* 494**,** 185-194.

VERGHESE, P. B., CASTELLANO, J. M. & HOLTZMAN, D. M. 2011. Apolipoprotein E in Alzheimer's disease and other neurological disorders. *The Lancet Neurology,* 10**,** 241-252.

VERMA, S., KUMAR, A., TRIPATHI, T. & KUMAR, A. 2018. Muscarinic and nicotinic acetylcholine receptor agonists: current scenario in Alzheimer's disease therapy. *Journal of Pharmacy and Pharmacology,* 70**,** 985-993.

VIGOUROUX, R. J., BELLE, M. & CHÉDOTAL, A. 2017. Neuroscience in the third dimension: shedding new light on the brain with tissue clearing. *Mol Brain,* 10**,** 33.

VINTERSTEN, K., MONETTI, C., GERTSENSTEIN, M., ZHANG, P., LASZLO, L., BIECHELE, S. & NAGY, A. 2004. Mouse in red: red fluorescent protein expression in mouse ES cells, embryos, and adult animals. *genesis,* 40**,** 241-246.

VOGEL, J. W., YOUNG, A. L., OXTOBY, N. P., SMITH, R., OSSENKOPPELE, R., STRANDBERG, O. T., LA JOIE, R., AKSMAN, L. M., GROTHE, M. J., ITURRIA-MEDINA, Y., WEINER, M., AISEN, P., PETERSEN, R., JACK, C. R., JAGUST, W., TROJANOWKI, J. Q., TOGA, A. W., BECKETT, L., GREEN, R. C., SAYKIN, A. J., MORRIS, J., SHAW, L. M., LIU, E., MONTINE, T., THOMAS, R. G., DONOHUE, M., WALTER, S., GESSERT, D., SATHER, T., JIMINEZ, G., HARVEY, D., BERNSTEIN, M., FOX, N., THOMPSON, P., SCHUFF, N., DECARLI, C., BOROWSKI, B., GUNTER, J., SENJEM, M., VEMURI, P., JONES, D., KANTARCI, K., WARD, C., KOEPPE, R. A., FOSTER, N., REIMAN, E. M., CHEN, K., MATHIS, C., LANDAU, S., CAIRNS, N. J., HOUSEHOLDER, E., REINWALD, L. T., LEE, V., KORECKA, M., FIGURSKI, M., CRAWFORD, K., NEU, S., FOROUD, T. M., POTKIN, S., SHEN, L., KELLEY, F., KIM, S., NHO, K., KACHATURIAN, Z., FRANK, R., SNYDER, P. J., MOLCHAN, S., KAYE, J., QUINN, J., LIND, B., CARTER, R., DOLEN, S., SCHNEIDER, L. S.,

PAWLUCZYK, S., BECCERA, M., TEODORO, L., SPANN, B. M., BREWER, J., VANDERSWAG, H., FLEISHER, A., HEIDEBRINK, J. L., LORD, J. L., MASON, S. S., ALBERS, C. S., KNOPMAN, D., JOHNSON, K., DOODY, R. S., MEYER, J. V., CHOWDHURY, M., ROUNTREE, S., DANG, M., STERN, Y., HONIG, L. S., BELL, K. L., ANCES, B., MORRIS, J. C., CARROLL, M., LEON, S., MINTUN, M. A., SCHNEIDER, S., et al. 2021. Four distinct trajectories of tau deposition identified in Alzheimer's disease. *Nature Medicine,* 27**,** 871-881.

VOLPICELLI, L. A. & LEVEY, A. I. 2004. Muscarinic acetylcholine receptor subtypes in cerebral cortex and hippocampus. *Progress in brain research,* 145**,** 59-66.

VON STETTEN, D., NOIRCLERC-SAVOYE, M., GOEDHART, J., GADELLA, T. W. & ROYANT, A. 2012. Structure of a fluorescent protein from Aequorea victoria bearing the obligate-monomer mutation A206K. *Acta Crystallographica Section F: Structural Biology and Crystallization Communications,* 68**,** 878-882.

VOSS, T., LI, J., CUMMINGS, J., FARLOW, M., ASSAID, C., FROMAN, S., LEIBENSPERGER, H., SNOW-ADAMI, L., MCMAHON, K. B. & EGAN, M. 2018. Randomized, controlled, proof-of-concept trial of MK-7622 in Alzheimer's disease. *Alzheimer's & Dementia: Translational Research & Clinical Interventions,* 4**,** 173-181.

VOYTKO, M. & TINKLER, G. 2004. Cognitive function and its neural mechanisms in nonhuman primate models of aging, Alzheimer disease, and menopause. *Front Biosci,* 9**,** 1899-1914.

VUCKOVIC, Z., GENTRY, P. R., BERIZZI, A. E., HIRATA, K., VARGHESE, S., THOMPSON, G., VAN DER WESTHUIZEN, E. T., BURGER, W. A. C., RAHMANI, R., VALANT, C., LANGMEAD, C. J., LINDSLEY, C. W., BAELL, J. B., TOBIN, A. B., SEXTON, P. M., CHRISTOPOULOS, A. & THAL, D. M. 2019. Crystal structure of the M5 muscarinic acetylcholine receptor. *Proceedings of the National Academy of Sciences,* 116**,** 26001-26007.

WACKER, D., STEVENS, R. C. & ROTH, B. L. 2017. How ligands illuminate GPCR molecular pharmacology. *Cell,* 170**,** 414-427.

WALSH, D. M. & SELKOE, D. J. 2007. Aβ oligomers–a decade of discovery. *Journal of neurochemistry,* 101**,** 1172-1184.

WALSH, S., MERRICK, R., MILNE, R. & BRAYNE, C. 2021. Aducanumab for Alzheimer's disease? *BMJ,* 374**,** n1682.

WANG, R. & REDDY, P. H. 2017. Role of glutamate and NMDA receptors in Alzheimer's disease. *Journal of Alzheimer's Disease,* 57**,** 1041-1048.

WANG, X., SMITH, K., PEARSON, M., HUGHES, A., COSDEN, M. L., MARCUS, J., HESS, J. F., SAVAGE, M. J., ROSAHL, T., SMITH, S. M., SCHACHTER, J. B. & USLANER, J. M. 2018. Early intervention of tau pathology prevents behavioral changes in the rTg4510 mouse model of tauopathy. *PLOS ONE,* 13**,** e0195486.

WANG, X., ZHANG, C., SZÁBO, G. & SUN, Q. Q. 2013. Distribution of CaMKIIα expression in the brain in vivo, studied by CaMKIIα-GFP mice. *Brain Res,* 1518**,** 9-25.

WANG, Y., MACKE, J. P., ABELLA, B. S., ANDREASSON, K., WORLEY, P., GILBERT, D. J., COPELAND, N. G., JENKINS, N. A. & NATHANS, J. 1996. A Large Family of Putative Transmembrane Receptors Homologous to the Product of the Drosophila Tissue Polarity Gene frizzled (∗). *Journal of Biological Chemistry,* 271**,** 4468-4476.

WANG, Z., JENSSON, O., THORSTEINSSON, L. & VINTERS, H. 1997. Microvascular degeneration in hereditary cystatin C amyloid angiopathy of the brain. *Apmis,* 105**,** 41-47.

WANG, Z., KAI, L., DAY, M., RONESI, J., YIN, H. H., DING, J., TKATCH, T., LOVINGER, D. M. & SURMEIER, D. J. 2006. Dopaminergic control of corticostriatal long-term synaptic depression in medium spiny neurons is mediated by cholinergic interneurons. *Neuron,* 50**,** 443-452.

WEERARATNA, A. T., KALEHUA, A., DELEON, I., BERTAK, D., MAHER, G., WADE, M. S., LUSTIG, A., BECKER, K. G., WOOD, W., WALKER, D. G., BEACH, T. G. & TAUB, D. D. 2007. Alterations in immunological and neurological gene expression patterns in Alzheimer's disease tissues. *Experimental Cell Research,* 313**,** 450-461.

WEIKOP, P., JENSEN, K. L. & THOMSEN, M. 2020. Effects of muscarinic M1 receptor stimulation on reinforcing and neurochemical effects of cocaine in rats. *Neuropsychopharmacology,* 45**,** 1994-2002.

WEINER, D. M., LEVEY, A. I. & BRANN, M. R. 1990. Expression of muscarinic acetylcholine and dopamine receptor mRNAs in rat basal ganglia. *Proceedings of the National Academy of Sciences,* 87**,** 7050.

WELDEMICHAEL, D. A. & GROSSBERG, G. T. 2010. Circadian Rhythm Disturbances in Patients with Alzheimer's Disease: A Review. *International Journal of Alzheimer's Disease,* 2010**,** 716453.

WELDON, D. T., ROGERS, S. D., GHILARDI, J. R., FINKE, M. P., CLEARY, J. P., O'HARE, E., ESLER, W. P., MAGGIO, J. E. & MANTYH, P. W. 1998. Fibrillar β-amyloid induces microglial phagocytosis, expression of inducible nitric oxide synthase, and loss of a select population of neurons in the rat CNS in vivo. *Journal of Neuroscience,* 18**,** 2161-2173.

WESS, J. 2004. Muscarinic Acetylcholine Receptor Knockout Mice: Novel Phenotypes and Clinical Implications. *Annual Review of Pharmacology and Toxicology,* 44**,** 423-450.

WHISTLER, J. L., ENQUIST, J., MARLEY, A., FONG, J., GLADHER, F., TSURUDA, P., MURRAY, S. R. & VON ZASTROW, M. 2002. Modulation of postendocytic sorting of G protein-coupled receptors. *Science,* 297**,** 615-620.

WHITEHOUSE, P. J., PRICE, D. L., CLARK, A. W., COYLE, J. T. & DELONG, M. R. 1981. Alzheimer disease: evidence for selective loss of cholinergic neurons in the nucleus basalis. *Annals of Neurology: Official Journal of the American Neurological Association and the Child Neurology Society,* 10**,** 122-126.

WHITEHOUSE, P. J., PRICE, D. L., STRUBLE, R. G., CLARK, A. W., COYLE, J. T. & DELONG, M. R. 1982. Alzheimer's disease and senile dementia: loss of neurons in the basal forebrain. *Science,* 215**,** 1237-1239.

WIESSNER, C., WIEDERHOLD, K.-H., TISSOT, A. C., FREY, P., DANNER, S., JACOBSON, L. H., JENNINGS, G. T., LÜÖND, R., ORTMANN, R. & REICHWALD, J. 2011. The second-generation active Aβ immunotherapy CAD106 reduces amyloid accumulation in APP transgenic mice while minimizing potential side effects. *Journal of Neuroscience,* 31**,** 9323-9331.

WILCOCK, G. K., GAUTHIER, S., FRISONI, G. B., JIA, J., HARDLUND, J. H., MOEBIUS, H. J., BENTHAM, P., KOOK, K. A., SCHELTER, B. O., WISCHIK, D. J., DAVIS, C. S., STAFF, R. T., VUKSANOVIC, V., AHEARN, T., BRACOUD, L., SHAMSI, K., MAREK, K., SEIBYL, J., RIEDEL, G., STOREY, J. M. D., HARRINGTON, C. R. & WISCHIK, C. M. 2018. Potential of Low Dose Leuco-Methylthioninium Bis(Hydromethanesulphonate) (LMTM) Monotherapy for Treatment of Mild Alzheimer's Disease: Cohort Analysis as Modified Primary Outcome in a Phase III Clinical Trial. *J Alzheimers Dis,* 61**,** 435-457.

WILTGEN, B. J., SANDERS, M. J., ANAGNOSTARAS, S. G., SAGE, J. R. & FANSELOW, M. S. 2006. Context fear learning in the absence of the hippocampus. *Journal of Neuroscience,* 26**,** 5484-5491.

WITTE, K., WITTE, E., SABAT, R. & WOLK, K. 2010. IL-28A, IL-28B, and IL-29: promising cytokines with type I interferon-like properties. *Cytokine Growth Factor Rev,* 21**,** 237-51.WOOTTEN, D., CHRISTOPOULOS, A., MARTI-SOLANO, M., BABU, M. M. & SEXTON, P. M. 2018. Mechanisms of signalling and biased agonism in G protein-coupled receptors. *Nature Reviews Molecular Cell Biology,* 19**,** 638-653.

WORLD HEALTH ORGANIZATION. 2021. *Dementia* [Online]. Available: https://www.who.int/news-room/fact-sheets/detail/dementia [Accessed 16 May 2022].

WORTHYLAKE, D. K., ROSSMAN, K. L. & SONDEK, J. 2000. Crystal structure of Rac1 in complex with the guanine nucleotide exchange region of Tiam1. *Nature,* 408**,** 682-688.

WOOTTEN, D., CHRISTOPOULOS, A., MARTI-SOLANO, M., BABU, M. M., & SEXTON, P. M. 2018. Mechanisms of signalling and biased agonism in G protein-coupled receptors. *Nature reviews Molecular cell biology*, 19(10), 638-653.

WU, Y.-H. & SWAAB, D. F. 2007. Disturbance and strategies for reactivation of the circadian rhythm system in aging and Alzheimer's disease. *Sleep Medicine,* 8**,** 623-636.

WYSSENBACH, A., QUINTELA, T., LLAVERO, F., ZUGAZA, J. L., MATUTE, C. & ALBERDI, E. 2016. Amyloid β ‐induced astrogliosis is mediated by β1 ‐integrin via NADPH oxidase 2 in Alzheimer's disease. *Aging Cell,* 15**,** 1140-1152.

XIANG, Z., THOMPSON, A. D., JONES, C. K., LINDSLEY, C. W. & CONN, P. J. 2012. Roles of the M1 muscarinic acetylcholine receptor subtype in the regulation of basal ganglia function and implications for the treatment of Parkinson's disease. *Journal of Pharmacology and Experimental Therapeutics,* 340**,** 595-603.

XU, W., TAN, L., WANG, H.-F., JIANG, T., TAN, M.-S., TAN, L., ZHAO, Q.-F., LI, J.-Q., WANG, J. & YU, J.-T. 2015. Meta-analysis of modifiable risk factors for Alzheimer's disease. *Journal of Neurology, Neurosurgery & Psychiatry,* 86**,** 1299-1306.

YAMADA, M., CHIBA, T., SASABE, J., NAWA, M., TAJIMA, H., NIIKURA, T., TERASHITA, K., AISO, S., KITA, Y. & MATSUOKA, M. 2005. Implanted cannula-mediated repetitive administration of Aβ25–35 into the mouse cerebral ventricle effectively impairs spatial working memory. *Behavioural brain research,* 164**,** 139-146.

YAMADA, M., LAMPING, K. G., DUTTAROY, A., ZHANG, W., CUI, Y., BYMASTER, F. P., MCKINZIE, D. L., FELDER, C. C., DENG, C.-X. & FARACI, F. M. 2001. Cholinergic dilation of cerebral blood vessels is abolished in M5 muscarinic acetylcholine receptor knockout mice. *Proceedings of the National Academy of Sciences,* 98**,** 14096-14101.

YAMASAKI, M., MATSUI, M. & WATANABE, M. 2010. Preferential localization of muscarinic M1 receptor on dendritic shaft and spine of cortical pyramidal cells and its anatomical evidence for volume transmission. *Journal of Neuroscience,* 30**,** 4408-4418.

YAMAZAKI, Y., ZHAO, N., CAULFIELD, T. R., LIU, C.-C. & BU, G. 2019. Apolipoprotein E and Alzheimer disease: pathobiology and targeting strategies. *Nature Reviews Neurology,* 15**,** 501-518.

YANG, B., TREWEEK, J. B., KULKARNI, R. P., DEVERMAN, B. E., CHEN, C.-K., LUBECK, E., SHAH, S., CAI, L. & GRADINARU, V. 2014. Single-cell phenotyping within transparent intact tissue through whole-body clearing. *Cell,* 158**,** 945-958.

YI, F., BALL, J., STOLL, K. E., SATPUTE, V. C., MITCHELL, S. M., PAULI, J. L., HOLLOWAY, B. B., JOHNSTON, A. D., NATHANSON, N. M. & DEISSEROTH, K.

2014. Direct excitation of parvalbumin‐positive interneurons by M1 muscarinic acetylcholine receptors: roles in cellular excitability, inhibitory transmission and cognition. *The Journal of physiology,* 592**,** 3463-3494.

YIANNOPOULOU, K. G. & PAPAGEORGIOU, S. G. 2013. Current and future treatments for Alzheimer's disease. *Therapeutic advances in neurological disorders,* 6**,** 19-33.

YOSHIYAMA, Y., HIGUCHI, M., ZHANG, B., HUANG, S.-M., IWATA, N., SAIDO, T. C., MAEDA, J., SUHARA, T., TROJANOWSKI, J. Q. & LEE, V. M.-Y. 2007. Synapse loss and microglial activation precede tangles in a P301S tauopathy mouse model. *Neuron,* 53**,** 337-351.

YOUNG, M. B. & THOMAS, S. A. 2014. M1-Muscarinic Receptors Promote Fear Memory Consolidation via Phospholipase C and the M-Current. *The Journal of Neuroscience,* 34**,** 1570.

YUE, M., HANNA, A., WILSON, J., RODER, H. & JANUS, C. 2011. Sex difference in pathology and memory decline in rTg4510 mouse model of tauopathy. *Neurobiology of Aging,* 32**,** 590-603.

ZAMAH, A. M., DELAHUNTY, M., LUTTRELL, L. M. & LEFKOWITZ, R. J. 2002. Protein kinase A-mediated phosphorylation of the β2-adrenergic receptor regulates its coupling to Gs and Gi: demonstration in a reconstituted system. *Journal of Biological Chemistry,* 277**,** 31249-31256.

ZHANG, X. C., LIU, J. & JIANG, D. 2014. Why is dimerization essential for class-C GPCR function? New insights from mGluR1 crystal structure analysis. *Protein Cell,* 5**,** 492-5.

ZHANG, X. X., TIAN, Y., WANG, Z. T., MA, Y. H., TAN, L. & YU, J.-T. 2021. The Epidemiology of Alzheimer's Disease Modifiable Risk Factors and Prevention. *The Journal of Prevention of Alzheimer's Disease,* 8**,** 313-321.

ZHOU, L., MCINNES, J., WIERDA, K., HOLT, M., HERRMANN, A. G., JACKSON, R. J., WANG, Y.-C., SWERTS, J., BEYENS, J. & MISKIEWICZ, K. 2017. Tau association with synaptic vesicles causes presynaptic dysfunction. *Nature communications,* 8**,** 1-13.

ZTAOU, S., MAURICE, N., CAMON, J., GUIRAUDIE-CAPRAZ, G., KERKERIAN-LE GOFF, L., BEURRIER, C., LIBERGE, M. & AMALRIC, M. 2016. Involvement of Striatal Cholinergic Interneurons and M1 and M4 Muscarinic Receptors in Motor Symptoms of Parkinson's Disease. *The Journal of Neuroscience,* 36**,** 9161.

ZUKOR, K. A., KENT, D. T. & ODELBERG, S. J. 2010. Fluorescent whole‐mount method for visualizing three‐dimensional relationships in intact and regenerating adult newt spinal cords. *Developmental dynamics,* 239**,** 3048-3057.